

NASA CR-179534
PWA-5594-333



ENERGY EFFICIENT ENGINE

PIN FIN AND CERAMIC COMPOSITE SEGMENTED LINER

COMBUSTOR SECTOR RIG TEST REPORT

by:

D. J. Dubiel, R. P. Lohmann, S. Tanrikut, and P. M. Morris

UNITED TECHNOLOGIES CORPORATION
Pratt & Whitney
Engineering Division

limitations shall be considered void after two (2) years after date of such data. These
~~_____~~

Prepared for:

NATIONAL AERONAUTICS AND SPACE ADMINISTRATION
Lewis Research Center
Cleveland, Ohio 44135

Contract NAS3-20646


(NASA-CR-179534) ENERGY EFFICIENT ENGINE
PIN FIN AND CERAMIC COMPOSITE SEGMENTED
LINER COMBUSTOR SECTOR RIG TEST REPORT
(PWA) 218 p

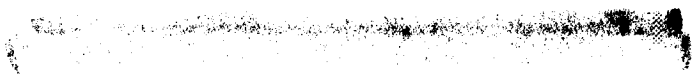
N90-28567

CSCL 21E

Unclass

G3/07 0304593

1. REPORT NO. NASA CR-179534	2. GOVERNMENT AGENCY	3. RECIPIENT'S CATALOG NO.	
4. TITLE AND SUBTITLE Energy Efficient Engine Pin Fin and Ceramic Composite Segmented Liner Combustor Sector Rig Test Report		5. REPORT DATE September 1986	
		6. PERFORMING ORG. CODE	
7. AUTHOR(S) D. J. Dubiel, R. P. Lohmann, S. Tanrikut, and P. M. Morris		8. PERFORMING ORG. REPT. NO. PWA-5594-333	
9. PERFORMING ORG. NAME AND ADDRESS UNITED TECHNOLOGIES CORPORATION Pratt & Whitney, Engineering Division 400 Main St., East Hartford, CT 06108		10. WORK UNIT NO.	
		11. CONTRACT OR GRANT NO. NAS3-20646	
12. SPONSORING AGENCY NAME AND ADDRESS National Aeronautics and Space Administration Lewis Research Center 21000 Brookpark Road, Cleveland, Ohio 44135		13. TYPE REPT./PERIOD COVERED Contractor Report	
		14. SPONSORING AGENCY CODE	
15. SUPPLEMENTARY NOTES Combustor Program Manager: Michael R. Vanco NASA-Lewis Research Center, Cleveland, Ohio			
16. ABSTRACT <p>Under the NASA-sponsored Energy Efficient Engine program, Pratt & Whitney has successfully completed a comprehensive test program using a 90-degree sector combustor rig that featured an advanced two-stage combustor with a succession of advanced segmented liners.</p> <p>Building on the successful characteristics of the first generation counter-parallel Finwall cooled segmented liner, design features of an improved performance metallic segmented liner were substantiated through representative high pressure and temperature testing in a combustor atmosphere. This second generation liner was substantially lighter and lower in cost than the predecessor configuration.</p> <p>The final test in this series provided an evaluation of ceramic composite liner segments in a representative combustor environment. It was demonstrated that the unique properties of ceramic composites, low density, high fracture toughness, and thermal fatigue resistance can be advantageously exploited in high temperature components.</p> <p>Overall, this Combustor Sector Rig Test program has provided a firm basis for the design of advanced combustor liners.</p>			
17. KEY WORDS (SUGGESTED BY AUTHOR(S)) Two-Stage Combustor, Segmented Liner, Energy Efficient Engine, Ceramic Composite Combustor		18. DISTRIBUTION STATEMENT 	
19. SECURITY CLASS THIS (REPT) Unclassified	20. SECURITY CLASS THIS (PAGE) Unclassified	21. NO. PGS	22. PRICE



1

FOREWORD

The Energy Efficient Engine Component Development and Integration Program is being conducted under parallel National Aeronautics and Space Administration (NASA) contracts with Pratt & Whitney Group and General Electric Company. The overall project at Pratt & Whitney under contract NAS3-20646 is under the current direction of Mr. Carl C. Ciepluch. Mr. Michael R. Vanco is the NASA Project Engineer responsible for the portion of the project described in this report. Mr. David E. Gray is the manager of the Energy Efficient Engine program at Pratt & Whitney. Drs. R. P. Lohmann, S. Tanrikut and Messrs D. J. Dubiel, W. Greene and P. M. Morris are the engineers responsible for the work described in this report.

TABLE OF CONTENTS

<u>Section</u>	<u>Page</u>
1.0 SUMMARY	1
2.0 INTRODUCTION	2
3.0 APPROACH	4
3.1 General Combustor Configuration	4
3.2 Liner Configurations	6
3.2.1 Segmented Counter-Parallel Finwall® (CPFW)	6
3.2.2 Segmented Pin-Fin Liner	9
3.2.2.1 Aerothermal Design Features	11
3.2.2.2 Mechanical Design Features	18
3.2.2.3 Pin-Fin Liner Advantages	18
3.2.3 Ceramic Composite	22
3.2.3.1 Design Background	22
3.2.3.2 Sector Rig Liner Definition	32
3.2.3.3 Ceramic Composite Material Selection	37
3.2.3.4 Sector Rig Liner Analysis	39
3.2.3.5 Liner Fabrication and Assembly	43
4.0 TEST PROGRAM PLAN, FACILITIES AND INSTRUMENTATION	56
4.1 Sector Rig Configuration	56
4.2 Test Facilities	56
4.2.1 Data Acquisition Systems	58
4.3 Test Instrumentation	59
4.3.1 Overall Performance Instrumentation	59
4.3.2 Exit Instrumentation	59
4.3.3 Combustor Liner Instrumentation	61
4.3.4 Radiometers	67
4.4 Test Plan	69
4.5 Test Procedures	73
4.6 Typical Test Run Chronology	73
5.0 COMBUSTOR SECTOR RIG TEST RESULTS AND ANALYSIS	76
5.1 Integration with Component Program	76
5.1.1 Background	76
5.1.2 Combustor Performance Assessment	78
5.1.3 Wall Temperature and Radiometer Measurements	84
5.1.4 Summary of Run 23 Results	85

TABLE OF CONTENTS

<u>Section</u>	<u>Page</u>
5.2 Pin Fin Liner Test Results	86
5.2.1 Airflow Distributions	87
5.2.2 Comparison of CPFW and Pin-Fin Liners	87
5.2.3 Pilot and Main Zone Wall Temperatures	91
5.2.4 Pilot and Main Zone Radiometers	92
5.2.5 Wall Temperature Variation with Pressure	98
5.2.6 Radiation Flux Variation with Pressure	98
5.2.7 Analysis	105
5.2.7.1 Estimation of Flame Temperature Distribution	105
5.2.7.2 Comparison of Calculated and Measured Quantities	108
5.2.7.3 Effect of Geometric Changes on Wall Temperature	108
5.3 Ceramic Composite Liner Evaluation Results	112
5.3.1 Nondestructive Inspection	119
5.3.2 Destructive Testing	124
6.0 CONCLUDING REMARKS	129
APPENDIX A DATA ANALYSIS PROCEDURES	130
A.1 Performance Data	131
A.2 Emission Data	132
APPENDIX B CERAMIC COMPOSITE MATERIAL CHARACTERIZATION	136
B.1 Introduction	136
B.2 Static Load Characteristics	137
B.3 Mechanical Fatigue Testing	147
B.4 Creep Characteristics	151
B.5 Thermal Fatigue Tests	154
B.6 Long Duration Thermal Durability	160
APPENDIX C RADIOMETER AND LINER THERMOCOUPLE TEST DATA	173
Radiometer Test Data	173
Liner Thermocouple Data	184
LIST OF SYMBOLS	202
REFERENCES	203
DISTRIBUTION LIST	204

LIST OF ILLUSTRATIONS

<u>Figure Number</u>	<u>Title</u>	<u>Page</u>
2-1	Energy Efficient Engine Sector Combustor Rig Test Program Major Milestones	3
3-1	Energy Efficient Engine Combustor Design and Features	5
3-2	Advanced Segmented Liner With Counter-Parallel Finwall® (CPFW) Cooling Technique	7
3-3	Sector Combustor Rig Outer Liner/Bulkhead Assembly	8
3-4	Conceptual Definition of Second Generation Segmented Liner	10
3-5	Parametric Design Variables for Pin-Fin Cooling Geometries	12
3-6	Combined Map for Runs 18, 20 and 22 with CPFW Streak Metal Temperature Predictions	13
3-7	Maximum Wall Temperature Versus Total Cooling Flux	13
3-8	Effect of Trailing Edge Pin Height on Maximum Panel Temperature	15
3-9	Sensitivity of Trailing Edge Temperatures and Cooling Flow to Pin-Tip Clearance	16
3-10	Recommended Design and Variations Evaluated	17
3-11	Comparison of CPFW and Pin-Fin Metal Temperature, °C (°F), and Cooling Flow Predictions	17
3-12	Segment Geometric and Flow Characteristics	19
3-13	Mechanical Features of the Pin-Fin Cast Segments	20
3-14	Location and Magnitude of Maximum Bending Stresses Calculated	<u>20</u>
3-15	Sector Rig Shell and Cast Segments	21
3-16	Ceramic Composite Combustor Liner Configuration	26
3-17	Axial Temperature Distribution in Composite Panel and Shell During Takeoff	27

LIST OF ILLUSTRATIONS

<u>Figure Number</u>	<u>Title</u>	<u>Page</u>
3-18	Schematic Representation of Fiber Orientations in Ceramic Composite Panel	29
3-19	Structural Model of SiC-LAS Composite Liner	31
3-20	Highlights of Stress Distribution in the Composite Liner Panel	31
3-21	Cross Section of the Sector Combustor Rig with Ceramic Composite Inner Liner	33
3-22	Ceramic Composite Inner Liner Design Features	34
3-23	Ceramic Composite Liner Panel Attachment Methods	36
3-24	Schematic Representation of Woven Fiber Composite Materials	38
3-25	Schematic Representation of Improved Fiber Orientation in Ceramic Composite Panels	38
3-26	Surface Temperature Distributions in Representative Composite Panels in the Sector Combustor Rig	41
3-27	Cooling Air Distribution and Peak Hot Side Panel Temperatures in the Sector Rig Ceramic Composite Inner Liner	44
3-28	Sensitivity of Composite Liner Surface Temperature to Cooling Air Slot Height	45
3-29	Die for Hot Pressing a Panel of the EEE Combustor Rig Liner	47
3-30	Eight Silicon Carbide Fiber Plies used to Construct a Liner Panel (Numbers Indicate Stacking Sequence)	48
3-31	Panels from Row 5 (Top) and Row 3 (Bottom) of Liner After Drilling and End Trimming Operations (Ruler Scale in Inches)	50
3-32	Complete Set of Ceramic Composite Liner Panels for EEE Combustor Rig Inner Liner (Ruler Scale in Inches)	52
3-33	Inner Burner Liner Sheet for Ceramic Composite Liner	54
3-34	Ceramic Composite Liner Panels Installed on Inner Liner Shell of Combustor Sector Rig	54

LIST OF ILLUSTRATIONS

<u>Figure Number</u>	<u>Title</u>	<u>Page</u>
3-35	External Surface of Inner Liner Shell After Installing Ceramic Composite Liner Panels	55
4-1	Cross Sectional View of Sector Combustor Test Rig	57
4-2	Installation of Chromel/Alumel Thermocouples	62
4-3	Thin Film Sensor Installation	62
4-4	Thermocouple Installation for Run 23	63
4-5	Thermocouple Installation for Run 24	64
4-6	Thermocouple Installation Layout for Run 25	64
4-7	Schematic Diagram of the Inner Liner of the Sector Combustor Rig Showing Thermal Paint Application on Ceramic Composite Liner Panels	66
4-8	Radiometer Installation in Outer Liner	68
4-9	Porous Plug Radiometer Schematic	68
4-10	Hot Side of Ceramic Combustor Inner Liner After Completion of Run 26 Durability Test	75
5-1	Comparison of Cast Component and Sheet Metal Sector Rig Carburetor Tubes	77
5-2	Comparison of Carburetor Tube Fuel Spray Characterization	79
5-3	Combustor Airflow Distribution	79
5-4	Idle Emissions	81
5-5	Approach Emissions - Run 23	81
5-6	Climb Emissions - Run 23	82
5-7	Exit Temperature Distribution - Run 23	83
5-8	Radial Profile - Run 23	83

LIST OF ILLUSTRATIONS

<u>Figure Number</u>	<u>Title</u>	<u>Page</u>
5-9	Pin-Fin Liner Airflow Distribution	88
5-10	Variation of Combustor Exit Temperature	89
5-11	Pin-Fin Inner Liner After Run 24. Peak Condition: $T_{T3} = 566^{\circ}\text{C}$ (1050°F); $P_{T3} = 2.8$ MPa (400 psia); $T_{T4} = 1466^{\circ}\text{C}$ (2670°F)	91
5-12	Comparison of Thermocouple Types Installed In Similar Locations	93
5-13	Effect of Combustor Inlet Temperature on Pin-Fin Liner Wall Temperature	94
5-14	Variations in Main Zone Panel Temperature (Thermocouple No. 29)	95
5-15	Pilot Zone Radiometer Measurements at $P_{T3} = 1.034$ MPa (150 psia); Radiometers 1 and 2	96
5-16	Pilot Zone Radiation Measurements at $P_{T3} = 2.758$ MPa (400 psia); Radiometers 1 and 2	97
5-17	Main Zone Radiometer Measurements at $P_{T3} = 2.758$ MPa (400 psia); Radiometers 3 & 4	99
5-18	Main Zone Radiometer Measurements at $P_{T3} = 2.758$ MPa (400 psia); Radiometer 5	100
5-19	Variation of Main Zone Panel Wall Temperatures with Pressure (T/C #30)	101
5-20	Variation of Pilot Zone Panel Wall Temperatures with Pressure (T/C #3)	102
5-21	Variation of Pilot Zone Radiation Flux with Pressure	103
5-22	Variation of Main Zone Radiation Flux with Pressure	104
5-23	Computational Fluid Dynamics Model of Combustor	106
5-24	One-Dimensional Flame Temperature Distribution vs. TEACH Prediction	107
5-25	Predicted vs. Measured Heat Flux	109
5-26	Comparison of Predicted and Wall Temperatures on Panel #5	110

LIST OF ILLUSTRATIONS

<u>Figure Number</u>	<u>Title</u>	<u>Page</u>
5-27	Effect of Removing Casting Blockage on Panel #1 Wall Temperature	111
5-28	Comparison of Dense (Run 25) vs Sparse (Run 24) Pin-Fin Array	113
5-29	Thermal Paint on Cold Side Surfaces of Ceramic Composite Liner Panels	114
5-30	Ceramic Composite Liner Panel Hot Side Temperature Distribution	116
5-31	Ceramic Composite Liner Panel Cold Side Temperature Distribution	118
5-32	Condition of Composite Ceramic Liner Panels Before and After Combustor Rig Testing	120
5-33	Post-Test View of Row 2 and 3 Panels Showing the Through Thickness Crack in the Corner of the Row 2 Panel	121
5-34	Surface Bubbling on the Hot Side of Row 1 and 2 Panels	123
5-35	Residual Strength of Specimens from Ceramic Composite Liner Panels	125
5-36	Fracture Morphology of Residual Strength Specimens from Ceramic Composite Liner Panels	128
B-1	High Temperature Flexural Test Facility	137
B-2	Four Point Flexural Test Geometry	138
B-3	Stress-Strain Behavior for SiC-LAS III Specimens at Room Temperature	139
B-4	Fracture Surfaces of SiC-LAS III Specimens Failed in Flexure at Room Temperature	140
B-5	Load-Deflection Characteristics of SiC-LAS III Composites at Elevated Temperatures	143

LIST OF ILLUSTRATIONS

<u>Figure Number</u>	<u>Title</u>	<u>Page</u>
B-6	Ultimate Strength of 12HS SiC-LAS III Composite in Air	144
B-7	Ultimate Strength of (0/+45/90/-45) SiC-LAS III Composite in Air	145
B-8	Ultimate Strength of (0/+45/90/-45) SiC-LAS II Composite in Air	146
B-9	Cyclic Fatigue Strength of SiC-LAS Composites in Air	148
B-10	Fracture Surface of 12 HS Woven Fiber Specimen After Static Failure Following 100,000 Fatigue Cycles at 1038°C (1900°F)	150
B-11	Fracture Surface of 0/+45/90/-45 SiC-LAS III Specimen After Static Failure Following 100,000 Fatigue Cycles at 1038°C (1900°F)	150
B-12	Creep Characteristics of 12 HS Woven SiC-LAS III Composite Material	152
B-13	Creep Characteristics of (0/+45/90/-45) SiC-LAS III Composite Material	152
B-14	Schematic View of Thermal Fatigue Test Apparatus	155
B-15	Hot Side of 0/+45/-45/90 SiC-LAS III Specimen After Sequence A Thermal Fatigue Test	158
B-16	Cold Side of 0/+45/-45/90 SiC-LAS III Specimen After Sequence A Thermal Fatigue Test	159
B-17	Test Apparatus for Long Duration Thermal Exposure Tests	160
B-18	SiC-LAS II Panels in Test Fixture After 100-Hour Thermal Durability Test	163
B-19	SiC-LAS III Panels in Test Fixture After 100-Hour Thermal Durability Test	164
B-20	Radiographic Analysis of SiC-LAS II Panels After Long Term Durability Tests	165
B-21	Radiographic Analysis of SiC-LAS III Panels After Long Term Durability Tests	166

LIST OF ILLUSTRATIONS

<u>Figure Number</u>	<u>Title</u>	<u>Page</u>
B-22	Photomicrograph of a Transverse Section through SiC-LAS III Panel 3 Showing "Deposit" Layer	168
B-23	SiC-LAS III Panels with Axial and Transverse Surface Fiber Direct Direction	173
C-1	Radiometer Nomenclature	174
C-2	Thermocouple Installation Layout for Run 24	185
C-3	Thermocouple Installation Layout for Run 25	185

LIST OF TABLES

<u>Table Number</u>	<u>Title</u>	<u>Page</u>
3-I	Breakdown of EEE Sector Rig CPFW Liner Costs	9
3-II	Combustor Operating Conditions for Design Analysis (Hot Day, 29°C (84°F) Sea Level Takeoff Conditions)	11
3-III	Comparison of Properties of Unidirectional Ceramic Composites with High Temperature Metals	23
4-I	Sector Combustor Rig Instrumentation List	60
4-II	Sector Combustor Rig Test Program	69
4-III	Test Matrix for Test 1 -- Baseline Thermal, Emissions and Performance Evaluation	70
4-IV	Test Matrix for Tests 2 and 3 -- Pin Fin Liner Thermal Mechanical Evaluation	72
4-V	Test Matrix for Evaluation of Ceramic Composite Liner	73
5-I	Carburetor Tube Air Flow Test Summary	78
5-II	Summary of Run 23 Results	86
5-III	Peak Thermal Load Conditions	87
5-IV	Comparison of CPFW and Pin-Fin Liner Maximum Wall Temperatures	90
5-V	Survival Rate of Thermocouple Types	91
A-I	Summary of Reported Combustor Performance Parameters	131
A-II	Definition of EPAP Conditions and EPAP Coefficients for Energy Efficient Engine	135
B-I	Static Strength Characteristics of SiC-LAS III Composites at Room Temperature	142
B-II	Results of SiC-LAS Specimen Fatigue Tests	149
B-III	Results of Flexural Creep Testing of SiC-LAS Material in Air	153
B-IV	Thermal Fatigue Test Sequence A	156

LIST OF TABLES

<u>Table Number</u>	<u>Title</u>	<u>Page</u>
B-V	Maximum Panel Surface Temperature During Long-Term Thermal Durability Tests	161
B-VI	Residual Strength and Fracture Morphology of Specimens Cut from SiC-LAS III Panel Used in 100-Hour Thermal Endurance Test	170

SECTION 1.0 SUMMARY

Under the NASA-sponsored Energy Efficient Engine Program, Pratt & Whitney has completed a comprehensive test program using a 90-degree combustor sector rig that features an advanced two-stage combustor with a succession of segmented combustor liners. The combustor sector rig has proved to be a very valuable platform for the evolution of the segmented liner concept. Building on the successful characteristics of the first generation CPFW liner, design features for a second generation of a light weight, lower cost, and improved performance metallic segmented liner were identified. These design features, which were a natural extension to the successful CPFW liner, were substantiated through representative high pressure and temperature testing in a combustor environment.

The combustor sector rig testing of the ceramic composite liner panels demonstrated that, while additional development of these materials is required for long term operation, they have significant potential for use in the hot section of future engines. This program demonstrated that the unique properties of ceramic composites of low density, high fracture toughness and thermal fatigue resistance can be advantageously exploited in high temperature components.

As engine pressure ratios increase with demand for higher efficiency cycles in future engines, the radiant portion of the total heat flux to the combustor liner increases substantially. The ability to test the sector rig at elevated pressure and temperature levels provided a vehicle to supplement the meager radiation heat flux data base previously available. As a complement to radiation measurements, more accurate and effective ways to measure liner wall temperatures were explored in a realistic combustion environment.

Closure with the Annular Component Program was effected by the demonstration of main zone fuel injection modifications that substantially reduced inefficiency at part power conditions where fuel staging between the two zones takes place. The demonstrated reductions in carbon monoxide (CO) and total unburned hydrocarbon (THC) emissions were adequate to meet program emissions goals.

Overall, the Combustor Sector Rig Test Program has provided a firm basis for the design of advanced combustor liners. The technology evolved through these efforts is applicable to the next generation of gas turbine engine combustors. Furthermore, it has provided a significant step toward the design of light weight, highly durable, and cost effective combustor liners that meets the operating demands for commercial or military aircraft operating in the late 1980's to early 1990's time period and provided direction for development of even more advanced concepts.

SECTION 2.0 INTRODUCTION

The Energy Efficient Engine Component Development and Integration Program, sponsored by the National Aeronautics and Space Administration, is directed towards developing the technology to achieve greater fuel efficiency for future commercial aircraft gas-turbine engines. The goals established for the overall program include a reduction in fuel consumption of at least 12 percent and a reduction in direct operating costs of at least 5 percent relative to the Pratt & Whitney JT9D-7A base engine. To demonstrate the technology to attain these goals, the Energy Efficient Engine Program is organized into three tasks which involve the following:

- Task 1 Propulsion System Analysis, Design and Integration
- Task 2 Component Analysis Design and Development
- Task 4 Integrated Core/Low Spool Design, Fabrication and Test.

Under Task 2, a Combustor Component Test Program has been established to evaluate and verify advanced combustion technology concepts for the Energy Efficient Engine combustor component. This combustor is an annular two-stage design with counter-parallel Finwall[®] cooled segmented liners. Previous tests, both with a sector combustor rig and a full annular combustor rig, have successfully demonstrated the design features for lower emissions and improved durability. In a continuation of the technology extension process, additional sector combustor rig testing was conducted with the main purpose of evaluating a second generation of the segmented liners. The new designs offer a potential to significantly reduce fabrication costs and weight as well as improve durability. A supporting aero/thermal design effort identified two promising ceramic composite constructions. The ceramic composite material has about one-third the density of current metallic liner materials and offers potentially lower fabrication costs and higher temperature capability. The final phase of testing evaluated these ceramic composite liner segments. In addition, these series of tests provided generically useful heat flux data for the design of advanced combustion systems operating in a high pressure environment.

This report presents the results of the Pin Fin Liner and Ceramic Composite Liner Combustor Sector Rig Test Program. The period of time over which the program was conducted is presented in Figure 2-1. The following section, Section 3, presents a description of the baseline Energy Efficient Engine combustor and an overview of the aerothermal and mechanical design details of the two new combustor liner designs. Section 4 describes the test program, test facilities, and instrumentation. In Section 5, a complete discussion of the test results is presented. Concluding remarks pertaining to the tests are in Section 6.

Three appendices are included in this report. Appendix A provides a description of data analysis procedures utilized in formulating aero/thermal performance parameters from test measurements. Appendix B contains a detailed description of the ceramic composite material characterization program. Appendix C contains all combustor performance data, as well as compilations of wall temperatures and radiometer data.

CERAMIC COMPOSITE
CHARACTERIZATION

RIG ASSEMBLY

RIG TEST 23

RIG TEST 24

RIG TEST 25

RIG TEST 26

DATA ANALYSIS

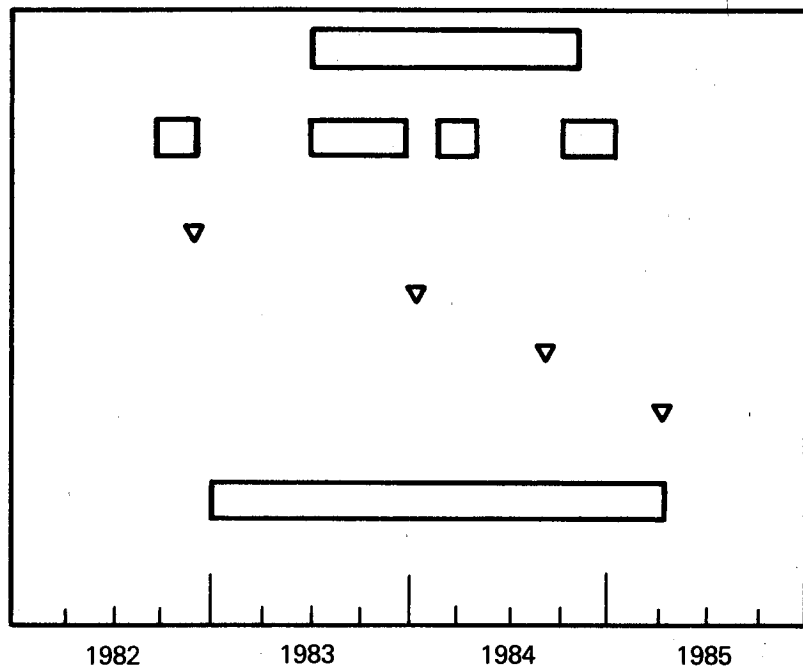


Figure 2-1 Energy Efficient Engine Sector Combustor Rig Test Program Major Milestones

SECTION 3.0 APPROACH

3.1 GENERAL COMBUSTOR CONFIGURATION

The Energy Efficient Engine combustor design is based on the technology investigated in the Experimental Clean Combustor Program sponsored by the National Aeronautics and Space Administration. It combines this technology with advances in the areas of aerodynamics and structure-mechanics to provide a compact system capable of low emissions and high performance. For commercial acceptance, the design also addresses durability, mechanical simplicity and the capability to operate on broad specification fuels. Figure 3-1 presents a cross-sectional view of the combustor and identifies the salient features. These include a high performance diffuser, two-zone combustion system and segmented liners.

The diffuser section consists of a short prediffuser and dump region and the inner and outer annuli around the combustor liners. The prediffuser flowpath is a strutless, curved-wall design that turns the high-pressure compressor exit flow towards the combustor center line to reduce pressure loss from flow turning in the combustor hood section. The dump region contains the structural struts which are designed as aerodynamic members of the diffuser to minimize combustor flow maldistribution and to enhance liner durability and pattern factor.

The combustor has two distinct combustion zones - a pilot and a main zone. The pilot zone operates at all flight conditions and is designed to minimize emissions at idle, plus ensure adequate stability and relight characteristics. In the main zone, lean combustion occurs to minimize oxides of nitrogen and smoke. This zone is operative at conditions above idle. In comparison to current single-zone combustors, this two-zone system provides more effective control of exhaust emissions throughout the flight spectrum.

Emissions reduction is further enhanced by the adaptation of the Vorbix combustion method (vortex mixing and burning) in the main zone. This approach, as demonstrated under the Experimental Clean Combustor Program, exploits the benefit of swirling airflow to promote a rapid and thorough mixing of the fuel and air for a more uniform combustion process. The fuel injector in the pilot zone is a single pipe aerated design that relies on the shearing action of low velocity fuel surrounded by high velocity air streams for improved atomization. In the main zone, a compact carburetor tube injection system mixes the fuel and air prior to introduction into the combustion zone for better atomization and lower smoke emissions.

Both combustion zones are enclosed by a unique segmented liner construction. Although it represents a considerable departure from conventional louvered designs, this concept offers the potential for superior durability, better maintainability and the capability to operate at higher combustion pressure levels expected in future commercial aircraft propulsion systems. Advanced metallics as well as ceramic composite materials are both suitable for the segmented liner concept.

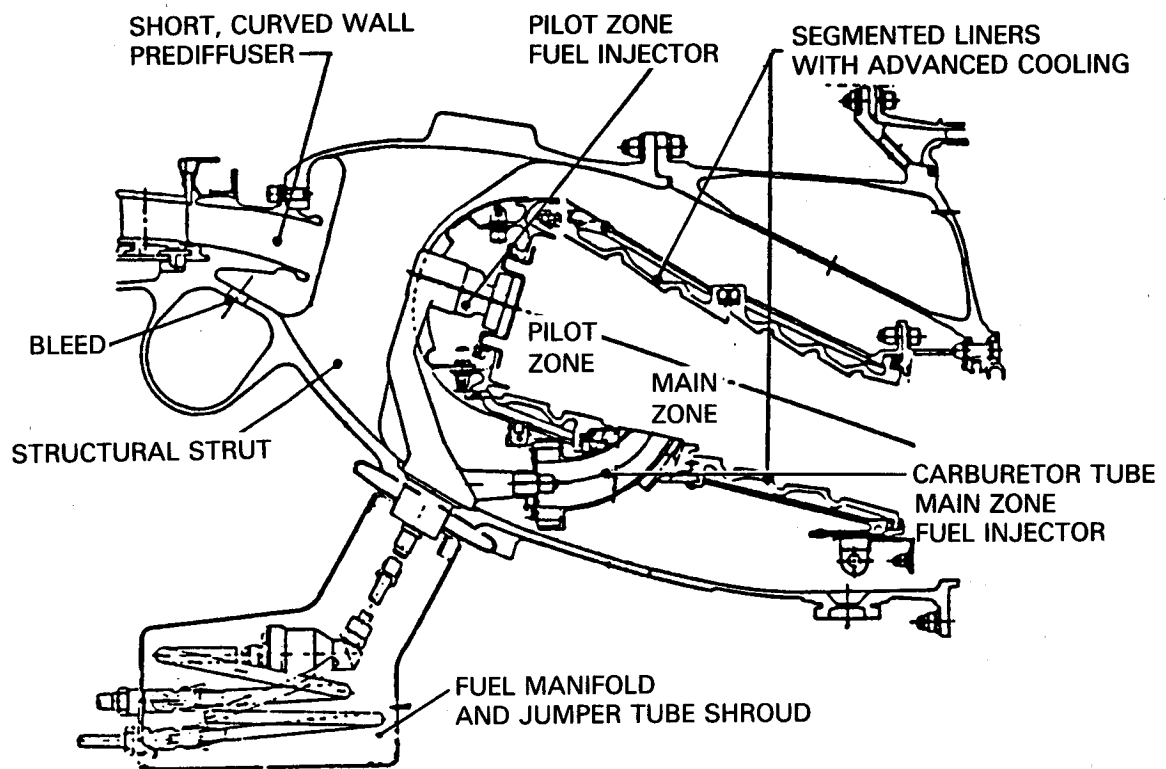


Figure 3-1 Energy Efficient Engine Combustor Design and Features

3.2 LINER CONFIGURATIONS

Aerothermal performance, emissions limits and durability requirements of the Energy Efficient Engine established the need for a segmented combustor liner design. Three generations of segmented liners have evolved starting from the original component program through the subsequent technology extension programs. The design features of these combustor liner configurations are discussed in this section.

3.2.1 Segmented Counter-Parallel Finwall[®] (CPFW)

The CPFW liner configuration, shown in Figure 3-2, was the foundation on which the technology extension programs were built. The design details of this liner are fully documented in References 10 and 11. A brief overview is provided here for completeness.

The design objectives for the segmented liner were to:

1. eliminate stress in the hoop direction that plagues conventional sheet metal and rolled ring liners
2. utilize high temperature capable materials such as turbine alloys or ceramics
3. use efficient convective cooling schemes.

The viability of this approach was successfully demonstrated in both the Sector Combustor Rig Technology Program and the Combustor Component Test Program (References 10 and 12).

The flowpath for the CPFW cooling scheme consists of a series of axial cooling channels supplied by cooling air through slots located approximately half-way along the length of the panel. The air flows both upstream and downstream in the discrete cooling passages, and the exiting air flows along the hot liner surface to provide a cooling film. There are generally three or four cooling panels integral in the liner segment. The segments are stacked on a machined support cage in both axial and circumferential direction. Axial and circumferential feather seals on the sides of the segments are used to control leakage between adjacent segments.

The liner segments, which are an investment cast nickel base alloy (B1900+Hf), required a series of different finish machining operations prior to final assembly. These processes included electro-discharge machining (EDM), electro-chemical machining (ECM) and conventional grinding. The need to support the total pressure drop across the combustor liner and the increased wall thickness to accommodate machining processes result in a structure that is heavier than a conventional sheet metal liner.

The CPFW outer liner and combustor bulkhead were used in all phases of the Sector Combustor Rig Test Program. A view of this assembly is shown in Figure 3-3.

ORIGINAL PAGE 13
OF POOR QUALITY

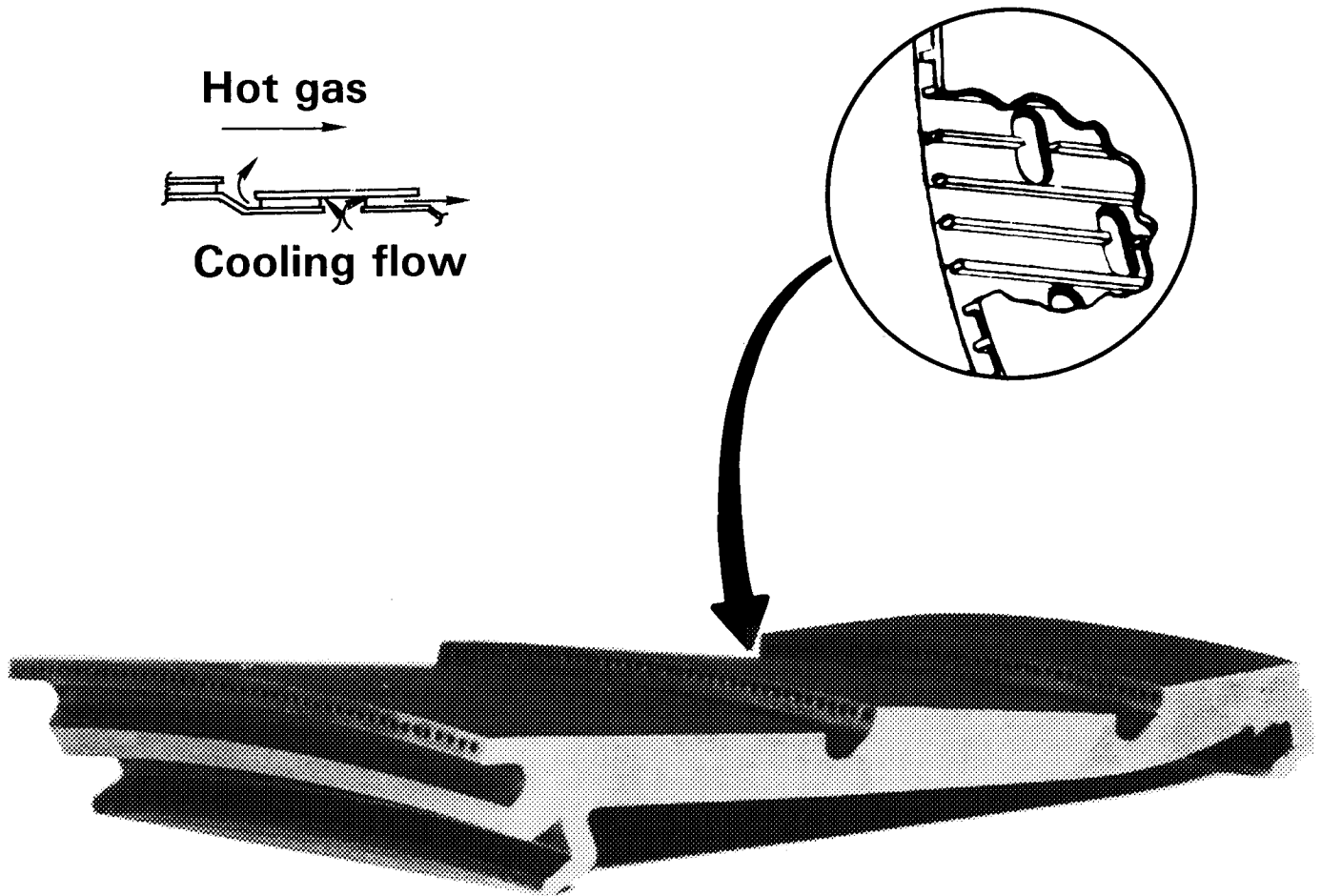
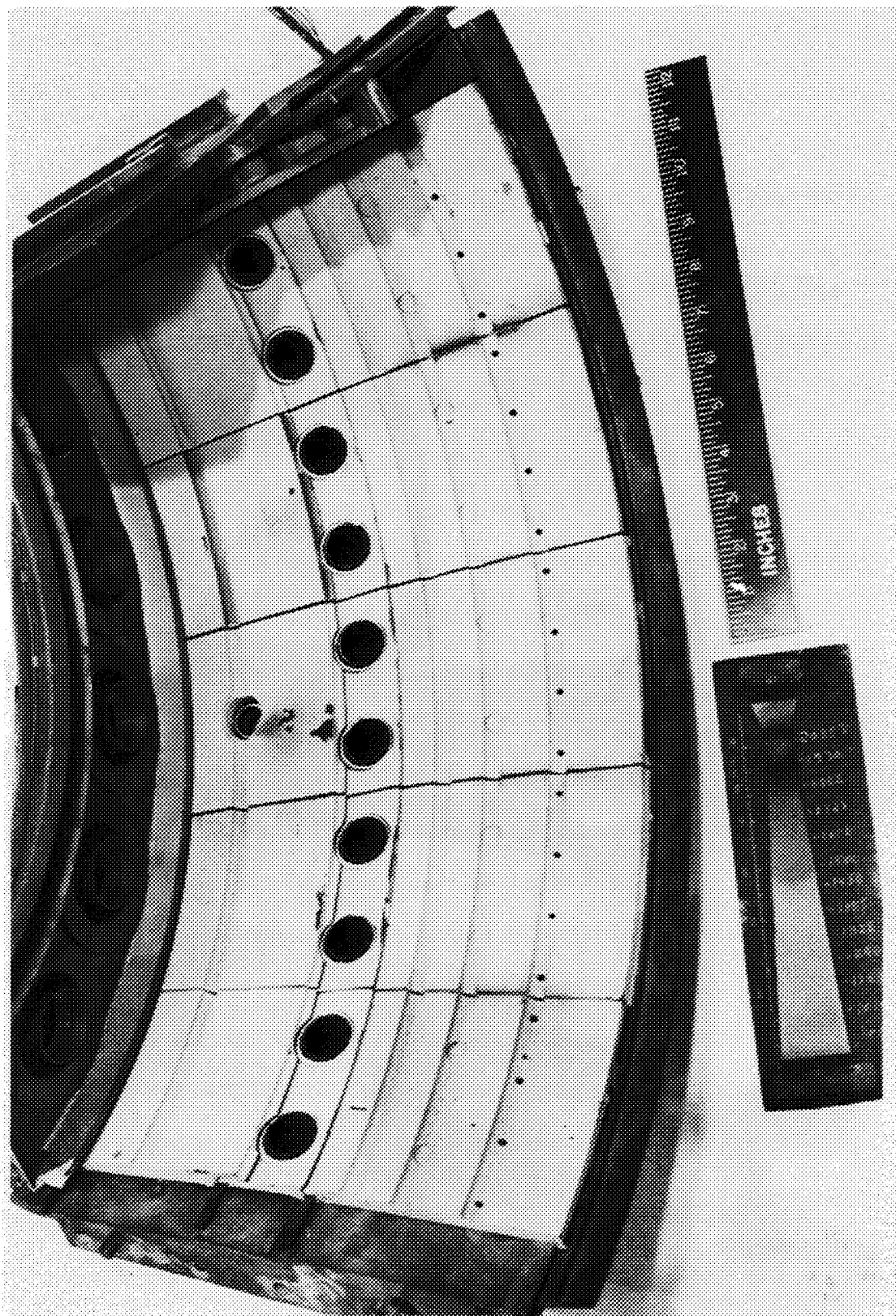


Figure 3-2 Advanced Segmented Liner With Counter-Parallel Finwall[®] (CPF) Cooling Technique

ORIGINAL PAGE
BLACK AND WHITE PHOTOGRAPH

ORIGINAL PAGE IS
OF POOR QUALITY



1
Figure 3-3 Sector Combustor Rig Outer Liner/Bulkhead Assembly

3.2.2 Segmented Pin-Fin Liner

In a continuation of the technology extension process, additional efforts were defined in the Sector Combustor Rig Test Program with the purpose of evaluating a second generation of segmented liners. The new design retained the successful features of the first generation counter-parallel Finwall® while improving on the shortcomings.

Two of the drawbacks to the highly successful CFW liner have already been mentioned: cost and weight. The relative factors comprising the sector rig liner costs are presented in Table 3-I. It was apparent that an "as cast" segment and a formed sheet metal support shell would yield great cost benefits. If both the segment and the support shell can be configured as thin wall structures, then the weight problem could also be addressed.

TABLE 3-I
BREAKDOWN OF EEE SECTOR RIG CFW LINER COSTS

<u>Category</u>	<u>Percent of Total Cost*</u>
Casting	14
ECM Cooling Holes	14
EDM Coolant Inlet Slots	25
Grinding (hooks)	30
EDM Feather Seal Slots	10
Misc. EDM	<u>7</u>
	100

*Tooling costs not included

The second generation liner, shown conceptually in Figure 3-4, features a sheet metal structural shell from which cast tiles are mechanically suspended on the combustor side. Cooling flow enters the shell through discrete holes at approximately mid-panel of each segment and flows in both the upstream and downstream directions through arrays of pin-fins. The parallel flow from one segment mixes with the counter flow from the downstream panel and is injected tangentially as film cooling air on the hot surface.

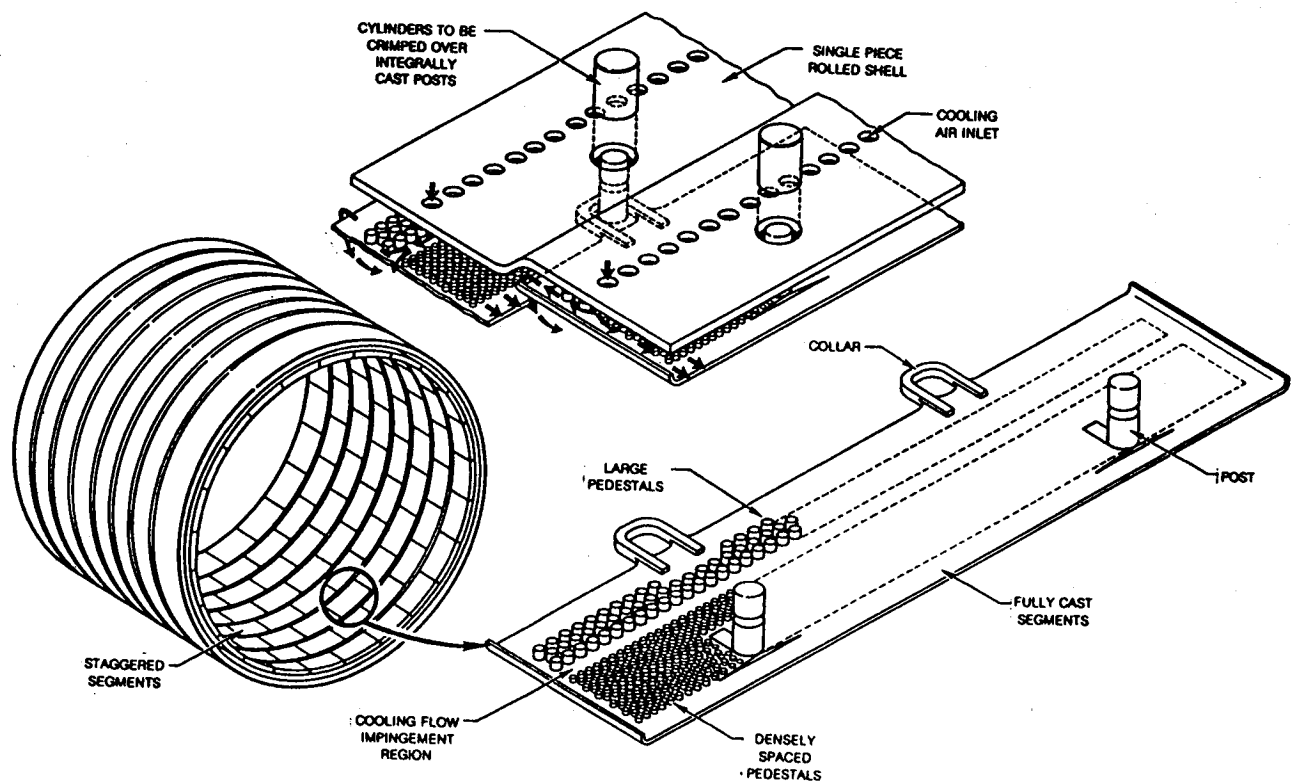


Figure 3-4 Conceptual Definition of Second Generation Segmented Liner

3.2.2.1 Aerothermal Design Features

The aerothermal design effort included parametric studies evaluating pin axial and circumferential spacing, pin height, axial location of coolant entry (impingement) holes, as well as the sensitivity of the design to pin tip clearance resulting from fabrication and assembly tolerances. Pin-fin liner design variables and analysis matrix are shown in Figure 3-5.

The thermal design was conducted at conditions representative of a hot day SLTO (sea level takeoff) condition with appropriate factors for engine deterioration (see Table 3-II). Total inner liner cooling level was maintained at 16 percent of combustor airflow with 2.8 percent of Pt3 liner pressure drop. Both of these parameters were consistent with the CPFW configuration tested in the sector rig.

Gaspath boundary conditions for the analysis were obtained by first constructing a composite thermal map from the CPFW thermal paint test results of sector rig Runs 18, 20 and 22. The CPFW analysis model was then used to back calculate the gas temperature and effective fuel/air ratio distributions along the centerline of the combustor to match the composite thermal map. The resulting panel-by-panel average and streak (i.e., hot spot) temperature observations and the corresponding predictions are presented in Figure 3-6. This allowed for realistic and consistent evaluation of the pin-fin liner design relative to the established CPFW design.

Variation of a typical panel maximum wall temperature with cooling flow is shown in Figure 3-7. Cooling flow is modulated by the diameter of the support shell holes for the three configurations with varying counterflow section pin diameters. Also shown are casting technology limitations on pin spacing and design cooling flow. This is a typical design window encountered for all of the panels.

TABLE 3-II
COMBUSTOR OPERATING CONDITIONS FOR DESIGN ANALYSIS
(HOT DAY, 29°C (84°F) SEA LEVEL TAKEOFF CONDITIONS)

Combustor Inlet Temperature °C (°F)	580 (1077)
Combustor Exit Temperature °C (°F)	1482 (2700)
Combustor Inlet Pressure MPa (psia)	3.1 (456)
Overall Fuel/Air Ratio	0.028
Liner Pressure Drop, %Pt3	2.8

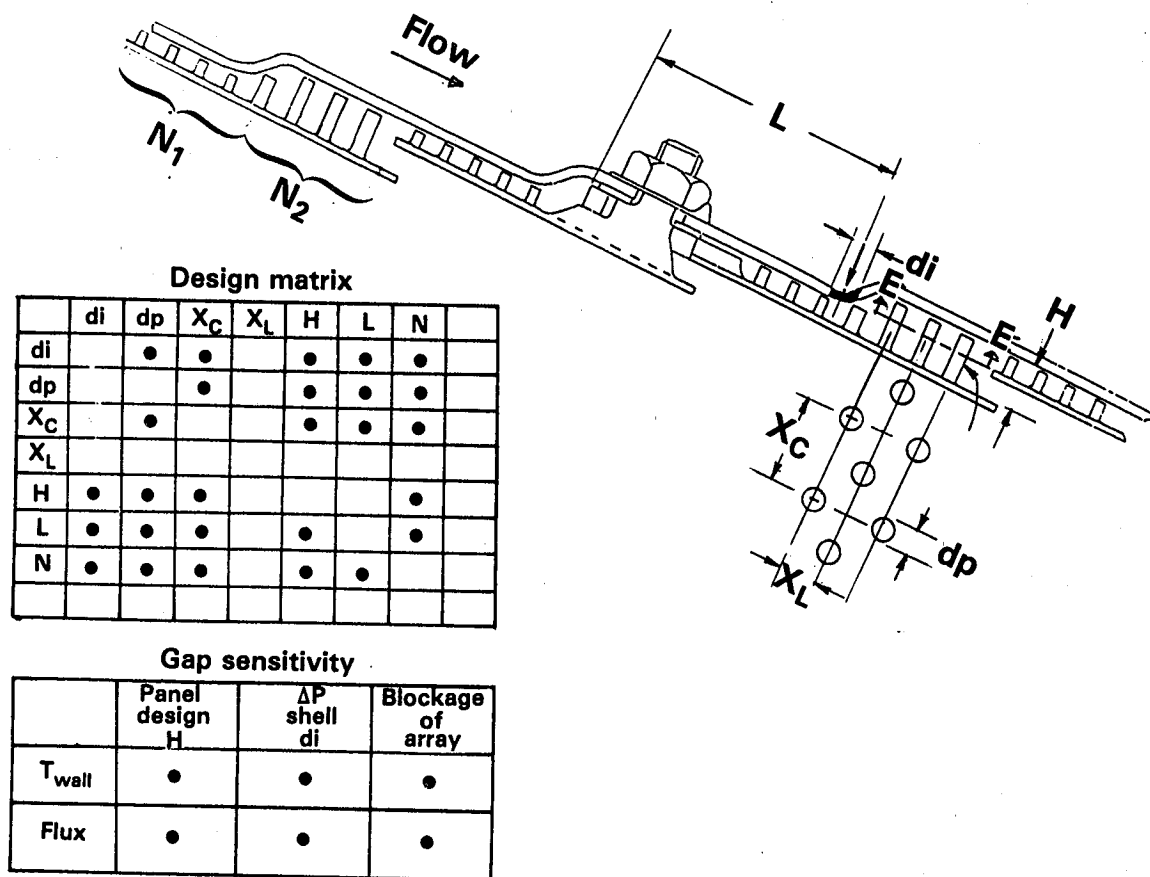


Figure 3-5 Parametric Design Variables for Pin-Fin Cooling Geometries

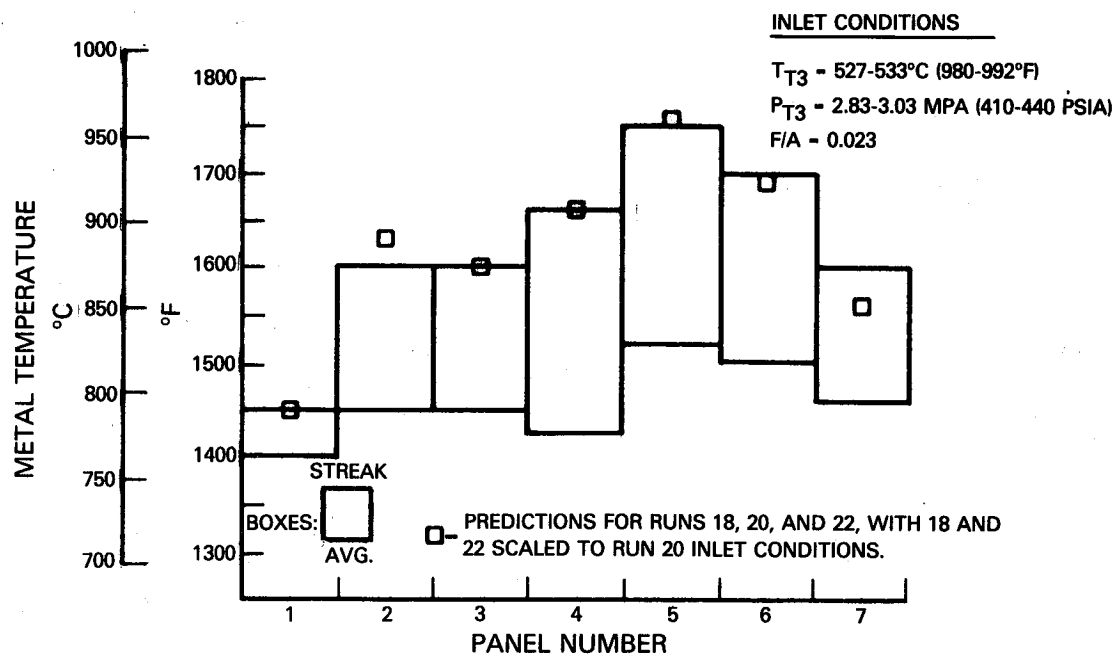


Figure 3-6 Combined Map for Runs 18, 20 and 22 with CFW Streak Metal Temperature Predictions

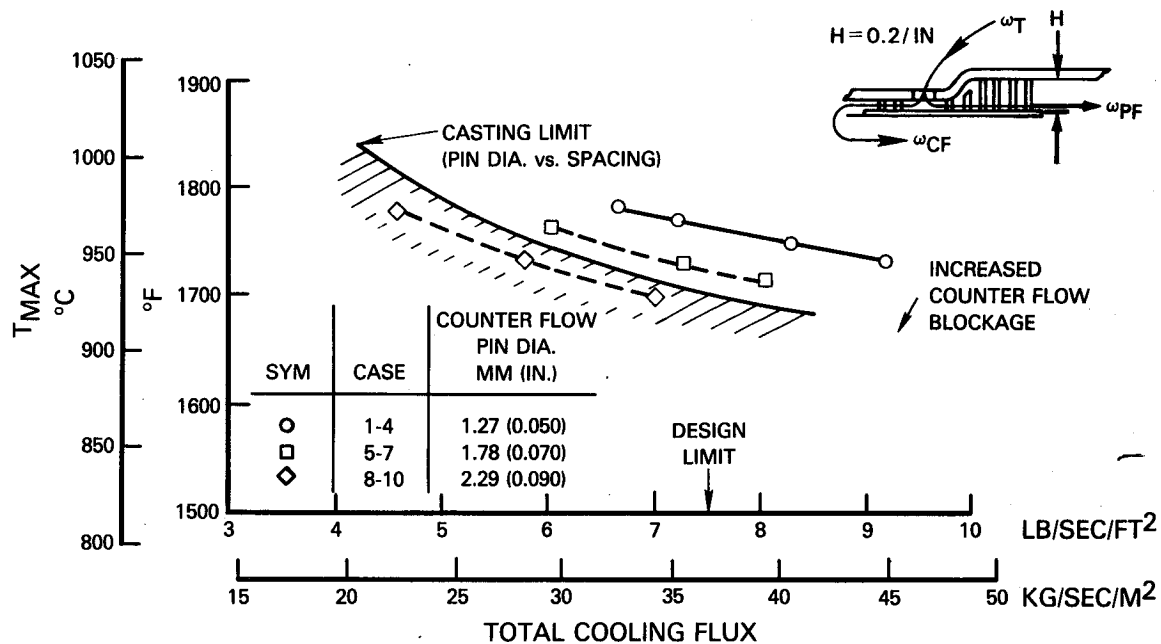


Figure 3-7 Maximum Wall Temperature Versus Total Cooling Flux

The effect of pin height on maximum temperature in the parallel flow trailing edge region is presented in Figure 3-8. The reduced flow area and the associated increase in heat transfer coefficient with the shorter pins is evident. As the inlet hole diameter is enlarged to increase overall cooling flow, there is a trade-off between the deterioration in impingement heat transfer at the holes and the improved heat transfer at the lip. At some optimum point, mid-panel temperature and the trailing edge temperatures are approximately equivalent. The minima of the curves define the optimum shell hole diameter for minimum panel temperatures. Based on this analysis, 2 mm (0.080 inch) high pins were selected throughout the panel, and optimum shell hole diameters were established.

Relative movement between the shell and the pin-fin panel due to thermal excursions or assembly fit-ups could result in a tip clearance between the shell and the panel. Since this impacts the coolant flow area, hence heat transfer, sensitivity studies were conducted to assess the magnitude of the effect on cooling flow rates and wall temperatures. Results are presented in Figure 3-9 for both cooling flow and wall temperatures respectively. Increased sensitivity to pin-tip clearance can be observed as higher percentage of the total liner pressure drop is taken across the pin arrays. In order to minimize the effect of tip clearance on liner performance, array pressure drop was limited to 40 percent of the total.

The effect of variations in other design parameters on wall temperature and cooling flux are compared to the baseline design in Figure 3-10. The chosen design is seen to be relatively insensitive to these parameters.

The resulting design cooling air flow distributions and the associated wall temperatures are compared on a consistent basis to the CPFW design in Figure 3-11. The pin-fin liner is 50-100°C (90-180°F) cooler than the CPFW liner in the main zone. The aft two panels in the pilot zone are comparable. The higher pin-fin panel temperature in the first panel is due to the greater than 2X surface area cooled by approximately the same amount of cooling flow.

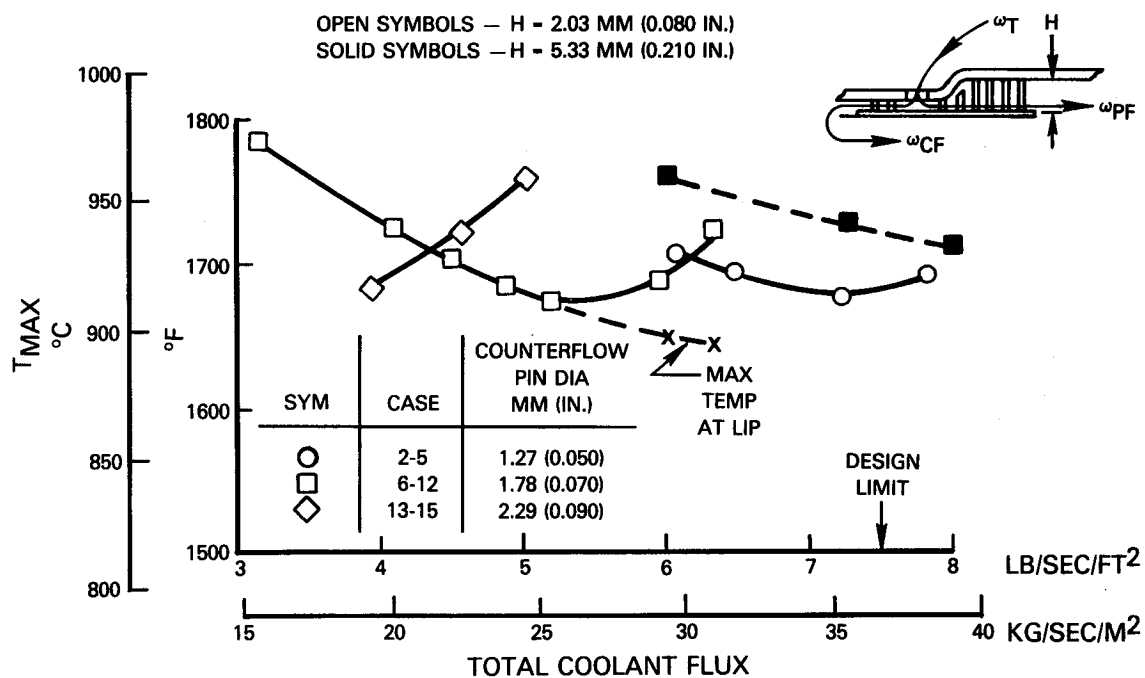


Figure 3-8 Effect of Parallel Flow Region Trailing Edge Pin Height on Maximum Panel Temperature

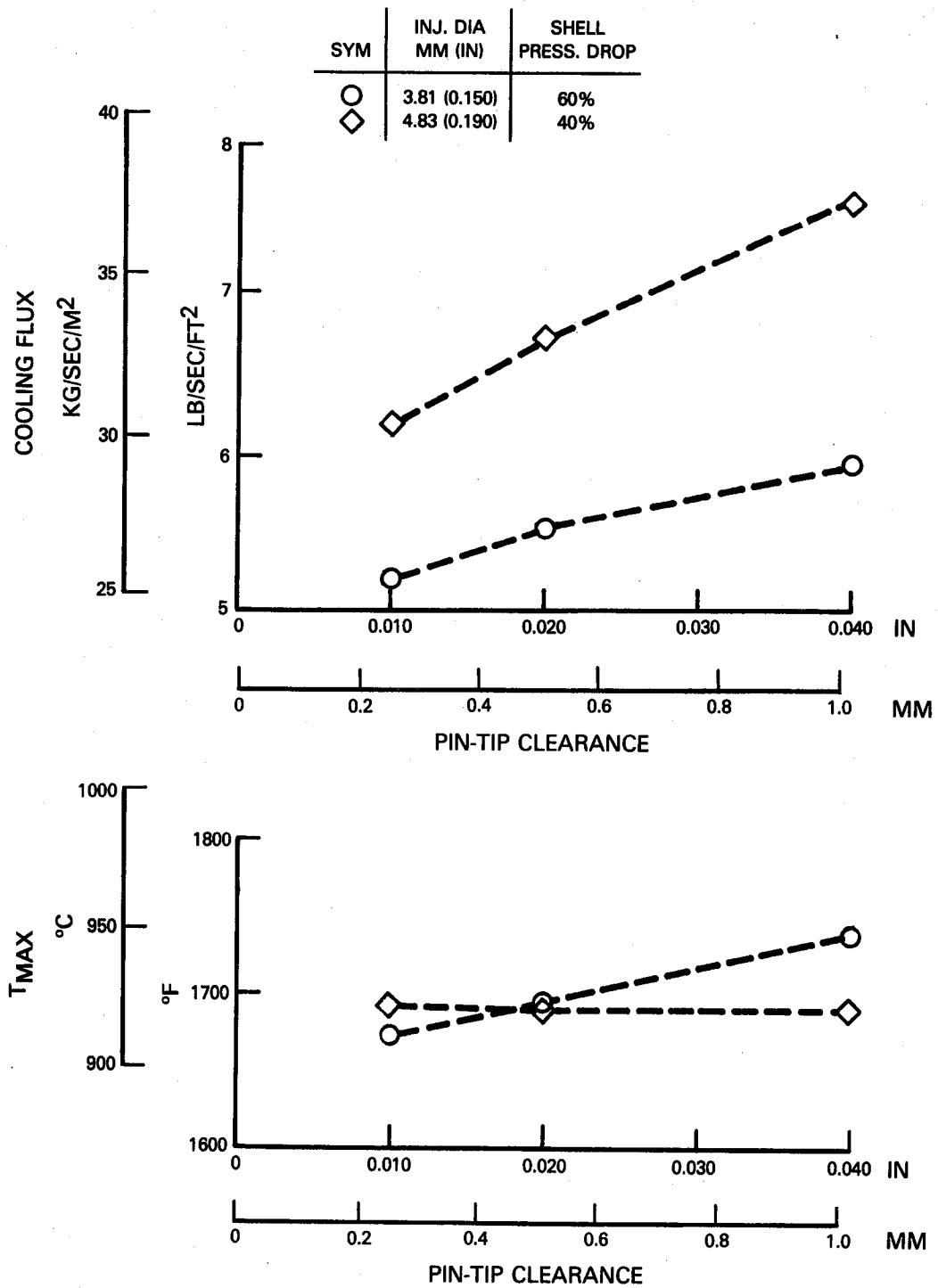


Figure 3-9 Sensitivity of Trailing Edge Temperatures and Cooling Flow to Pin-Tip Clearance

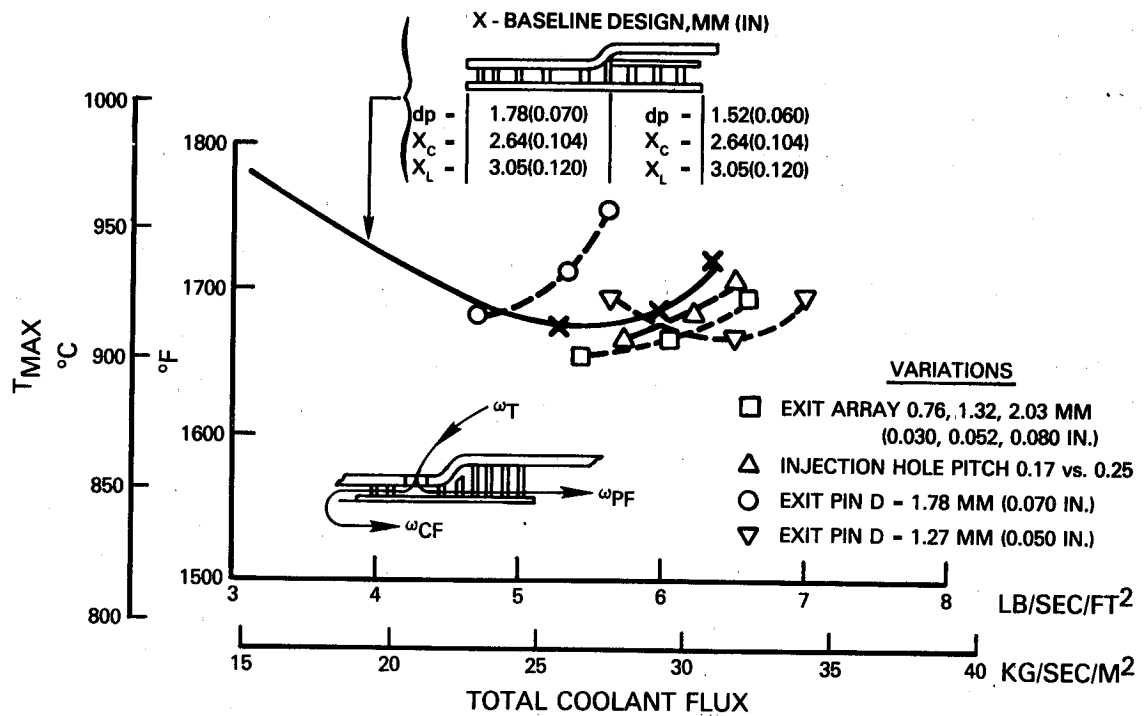


Figure 3-10 Recommended Design and Variations Evaluated

- EVALUATED AT TABLE 3-II CONDITIONS
- COOLING FLOW AS % COMBUSTOR AIR FLOW

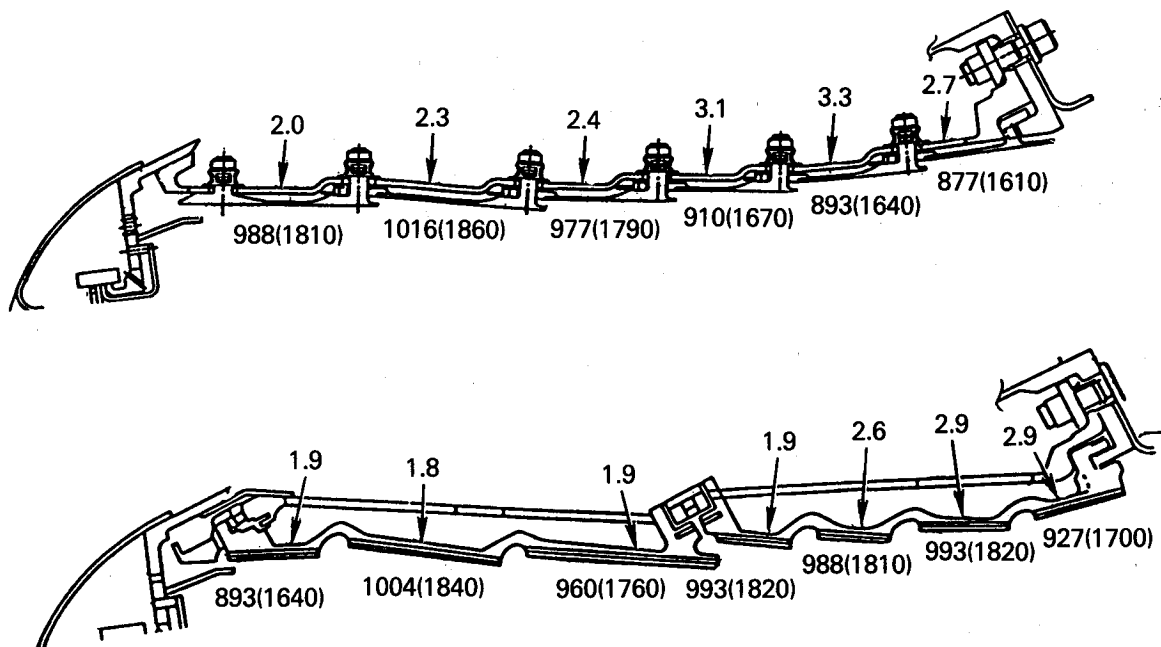


Figure 3-11 Comparison of CPFW and Pin-Fin Metal Temperature, °C (°F), and Cooling Flow Predictions

3.2.2.2 Mechanical Design Features

The existing inner liner assembly for the Sector Rig was redesigned to incorporate the advanced characteristics of the second generation pin-fin liner. The cooling pin geometries from the thermal design are shown in Figure 3-12.

Circumferential arcs of 37.5 and 25 degrees comprised the pilot zone and main zone segments respectively. A total of 6 axial segments resulted in 4 panels of 36.3 mm (1.430 inch) and 2 panels of 47.5 mm (1.870 inch) length. An interlocking mechanism of a collar on the leading edge of a panel engaging the threaded posts on the trailing edge of the preceding panel was utilized. This feature minimized the number of shell penetrations and the number of nuts utilized while preserving a high degree of redundancy in attachments. The base regions of the attachment posts feature a 7 degree taper all the way around in order to minimize the punch-through loads. These mechanical features are shown in Figure 3-13.

Positioning and number of attachment posts/collars were determined by the limiting bending stress of 50 ksi resulting from thermal gradients and pressure loads. Figure 3-14 shows the maximum value and the location of the limiting bending stress.

The panels are investment cast inclusive of all design features of a nickel alloy (INCO 713) with no finish machining required. INCO 713 was chosen because it contains no cobalt which is a strategic material and fulfills the strength requirements (Table 3-III). The shell is formed using Hastelloy-X material. Figure 3-15 shows the liner assembly with several of the segments removed to expose features of the support shell.

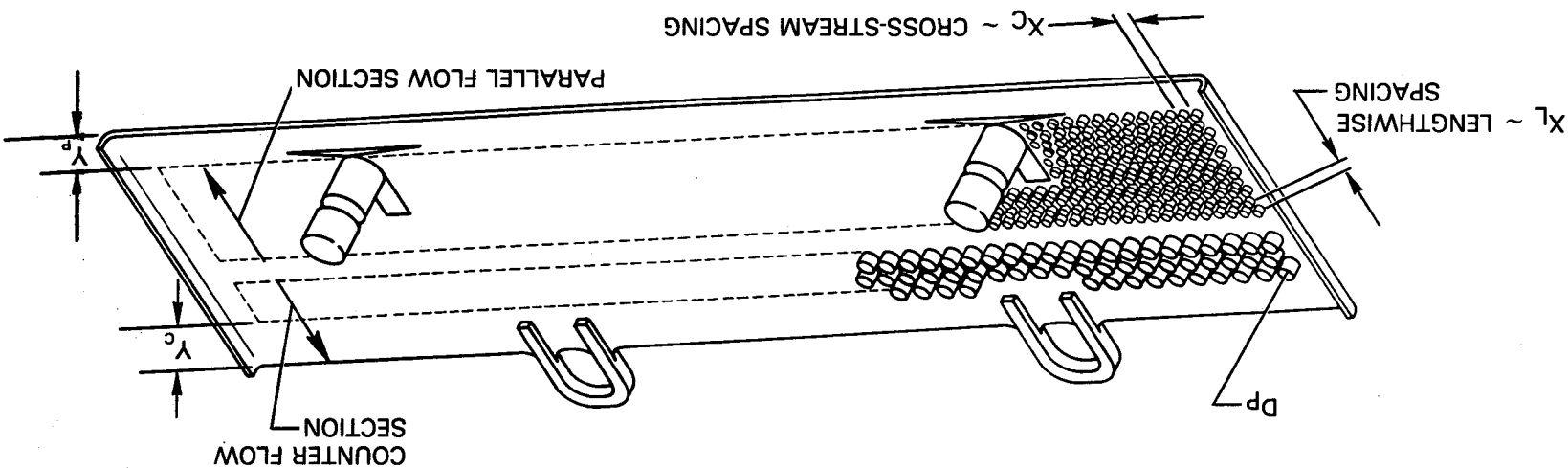
3.2.2.3 Pin-Fin Liner Advantages

Although similar in concept to the original CPFW segmented liner, the new approach offers the following benefits:

1. A large percentage of the liner pressure drop is taken through the structural shell and thus minimizes the leakage between segments and eliminates the need for feather seals
2. Isolating the structural member from the hot gaspath member allows the use of "as cast" tiles with even more efficient convective — cooling schemes such as pin-fins
3. The ability to vary axial stacking of panels permits small degrees of overlap which results in improved hot side film effectiveness from tangential injection of the film
4. The formed sheet metal structural shell replaces a machined support cage and the "as cast" tiles replace heavily machined segments thus providing significantly reduced fabrication costs
5. Thinner walls in both shell and segments result in reduced weight.

Figure 3-12 Segment Geometric and Flow Characteristics

PANEL NO.	X_C CM (IN)	X_L CM (IN)	D_P CM (IN)	Y_P CM (IN)	X_C CM (IN)	X_L CM (IN)	D_P CM (IN)	Y_C CM (IN)	FLOW SPLIT (PERCENT PANEL FLOW)
1	0.3048 (0.120)	0.2642 (0.104)	0.1524 (0.060)	0.2540 (0.100)	0.3048 (0.120)	0.2642 (0.104)	0.1270 (0.050)	0.2540 (0.100)	48
2	0.3048 (0.120)	0.2642 (0.104)	0.1524 (0.060)	0.2540 (0.100)	0.3048 (0.120)	0.2642 (0.104)	0.1270 (0.050)	0.2540 (0.100)	43
3	0.3048 (0.120)	0.2642 (0.104)	0.1524 (0.060)	0.2540 (0.100)	0.3048 (0.120)	0.2642 (0.104)	0.1270 (0.050)	0.2540 (0.100)	48
4	0.3048 (0.120)	0.2642 (0.104)	0.1524 (0.060)	0.2540 (0.100)	0.3048 (0.120)	0.2642 (0.104)	0.1270 (0.050)	0.2540 (0.100)	48
5A/5B	0.3048-0.2032 (0.120/0.080)	0.2642-0.1016 (0.104/0.040)	0.0762 (0.030)	0.2540 (0.100)	0.3048 (0.120)	0.2642 (0.104)	0.1778 (0.070)	0.2540 (0.100)	46
6	0.3048 (0.120)	0.2642 (0.104)	0.1524 (0.060)	0.2540 (0.100)	0.3048 (0.120)	0.2642 (0.104)	0.1778 (0.070)	0.2540 (0.100)	49



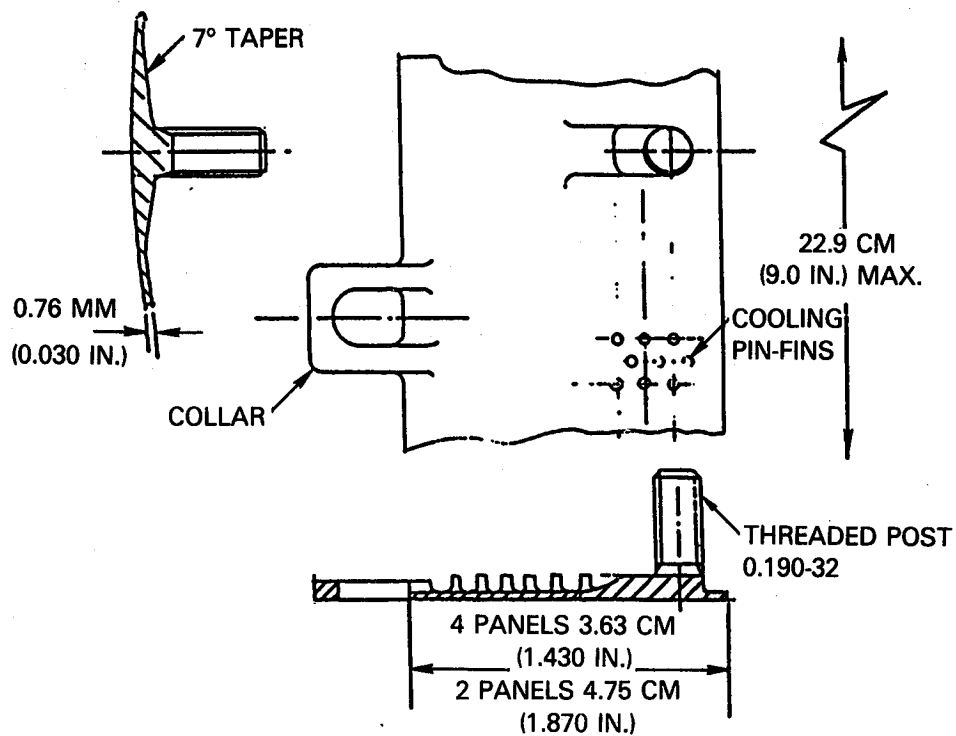


Figure 3-13 Mechanical Features of the Pin-Fin Cast Segments

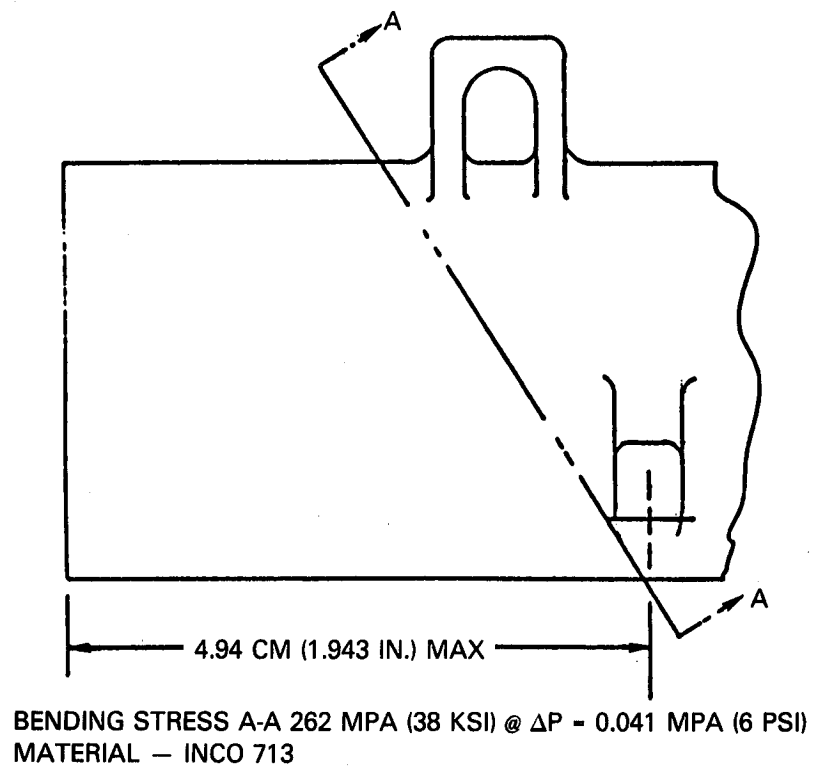


Figure 3-14 Location and Magnitude of Maximum Bending Stresses Calculated

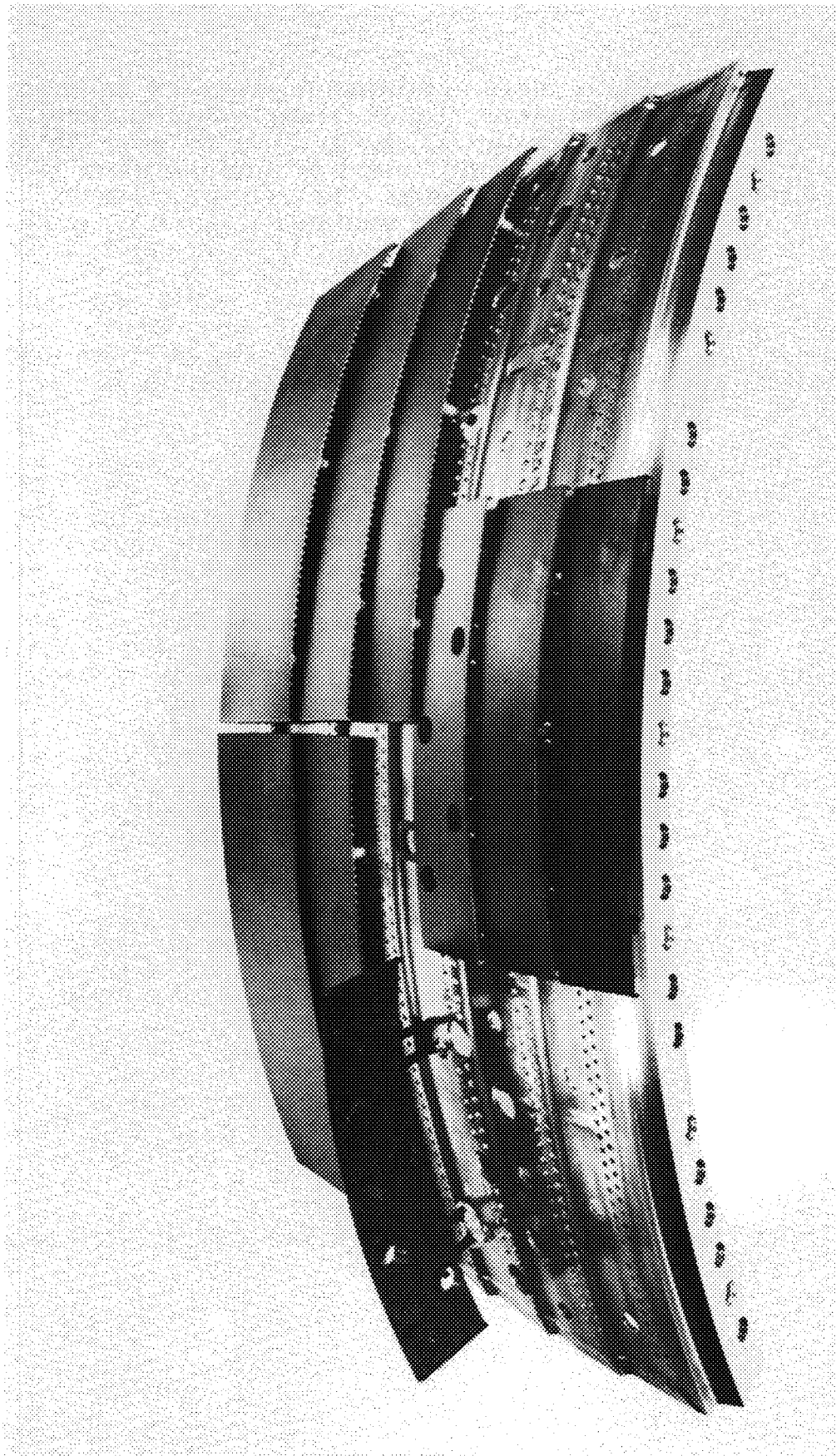


Figure 3-15 Sector Rig Shell and Cast Segments

1

3.2.3 Ceramic Composite

Run 26 of the sector combustor rig was conducted to assess the performance and integrity of a combustor liner constructed of ceramic composite materials. This activity was motivated by analytical studies conducted under the NASA/P&W Advanced Composite Combustor Structural Concepts Program (Reference 1) which indicated that the use of ceramic composites offered several potential benefits for combustor liners. This effort consisted of screening candidate composite materials, very limited laboratory testing of the selected material for critical property definition, the conceptual definition of a liner construction consistent with the use of this material, a structural design study of that configuration, and an economic analysis to ascertain its benefits and deficiencies. Since the liner for the Energy Efficient Engine sector combustor rig was a direct extension of the concepts identified in this study, they are summarized herein as design background.

3.2.3.1 Design Background

The effort under the Advanced Composite Combustor Structural Concepts Program was initiated with a screening of candidate high temperature composite materials to select the best material consistent with near term application. While carbon-carbon composites and superalloys reinforced with tungsten wire were considered, a ceramic base composite appeared most attractive. United Technologies Research Laboratories has been investigating several ceramic composite systems and developing these materials under the trade name of Compglas[®] since 1976. This activity has been supported in part by the Office of Naval Research (References 2 through 6) and the Naval Air Systems Command (Reference 7) and has led to encouraging results. In particular, a composite consisting of a lithium aluminosilicate (LAS) matrix reinforced with silicon carbide (SIC) fibers appeared to have properties that were uniquely suited to use in combustor liner applications and was selected as the reference material for the study.

Table 3-III presents a summary of some of the critical properties of the silicon carbide, lithium aluminosilicate composite system and reveals some of the advantages associated with this material as well as unique properties that dictated different design approaches. For comparison the table includes the corresponding properties of two advanced turbine airfoil alloys -- both of which have been used in the Energy Efficient Engine combustor liner -- the B-1900 in the CPFW cast liner segments and Inco 713 in the Pin-Fin liner segments of Runs 24 and 25. The properties of the SIC-LAS material are based on data obtained from specimens with all of the fibers oriented in the axial directions. The subscript "II" on the LAS in this table refers to a particular formulation of the lithium aluminosilicate matrix. More recent development led to an improved formulation identified by the subscript "III," and most of the components of the liner for the Energy Efficient Engine sector combustor rig were made from this matrix material.

TABLE 3-III
COMPARISON OF PROPERTIES OF UNIDIRECTIONAL
CERAMIC COMPOSITES WITH HIGH TEMPERATURE METALS

PARAMETER	SIC-LAS II COMPOSITE	ISOTROPIC TURBINE ALLOYS	
		MODIFIED B-1900	INCO-713
MATRIX TEMPERATURE LIMITS °C (°F)	1205 (2200)	982-1095 (1800-2000)	982-1095 (1800-2000)
DENSITY — GM/CM ³ (LB/IN ³)	2.50 (0.09)	8.20 (0.297)	7.90 (0.286)
USE OF STRATEGIC ELEMENTS	NONE	10%-Co 8%-Cr 6%-Mo 4.3%-Ta 1.5%-Hf	14%-Cr 4%-Mo 2%-Cb 1%-Ti
THERMAL CONDUCTIVITY W/M °C (BTU/FT HR °F)	1.6 (1.0)	10.0 (5.8)	8.65 (5.0)
COEFFICIENT OF THERMAL EXPANSION °C ⁻¹ (°F ⁻¹)×10 ⁶	2.9 (1.6)	11.7 (6.5)	11.9 (6.6)
ELASTIC MODULUS GPa (MSI)	139 (20)	200 (29)	206 (30)
COEFFICIENT OF EXPANSION ×ELASTIC MODULUS GPa/°C (MSI/°F)	403 (32)	2340 (189)	2455 (198)
TENSILE STRENGTH (ULTIMATE) MPa (KSI)	338 (49)	795 (115)	620 (90)
HIGH CYCLE FATIGUE STRENGTH MPa (KSI)	262 (38) AT 800°C (1472°F)	290 (42) AT 760°C (1400°F)	304 (44) AT 760°C (1400°F)
<div style="text-align: center;">HCF STRENGTH</div> <div style="text-align: center;">DENSITY</div> <div style="display: flex; justify-content: space-around;"> <div> $\frac{\text{MPa}}{\text{GM/CM}^3}$ </div> <div> $\frac{\text{KSI}}{\text{LB/IN}^3}$ </div> </div>	105.5 (422) AT 800°C (1472°F)	35 (141) AT 760°C (1400°F)	38.4 (154) AT 760°C (1400°F)

ALL PROPERTIES AT ROOM TEMPERATURE UNLESS INDICATED OTHERWISE.

The table indicates that the limiting temperature capability of the SIC-LAS composite was considered to be about 1200°C (2200°F) at which the matrix would start to soften. This temperature is 111°C to 222°C (200°F to 400°F) above the capabilities of the metals which are limited by cyclic fatigue or oxidation considerations. The SIC-LAS ceramic composite also shown to have only one third the density of the metals and requires none of the strategically critical raw materials. The thermal conductivity of the composite ceramic is also less than those of the metals. Significant differences in thermal conductivity can dictate a change in emphasis on cooling system design. For example high thermal conductivity, at least in the through thickness direction of the material, is a desirable property for combustor liner concepts in which extensive use is made of heat transfer from the cold side surface of the liner as in the metallic Pin-Fin liner construction of Section 3.2.2.

The SIC-LAS ceramic composite is shown to have a lower coefficient of thermal expansion than the metals. This is both an asset and a liability because it reduces internal thermal stresses but complicates attachments to adjacent metal structures -- particularly when these attachments are located in high temperature regions. The influence of thermal expansion on thermal stress is best recognized by the product of the expansion coefficient and the elastic modulus listed on Table 3-III. This parameter is a measure of the thermal stress induced per unit of temperature differential in the material and is shown to be only about one-sixth the magnitude of that in the metals.

Combustor components can also be subject to vibratory loading and the table indicates the SIC-LAS ceramic composite has a high cycle fatigue strength approaching that of the metals and when scaled by the density to form a parameter that is a measure of resistance to vibratory fatigue caused by inertia effects it is shown to have three times the fatigue resistance.

While the potentially higher operating temperature capability, lower density and lack of use of strategically critical materials are substantial advantages to the use of ceramic composites over metals the lower thermal conductivity and lower thermal expansion, and hence reduced thermal stresses exert the strongest influence on the design of a combustor liner relative to one using more conventional metallic materials. The potential of the SIC-LAS material was demonstrated during an experiment conducted under the Advanced Composite Combustor Structural Concepts Program to assess the thermal shock resistance of the material. The test apparatus had the capability to substantially reproduce localized creep-buckling failures (bulges) similar to those observed in engine operated metal burner liners. Testing involves repetitive creation of a small diameter high temperature hot spot in the center of a rotating test specimen using a focused oxy-acetylene torch. The cyclic heating was caused by shuttling the torch laterally into and out of position in front of the specimen. This apparatus and the results of tests conducted on additional ceramic composite specimens are discussed in more detail in Appendix B. During company-sponsored tests with metallic materials, cycling the center of the disk from 540°C (1000°F) to a maximum temperature in the range of 870°C to 1090°C (1600°F to 2000°F) was found to produce a progressive permanent deflection of the disk surface. In particular, disks made of Hastelloy X

developed sizable central deflection after only five or ten thermal cycles and cracks developed on the hot surface after about 500 cycles. Conversely, when the first SIC-LAS₁₁ composite specimen was subjected to the same thermal cycle for 1,000 cycles, distress was limited to a slight discoloration of the hot side surface despite the presence of through thickness temperature gradients of more than 200°C/mm (8900°F/in) at the peak of the thermal cycle. Subjecting a second specimen to 55°C (100°F) higher peak hot side temperatures of 1150°C (2100°F) for 2400 thermal cycles produced similar results and sectioning of the specimen revealed no internal distress.

A third specimen was subjected to the same thermal cycling as the second but the duration was extended to 3500 cycles in an attempt to induce internal thermal fatigue distress in the specimen. At the conclusion of the test there was still no evidence of deflection or change in thickness of the specimen. However, visual examination revealed surface cracks rather than just discoloration in the jet impingement area in the center of this disc. Following the test, this specimen was also sectioned along a diameter and photomicrography revealed the presence of a few internal microcracks.

These results led to the conclusion that the SIC-LAS composite had excellent thermal fatigue resistance despite high through thickness temperature gradients. This phenomena must be attributable to the low thermal stress associated with its low coefficient of thermal expansion and offered unique combustor liner design potential.

The combustor liner structural design studies conducted under the Advanced Composite Combustor Structural Concepts Program program were based initially on an aerothermal assessment of the most advantageous use of the ceramic composite material. Because of the unique combination of a low thermal conductivity that reduced the effectiveness of cooling the liner from the back or cold side and the material's demonstrated capability of the materials to withstand severe through thickness temperature gradients, thermal analyses led to the conclusion that the optimum liner configuration was a film cooled panel type of liner construction. As shown in Figure 3-16, multiple rows of ceramic composite panels are attached to a metallic shell in this concept. As in the case of the metallic Pin-Fin liner, the panels are segmented in the circumferential direction to avoid hoop stresses. The attachments between panel and shell are located in the cooler regions under the panel overlap to minimize stresses caused by differential thermal expansion between these parts and to shelter the head of the attachment pin or bolt from the hot combustion gases.

As part of the design studies a detailed thermal analysis was conducted of this liner construction under the assumption it was incorporated in the liner of the combustor of the PW 2037 high pressure ratio turbofan engine. Figure 3-17 shows the computed temperature distribution in the composite panel when subjected to the heat loads encountered near the front end of that combustor at takeoff power level. The results indicate that the temperature of the composite panel is low over the first 12-15 cm (0.5 to 0.6 in.) of its length where it is shielded from the hot gases by the overhang of the upstream panel.

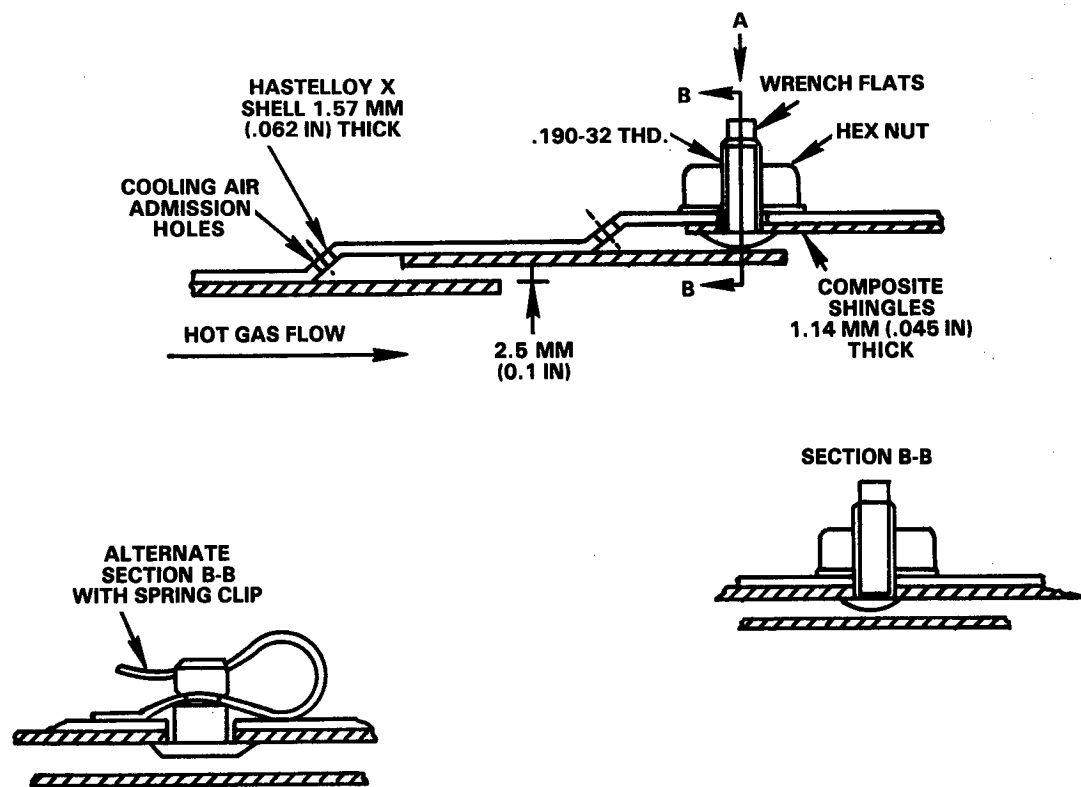


Figure 3-16 Ceramic Composite Combustor Liner Configuration

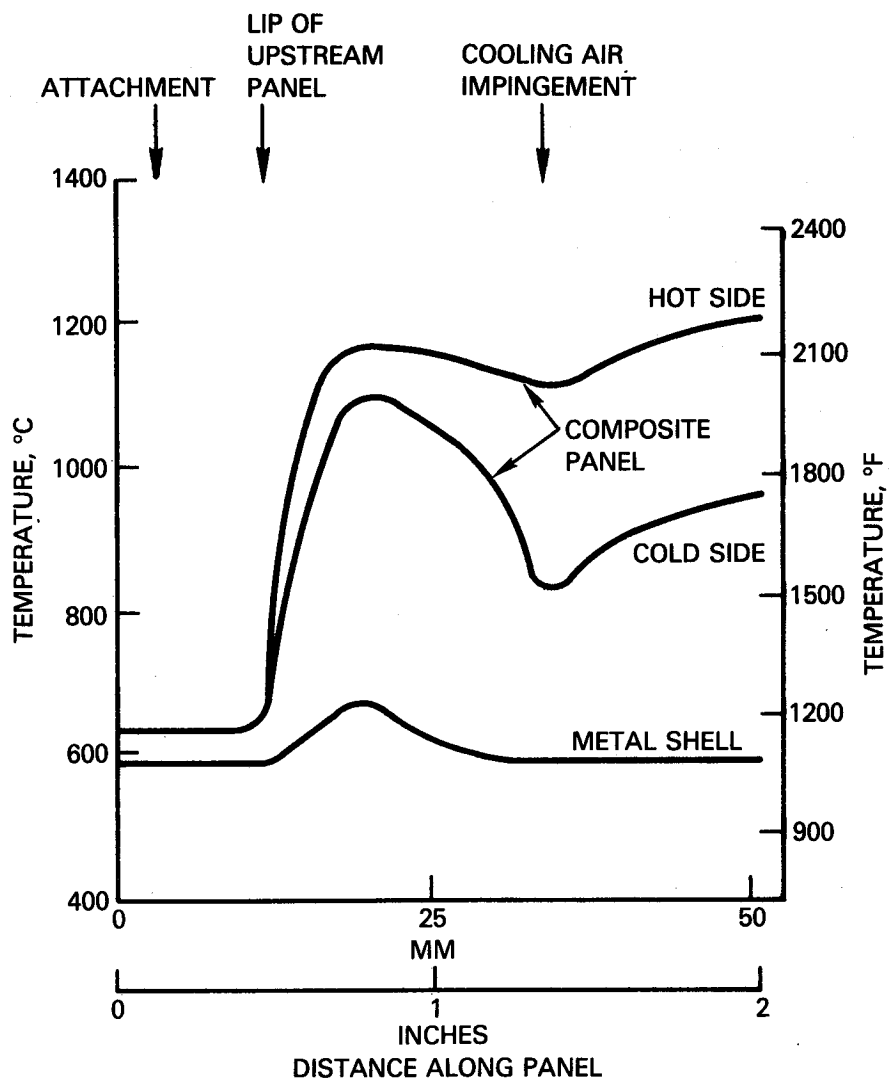


Figure 3-17 Axial Temperature Distribution in Composite Panel and Shell During Takeoff

The low and nearly identical temperatures of the panel and the shell in this location minimize extraneous loading of the attachment bolts/pins. Downstream of the lip the entire surface of the panel is hot and there are significant through thickness temperature differentials. These differentials are affected by the mode of heat transfer from the cold side of the panel. While the cooling effectiveness of the film on the hot side of the panel is higher immediately downstream of the louver lip, the heat rejection from the cold side of the panel is limited to radiation to the shell at this axial position. Conversely, further downstream cold side heat rejection is enhanced by the convective effect of the cooling air flow entering the louver and offsets the deterioration in cooling effectiveness of the louver film. The results indicate that the maximum hot side surface temperature of the composite panel and the maximum through thickness temperature gradient occur at the downstream lip of the panel. The 1200°C (2190°F) maximum temperature of the panel is consistent with the projected maximum useful temperature of SIC-LAS_{II} in Table 3-III. The maximum temperature differential across the 1.14 mm (0.045 in.) thick panel also occurs at the downstream end. The 247°C (445°F) differential is consistent with the through thickness temperature gradients encountered by specimens of SIC-LAS in the previously discussed thermal fatigue tests.

The temperature variations in the Hastelloy X shell are minimal except for a band of about 85°C (150°F) higher temperature upstream of the step. This is due to the radiant heat transfer from the hot composite panel in this area. Radial temperature differences through the Hastelloy X shell were computed to be very small, of the order of 1°C (2°F).

With the temperature distribution established in the liner, the design study progressed to a structural analysis using the NASTRAN (Reference 8) computer program. In formulating a constitutive model for the ceramic composite material for the analysis it became necessary to provide a better definition of the construction of the panels. Composite materials are generally fabricated with the fibrous materials aligned parallel to the direction of the anticipated load for most effective reinforcement. However, in a combustor liner application, there is no preferred orientation of the fibers for maximum strength. To the contrary, the uncertainties in the locations of regions of high temperature gradients and their direction dictate that the material lay-up be selected so as to provide an essentially isotropic composition in the in-plane direction. Since the SIC-LAS composite panels are fabricated by stacking thin layers of bonded fibers oriented in the same direction it was concluded that the desired in plane isotropicity could be achieved by stacking the layers in the 0°/+45°/-45°/90° sequence shown schematically in Figure 3-18. Since it took eight layers of fibers to produce the desired 1.14 mm (0.045 inch) panel thickness the stacking sequence of Figure 3-18 was repeated on both sides of the panel midplane to produce a symmetrical construct. With this fiber orientation sequence the composite panel could be modeled in the NASTRAN program as having isotropic in-plane properties but with entirely different moduli in the radial or through thickness direction because of its laminar construction.

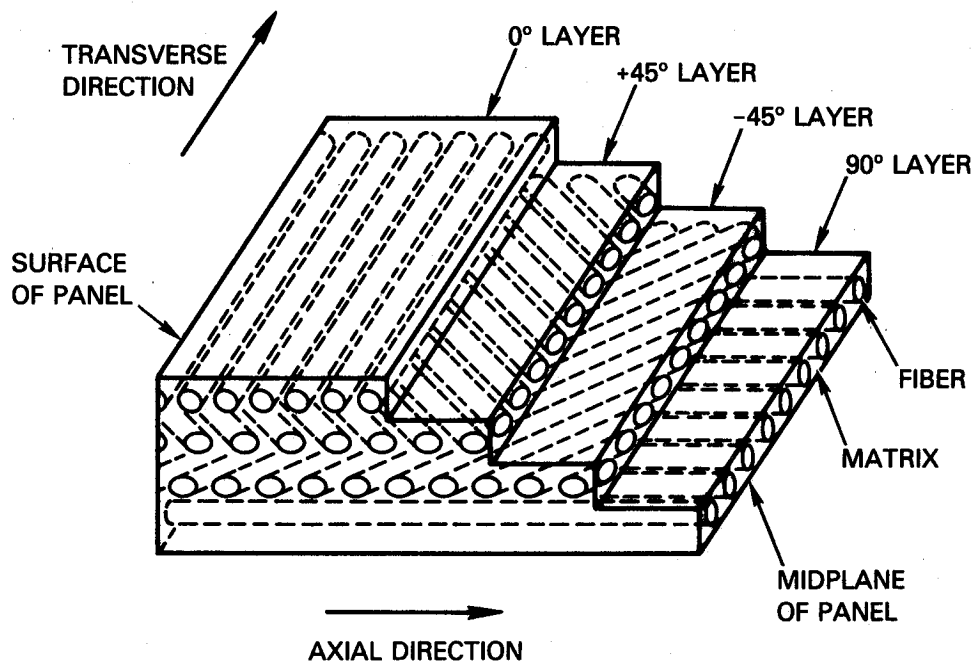


Figure 3-18 Schematic Representation of Fiber Orientations in Ceramic Composite Panel

Figure 3-19 shows the finite element breakup that was used for this elastic stress analysis. The individual composite panels were assumed to be 30 degrees in circumferential width. The panels are symmetrical and the domain of the structural analysis consisted of one-half the panel width. The panel is attached to a 1.14 mm (0.045 inch) thick Hastelloy X shell which was also modeled over the same domain. The bolted attachment of the panel to the shell was modeled using a multi-point option in NASTRAN that constrained the attachment radially but permitted axial and circumferential motion to simulate clearance in the bolt hole. A previous analysis, also using the NASTRAN program, had demonstrated that the panel had more than adequate margin over vibratory excitement if it was retained by three attachments. Since the program was incapable of modeling an attachment on the plane of symmetry the center attachment was simulated by one either side of this plane.

Figure 3-20 shows the highlights of the results of the structural analysis at temperature and pressure representative of takeoff operation of a high pressure ratio transport engine. The magnitude of the three components of stress in the cylindrical coordinate system are shown at selected critical locations in the panel including those where each is a maximum or most critical. The results show that the stress levels in the panel are low, and since the panel grows relatively independent of the shell, they are primarily due to local temperature gradients and not mechanical loads. The traverse stress component is dominant and over the downstream part of the panel they are tensile on the cold surface and compressive on the hot side. This stress distribution is caused by the high through thickness temperature differential in this part of the segment.

The radial stress components in the panel are higher near the attachments and almost nonexistent at the hot downstream lip. The radial stress is 22.7 MPa (3.29 ksi) in the compressive direction at the center attachment, while it is tensile and of considerably lower magnitude at the attachment near the free end. These stresses are caused by the changes in the radius of curvature of the panel and the shell. When both are heated to about the same temperature level, but with significantly different coefficients of expansion, radial loads develop in the attachments. This analysis was conducted for a composite panel on the inside surface of an outer liner shell. The loading would be reversed for a segment on the inner liner shell in that the center attachment would be loaded in tension and those at the free end in compression.

The magnitude of the axial components of stress in the panel was low and consequently the magnitude of the maximum stresses in the plane of the fibers is essentially that of the transverse components. On this basis, the highest stress levels encountered are about 58 MPa (8.5 ksi) in tension and these are in the cooler region near the attachment. In the hot regions of the panel, the maximum stresses are lower being nominally 55 MPa (8.5 ksi) in compression and 48 MPa (7 ksi) in tension. Based on flexure tests of the SIC-LAS material stresses of this magnitude are only about half those of the proportionality limit of the material. The use of the NASTRAN linear elastic analysis was appropriate and the in-plane stress levels in this type of liner constructions are low.

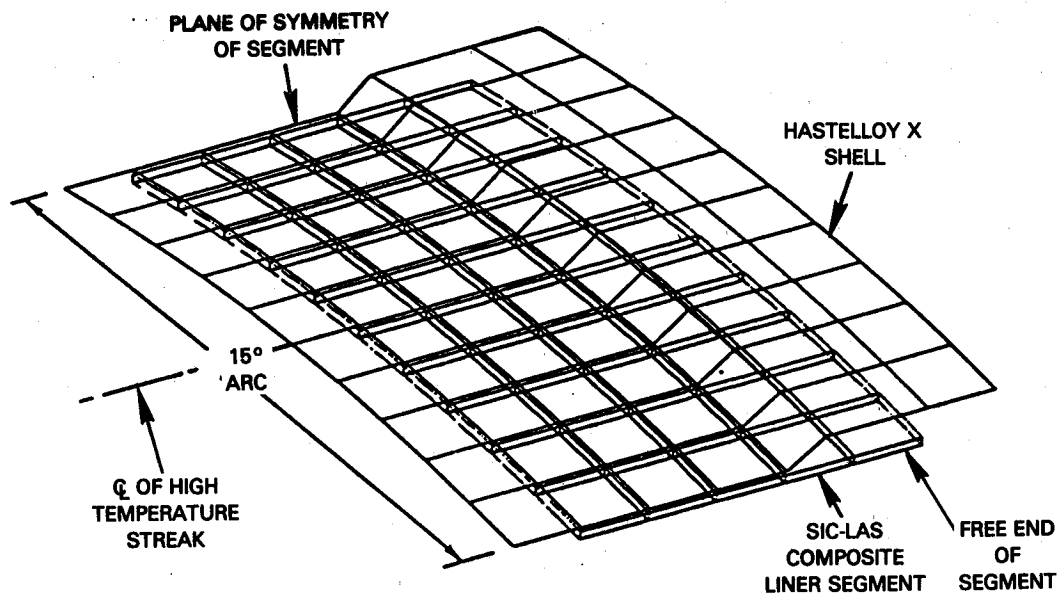


Figure 3-19 Structural Model of SiC-LAS Composite Liner

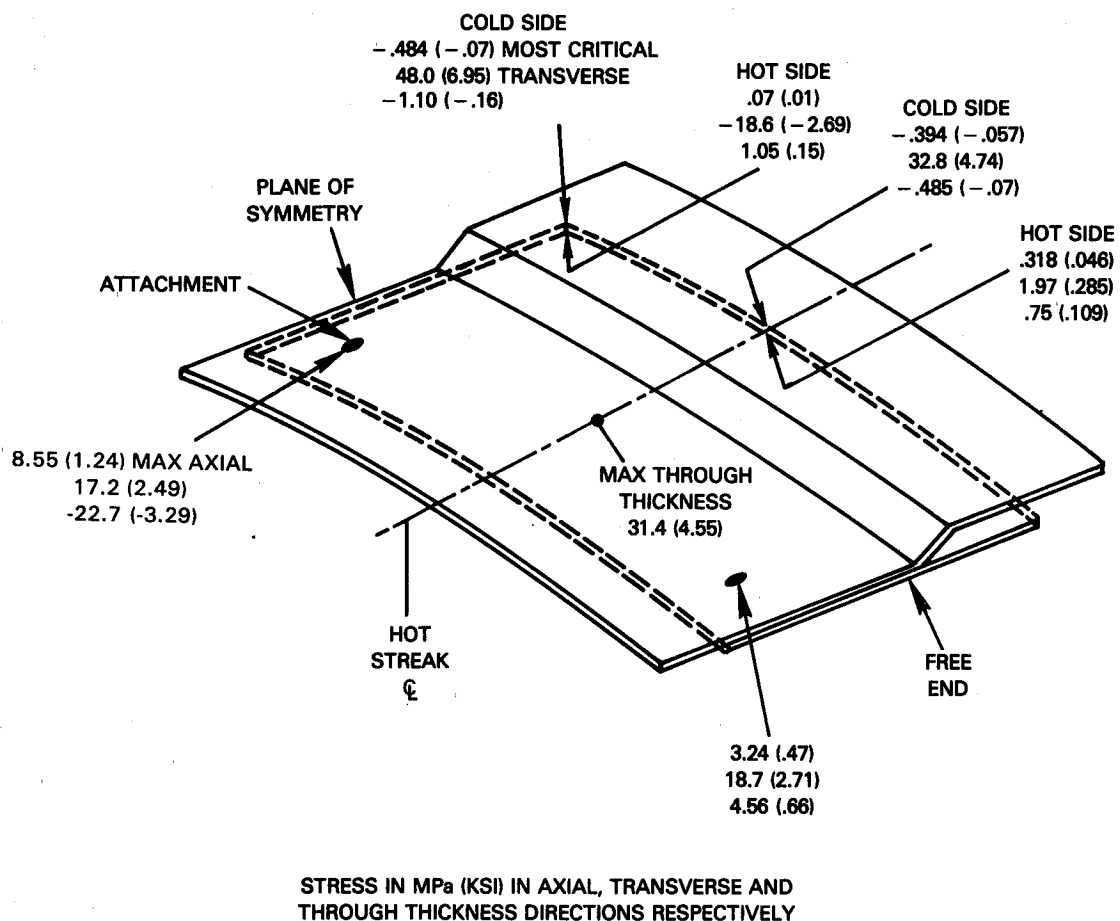


Figure 3-20 Highlights of Stress Distribution in the Composite Liner Panel

3.2.3.2 Sector Rig Liner Definition

The ceramic composite liner concept was adapted to the Energy Efficient Engine sector combustor rig in the same manner as the previously described Pin-Fin liner constructions. As shown in Figure 3-21 existing Counter Parallel Flow Finwall segments were retained on the outer liner but the inner liner of the rig was replaced with a new shell on which the SIC-LAS ceramic composite panels were mounted. The general aerothermal definition of the shell-panel construction is the same as that established in the studies conducted under the Advanced Composite Combustor Structural Concepts Program. A total of seven rows of composite panels are required to protect the full length of the combustor. The panels are segmented in the transverse direction with two panels being used at the three upstream locations enclosing the pilot combustion zone and three panels at the remaining downstream locations. With the 72 degree nominal width of the rig and the high cant angle of the inner wall of the combustor this required the panels to have transverse dimensions between 14 and 21 cm (5.5 and 8.2 inches). The axial length of the panels varied between 40 and 54 cm (1.6 and 2.1 inches).

While the basic aerothermal definition of the liner construction was that evolved in the preceding study program, several variations in detail were incorporated to assess their impact on the thermal performance of the liner. These variations are identified on Figure 3-22 and involve primarily changes to the panel to shell attachment to modify the local heat transfer characteristics. The attachment of Panels 2, 3, 6, and 7 to the shell follow the approach of the previous study as exemplified by Figure 3-16. The attachment bolts/pins are located under the lip of the upstream panel and their heads are flattened to minimize local distortion of the cooling airflow being discharged past them. There was some concern that even with flattening the head of the attachment bolt they would still cause excessive distortion of the cooling air film on the downstream surface. The region of the attachment of Row 5 was modified to investigate a potentially improved configuration. The shell was stepped out further at this panel to create a wedge shaped plenum between the shell and the cold side of Row 4. This moved the head of the attachment bolts for Row 5 out of the discharging airflow to avoid creating downstream wakes. The plenum also provides greater opportunity for coalescence of the discrete cooling air jets entering through the shell before they discharge as a cooling film.

This approach was carried further in the design of the attachment for Row 4. The shell had the same high step employed at the Row 5 attachment but part of the resultant cavity was filled with a wedge-shaped ring extending the full transverse width of the panels of Row 4. The heads of the attachment bolts for the Row 4 panels were kept out of the cooling air flow by countersinking them into this ring. The ring also formed a confining surface parallel to the cold side of the Row 3 panels to increase the cooling air velocity and hence the heat extraction from the surface of the panels of Row 3.

These design variations in Rows 4 and 5 also lead to greater risks in the fabrication of these components. While all of the other panels are simple frustroconical in shape these panels have two conical frustum sections and continuity of material properties must be maintained across the juncture of the two surfaces during fabrication.

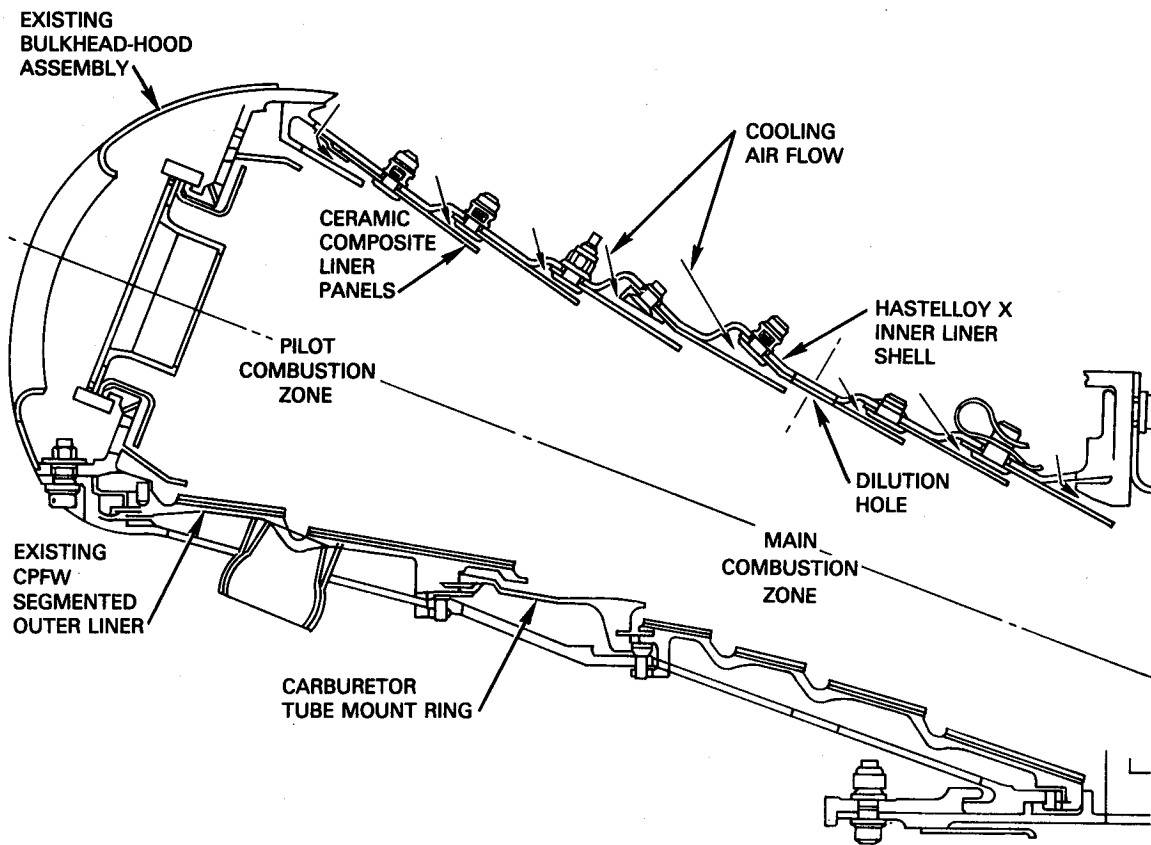


Figure 3-21 Cross Section of the Sector Combustor Rig with Ceramic Composite Inner Liner

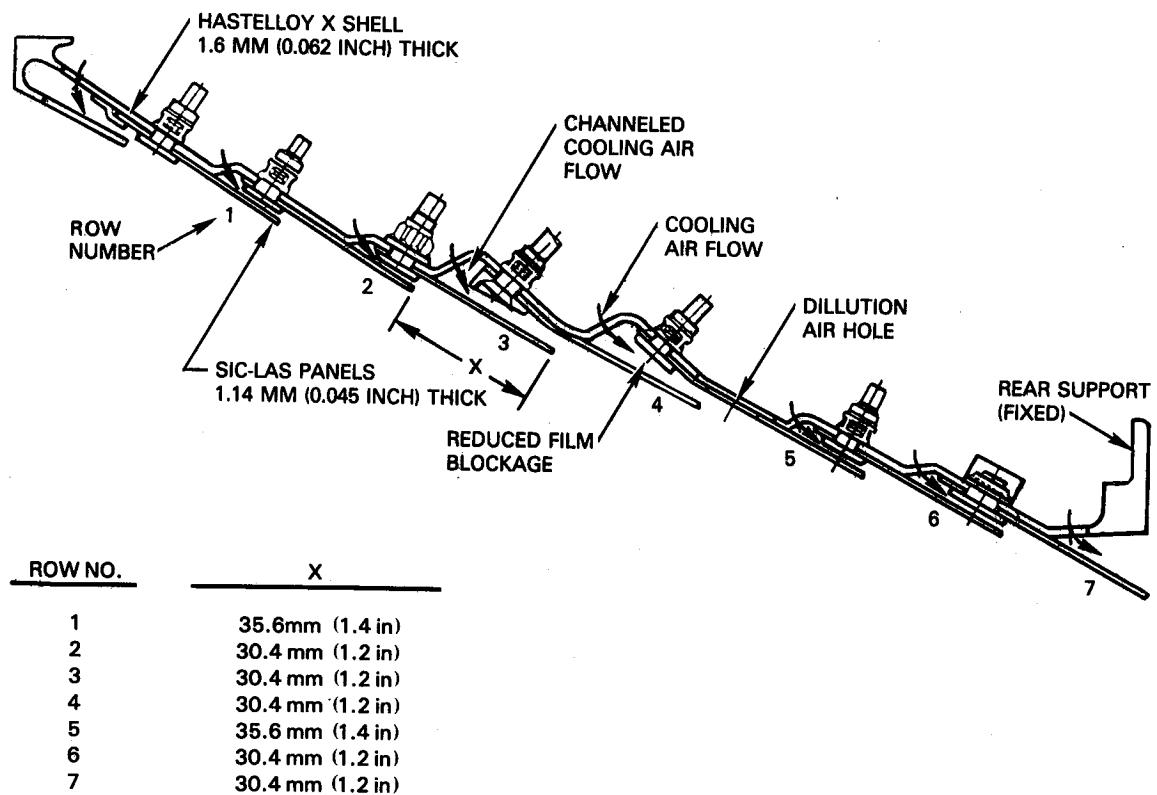


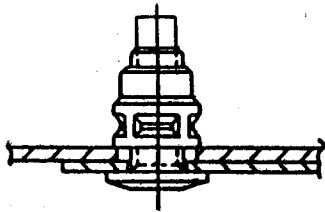
Figure 3-22 Ceramic Composite Inner Liner Design Features

The installation of the panels in Row 1 required a more aggressive attachment approach. While a metal lip was incorporated on the front end of the liner shell to form a cooling air film on the exposed surface of the panel there was not enough room for both the cooling air admission holes and the attachment bolts under the lip. In addition the lip would have to be welded on after the liner was assembled if the bolt was located underneath it. For this reason the attachment was located just downstream of the louver lip where the cooling film integrity was expected to be adequate to maintain reasonable temperatures in the bolt head.

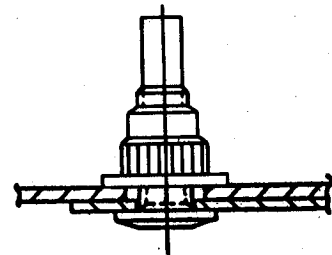
It was necessary to introduce dilution air through Row 5 of the inner liner to maintain the airflow schedule of the combustor. This was accomplished by boring concentric holes through the shell and the liner panels independently. The holes in the panels were smaller than those in the shell and served as the metering area as well as providing thermal shielding of the shell. A total of five transversely spaced holes were required in each of the three panels at this position.

The attachments of the ceramic composite combustor liner panels to the shell are subject to many of the problems encountered in the Pin-Fin liner constructions of Section 3.2.2 including thermal fatigue, wear, differential thermal expansion and vibration. The problem can be more acute with ceramic composites because of the more severe differential thermal expansion, the possibility of mechanical fretting of the surface of the composite panel and chemical interactions with nickel base alloys. For this reason several different attachment schemes, shown on Figure 3-23, were incorporated in the ceramic composite liner for evaluation during this program. These included the bolt and swagged nut arrangement used on the Pin-Fin metallic liner segments of Runs 24 and 25. They were used to attach the panels of Rows 1, 2, and 6 and at half the attachment locations of the panels in Rows 4 and 5 of Figure 3-22. The self-locking nut attachment was used on the panels of Row 3 and at the other half of the attachments of panels in Rows 4 and 5. The attachments used the same type bolt as the swagged nut arrangement but the nut was formed in an oval shape that deformed the bolt threads as it was installed to preclude loosening. Bolts with a beveled rather than flat head were used, in conjunction with both types of nuts in the attachment of the panels in Row 4. The beveled heads fit into countersunk holes in the filler ring installed over that attachment to avoid interference with the airflow. In addition, if it were to become necessary to make the attachment bolts themselves from a ceramic composite material it would probably not be possible to fabricate them with a fully flattened head and the beveled head shape would be more representative. The panels of Row 7 were attached to the shell with a pin rather than bolts. The pin was retained with a self locking preloaded spring clip as shown on Figure 3-23. All of the attachment bolts, nuts and pins were machined from A286 alloy. The spring clip retainers were made from Inco 718.

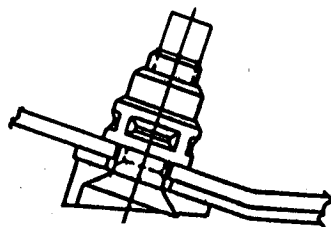
BOLT AND SWAGED NUT



BOLT AND SELFLOCKING NUT



COUNTERSUNK BOLT HEAD



PIN AND SPRING CLIP

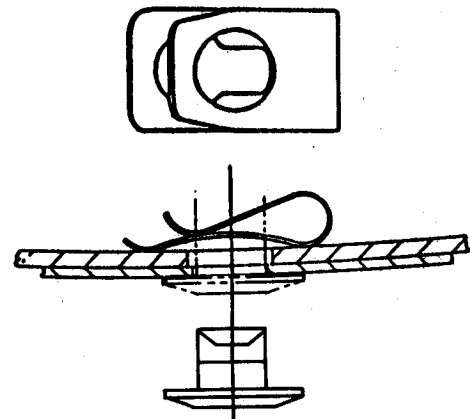


Figure 3-23 Ceramic Composite Liner Panel Attachment Methods

3.2.3.3 Ceramic Composite Material Selection

Because of the rapid advances being made in the field of ceramic composites several new material and construction approaches had developed since the Advanced Composite Combustor Structural Concepts Program had been initiated. These included the development of a new lithium aluminosilicate matrix material designated LAS_{III}, as opposed to the LAS_{II} formulation discussed in Section 3.2.3.1. The improved LAS was expected to have as much as 111°C (200°F) higher temperature capability than the earlier LAS_{II} formulation. Another development was the consideration of woven rather than layered fiber constructions. As shown in Figure 3-24, in a woven construction there is some reinforcement in the through thickness direction that can be exploited to support high through thickness thermal stresses or resist interlaminar shearing. The use of a plain weave, in which fibers are aligned in nominally perpendicular directions and cross alternating over and under each transverse fiber, was precluded from consideration for immediate application to the combustor liner because of concerns over the ability to make the fiber mat conform to a conical mold shape and the ability to completely consolidate the matrix inside the weave with then available fabrication techniques. A harness satin weave, in which perpendicular fiber cross under only at periodically spaced intervals rather than every other fiber as shown on Figure 3-24, was considered.

A change in the fiber layup for the basic multi-directional fiber layer type of construction was also introduced. With reference to Figure 3-18 the sequence of orientations of the fiber layers in the original panel definition was 0°/+45°/-45°/90° when progressing from the surface to the mid-depth plane. However, it was observed that the change in fiber direction at each interface was 45° except for the 90° change encountered between the +45° and the -45° layer and it was felt that the resistance to interlaminar shear could be increased if the changes in direction of the fibers were restricted to 45° at all interfaces. This could be readily accomplished by changing to the 0°/+45°/90°/-45° fiber orientation sequence shown on Figure 3-25 without compromising the desired orthotropy of properties in the in-plane direction.

Because of the lack of substantiating data on these new developments a materials characterization subtask was conducted to screen and acquire data on these new approaches to select the best material and construction for the Energy Efficient Engine sector combustor rig liner panels. The results of this effort are described in detail in Appendix B. The first phase consisted of acquiring basic property data on these newer materials for comparison with the existing data on the SIC-LAS_{II} system with multi-direction layered fiber orientation. These tests, consisted of assessment of the static and dynamic mechanical load carrying capacity, the creep characteristics and cyclic thermal fatigue resistance of the various materials and constructions.

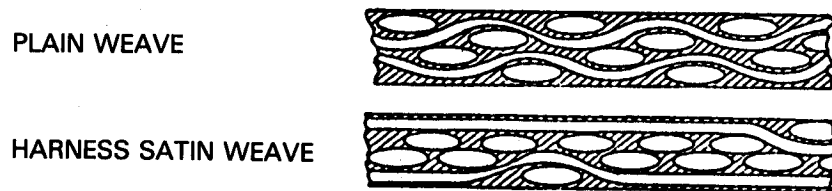


Figure 3-24 Schematic Representation of Woven Fiber Composite Materials

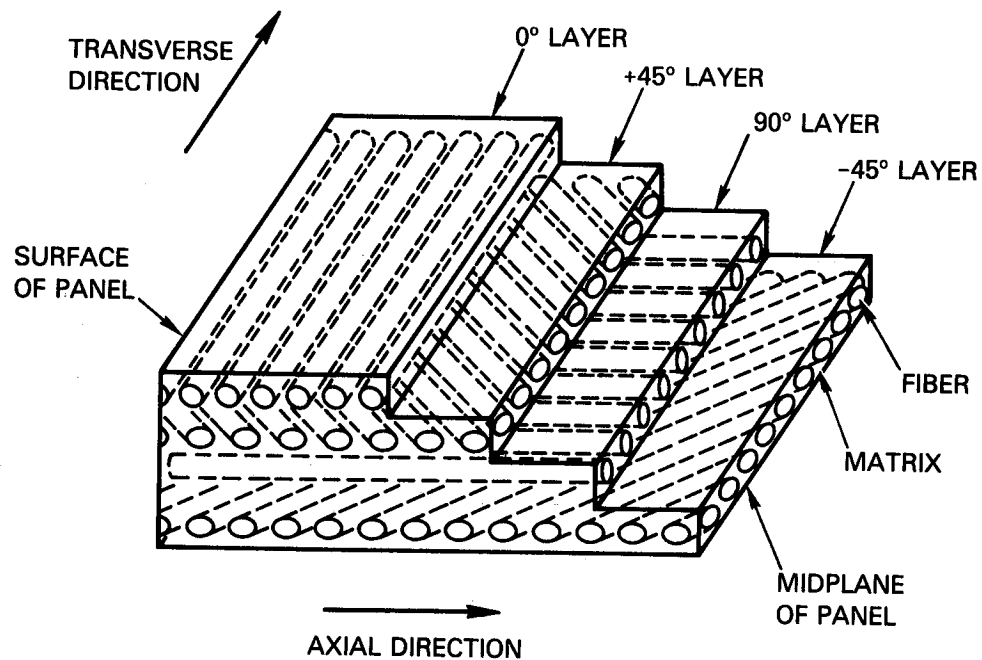


Figure 3-25 Schematic Representation of Improved Fiber Orientation in Ceramic Composite Panels

The studies conducted under the Advanced Composite Combustor Structural Concepts Program had led to the conclusion that the life limiting process for a ceramic composite liner would be some form of thermal degradation as opposed to the thermal cyclic fatigue failures encountered with metallic components. Lacking data to quantify this process the material characterization tasks also included tests in which specimens of SIC-LAS composite materials were exposed to elevated temperature levels in simulated combustor environment for as long as 100 hours to investigate the thresholds of deterioration.

As documented in Appendix B the results of these tests, in combination with accumulated experience with the SIC-LAS ceramic composite system led to a preference for the 0°/+45°/90°/-45° layered fiber construct over the woven fiber approach. In addition the cyclic thermal fatigue and the long duration thermal exposure tests conducted under this task demonstrated that the LAS_{III} matrix material did have the anticipated higher temperature capability relative to LAS_{III}. Consequently, it was concluded that all of the ceramic composite liner panels in the Energy Efficient Engine combustor sector rig would be fabricated with the 0°/45°/90°/-45° layered fiber construction and that the majority of these panels would have the LAS_{III} matrix material.

3.2.3.4 Sector Rig Liner Analysis

The primary analysis conducted on the ceramic composite liner for the Energy Efficient Engine sector combustor rig consisted of a detailed thermal analysis of each liner panel and the adjacent shell. This analysis was used to ascertain that the maximum panel temperatures were consistent with limitations on the SIC-LAS material and to establish the temperature distributions in the panels. The thermal design point for the liner was the sea level takeoff condition of the Energy Efficient Engine which was also used as the reference for the design of the Counter Parallel Finwall[®] and the Pin-Fin liners. These conditions included:

Combustor Inlet Total Pressure =	3.09MPa (450 psia)
Combustor Inlet Total Pressure =	563C (1050F)
Combustor Exit Total Temperature =	1449C (2640F)
Fuel/Air Ratio =	0.027
Fraction of Fuel in Pilot Zone =	15%
Nominal Total Inner Liner Cooling Air =	16%Wab
Inner Liner Pressure Drop =	3%

The stipulated inner liner pressure drop and total cooling air flow are consistent with the original Counter Parallel Flow Finwall[®] segmented liner design and are maintained at the same level in order to avoid perturbing the overall airflow distribution in the combustor since these changes could alter the local stoichiometry and hence the gas temperature history. With this constraint of invariant total liner cooling air flow potential benefits associated with the ceramic composite liner concept must be manifest in greater liner durability and life. Based on interpretation of the results of the thermal fatigue tests and the long duration thermal exposure tests conducted on the SIC-LAS material during the material characterization task described in Appendix B, maximum design temperature limits of 1150°C (2100°F) and (2300°F) were established for panels made with the LAS₁₁ and LAS₁₃ matrix respectively.

The thermal analysis of the inner liner of the rig involved independent analysis of each of the seven rows of liner panels and the adjacent parts of the shell using the finite element procedure employed in the assessment of the initial conceptual definition of the liner construction described in Section 3.2.3.1. The hot gas temperature and velocity distributions used in the analysis were consistent with the airflow distributions and stoichiometry of the Energy Efficient Engine and identical to that used in the thermal analysis of the Pin-Fin segmented liner of Section 3.2.2. The design procedure consisted of computation of the temperature distribution in each panel for a range of cooling air flow rates and then optimizing the distribution of cooling air between the panels to achieve nearly the same peak temperature levels in all panels without violating the maximum panel temperature or total liner cooling air flow criteria.

Figure 3-26 shows the computed temperature distributions on the surfaces of panels in Rows 2 and 4 in the combustor liner. The Row 2 panel has a relatively long part of the panel downstream of the lip in contact with the shell and a shorter region with active convective cooling on the cold side and is representative of Rows 1, 2, 5, 6, and 7 in this respect. Conversely Row 4 panels have active cold side convective cooling over a greater part of its length which is also typical of Row 3 panels. The thermal analyses were conducted for two different sets of thermal boundary conditions: a nominal or circumferential average condition and a hot-streak condition which could occur at circumferential positions where the local combustion gas temperature was higher than average because of proximity to a fuel injector or the cooling film or the surface of the panel was deteriorated by blockage by an attachment bolt head or interaction with a dilution air jet. The temperature distributions shown in Figure 3-26 were computed at the streak locations and hence are the maximum anticipated temperatures in the panel.

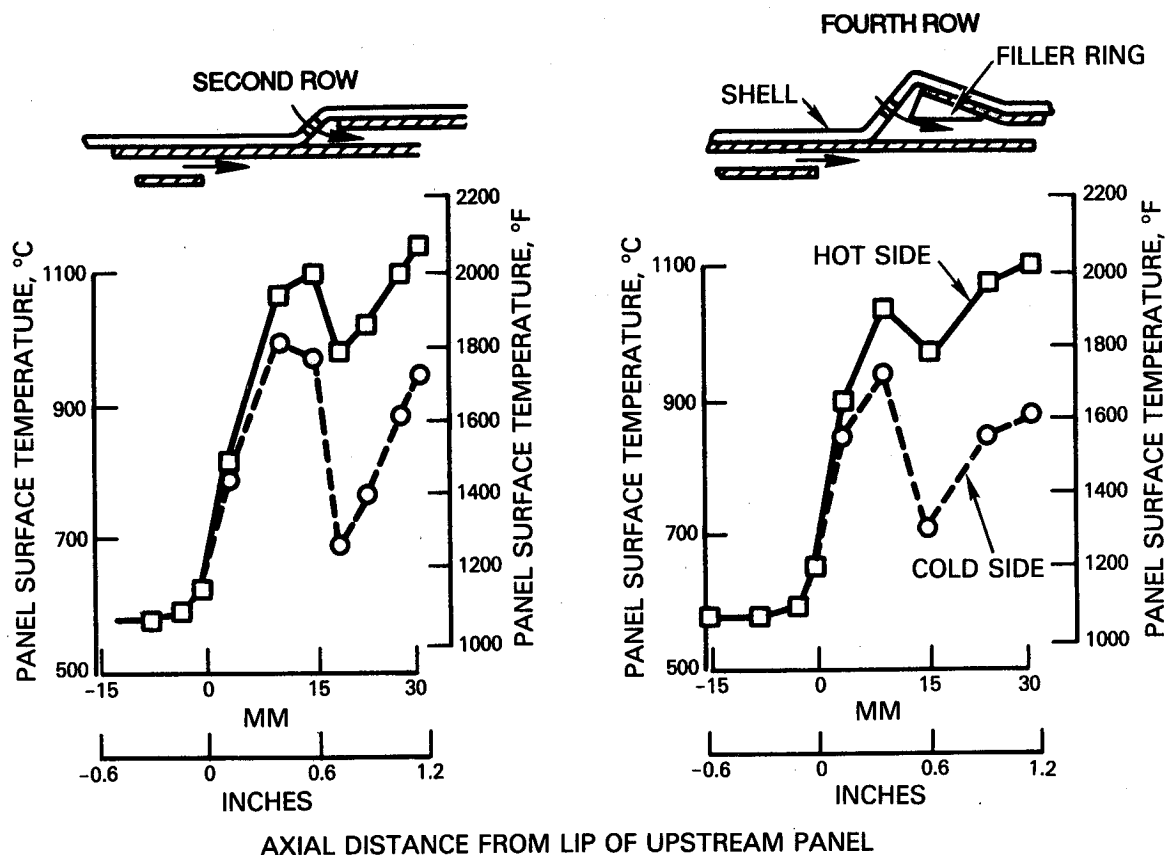


Figure 3-26 Surface Temperature Distributions in Representative Composite Panels in the Sector Combustor Rig

The computed temperature distributions show strong parallels with that of Figure 3-17 which was generated during the initial conceptual design study. Progressing downstream from the lip of the preceding panel, the surface temperatures increase abruptly reaching a first peak prior to the point of cooling air injection behind the panel and then progress to a second peak at the downstream end as the cooling air film deteriorates on the hot surface. Through thickness temperature differentials reach 200°C to 250°C (360°F to 450°F) and are highest either in the vicinity of the point of impingement of the cooling air on the cold surface or at the downstream lip. The maximum face temperatures occur at the downstream lip and are between 1100°C and 1150°C (2000°F to 2100°F).

Figure 3-27 shows the results of the analysis of all the panels in the sector rig liner. Hot side surface temperatures are shown at the downstream lips and other critical locations at the nominal and hot streak thermal conditions in each panel. The maximum panel lip temperature is 1147°C (2090°F) and occurs on Row 2 while the highest local temperature is 1152°C (2100°F) and occurs in the streak region immediately downstream of the dilution air holes in Row 5. These temperatures are consistent with the imposed design limit of 1150°C (2100°F) for panels constructed from the SIC-LAS_{III} material and offer more than 111°C (200°F) margin relative to the corresponding limit for SIC-LAS_{IIII}. The figure also shows the required distribution of cooling air to the inner liner to achieve these temperatures. A total of 14.8 percent of the combustor airflow is required. This is slightly less than the targeted 16 percent level but is acceptably close to that value.

The thermal analysis included an assessment of the effect of geometric perturbations of the components on the temperature levels in the composite panels. Of particular interest was variations in the height of the cooling air discharge slot between panels. Tolerance variations and panel or shell deflections can alter this height and vary the quantity of cooling air admitted which is reflected in the convective heat transfer from the cold side of the panel lip and the effectiveness of the cooling film on the downstream panel. Figure 3-28 shows the results of this sensitivity study and indicated that a reduction of the slot height increases the panel lip temperature. The design intent was to limit these changes in slot height to 20 percent of nominal and the figure indicates a reduction in height of this magnitude would increase the temperature of the lip of the downstream panel by about 36°C (65°F). While the SIC-LAS_{III} panels would have adequate margin to accept such a temperature excursion such a closure of the slot upstream of a SIC-LAS_{III} panel at a circumferential position near a hot streak would lead to locally exceeding the imposed design limit for that material.

The split of fuel flows between the pilot and main stages is a primary operational variable for a staged combustor. The foregoing analysis was conducted with a pilot fuel flow of 15 percent of total but the combustor has been operated at richer mixture strengths in that zone. This would lead to higher heat loads on the panels enclosing the pilot combustor zone, i.e., Rows 1, 2, and 3. Analysis of Row 2 indicated that when the pilot stage fuel flow

was increased to 20 percent of the total the axial temperature distribution in the liner panel retained the same characteristic shape shown on Figure 3-26 but that the maximum hot side temperature in a streak location increased by about 195°C (350°F) to the order of 1320°C (2400°F). Since this was well in excess of the imposed design limit for even the SIC-LAS_{III} material it was recognized that fuel flow split excursions during operation of the sector rig at high power levels would have to be avoided.

With the completion of the thermal structural analysis of the liner for the Energy Efficient Engine sector combustor rig the design process would normally have proceeded to a structural analysis. However, the liner design closely parallels the initial definition of the ceramic composite liner that was conceived and analyzed in detail under the Advanced Composite Combustor Structural Concepts Program and it was concluded that it was not necessary to repeat the analysis on this configuration. In particular, with reference to Section 3.2.3.1 the panels of the Energy Efficient Engine design have similar nominal dimensions and exactly the same thickness and number of attachments per panel as the initial conceptual design. The temperature distributions in the panels are similar and the peak temperature levels in the Energy Efficient Engine liner design are lower than those used in the structural analysis of the initial design concept. The dynamic analysis of the initial design concept had indicated substantial margin against high frequency fatigue from engine induced vibrations while a static structural analysis indicated tolerable stress levels attributed primarily to thermal effects. Consequently there was no reason to alter the conclusion reached under the Advanced Composite Combustor Structural Concepts Program that the liner panels were not stress limited and that the failure mode for the ceramic composite liner panels in the Energy Efficient Engine sector combustor rig would also be some form of deterioration at elevated temperatures.

3.2.3.5 Liner Fabrication and Assembly

The silicon carbide reinforced lithium aluminosilicate (SIC-LAS) combustor liner panels were fabricated in the Composite and Nonmetallics Laboratory at United Technologies Research Center. The SIC fiber used in all of the panels was ceramic-grade Nicalon silicon carbide yarn. This fiber typically has a tensile strength of 2206 MPa (320,000 psi) and a modulus of elasticity of 193 GPa (28 Msi). The average fiber diameter is about 12 microns. The lithium aluminosilicate, both the LAS_{II} and the LAS_{III} formulations was procured as a glassy powder from Corning Glass Company.

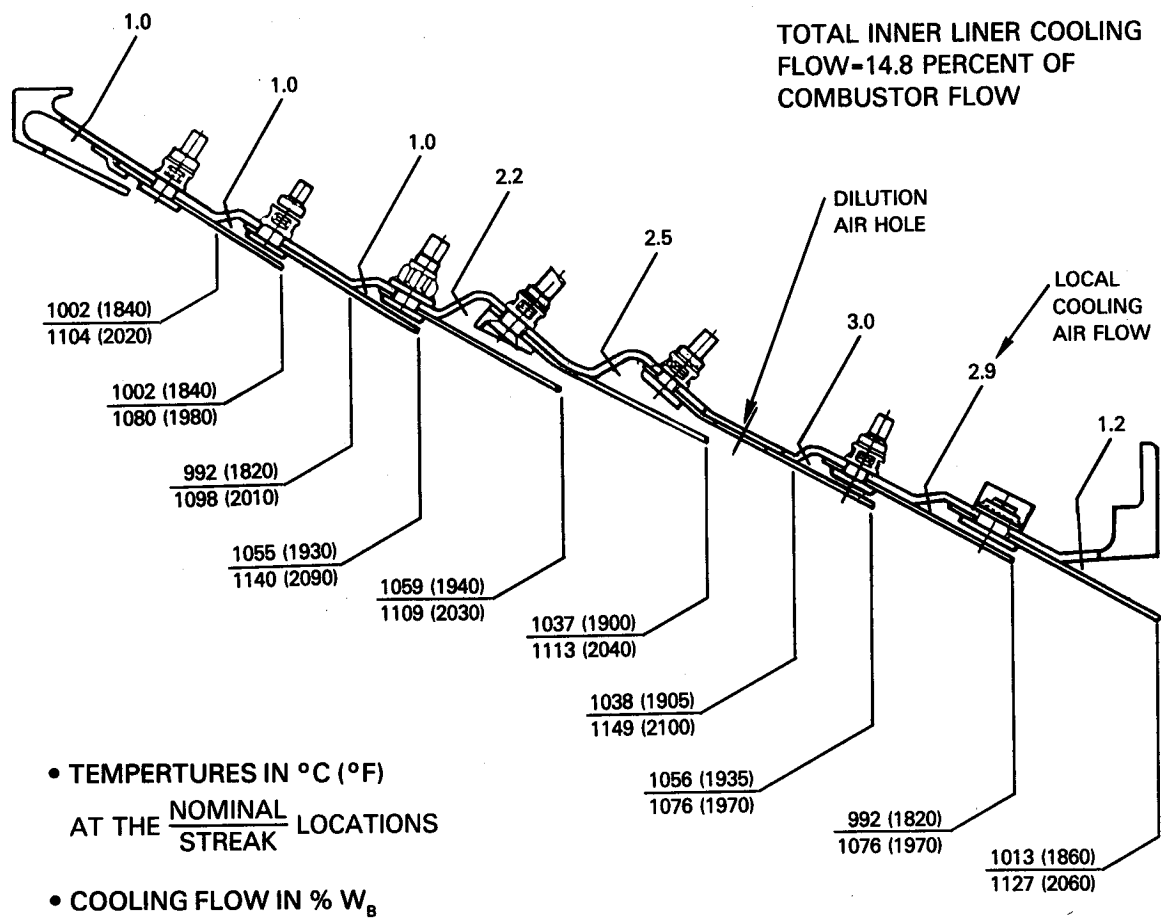


Figure 3-27 Cooling Air Distribution and Peak Hot Side Panel Temperatures in the Sector Rig Ceramic Composite Inner Liner

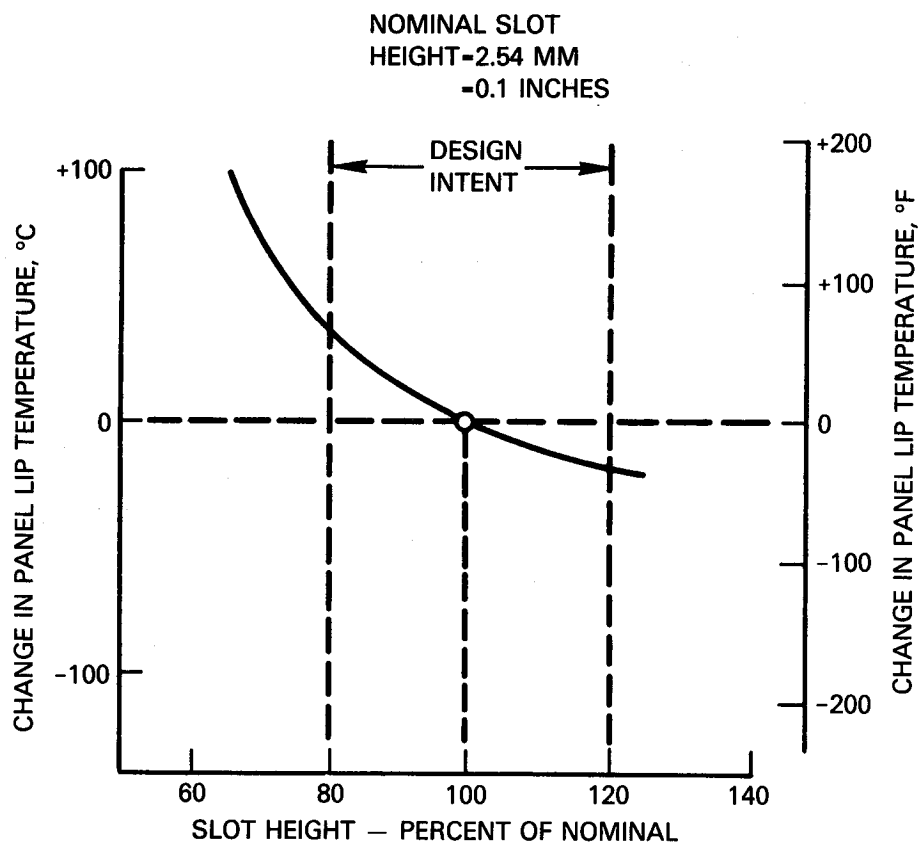


Figure 3-28 Sensitivity of Composite Liner Surface Temperature to Cooling Air Slot Height

A major element in the fabrication of the liner panels is the tooling required for hot pressing the panels. These were fabricated from graphite by American Graphite Corporation and conformed to the frustroconical shape of the panel. A total of seven sets of tooling were required sized to the distinct geometry of each row of panels in the inner liner. Figure 3-29 shows the tooling for the panels of Row 1 of the liner. The tooling was used for several purposes in addition to its primary function of hot pressing the panels. After the tooling was inspected, a tracing was made from the convex ram of each die. Since this tracing reproduced the final shape of the panel, it could be used as a pattern of cutting the individual plies from tapes of the fiber. Next, a 1.91 cm (0.75 in) thick rubber section, having a face which was a facsimile of the panel, was cast from each tool. This rubber section was used to cast grooved ceramic platens which were used to support the, as yet, unconsolidated panels during intermediate fabrication steps. The last procedure performed on the tooling was a vacuum burn-out to remove impurities.

The first step in the process of fabricating the liner panels was to impregnate the silicon fibers with lithium aluminosilicate and bond them together in layers with the fibers aligned in the same direction. This was accomplished by passing the Nicalon Silicon carbide (SiC) yarn through a lithium aluminosilicate (LAS) binder slurry and winding on a hexagonal drum. By properly controlling winding and traverse speeds, flat sheets of tape were produced with uniform, continuous fiber spacing. Using patterns traced from the tooling rams, plies were cut from these flat sheets with the fibers aligned in the appropriate directions. A total of eight plies of fiber tape were required for the symmetric $0^\circ/+45^\circ/90^\circ/-45^\circ$ sequence of fiber directions selected in Section 3.2.3.3 and shown schematically in Figure 3-25. Figure 3-30 shows the eight plies used to construct one of the liner panels and the fiber directions are evident. The photograph shows another feature of the construction in which the plies with 45° fiber orientation were cut in half and a half interchanged with one of the opposite direction. This maintained the desired sequence of successive 45° changes in fiber direction between layers but produced superior corner reinforcement.

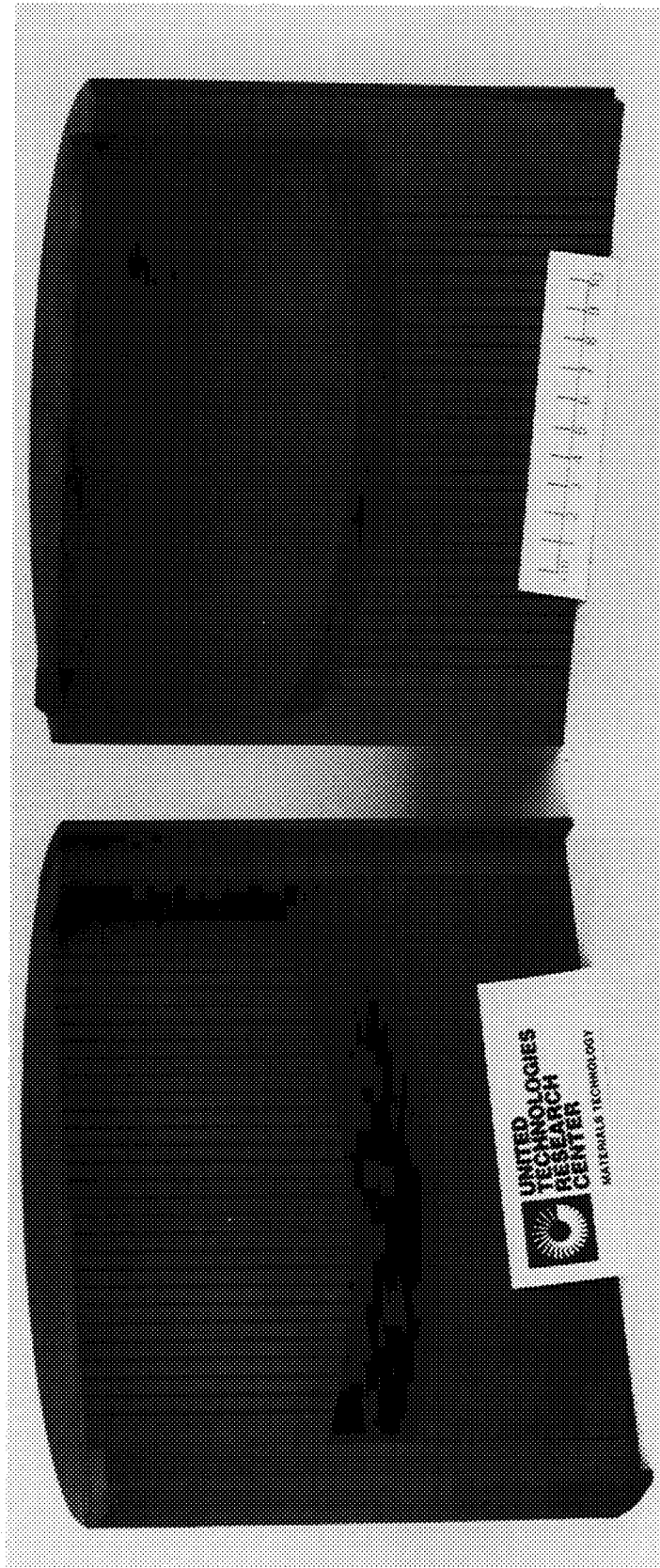


Figure 3-29 Die for Hot Pressing a Panel of the EEE Combustor Rig Liner

ORIGINAL PAGE 48
OF POOR QUALITY

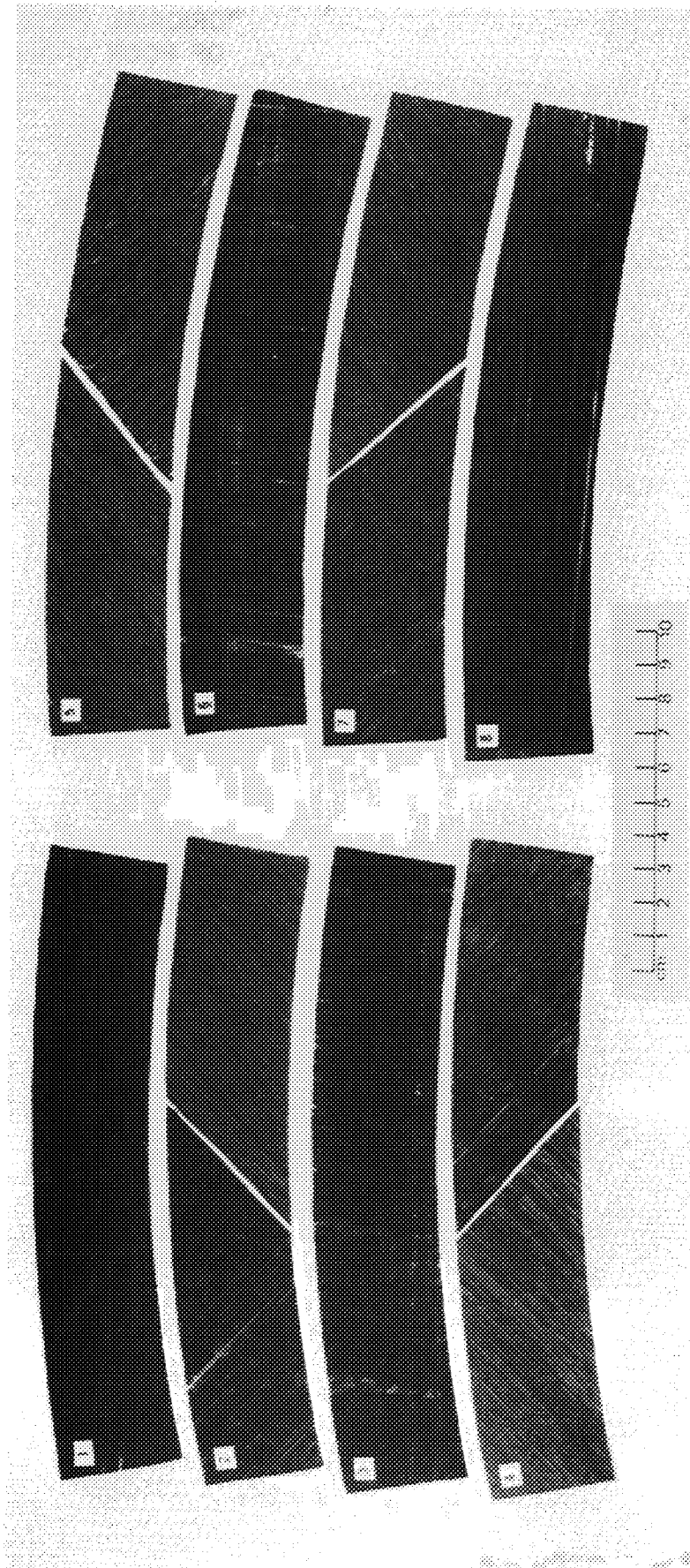


Figure 3-30 Eight Silicon Carbide Fiber Plies used to Construct a Liner
Panel (Numbers Indicate Stacking Sequence)

ORIGINAL PAGE
BLACK AND WHITE PHOTOGRAPH

The eight fiber plies were stacked in the graphite die and the panel was warm molded. In the process, sufficient heat and pressure were applied to flow the acrylic binder. After warm molding, the lay-up approximates its final shape but is twice its final thickness. Next, the burn-out and sintering was performed using the previously described grooved ceramic platens prepared from the tooling. The warm molded panel was inserted between the platens to maintain fiber placement. During the burn-out cycle, the binder was removed from the panel. In the sintering cycle, the thermal treatment was sufficient to lightly fuse the LAS matrix together. The sintering operation was not intended to consolidate the composite. This was accomplished by hot pressing which was performed on a Brew single-ram action hot press. The pressing was done "to stops" since the goal was to produce near net shape panels. Pressing "to stops" was accomplished by using the top of the die tooling as a stop for ram motion and providing flash grooves on the side of the die molding cavity to allow space for the removal of excess glass.

The final step in the fabrication process of ceraming the matrix from a powdery glass constituency into a polycrystalline material, capable of withstanding high temperatures, was accomplished by exposure to elevated temperatures above the melting point of the matrix for a period of time, while being confined in the graphite die.

Following fabrication, holes for the attachment bolts and dilution air holes were machined into the panels. Additionally, a small amount of edge trimming was required to ensure that adequate transverse clearance was maintained between the panels. Three attachment holes, 5.18 to 5.44 mm (0.204 to 0.214 inch) diameter, were machined on the leading edge of each panel. The panels were waxed to a flat glass plate, convex side down, to secure them during drilling. A Bostomatic NC milling machine with diamond impregnated core drills was used. Holes were drilled at a cutting speed of 4000 rpm and a down-feed rate of 0.043 mm/min (0.017 in/min). The operation was cooled with a portable pneumatic mist system using water as the coolant.

The Row 5 panels each had five dilution air holes, 1.07 to 1.12 cm (0.430 to 0.440 inch) diameter, spaced along the center line. A 0.66 cm (0.259 inch) diameter core drill made this hole by translating the bit out to the edge of the radius from an initial hole, then moving the bit in a circular arc. The feed rates and coolant were the same as used for the mounting holes. There was no visible sign of edge damage on these holes.

During a trial assembly the short ends of the panels were trimmed to achieve the proper cold transverse clearance between adjacent panels and to provide for panel to endwall gap. The trimming operation was performed with a hand held grinding wheel removing material to a scribed line using a diamond bonded wheel. Figure 3-31 shows a closeup view of a panel from Row 3 and from Row 5 of the liner after these machining operations were completed.

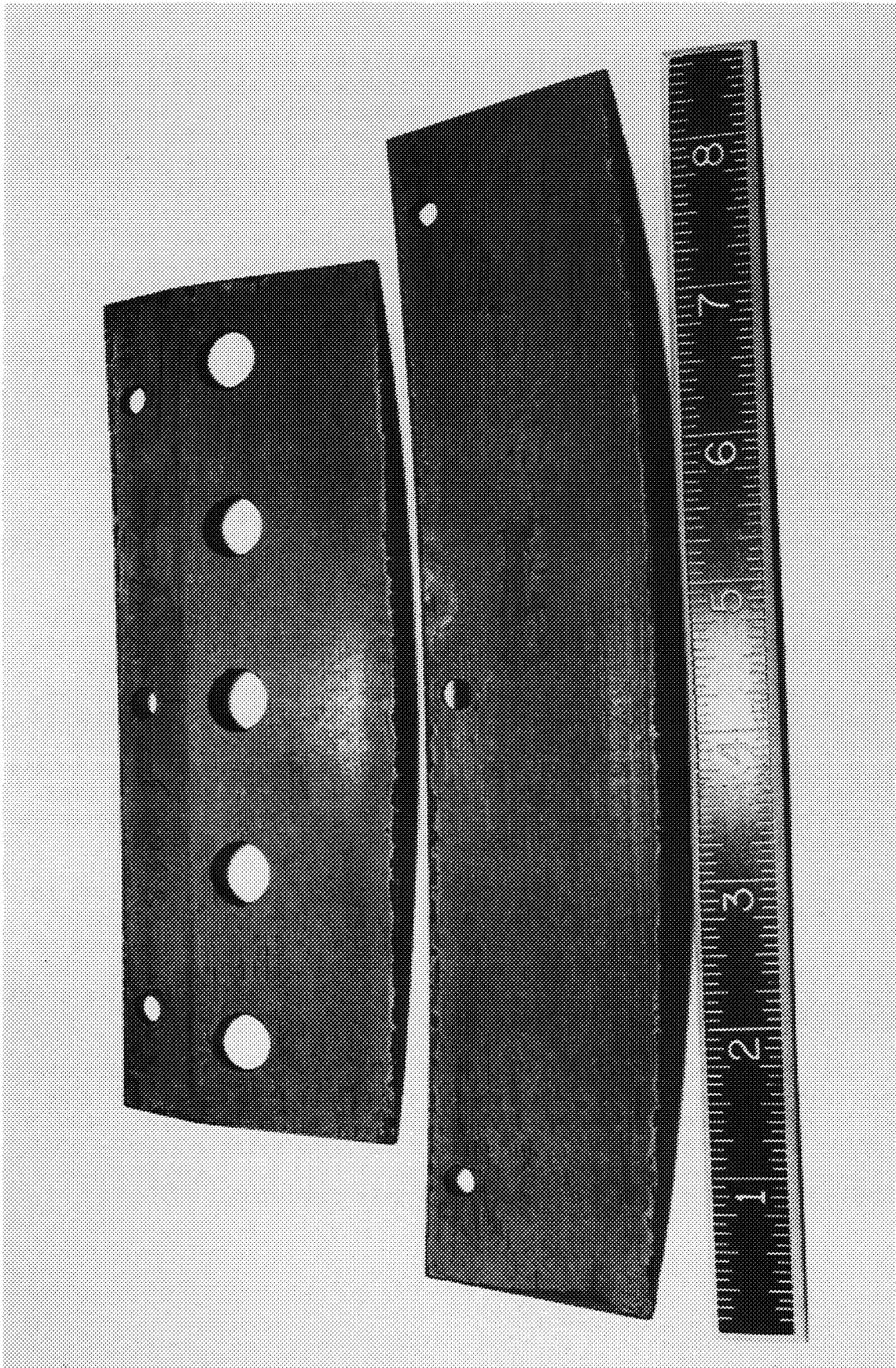


Figure 3-31 Panels from Row 5 (Top) and Row 3 (Bottom) of Liner After
Drilling and End Trimming Operations (Ruler Scale in Inches)

While the inner liner of the sector rig required a total of eighteen panels, twenty seven panels were fabricated to allow for spares and defective parts. The panels were inspected during and following the fabrication process. Inspection techniques included visual examination, dimensional inspection and density measurements. The latter are critical because they can determine the extent of consolidation of the composite matrix. The apparent density, as determined by liquid displacement were in the narrow and acceptable range of 2.52 to 2.60 grams/cc. Comparison with bulk densities determined from calculated volumes indicated surface porosity of the panels was in the range of 1.4 to 3.2 percent.

Dimensional measurements were made on the panels after fabrication. The thickness of the panels ranged from an average of 1.17 to 1.45 mm (0.046 to 0.057 inch) with a standard deviation generally between 0.051 and 0.076 mm (0.002 and 0.003 inch). This variation in thickness was the result of variations between the different sets of tooling. The thickness increase during ceraming was approximately 0.0254 mm (0.001 inch) for all panels. The thickness measurements are the average of twelve measurements per panel.

The general appearance of the majority of the as-fabricated panels was excellent. The calculated fiber volume fractions were in the target range of 38 to 42 percent. There was no evidence of cracking or delamination on the panels, except for an unconsolidated corner on two panels for Row 2 and one for Row 3. In the case of the panels for Row 2 this was traced to incorrect machining of the angles on the hot press tooling. This situation was corrected by minor modification to the top ram and two good panels were subsequently fabricated from this tool.

The machining of the ends of the panels to obtain proper transverse clearance between the panels apparently induced some stresses in the panel because a few minor defects were found in inspection after this operation. Two of the panels for Row 2 had a crack on an upstream corner that was approximately 0.75 cm (0.3 inch) long and through the thickness of the panel. Because the only spares for these panels were those cited above with the unconsolidated corners the cracked panels were used in the sector combustor rig. Other machining induced damage consisted of delamination along one of the ground ends on two panels for Row 6. One of the panels was replaced with a spare while the delamination was not considered severe in the other and it was included in the rig hardware set.

As was indicated in Section 3.2.3.3, while there was a strong preference for the use of 8 panels with the LAS III matrix formulation, it was intended that at least a few panels fabricated with LAS II be included in the combustor rig. Four such panels were fabricated; one each for Rows 6 and 7 and two for Row 2. Surface quality of the panels made with LAS II was not as good as those incorporating a LAS III matrix because they did not release as readily from the tooling after hot pressing. As a result only one panel with the SIC-LAS II matrix was included in the sector combustor rig build. This panel was located near the left sidewall (as viewed upstream) of the rig in Row 6. Figure 3-32 shown the entire complement of 18 SIC-LAS panels used in the combustor sector rig.

ORIGINAL PAGE IS
OF POOR QUALITY

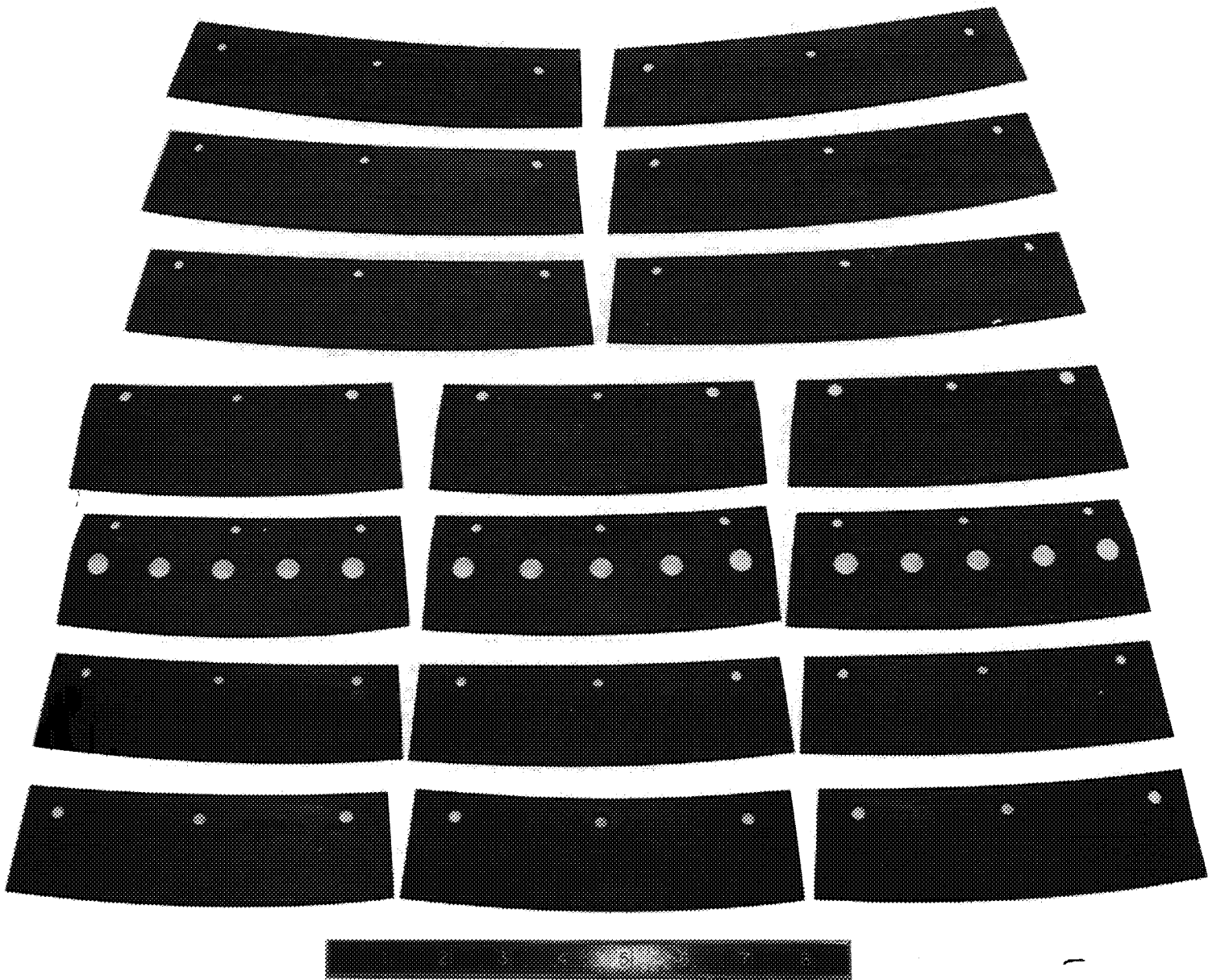


Figure 3-32 Complete Set of Ceramic Composite Liner Panels for EEE Combustor
Rig Inner Liner (Ruler Scale in Inches)

The shell upon which the individual panels were mounted was machined from Hastelloy X. By machining the shell, as opposed to forming it from sheet metal, as was done for the shell on which the Pin-Fin metallic liner panels were mounted, a more dimensionally precise part was obtained. After the shell was machined, cooling air holes, panel attachments, dilution air holes, and flange bolt holes for installing the liner in the combustor sector rig were drilled. Figure 3-33 shows the shell prior to installing the liner panels.

Prior to being mounted on the liner shell the cold side surfaces of all of the liner panel and the hot sides surfaces of selected panels were painted with thermal paint as described in Section 4.3.2. The panels were attached to the shell using the three different types of attachments described in Section 3.2.3.2. Since all of the panels had been pre-fit to the shell when their ends were trimmed there was no need of further machining of the panels during final assembly. Figure 3-34 shows the gaspath side of the inner liner of the combustor sector rig with all of the panels attached. Figure 3-35 shows the external or shroud side of the inner liner shell after the panels were installed. The smaller diameter dilution air holes in the Row 5 liner panels are visible through the holes in the shell. The different type of attachment devices are also evident in this figure. (The longer bolts have the self locking nuts while the short bolts have swaged nuts per Figure 3-23).

ORIGINAL PAGE IS
OF POOR QUALITY

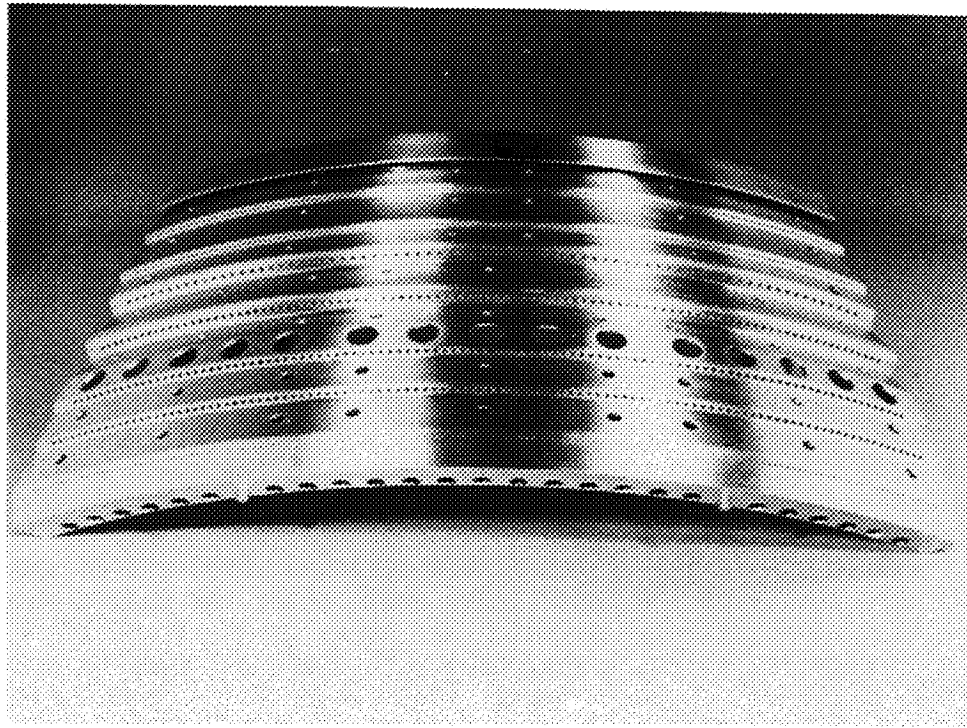


Figure 3-33 Inner Burner Liner Shell for Ceramic Composite Liner

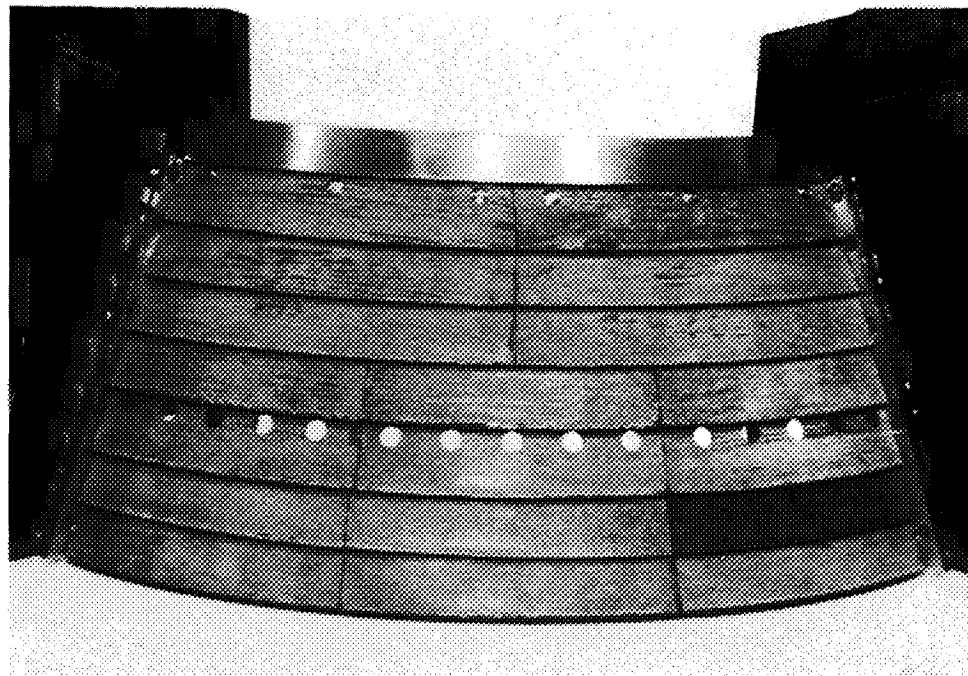


Figure 3-34 Ceramic Composite Liner Panels Installed on Inner Liner Shell of Combustor Sector Rig

ORIGINAL PAGE IS
OF POOR QUALITY

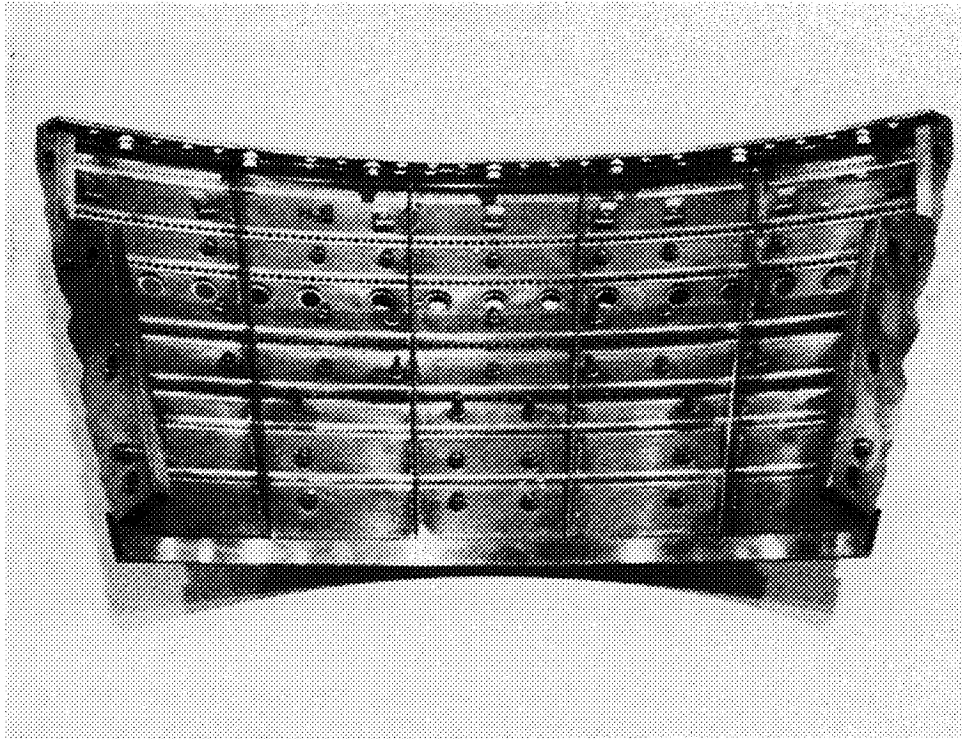


Figure 3-35 External Surface of Inner Liner Shell After Installing Ceramic Composite Liner Panels

ORIGINAL PAGE
BLACK AND WHITE PHOTOGRAPH

SECTION 4.0 TEST PROGRAM PLAN, FACILITIES AND INSTRUMENTATION

4.1 SECTOR RIG CONFIGURATION

The combustor sector rig used in the previous test program was utilized for all four tests. This rig, as shown in Figure 4-1, is a 90-degree sector of the Energy Efficient Engine combustor component, with essentially all of the technology features. The diffusion section contains the short, strutless prediffuser with a curved wall flowpath. In the two-stage combustor, fuel is supplied to the pilot zone through single pipe aerated nozzles and to the main combustion zone through pressure atomizing fuel nozzles. The liners are a segmented design using the counter-parallel Finwall® cooling technique.

All tests were conducted with the segmented outer liner assembly featuring the counter-parallel Finwall® cooling technique. However, the inner liner assembly was comprised of the pin fin cooling technique segments for the second and third series of tests and ceramic composite segments for the fourth and final series of tests.

Certain instrumentation was installed to ensure the safety of the test vehicle. Thermocouples were installed at different locations throughout the combustor to measure metal surface temperatures and detect hot spots. If the measured level exceeded a predetermined limit, an alarm was actuated so that emergency corrective control action could be implemented.

A light-off detection unit was used to provide an indication of ignition as well as to detect the occurrence of a blowout condition. Upon the detection of a blowout, the system simultaneously initiated the termination of fuel flow, thereby eliminating a hot relight situation.

Hydrocarbon detectors were installed in the outer and inner combustor shroud area and near the fuel manifold. These sensors obtained samples of flow in these environments to provide a measurement of the hydrocarbon content. If the level exceeded the limit, an alarm was actuated and the fuel flow to the test vehicle was terminated.

4.2 TEST FACILITIES

The test program was conducted in Stand X-903, which is one of five pressurized combustor development stands located in the Pratt & Whitney complex in Middletown, Connecticut.

In this stand, the test rig was mounted within a cylindrical pressure tank. Tank pressurization was automatically controlled to 6 psi above rig pressure. In this manner, the pressure load was supported by the facility pressure vessel, permitting the experimental hardware to be of relatively light construction. The thermal load was carried by the test rig. The main tank was cooled with an amount of purge air equal to 5 to 10 percent of combustor inlet airflow. A retractable tank section with a quick-connect breech-lock seal was provided to enable easy access to the test rig.

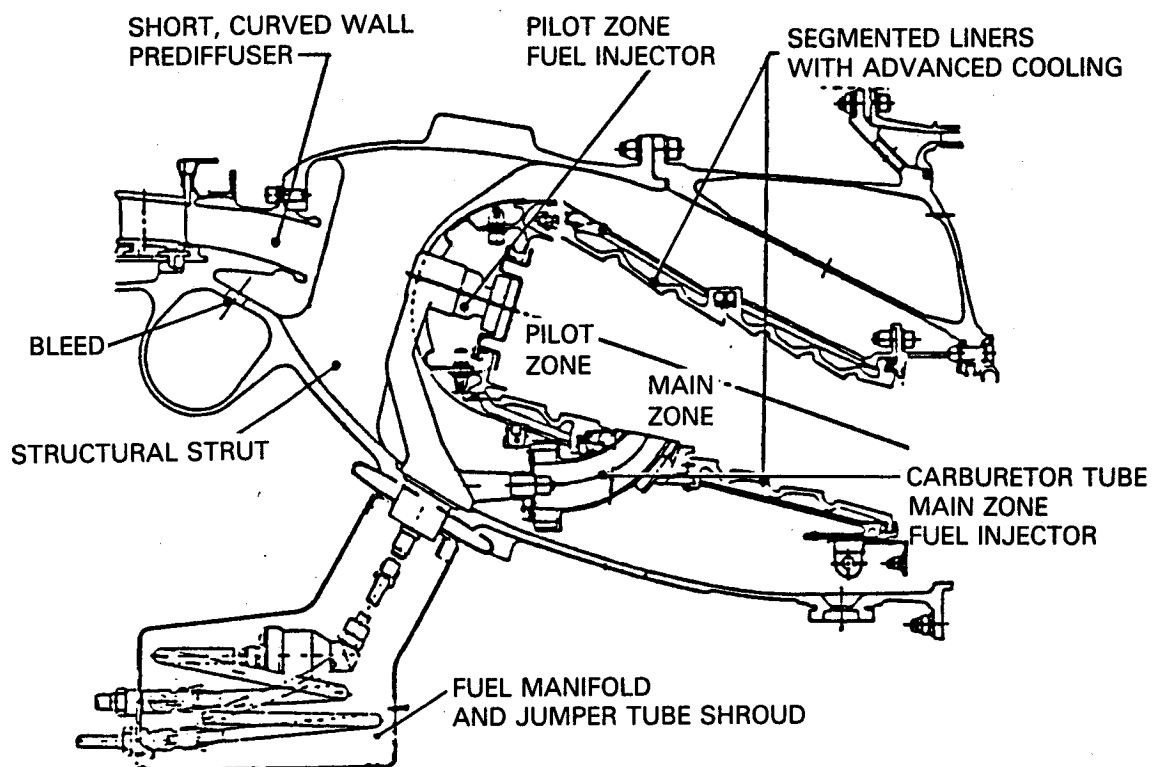


Figure 4-1 Cross Sectional View of Sector Combustor Test Rig

The control room, located adjacent to the test cell, contains the equipment necessary to monitor the test rig and facility and to control and maintain required test conditions, thereby ensuring safe operation at all times.

Nonvitiated inlet air at temperatures up to 1200°F was supplied by a gaseous/liquid fuel-fired heat exchanger. Air up to a flow rate of 25 lb/sec and pressure of 625 psia was provided by two steam-driven, two-stage turbocompressors and one six-stage, steam-driven boost compressor. However, when sector rig testing was conducted at simulated hot day takeoff conditions, it was necessary to use air supplied from Stand X-960 to achieve the desired pressure level.

A wide range of fuels, including Jet-A, could be supplied at pressures up to 1500 psia and flow rates up to 1.5 lb/sec by the facility fuel system. Fuel flow measurements were obtained by using multiple turbine flowmeters (in series) in each fuel line.

Secondary services included high-pressure cooling water, steam and air, various electric power supplies, and inert gas purge systems. Exhaust gases were collected in a water cooled exhaust duct and are then ducted underground to an expansion and liquid separation pit at the base of the main exhaust stack.

4.2.1 Data Acquisition Systems

Stand X-903 is serviced by automated data acquisition and recording systems. Data required for configuration analysis are recorded and processed in real time by a large digital automatic data reduction computer (Univac). Raw data are transmitted in millivolts from the test facility to the computer center via a telephone link. The computer reduces the data, converts it to engineering units, and displays the results on a data display scope at the test facility. The data can then be reviewed, after which printed output can be obtained at the test location or at the computing center. Three systems are available for data logging processing. The first system, especially helpful in troubleshooting problems after the test, consists of two Texas Instruments four-pen recorders that monitor the output of the instruments and provide a continuous real time record for either immediate inspection or subsequent analysis. The second system, a Tektronix digital magnetic tape cartridge recorder (X-960) or punch paper tape (X-903), records data on command for storage or later processing on an IBM 370 computer. The third system is an on-line Univac that provides essentially real time data recording and analysis. Data are either visually presented or printed.

The stand has separate and permanently installed emissions and smoke measurement systems that are available to support the test. The emissions instrumentation and sample-handling system were designed to conform to specifications in the Society of Automotive Engineers (SAE) Aerospace Recommended Practice, ARP-1256 and Environmental Protection Agency 40CFR87. Combustor exhaust smoke measurements were obtained by a smoke measuring system that conforms to specifications of the SAE ARP-1179.

4.3 TEST INSTRUMENTATION

The test rig incorporated a variety of instrumentation to monitor operating conditions such as inlet flows, temperatures and pressures as well as to record combustor performance, radiant heat flux, emissions, and structural characteristics. Thin-film temperature sensors were installed on the metallic liners to record surface metal temperatures, and radiometers were used to determine the total radiant heat flux. Instrumentation requirements, including the type of sensor, quantity and location, were determined on the basis of analyses, previous sector rig testing and Pratt & Whitney's experience in the development of advanced combustion systems.

4.3.1 Overall Performance Instrumentation

The rig was equipped with pressure, temperature and gas sampling sensors for a complete documentation of performance and emissions. Table 4-I lists the type, location and quantity of the performance instrumentation. As indicated, the combustor inlet and exit locations were extensively instrumented. Six total pressure probes and five total temperature probes were used along with a series of wall static pressure taps to measure combustor inlet conditions.

Exit total pressures and temperatures were recorded by stationary vane packs. Also, exhaust emissions were obtained at the combustor exit with eight stationary vanes. The exit probes were air cooled and the gas sample lines were steam cooled. The gas sampling lines were manifolded so that emissions were averaged.

4.3.2 Exit Instrumentation

Development of the combustor through the sector rig test program was aided by the use of a fully instrumented stationary vane pack at the exit plane. Exit total pressures and temperatures were evaluated to assess performance characteristics, and in conjunction with gas sampling techniques, were used to recommend changes in configurations in order to meet program performance goals.

The Combustor Sector Rig Test Program consisted of a series of four high pressure tests, only the first of which required full assessment of combustor overall performance and emissions. In the remaining three tests, the sector rig was utilized as a vehicle for the evaluation of segmented liner (both metallic and ceramic composite) thermal performance and radiation measurements at elevated inlet pressures and temperatures. The hostile combustor environment needed to be simulated at test facility limits of pressure and temperature in order to discern the subtle thermal characteristics of advanced liners and to collect fundamental data on liner thermal loads.

TABLE 4-I
COMBUSTOR SECTOR RIG INSTRUMENTATION LIST

LOCATION	MEASUREMENT/TYPE	QUANTITY	PURPOSE
INLET	o 4-ELEMENT TOTAL PRESSURE PROBES	6	o RIG INLET TOTAL PRESSURE AND TEMPERATURE PROFILES
	o 4-ELEMENT TOTAL TEMPERATURE PROBES	5	
	o INNER AND OUTER WALL STATIC PRESSURE TAPS	5/5	
PREDIFFUSER	o INNER WALL STATIC PRESSURE TAPS (2 ROWS)	6 EACH ROW	o PREDIFFUSER PERFORMANCE
	o OUTER WALL STATIC PRESSURE TAPS (2 ROWS)	6 EACH ROW	
DIFFUSER CASE STRUTS	o 5-LEADING EDGE TOTAL PRESSURE	4 STRUTS	o PREDIFFUSER EXIT PROFILE
OUTER SHROUD	o 2 ROWS-WALL STATIC PRESSURE TAPS	4 EACH ROW	o LINER FEED PRESSURE MAP o SAFETY
	o HYDROCARBON DETECTOR	1	
INNER SHROUD	o 2 ROWS-WALL STATIC PRESSURE TAPS	6 EACH ROW	o LINER FEED PRESSURE MAP o SAFETY
	o HYDROCARBON DETECTORS	1	
COMBUSTOR HOOD	o STATIC PRESSURE TAPS	2	o BULKHEAD FEED PRESSURE
EXIT	o VANE PACK 5 LEADING EDGE THERMOCOUPLE 4 LEADING EDGE GAS SAMPLING PORTS 5 TOTAL PRESSURE PORTS	8 VANES 8 VANES 4 VANES	o EXIT TEMPERATURE PROFILE o EMISSIONS

Vane pack cooling air and thermocouple sensor temperature limitations (approximately 3000°F for Pt-Pt/Rh thermocouples) along with a typical combustor pattern factor of 0.40 limited the average combustor exit temperature to 2300°F. This was at least 300°F cooler than the desired exit temperature level to fully exercise liner schemes. Accordingly, subsequent to the completion of Run 23, the instrumented vane pack was removed. In order to fulfill facility safety requirements and to allow for some degree of data verification, water cooled aspirating probes with Pt-40 Rh/Pt-40 Ir sensors were installed at three locations. These sensors are capable of operating at temperatures up to 3300°F. Placement was determined from hot spot locations observed in previous tests.

4.3.3 Combustor Liner Instrumentation

Liner surface temperatures were recorded by three different measurement techniques. Conventional installation of imbedded and surface mounted of chromel/alumel sensors comprised two of the methods (Figure 4-2). Thin film (sputtered) temperature sensors were also used extensively. An installation technique (Figure 4-3) developed in a joint NASA/P&W technology program was utilized. This type of sensor is capable of minimizing the uncertainty in temperatures measured by imbedded thermocouples caused by heat path distortion as well as the uncertainty in exact location of the thermocouple. In addition to local measurements with thermocouples, thermal sensitive paint was employed on the inner and outer liner surfaces in order to determine large-scale surface temperature gradients.

Figure 4-4 identifies the location of instrumentation for Run 23, in which both inner and outer liners are of the CFW configuration. As indicated, most of the instrumentation, particularly the thin-film type, is concentrated on the inner rear liner. This location is opposite the main zone carburetor tubes, which in previous testing was the highest heat load region in the combustor. Other sensors are dispersed on the outer liner, covering both the pilot and main zones.

As indicated in Figure 4-5, 16 imbedded, 7 surface and 14 thin film sensors were installed throughout the inner pin-fin liner for Run 24. Basically, the sensors are in the same general area as the CFW liner. These measurements were used to assess overall thermal efficiency and monitor any non-symmetrical temperature patterns caused by disturbances from dilution holes or mount posts.

The instrumentation scheme for Run 25 is shown in Figure 4-6. The number of sensors were slightly increased to 18 imbedded, 9 surface, and 13 thin film types. Installation locations were kept as close as possible to those of Run 24.

Pre- and post-test calibration of the thin film thermocouples showed that the indicated temperature two-sigma error was respectively less than 2.0 and 3.0 percent of the applied 900°F gradient. The calibration reference surface thermocouples were estimated to be accurate to within 1 percent under the conditions of the test. Thus, no correction was applied to the sputtered thermocouple data.

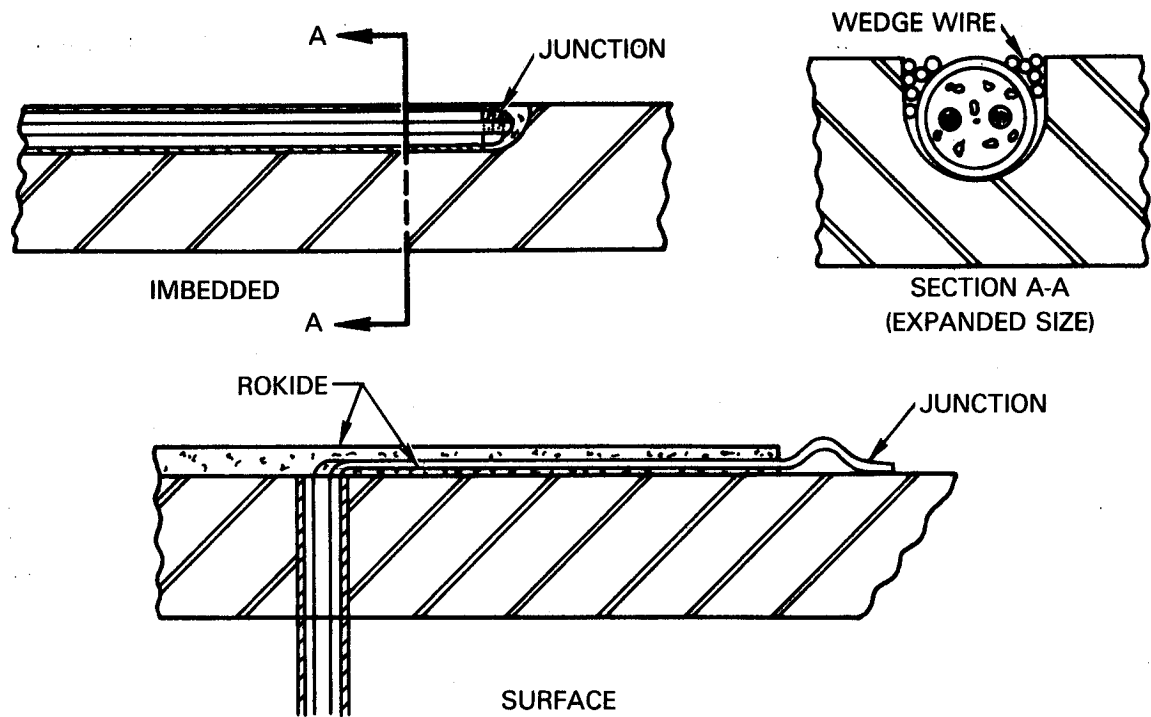


Figure 4-2 Installation of Chromel/Alumel Thermocouples

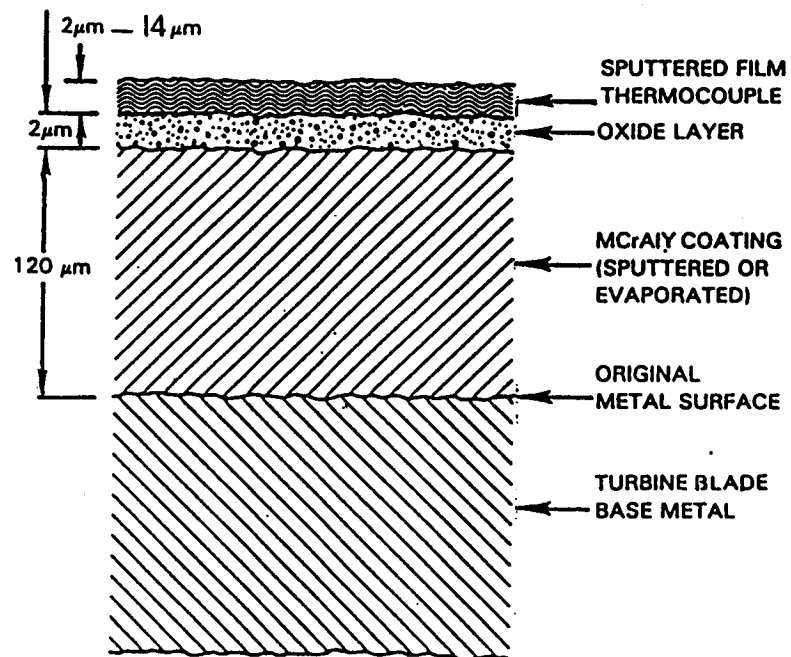


Figure 4-3 Thin Film Sensor Installation

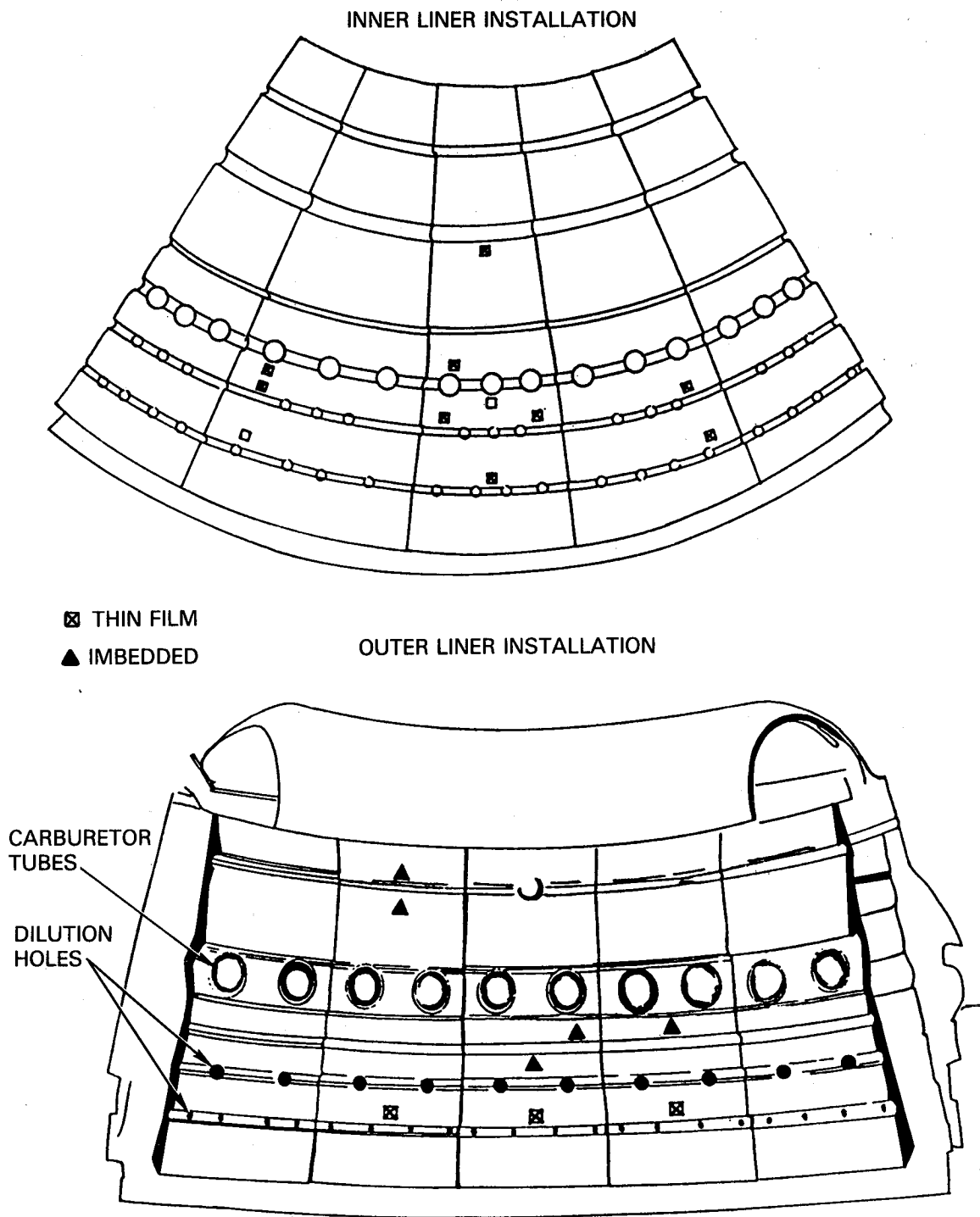


Figure 4-4 Thermocouple Installation for Run 23

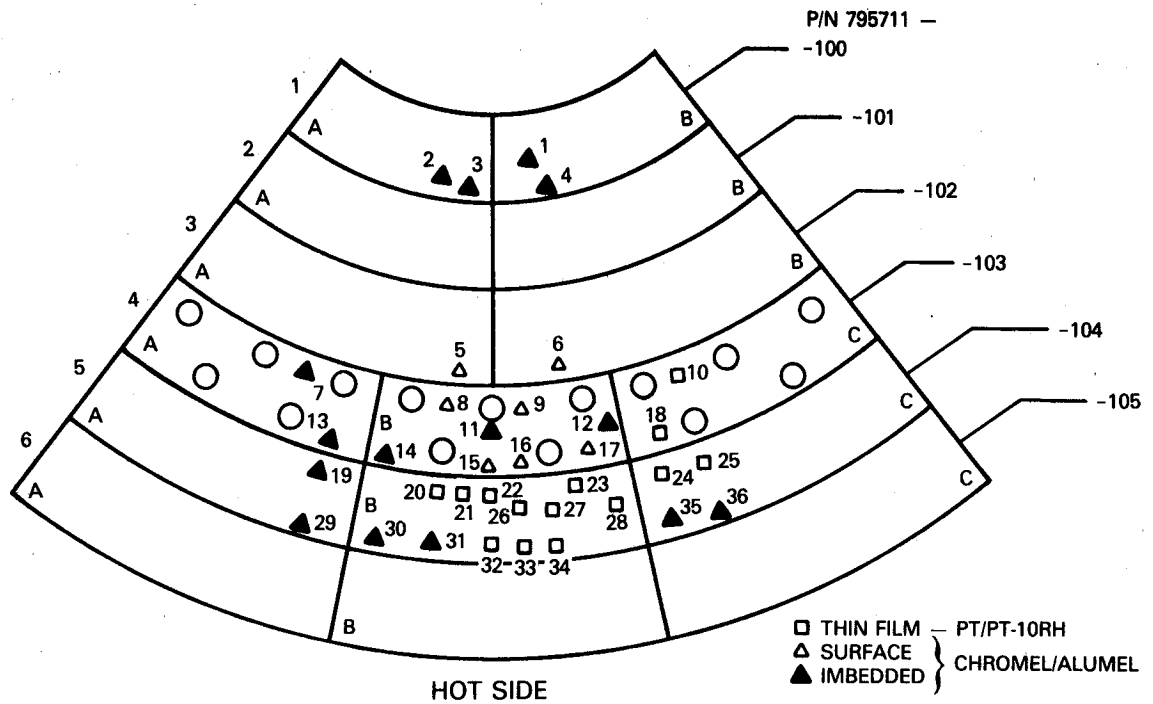


Figure 4-5 Thermocouple Installation for Run 24

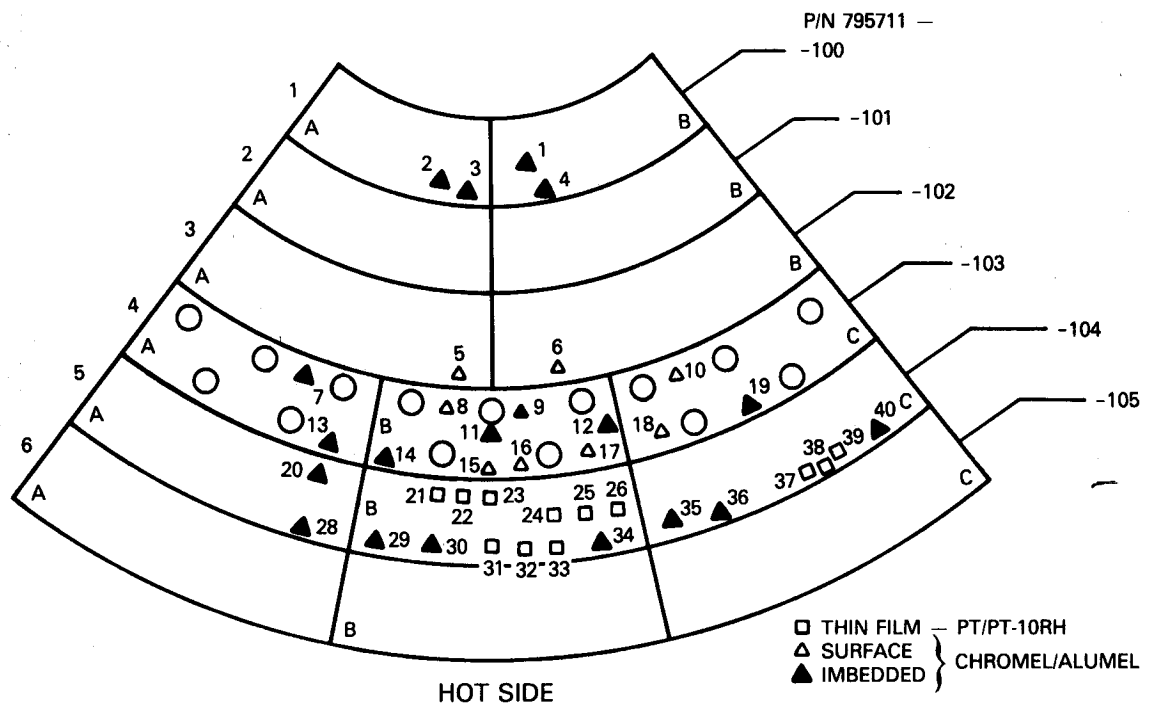


Figure 4-6 Thermocouple Installation Layout for Run 25

The measurement of temperatures in or on the SIC-LAS ceramic composite liner panels presented some unique problems. The use of surface or sputtered metal thermocouples such as those used on the pin-fin metallic liner was considered, and trials were conducted to ascertain that sputtered thermocouple metals would adhere to the ceramic surfaces. While these were reasonably successful this approach was not pursued further because of anticipated difficulties in retaining the lead wires near the point where they are attached to the sputtered surface layer.

The use of embedded thermocouples, as also used on the pin-fin liner panels, was also precluded because of the low thermal conductivity ceramic material. Even if the junction were miniaturized to preclude conduction errors, the high temperature gradients expected through the liner panels would require precise knowledge of the depth of the junction within the panel to be of any value.

These considerations led to the selection of thermal paints as the means for determining the temperature levels encountered by the ceramic composite liner panels during the Run 26 test. Two different types of thermal paints were considered: those which go through one color transition at a particular temperature and those which go through a series of color changes as temperature is progressively increased. Tests reported in Appendix B were conducted to assess the relative merits of each. The continuous change type paints were selected on the basis of their adhering better to the ceramic surface and providing more, if not quite as accurate, information on the surface temperature distribution. Two different types of continuous change paints were available. Type GT-1 has an initially blue color and transits through shades of purple as temperature increases, while Type C-3 is initially orange and changes through shades of yellow and brown with increasing temperature. Both are sensitive to the temperature range of 510 to 1065°C (950 to 1950°F) and oxidize to a black color at temperatures above 1091°C (2000°F). The Type C-3 paint provides better temperature resolution because it passes through more color transitions, but the Type GT-1 appeared to adhere better to the ceramic composite material.

Figure 4-7 shows a schematic diagram of the composite panels on the inner liner of the rig and indicates the type of thermal paint applied to the panels. The cold side of all of the panels was painted. Those on the right side (as viewed from downstream) and center were painted with the Type C-3 paint which offered better temperature resolution, while the panels in the row on the left side were painted with the Type GT-1 to provide some backup if the Type C-3 did not adhere well on the remaining panels. While there was some concern over paint erosion, the hot side of some panels was painted with the Type GT-1 paint. Coverage was limited because there was a possibility that the presence of the paint could promote or inhibit the development of surface reactions on the panels. Consequently, only the panels on the left side of the inner liner, exclusive of that in Row 6, were painted with GT-1 on the hot side. The panel in Row 6 was excluded because it was the only one in the rig that had been fabricated with the LAS II matrix material.

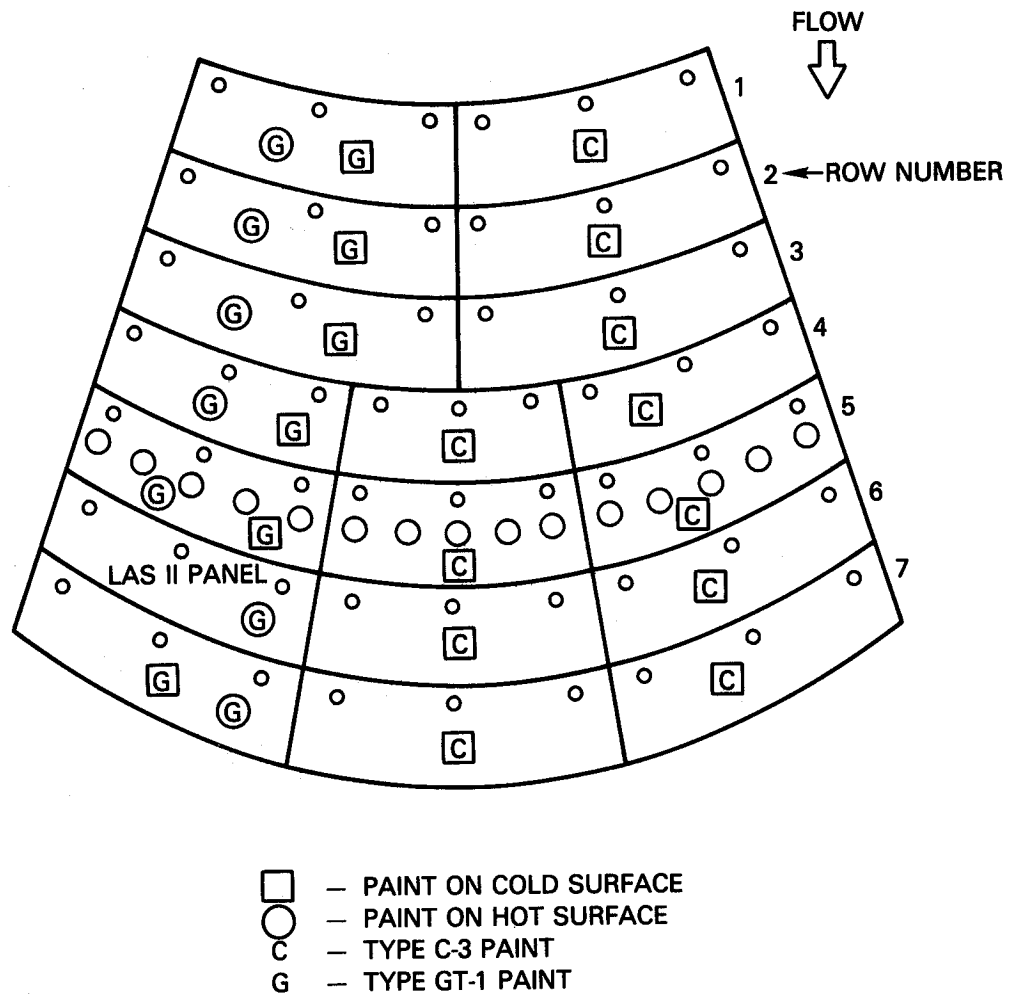


Figure 4-7 Schematic Diagram of the Inner Liner of the Combustor Sector Rig Showing Thermal Paint Application on Ceramic Composite Liner Panels

4.3.4 Radiometers

Porous plug and Medtherm radiometers were installed through openings in the outer liner in both the pilot and main zones at the locations shown in Figure 4-8.

The porous plug radiometer probe, shown schematically in Figure 4-9, was developed at Pratt & Whitney. In this design, the convective heat load on the probe screen is removed by a transpiration flow of gas through the porous material. A radiative heat load causes the porous screen to heat up, and the temperature difference between the incoming purge gas and the screen temperature is calibrated to measure the incident radiant heat load. In order to measure the total radiant heat load incident on the combustor liner, the porous plug radiometer is designed to have a wide field of view (180 degrees).

Experience has shown that porous plug radiometers also require individual calibrations. Calibrations at elevated pressures were required to confirm probe operating characteristics with varying mass flows, volume flows, and pressure ratios across the porous screen.

The Medtherm radiometer probe is a commercially available unit. The convective heat load is isolated from the sensor by the use of a sapphire window. The sensor is a Gardon gauge type sensor and is calibrated by the manufacturer. A gas purge is supplied to keep the window clean during the operation of the probe. The Medtherm radiometer has a 50 degree field of view.

The Medtherm radiometers were supplied with calibrations by the vendor. A one point check was performed to confirm the validity of those calibrations.

ORIGINAL PAGE
BLACK AND WHITE PHOTOGRAPH

ORIGINAL PAGE IS
OF POOR QUALITY

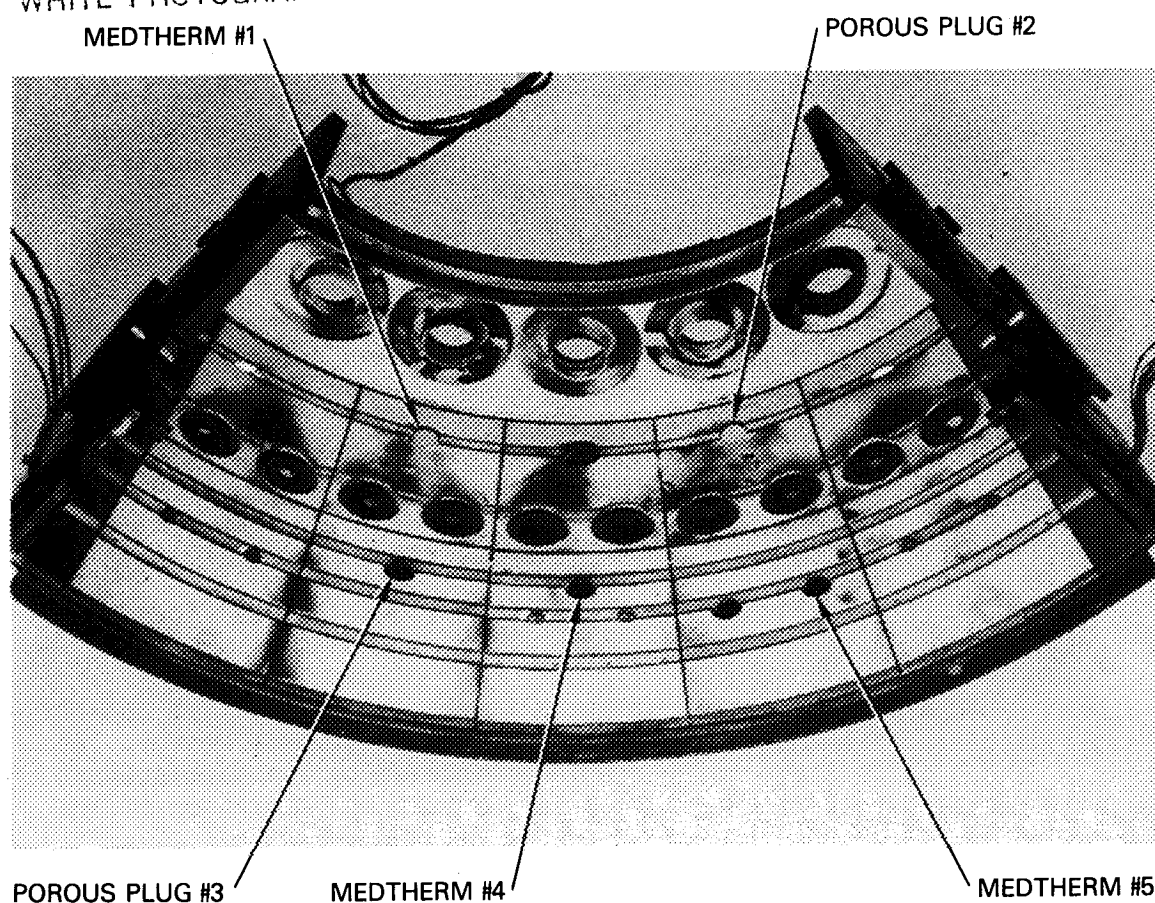


Figure 4-8 Radiometer Installation in Outer Liner

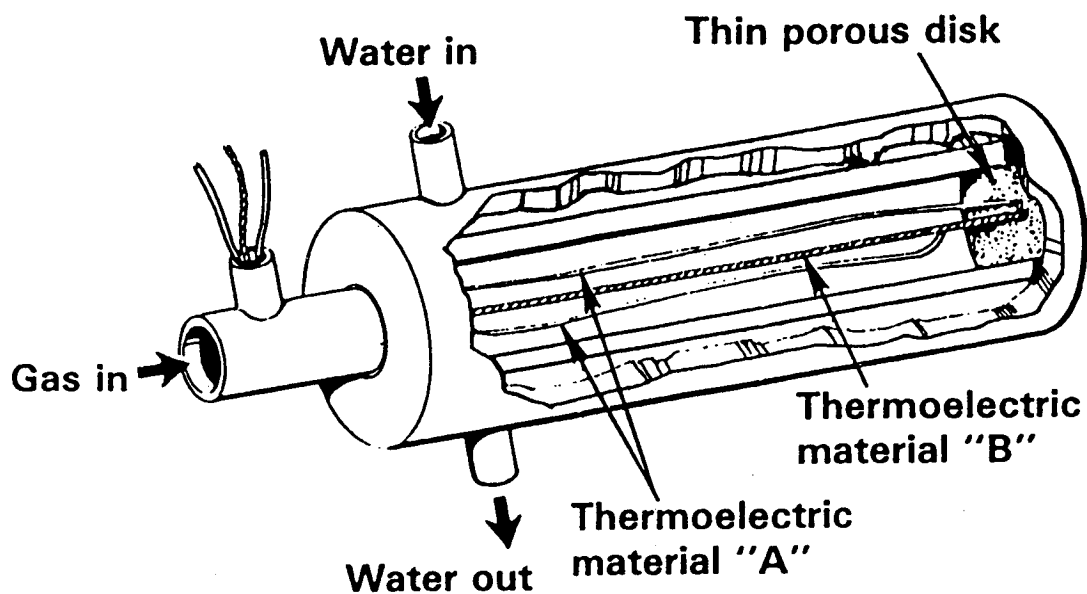


Figure 4-9 Porous Plug Radiometer Schematic

4.4 TEST PLAN

The Combustor Sector Rig Test Program was comprised of three tests with metallic inner liner segments followed by one test with ceramic composite inner liner segments as shown in Table 4-II.

TABLE 4-II
COMBUSTOR SECTOR RIG TEST PROGRAM

	<u>Type</u>	<u>Configuration</u>	<u>Purpose</u>
Test 1 (Run #23)	Liner temperature/ radiation and per- formance/emissions	Counter-parallel Finwall [®] liner with modified carburetor tubes	Thermal, emissions and performance evaluation at full sea level conditions.
Test 2 (Run #24)	Liner temperature/ radiation character- ization	Pin fin segmented liner on inner wall	Baseline evaluation of liner temperature at sea level takeoff conditions. Limited performance evaluation.
Test 3 (Run #25)	Liner temperature/ radiation character- ization	Refinements to baseline pin fin design	Liner temperature assess- ment at sea level takeoff conditions. Limited performance evaluation.
Test 4 (Run #26)	Liner temperature/ radiation character- ization	Ceramic composites on inner wall	Thermal/mechanical char- acterization of ceramic composites in combustor environment at simulated sea level takeoff conditions. Limited performance evaluation.

The baseline evaluation was conducted at the conditions outlined by the test matrix in Table 4-III. The test was comprised of 26 different test conditions, 9 of which encompassed the low-power range and 14 at simulated takeoff conditions with varying inlet pressure levels.

TABLE 4-III
TEST MATRIX FOR TEST 1 -- BASELINE THERMAL,
EMISSIONS AND PERFORMANCE EVALUATION

<u>Point</u>	<u>Condition</u>	<u>T_{T3}</u> (°F)	<u>P_{T3}</u> (psia)	<u>(F/A)</u>	<u>W_{A3}</u> (pps)	<u>Pilot/Main</u> <u>Fuel Split</u>	<u>Comments</u>
1	CFPL	300	100	-	12.3	-	Cold Flow Pressure Loss
2				-	13.1	-	
3				-	14.0	-	
4	Idle	391	63	0.0090	8.54	100/0	Fuel/Air Variation Lean Blowout
5				0.0098			
6				0.0110			
7				Min.			
8	Approach	659	167.7	0.015	18.2	100/0 85/15 70/30	Fuel Split Variation Fuel/Air Variation at Design Split
9							
10							
11				0.014			
12				0.016			
13	SLTO Reduced	1055	210	0.020	20	15/85 30/70	Fuel/Air Variation at Design Split
14				0.020			
15				0.016			
16				0.023			
17				0.025			
18	SLTO Reduced	1055	320	0.016	30		X-960 Air Supply Fuel/Air Variation at Design Split
19				0.021			
20				0.023			
21				0.025			
22	SLTO, Hot	1055	444	0.016	41.4	15/85	X-960 Air Supply Temperature Evaluation
23				0.020			
24				0.022			
25				0.024			
26				Maximum			

The combustor was configured the same as for the previous combustor sector rig test of the advanced segmented liner (Run 22), except for a slight modification to the carburetor tube design. This modification consisted of reducing the tube secondary passage area to a value which produced low levels of unburned hydrocarbons and carbon monoxide at approach conditions during earlier testing.

The next two series of tests were directed towards a thermal-mechanical characterization of the pin fin liner design. Table 4-IV shows the typical test matrix of conditions comprising Runs 24 and 25.

The combustor incorporated the pin fin liner configuration on the inner combustor wall for Runs 24 and 25. Testing concentrated on establishing liner durability characteristics, including temperature gradients and total radiant heat flux. Because of the objectives of this test, only a limited amount of performance data was acquired. This information was used to determine the effect, if any, of this liner design on aerothermal performance.

On the basis of results obtained from Run 24, certain refinements were evaluated in Test 25. The modifications incorporated were:

1. Variation of the pin geometry to evaluate cooling effectiveness of several pin designs
2. Variations in coolant air flow to assess tailoring capabilities and counter to parallel flow splits
3. Variations in dilution hole geometry as well as location to evaluate the impact on coolant distribution.

The final test of the combustor sector rig was Run 26, with the objective to assess the durability of the SIC-LAS ceramic composite combustor liner segments.

The details of the test program for Run 26 of the combustor sector rig are summarized in Table 4-V. The program was structured in two phases with the first confirming the operating conditions of the rig while allowing for acquisition of data from the radiometer probes installed through the outer liner of the combustor. The second phase involved the extended duration thermal exposure of the ceramic composite liner.

TABLE 4-IV
TEST MATRIX FOR TESTS 2 AND 3 -- PIN FIN LINER
THERMAL-MECHANICAL EVALUATION

Point	Condition	T _{T3} (°F)	P _{T3} (psia)	(F/A)	W _{A3} (pps)	Pilot/Main Fuel Split	Comments
1	CFPL	300	100	-	12.3	-	Cold Flow Pressure Loss
2				-	13.1	-	
3				-	14.0	-	
4	Idle	391	63	0.0090	8.54	100/0	Fuel/Air Variation
5				0.0098			
6	Approach	659	167.7	0.015	18.2	100/0	Fuel Split Variation Design Split
7						85/15	
8	SLTO Reduced	1055	210	0.020	20	15/85	Fuel/Air Variation at Design Split
9				0.020		30/70	
10				0.016			
11				0.023			
12				0.025			
13	SLTO Reduced	1055	320	0.016	30		Fuel/Air Variation at Design Split
14				0.021			
15				0.023			
16				0.025			
17	SLTO, Hot	1055	444	0.016	41.4	15/85	X-960 Air Supply Temperature Evaluation
18				0.020			
19				0.022			
20				0.024			
21				Maximum			

TABLE 4-V
TEST MATRIX FOR EVALUATION OF CERAMIC COMPOSITE LINER

Point	T_{T3}		P_{T3}		(F/A)	W_{A3}		Pilot/Main Fuel Split	Comments
	°C	(°F)	MPa	(psia)		Kg/s	(pps)		
1	149	(300)	0.69	(100)	-	5.60	(12.3)	-	Cold Flow
2	149	(300)	0.69	(100)	-	5.95	(13.1)	-	Pressure
3	149	(300)	0.69	(100)	-	6.37	(14.0)	-	Distribution
4	199	(391)	0.43	(63)	0.010	3.88	(8.54)	100/0	Radiant Heat Load
5	569	(1055)	1.03	(150)	0.018	5.65	(12.4)	20/80	Measurement and
6	569	(1055)	1.38	(200)	0.018	7.40	(16.3)	20/80	Comparison to
7	569	(1055)	1.73	(250)	0.018	9.36	(20.6)	20/80	Prior Experience
8	569	(1055)	1.73	(250)	0.021	9.36	(20.6)	17/83	
9	569	(1055)	1.73	(250)	0.023	9.36	(20.6)	17/83	
10	569	(1055)	1.73	(250)	0.027	9.36	(20.6)	13/87	10 hr Durability Condition
11	569	(1055)	1.03	(150)	0.018	5.65	(12.4)	20/80	Repeat Point

4.5 TEST PROCEDURES

Before the planned test sequence was initiated, a series of checks were made to verify the functional operation of facility equipment, data acquisition systems and test instrumentation. As part of this effort, the rig plumbing was pressurized and checked for leaks. Sample data were obtained at a test point to check for proper operation of both data acquisition and reduction systems. Facility interfaces, inhibiting and emergency shutdown systems were also checked for proper operation. Any discrepancies observed during these checks were corrected before the start of testing.

4.6 TYPICAL TEST RUN CHRONOLOGY

Test runs in the combustor sector rig were repetitious with very little difference in the matrix that was run. A chronology of Run 26 follows to provide a perspective of the test run.

Testing was initiated with the three unfired test points 1, 2 and 3 of Table 4-V with the objective of verifying that the pressure distribution, and hence the airflow distribution, in and around the combustor was consistent with the design intent before lighting the combustor. With this accomplished, the combustor was lit and stabilized at the conditions of point 4 of the table which corresponds to the ground idle operating condition of the Energy Efficient Engine. Thereafter, the combustor inlet temperature was increased to 569°C (1055°F) corresponding to the sea level takeoff operating condition of the Energy Efficient Engine, and the inlet total pressure and the overall fuel air ratio progressively increased through points 5 through 9 of the table.

The combustor rig had been run at these operating conditions during Runs 24 and 25, and limited measurements of the combustor exit and outer liner temperature were available to confirm that the combustor was operating correctly at these conditions. Measurements were also obtained of the radiant heat flux to the outer liner of the combustor at each of test points 4 through 9 with the Medtherm and porous plug radiometers. The results of these measurements are discussed in Section 5.2. Following completion of these test points, the test facility was shut down because it was too late in the day to start the intended ten hour durability test of point 10. To assure that conditions had not shifted, test point 5 of Table 4-V was repeated during the shutdown and startup the next morning. Operation at the ten hour durability test condition was achieved with the inlet temperature, fuel air ratio and stage fuel split being brought to the stipulated conditions slowly from below to avoid overshooting and invalidating the thermal paint data. The rig operating conditions at test point 10 of the table are the inlet total temperature, inlet Mach number and fuel air ratio of the Energy Efficient Engine at sea level takeoff, but the inlet total pressure of 1.73 MPa (250 psia) is about 56 percent of the design pressure level at that operating condition. This was the maximum achievable inlet total pressure within the capacity of the air supply system for X-903 stand while maintaining combustor inlet Mach number similarity.

The combustor exit temperature probes, the outer liner thermocouples and the radiometers were monitored during the duration of the durability test to assure there were no shifts in combustor operation. Likewise, liner pressure drops were monitored to detect any burnthrough of the liner. However, the ten hour endurance test proceeded without incident and the rig was subsequently shut down. During the shutdown, data were recorded again from all instrumentation at point 11 of Table 4-V, which was a repeat of the intermediate temperature point 5 that had been run previously to provide confirmation of repeatability with the pre-endurance measurements. The overall test program required a total of 25.3 hours of air time in the test facility of which the combustor was fired for 18.2 hours and operated at the simulated takeoff durability condition for 10.0 hours.

ORIGINAL PAGE IS
OF POOR QUALITY

After removing the rig from the test stand, it was disassembled for post-test examination and inspection. Initial examination indicated no substantial large-scale damage or distress to the composite liner panels. Figure 4-10 shows the inner liner assembly prior to the panels being removed from the metal shell. (The light colored regions on the panels on the left side of the liner are thermal paint.) In Section 5.3.2, the results of detailed inspections of the panels are discussed.

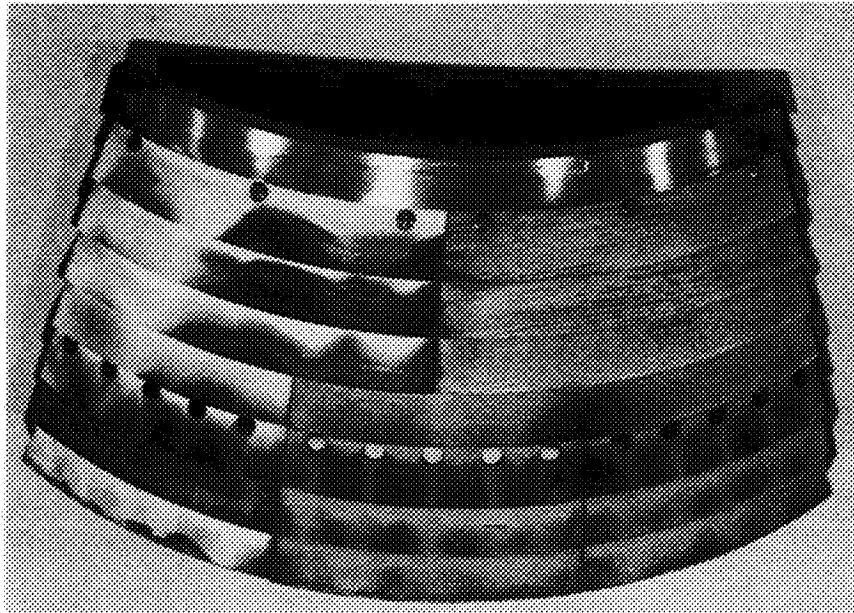


Figure 4-10 Hot Side of Ceramic Combustor Inner Liner After Completion of Run 26 Durability Test

ORIGINAL PAGE
BLACK AND WHITE PHOTOGRAPH

SECTION 5.0 COMBUSTOR SECTOR RIG TEST RESULTS AND ANALYSIS

5.1 INTEGRATION WITH COMPONENT PROGRAM

5.1.1 Background

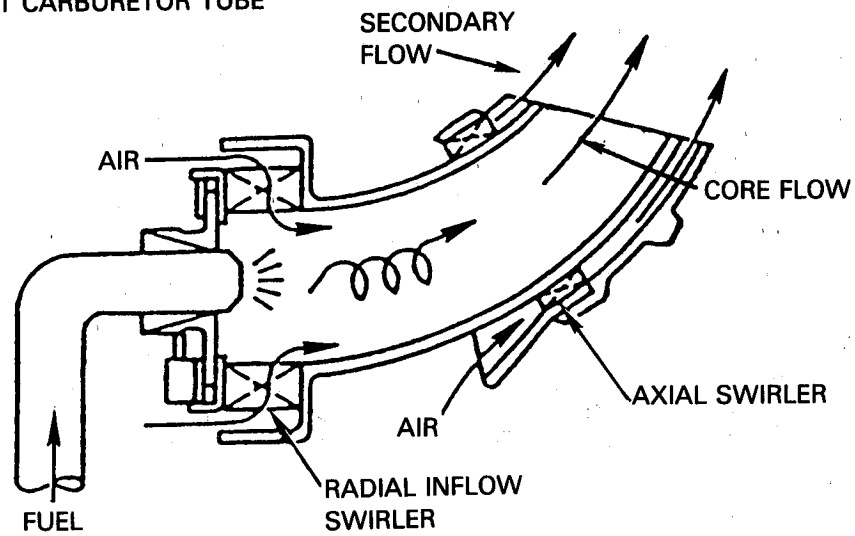
Subsequent to testing of the full annular combustor component (Reference 12), it was observed that the modifications made to the main zone fuel injectors (i.e., carburetor tubes) were detrimental to combustor emissions characteristics at intermediate engine power levels. These modifications were made in order to improve castability and to facilitate installation of the carburetor tubes. This anomaly was later confirmed with tests in the sector rig using cast carburetor tubes from the component rig.

A comparison of the original carburetor tube developed in the sector rig program with the cast version is shown schematically in Figure 5-1. Design changes made, the reason for the change and the perceived risks are summarized below.

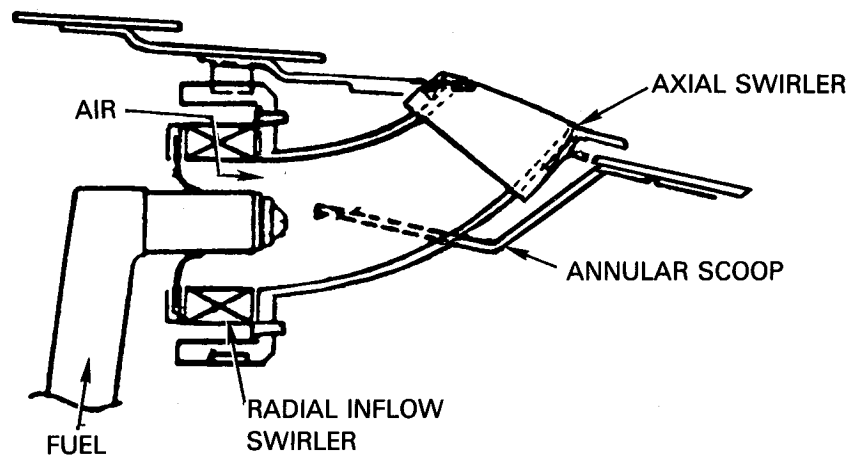
<u>Cast Tube</u>	<u>Reason</u>	<u>Risk</u>
o Increased secondary flow	Reduce NOx emissions	Fuel lean injector
o Remove annular scoop	Ease of installation	Non-uniform air feed pressure to axial swirler
o Increased wall thickness	Casting requirement	Deterioration in fuel droplet atomization
o Recessed axial swirler	Casting and installation requirement	Reduced swirl

Significant increases in unburned hydrocarbons and carbon monoxide levels measured at combustor inlet conditions corresponding to engine approach conditions (30 percent of full takeoff power) tended to confirm the first and third risk items. To gain better insight to the problem, both types of main zone fuel injector assemblies were tested for air and fuel flow characteristics. Effective flow areas for both configurations were at the design levels and are summarized along with swirl strength measurements in Table 5-I.

CAST CARBURETOR TUBE



BASELINE SECTOR RIG CARBURETOR TUBE



NOTE: SCHEMATICS NOT TO SAME SCALE

Figure 5-1 Comparison of Cast Component and Sheet Metal Sector Rig Carburetor Tubes

TABLE 5-I
CARBURETOR TUBE AIR FLOW TEST SUMMARY

	ACd - cm ² (in ²)		Swirl Strength* - cm (in)
	Core	Secondary	
Sheet Metal	1.74 (0.27)	0.645 (0.10)	1.8-2.0 (0.7-0.8)
Cast	1.68 (0.26)	0.839 (0.13)	1.8-2.0 (0.7-0.8)

* Swirl strength - (measured torque)/(measured thrust) at exit plane

Fuel distributions along the minor axis of the ellipse formed at the exit of the two carburetor tubes are presented in Figure 5-2. The fuel film accumulation was distinctly asymmetric with the cast configuration. As expected, non-uniform filming of the fuel was also reflected in larger measured droplet sizes and broader droplet distributions (i.e., not monodispersed).

In order to improve the emissions performance of the combustor, the main zone carburetor tubes were modified with new secondary air sleeve castings to decrease secondary air quantity while increasing velocity and swirl at the exit. In addition to shakedown testing of the radiometers and thin film thermocouples, Run 23 of the sector rig program was devoted to assessing the effect of carburetor tube modifications to overall combustor performance.

5.1.2 Combustor Performance Assessment

Testing was conducted consistent with the established procedures as in previous sector rig tests. Cold flow pressure loss measurements were made to ensure the proper pressure distributions. The resulting air flow distribution is compared to that of Run 22 in Figure 5-3. Pressure loss levels and airflow distributions were consistent between the two test sequences. Separate air flow testing of the modified carburetor tube secondary passage had already demonstrated the desired reduction in effective flow area (ACd) from 84 mm² (0.13 in²) to 52 mm² (0.08 in²). Fuel patternation showed some improvement, but did not achieve sheet metal tube levels of uniformity.

Combustor performance observed in Run 23 was compared to two previous configurations, each with different carburetor tube geometry. These tube features are reviewed below:

- Run 21 - Final sheet metal carburetor tubes geometry evolving from initial Combustor Sector Test Program
- Run 22 - Adaptation of the full annular component carburetor tubes made by investment casting
- Run 23 - Modification made to the outer sleeve casting to alleviate problems from Annular Rig Program and Run 22.

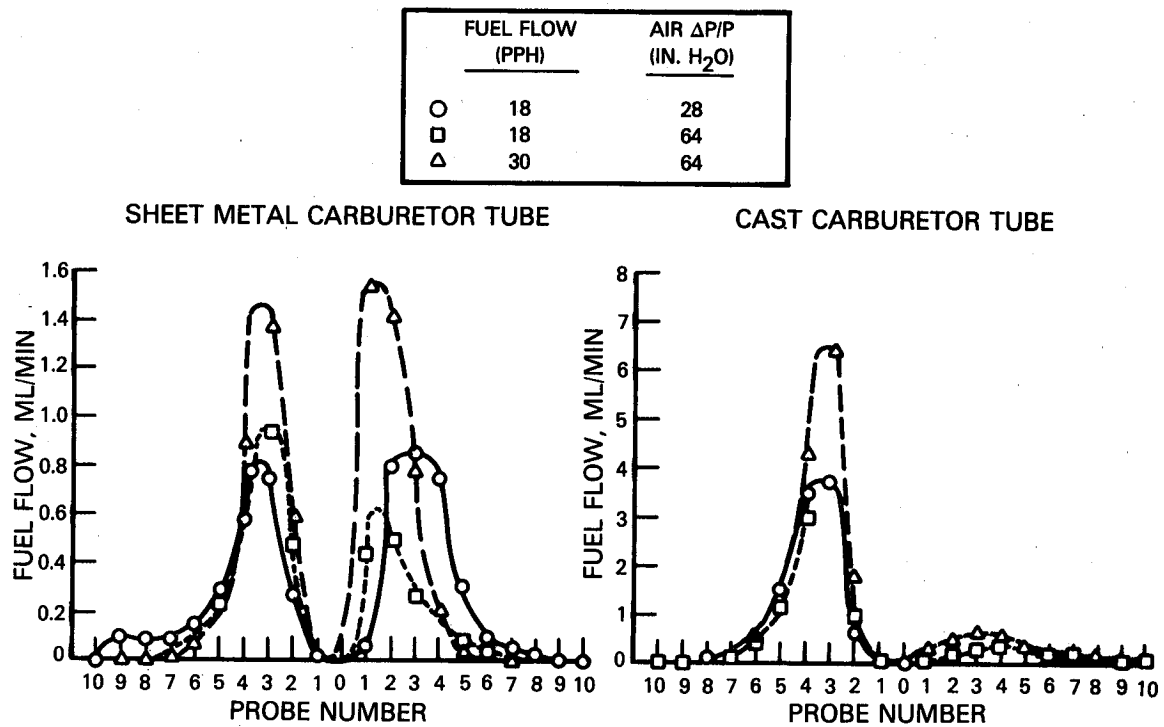


Figure 5-2 Comparison of Carburetor Tube Fuel Spray Characterization

TOP NUMBERS SHOWN REPRESENT SECTOR RIG (BUILD 22) VALUES
 BOTTOM NUMBERS SHOWN REPRESENT SECTOR RIG (BUILD 23) VALUES

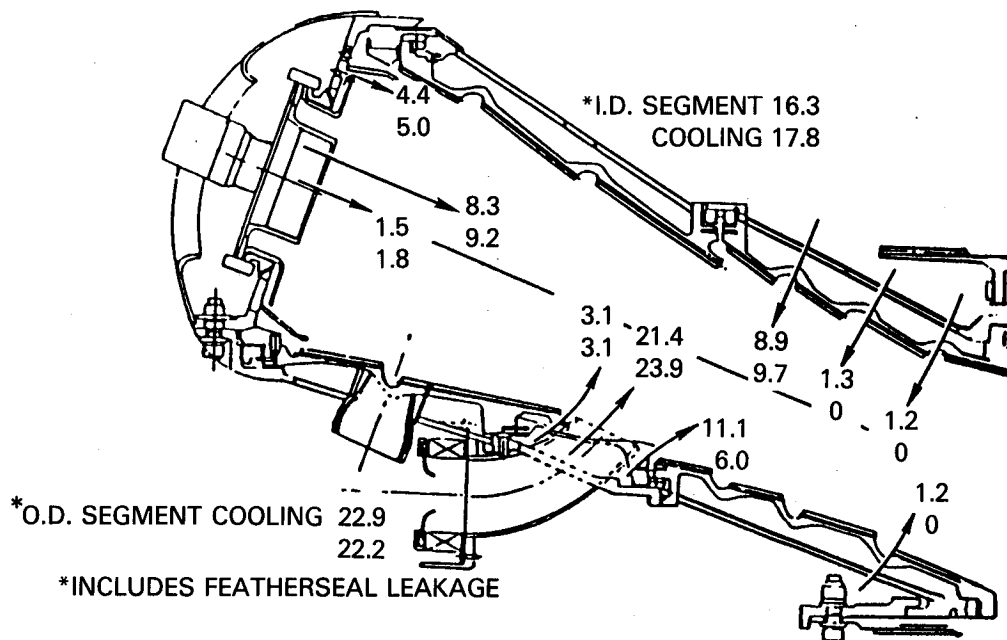


Figure 5-3 Combustor Airflow Distribution

Total unburned hydrocarbon (THC) and carbon monoxide (CO) emission characteristics as a function of combustor fuel/air ratio are presented in Figure 5-4. At this operating condition, there is no fuel flowing in the carburetor tubes; thus performance is determined by the aerodynamics of the pilot zone and its fuel injector. Accordingly, small variations would be expected depending on the run-to-run changes in combustor bulkhead pressure drop. Such is the case for CO emission indexes for Runs 21 and 23, but an unusual slope is observed in Run 22 data. Similarly, Run 21 and 23 THC emission indexes are consistent. Although post test inspection uncovered no reason to doubt the instrumentation, THC data for Run 22 still remain an enigma. These levels were the lowest measured at the design idle point.

The primary objective of the test series was to reduce approach condition emissions by modifying the carburetor tube design. Examination of Figure 5-5 shows that this goal was achieved. Parametric variations in pilot-to-main zone fuel flow split were conducted to find the optimum between CO/THC and NOx emissions. At the identical pilot fuel/air ratio of 0.0126, reductions relative to the Run 22 configuration in THC and CO emissions of 25 and 48 percent respectively were achieved. Increasing the pilot/main zone fuel split from 85/15 to 90/10 resulted in 79 percent reduction in THC and 73 percent reduction in CO emissions. These were achieved with only a 5 percent increase in NOx emissions at the approach condition. With the higher pilot flow, results were comparable to the Run 21 configuration. This clearly demonstrated that with some further modification to the cast carburetor tubes, previous low levels of THC and CO emissions can be achieved.

High power NOx emission characteristics are presented in Figure 5-6. Approximately 13 percent increase in NOx at climb operating conditions are observed relative to Run 21. Lack of sensitivity to the pilot-to-main zone fuel flow variations confirms the deterioration in atomization characteristics of the carburetor tube. In other words, the average droplet size is large and the number distribution is wide. What is gained in terms of decreased NOx production in the pilot zone by decreasing pilot fuel flow is offset by the increased droplet sizes produced by increased fuel flow in the main zone. Again, further modifications to the carburetor tube sleeve should rectify the problem.

Main zone injector performance strongly impacts exit temperature characteristics. Comparison of exit temperature variation (Figure 5-7) with pre-Run 22 data shows larger spatial fluctuations with the current configuration. This is attributed to fuel-rich pockets resulting from inhomogeneous carburetor tube fuel filming. The pattern factor for Run 23 was 0.40. Due to this high level, maximum combustor fuel/air ratio was limited to 0.021 at the elevated pressure and temperature points.

The average radial profile is shown in Figure 5-8. It is center peaked, similar to Run 22, but cooler at the innermost span location. Judicious use of dilution air in both inner and outer liners would reduce the peak. To get back to the Run 21 levels, however, dilution air and carburetor tube modifications have to be worked in consort.

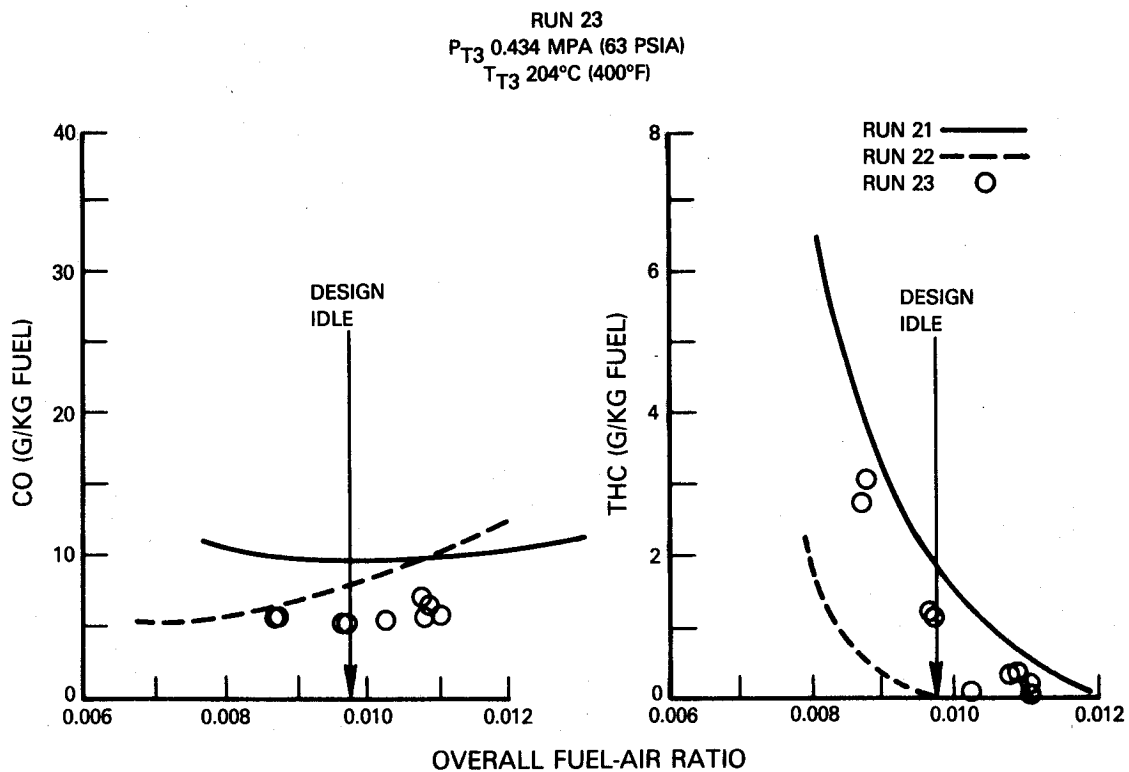


Figure 5-4 Idle Emissions

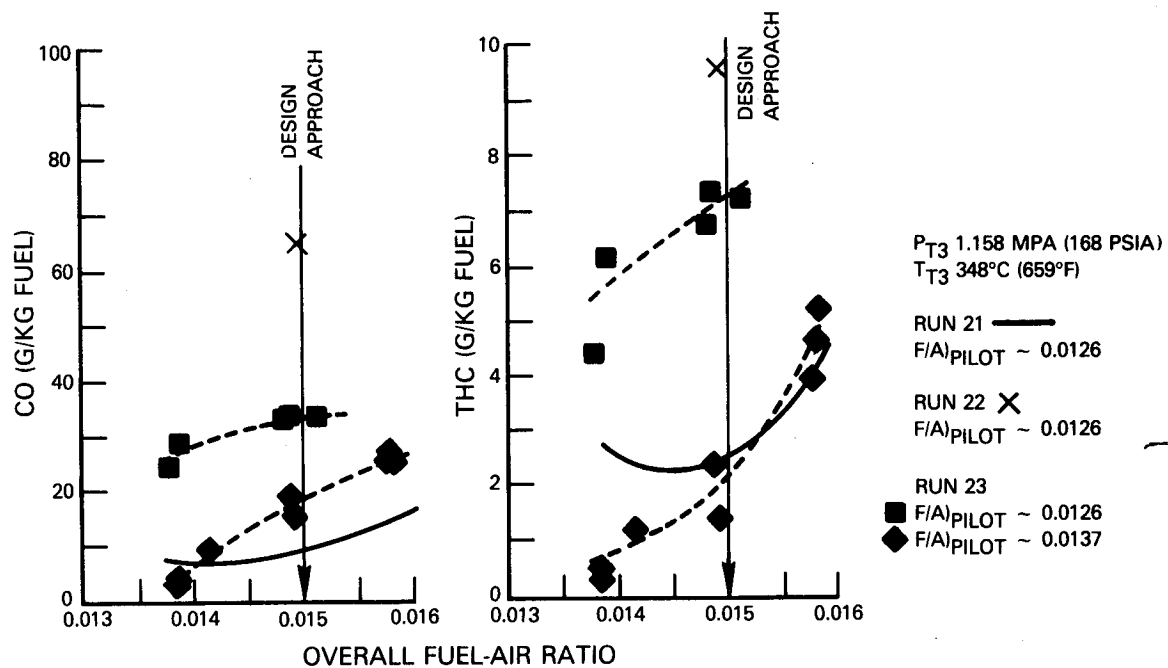


Figure 5-5 Approach Emissions - Run 23

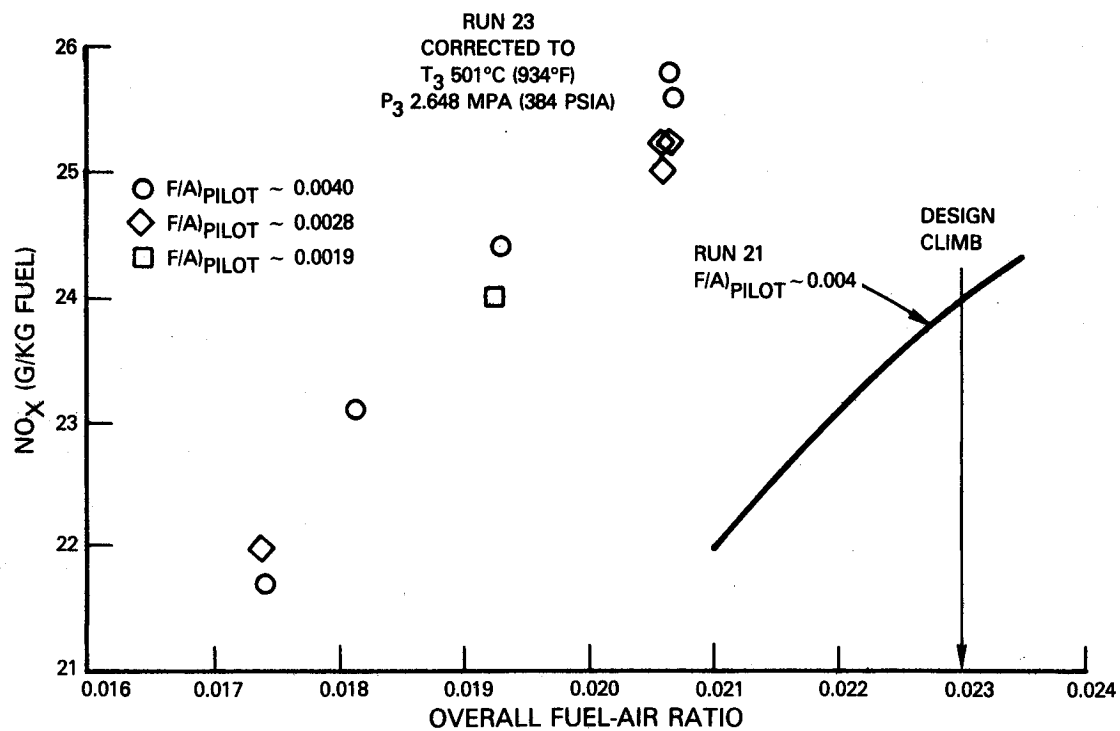


Figure 5-6 Climb Emissions - Run 23

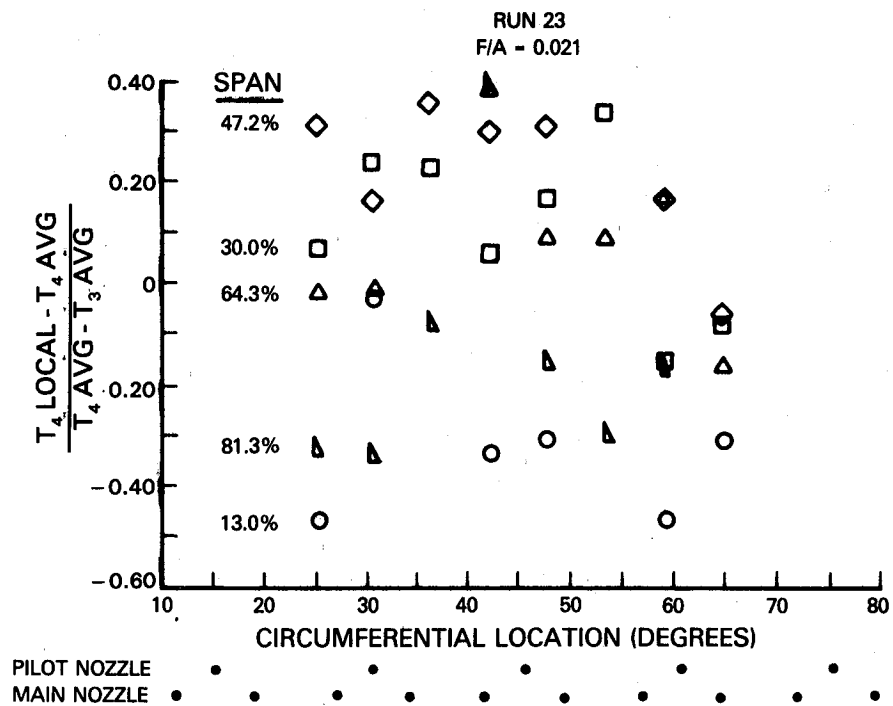


Figure 5-7 Exit Temperature Distribution - Run 23

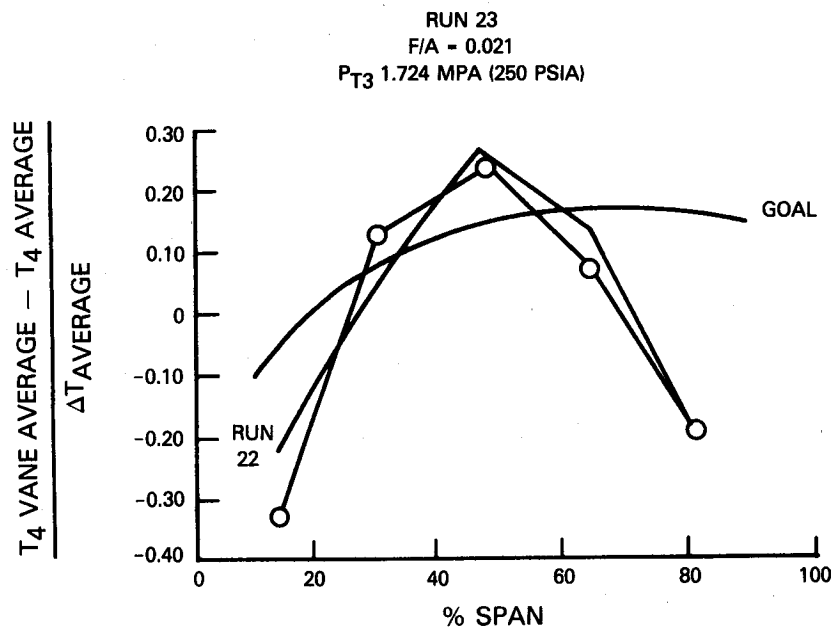


Figure 5-8 Radial Profile - Run 23

5.1.3 Wall Temperature and Radiometer Measurements

Two porous plug and two Medtherm radiometers with one of each type in the pilot and main combustion zones were installed on the outer liner for Run 23. During early portions of the test program, all four radiometers appeared to be operating properly. The measured radiation levels were lower than anticipated, but the trends in the data were as expected in that the measured radiant load increased with increasing pressure or fuel/air ratio. Approximately halfway through the test program, prior to high power points, both Medtherm radiometers and one porous plug radiometer failed.

Post test inspection of the Medtherm radiometers showed that the cause of the failure was the momentary loss of purge gas flow used to cool and clean the windows during the test. To preclude this problem from occurring in the subsequent tests, an independent supply of nitrogen was installed. Additional instrumentation was provided to closely monitor purge gas pressures at all times.

The porous plug radiometer failure was due to loss of a thermocouple junction internal to the probe. The history of several other porous plug radiometers produced at the same time period or subsequent to the failed probe showed no similar failures. The failure, therefore, did not appear to be related to the construction technique and no corrective action was identified.

Liner temperature readings were also lower than anticipated. Imbedded thermocouples were located in the cooler regions of the outer liner and thus were consistent with past runs. Although the durability of the thin film sensors was good, i.e., most were intact after the test, results were clouded by post-test calibration difficulties arising from oxidation of the rhodium in the jumper wires in the PT-10%Rh leg. Connection from the sputtered film to the sheathed wire on the back side of the panel was made by means of an 80 micron (3 mil) bare wire. This wire was located in the "joggle" region of the panels prior to passing through the walls. The joggle region is bathed in spent cooling air leaving the liner convective passages. Temperature of the coolant was predicted to be in the range 600°C (1100°F) to 700°C (1300°F) at the high power points. It was known that oxidation of rhodium reaches a peak in this range causing an error in the thermocouple system employing Pt-Rh alloy in one leg. The process is slow at one atmosphere pressure and is usually handled via post-test calibration of the wire. However, it was uncovered that the oxidation rate increases as the square or cube of pressure. Due to the excessive level of oxidation, reliable correction of the data after the test was unsuccessful.

The sputtered thermocouple installation technique for the pin-fin tests was revised in the following manner in order to minimize the oxidation potential of the Pt-Rh leg:

1. Eliminated or minimized exposure of the rhodium leg to temperatures in the 600°C (1100°F) to 700°C (1300°F) range
2. Replaced 80 micron (3 mil) jumper wire with 130 micron (5 mil) jumper wire. To reduce surface disturbances, the 5 mil wire was flattened to 3 mil thickness at the junction with the film sensor
3. Installation of jumper wire was also changed to bring the metal sheathed extension wire through the segment wall to the measuring surface
4. Number of Chromel/Alumel surface and imbedded thermocouples were increased.

The above precautions and/or revised operational procedures proved to be successful in the subsequent pin-fin liner tests.

Multi-range thermally sensitive paint used in Run 23 showed the inner liner temperatures to be somewhat lower than previous tests. The maximum inner liner wall temperature was estimated to be 900°C (1650°F). This observation is attributed to the reduced penetration of the carburetor tube jets, which is consistent with the center peaked exit temperature profile. Outer liner metal temperatures were consistent with previous tests with a maximum of approximately 1000°C (1850°F).

5.1.4 Summary of Run 23 Results

Objective of this test was to demonstrate main zone fuel injector modifications that would substantially reduce approach emissions to a level at or below program goals. Secondary objectives were to evaluate use of thin film thermocouple sensors for measuring wall temperatures and obtain radiation heat flux data in a combusting environment.

Combustor performance parameters for Run 23 are compared to Runs 21 and 22 along with program goals in Table 5-II. It can be observed that reductions in approach emissions were successful and that the HC EPAP meets program goals. NOx goals were exceeded with all configurations. Exit temperature pattern factor crept above goal with the peaked profile produced with the cast carburetor tube design. Conventional methods of dilution zone treatment would bring the pattern factor to goal levels.

In addition, through this test, sequence, operational procedures for radiometers and installation techniques for sputtered thermocouples were identified to ensure successful application of both of these elements in the remaining tests.

TABLE 5-II
SUMMARY OF RUN 23 RESULTS

	<u>Goal</u>	<u>Run 21</u>	<u>Run 22</u>	<u>Run 23</u>
Section Press. Loss (% Pt3)	5.5	5.4	N/A	5.5
Max. Pattern Factor	0.37	0.30	0.36	0.40
Emission EPAP's (1)				
CO	2.4	2.4	7.4	2.4
THC	0.40	0.47	0.80	0.35
NOx	3.0	5.7	5.3 (2)	6.1
Smoke No.	< 20	< 5	< 2	< 2

(1) Includes margins for development and variability

(2) Estimated

5.2 PIN-FIN LINER TEST RESULTS

This part of the combustor sector rig program demonstrated a successful test sequence covering severe liner operating conditions indicative of advanced gas turbine engine cycles. Thermal efficiency benefits of the 2nd generation segmented liner with pin-fin panels over the CPFW liner was demonstrated. Improved liner performance was obtained with a configuration that was lighter and less expensive than the baseline design.

Extensive radiation heat flux measurements were made in the pilot and main zones of the combustor. Data from the pilot zone is representative of radiation loads from the primary zone of conventional combustors, while main zone is more representative of future fuel lean swirl combustors. These measurements augment a very sparse data base in the field of gas turbine combustion.

Two tests (Runs 24 and 25) with liner modification in between tests were conducted over a total rig hot time of 34 hours. The results are discussed in the following sections. In addition, test data summaries for radiation and wall temperature measurements are included in Appendix C.

5.2.1 Airflow Distributions

The pin-fin liner was designed for the same total cooling and dilution air as the baseline CPFW inner liner. In addition to the shell coolant inlet holes and dilution holes, air can enter the liner as leakage through the mount post holes and through the annulus formed by the shell hole and the panel dilution hole tubes. In order to ensure consistent flow distributions detailed airflow calibrations were conducted in an atmospheric rig prior to high pressure combustion tests. Shell cooling hole pattern and diameters were revised as necessary to meet design goals. The resulting flow distribution and the liner pressure drops measured in high pressure testing is shown in Figure 5-9. This airflow distribution was used in the post test analysis to calculate combustor axial gas temperature distribution required as boundary conditions for wall temperature and radiation flux predictions.

5.2.2 Comparison of CPFW and Pin-Fin Liners

Testing was conducted according to the test matrix discussed in Section 4. The test matrix featured excursions in combustor inlet temperature, inlet pressure and, overall fuel air ratio with parametric variations in pilot to main zone fuel flow splits. Figure 5-10 shows the combustor exit temperature behavior as measured by three platinum/platinum-iridium thermocouples. Comparison with ideal temperature variation shows a well behaved combustor as a function of inlet pressure and pilot and main zone fuel flows.

Peak thermal load conditions for Runs 23 and 24, which provide the basis for comparison of the pin-fin and CPFW liners, are presented for comparison in Table 5-III. Removal of the instrumented exit vane pack allowed, as planned, higher operating conditions in Run 24.

TABLE 5-III
PEAK THERMAL LOAD CONDITIONS

	<u>Run 23</u>	<u>Run 24</u>
Combustor Inlet Temperature	533°C (990°F)	566°C (1050°F)
Combustor Inlet Pressure	2.76 MPa (400 psia)	2.76 MPa(400 psia)
Combustor Exit Temperature	1205°C (2200°F)	1466°C (2670°F)

For a consistent comparison of maximum temperatures of the two liners, the differences in the inlet and exit temperatures had to be accounted for. Since there was more liner temperature information available in Run 24, the results of the pin-fin liner test were scaled down to match those of the CPFW test.

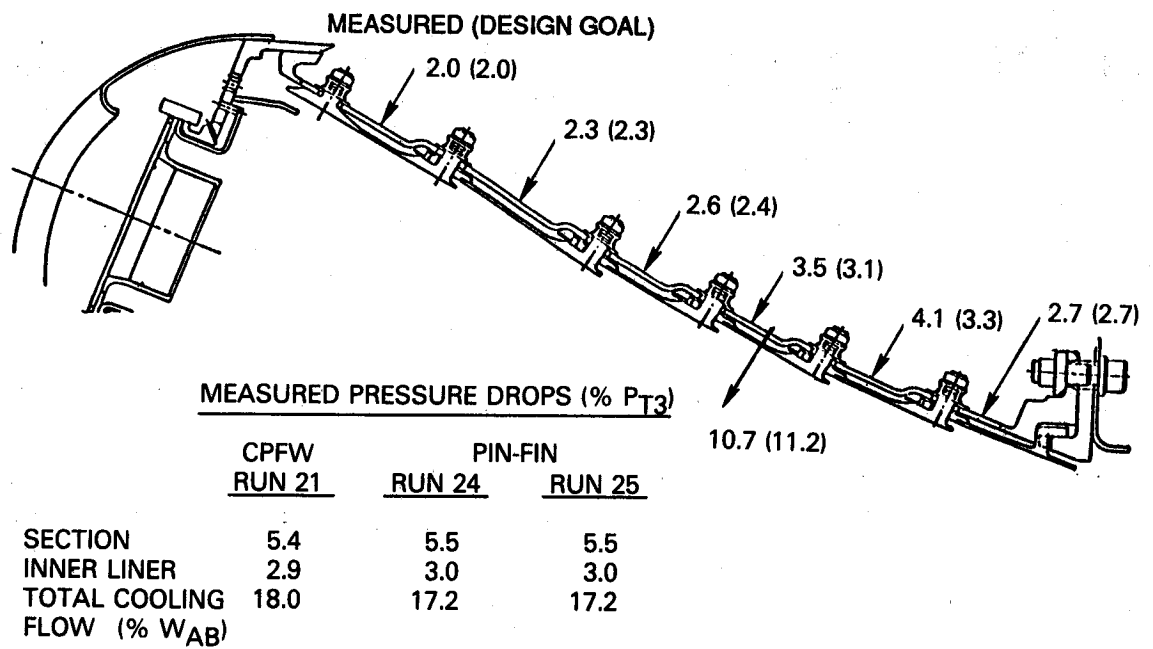


Figure 5-9 Pin-Fin Liner Airflow Distribution

Variation in wall temperature with changes in coolant temperatures was observed to be one for one. Inspection of the slope of thermocouple data with gas temperature variations in the main zone indicated on the average that there was approximately 14°C (25°F) wall temperature increase for 56°C (100°F) increase in combustion gas temperature. Use of these factors results in a correction of -100°C (-180°F) to the pin-fin data. Although, this correction is more appropriate for the main zone temperature, it was also applied to the pilot zone as well. Based on Run 23 results it was observed that the CPFW inner liner, both in the pilot and main zones, operated at 900°C (1650°F) at the peak thermal load point. None of the liner wall thermocouples in Run 24 exceeded 900°C (1650°F). This was confirmed by thermally sensitive paint readings in the main zone. The second panel in the pilot zone showed paint settings corresponding to 1040°C (1900°F) in vicinity of the mount posts. This was attributed to cooling flow blockage resulting from poor casting details. It should be noted that the pilot and main zone segments were cast by different vendors. Post test photo of the inner liner showing thermal sensitive paint settings and sputtered thermocouples is shown in Figure 5-11.

Results of maximum wall temperature comparison based on equivalent combustor operating conditions is shown in Table 5-IV where the 100°C (180°F) advantage of the pin-fin liner may be observed. The design predictions (see Section 3.2.2.1) had indicated comparable temperatures in the pilot zone but had projected a benefit of 50°C-100°C (90°F-180°F) for the pin-fin configuration. Temperature levels in Table 5-IV confirm original design predictions and also indicate the pin-fin liner thermal advantage to be in the higher end of the predicted range.

TABLE 5-IV
COMPARISON OF CPFW AND PIN-FIN LINER
MAXIMUM WALL TEMPERATURES

	<u>CPFW</u>	<u>Pin-Fin</u>
Pilot Zone	900°C (1650°F)	880°C (1620°F) 940°C (1720°F)*
Main Zone	900°C (1650°F)	800°C (1470°F)

*Locations of cooling flow blockage

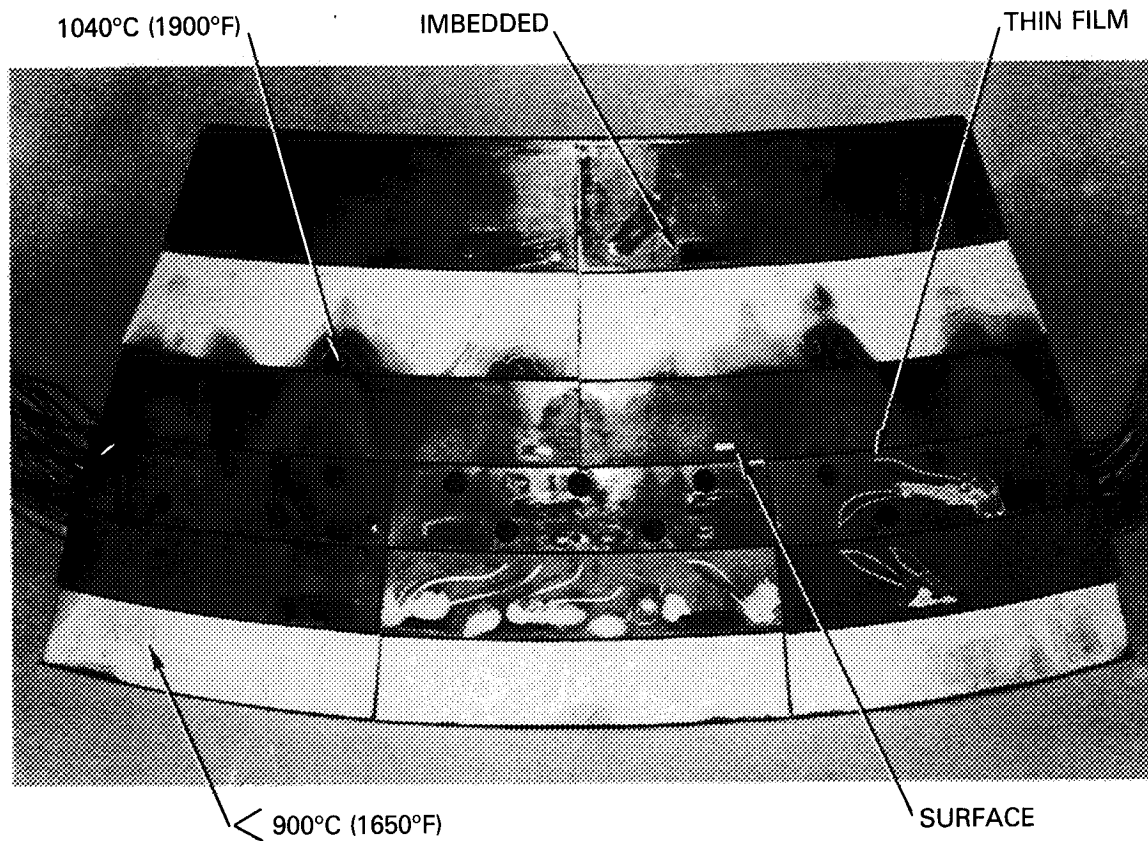


Figure 5-11 Pin-Fin Inner Liner After Run 24. Peak Condition: $T_{T3} = 566^{\circ}\text{C}$ (1050°F); $P_{T3} = 2.8 \text{ MPa}$ (400 psia); $T_{T4} = 1466^{\circ}\text{C}$ (2670°F)

5.2.3 Pilot and Main Zone Wall Temperatures

General survivability of the various types of thermocouples was considered good and is summarized in Table 5-V. Full survival indicates that the thermocouples were functional after the rig was removed from the test cell, While 80 percent is the percentage of the total test hot hours.

TABLE 5-V
SURVIVAL RATE OF THERMOCOUPLE TYPES

Type of T/C	Total Installed		80% Survival		100% Survival	
	Run 24	Run 25	Run 24	Run 25	Run 24	Run 25
Thin Film	9	13	8	7	1	5
Imbedded	12	18	12	8	12	8
Surface	7	9	6	0*	6	0*

*All destroyed before rig installation in test cell

When all three types of thermocouples were installed at similar axial/circumferential locations within a family of panels, the thin film generally tended to indicate higher levels. This is illustrated in Figure 5-12(a) and 5-12(b) where temperature readings at the trailing edge of the fourth panel in Run 24 are shown.

The effect of combustor inlet temperature on liner temperature is illustrated in Figure 5-13. The difference in going from 510°C (900°F) to 565°C (1050°F) can be observed on the panel. Regression analysis of this data indeed verified a 0.996 influence factor.

Variation of wall temperature with combustor fuel-air for four levels of combustor inlet pressure are presented in Figure 5-14. This data tracks a thermocouple on the trailing edge of the fifth panel during Run 25. Of interest to note is several instances where the wall temperature is higher at 2.4 MPa (350 psia) than 2.8 MPa (400 psia). This observation was also made in Run 24 but is not evident on all thermocouple locations.

5.2.4 Pilot and Main Zone Radiometers

Radiometer measurements in the pilot zone with porous plug and Medtherm radiometers are presented in Figure 5-15 for 1.0 MPa (150 psia) and in Figure 5-16 for 2.8 MPa (400 psia) combustor inlet pressures. Available data from Runs 24 and 25 as well as 26 (composite ceramic liner tests) are included. Levels are consistent between the two types of radiometers but the Medtherm indicates levels 20-25% higher than the porous plug. This variation is attributed to circumferential non-uniformities in the pilot zone temperatures. For the range of conditions tested, this corresponds to calculated gas temperature differences of 80 - 110°C (140 - 200°F) between fuel injector location 2 and 4. Referring to Figure 5-7 for exit temperature data near the outer wall where the radiometers are installed, the variation is quite possible. Due to fuel injector fuel pressure limitations, the pilot zone never gets as fuel rich as conventional single stage combustors operate. Extrapolating the 2.8 MPa (400 psia) data linearly to a pilot fuel-air of 0.025 yields a radiation flux value of 2.3×10^{-5} Btu/hr-sq ft-F. In reality, the level should be higher due to increased rate of soot formation in the fuel rich zones.

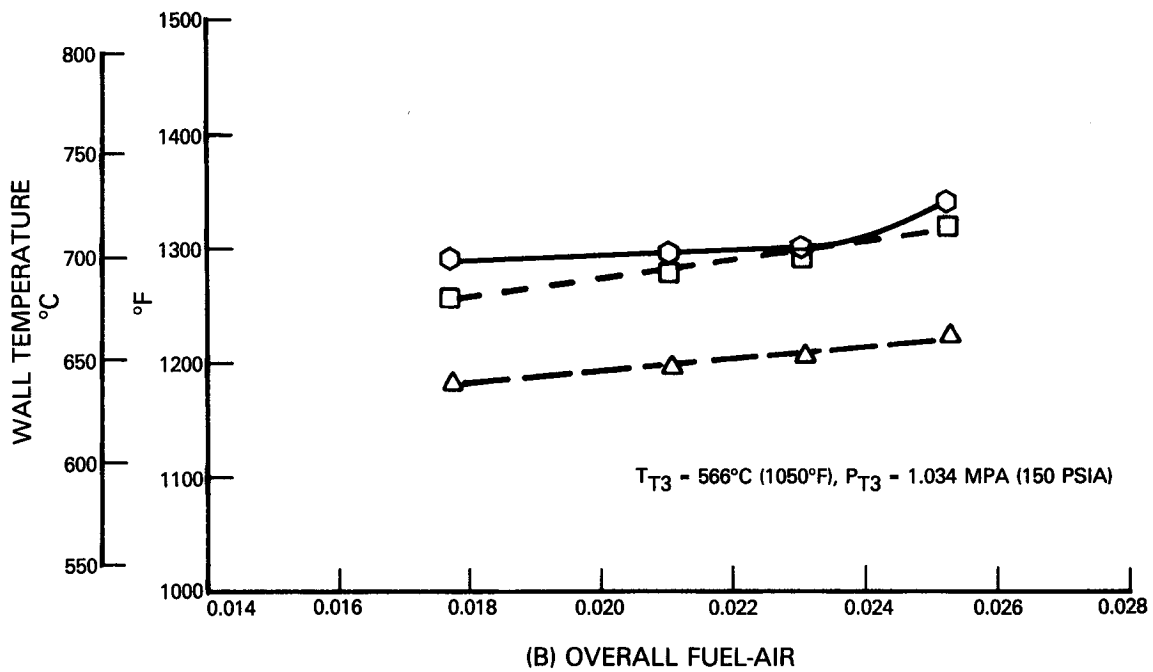
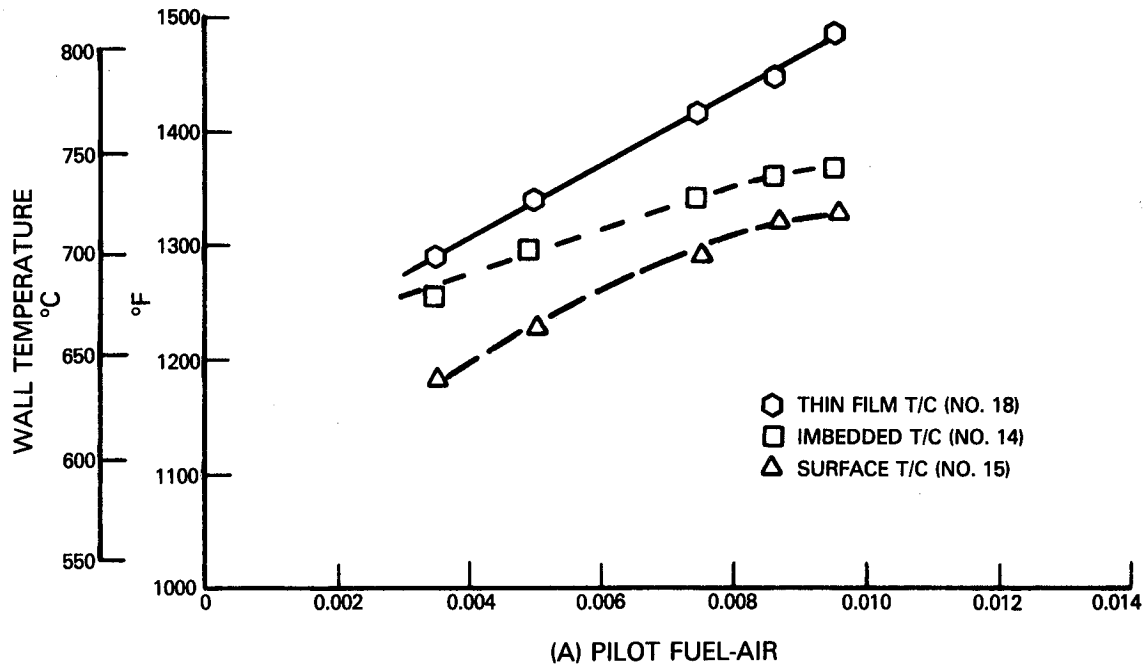


Figure 5-12 Comparison of Thermocouple Types Installed In Similar Locations

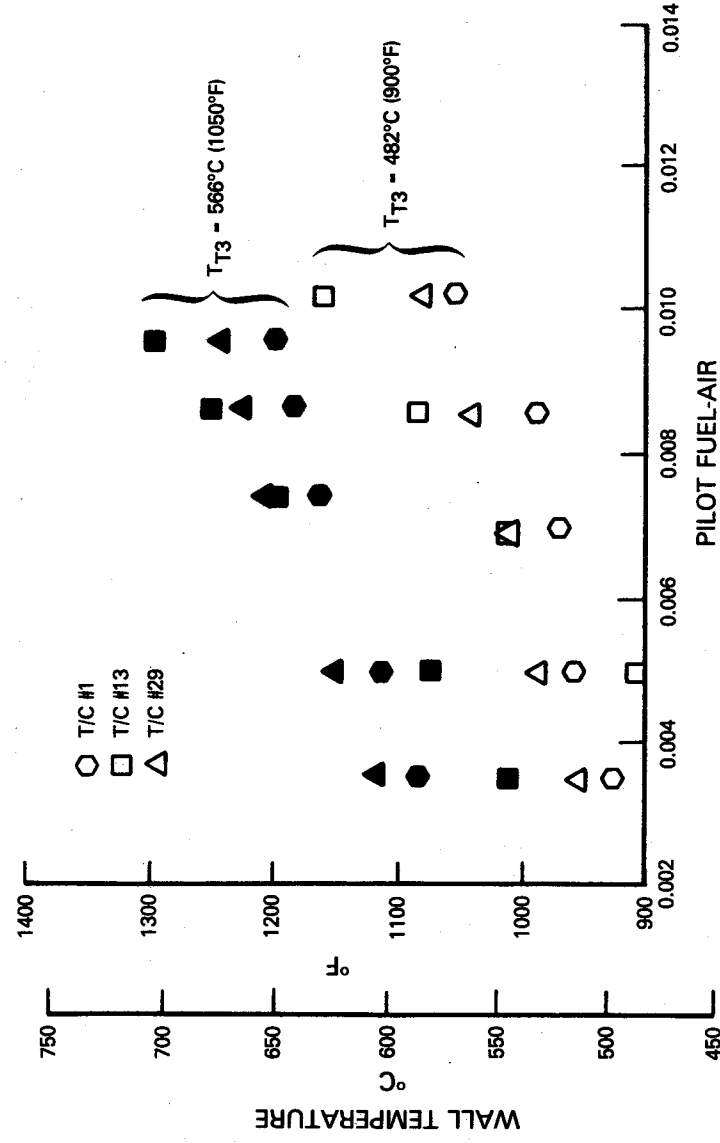


Figure 5-13 Effect of Combustor Inlet Temperature on Pin-Fin Liner Wall Temperature

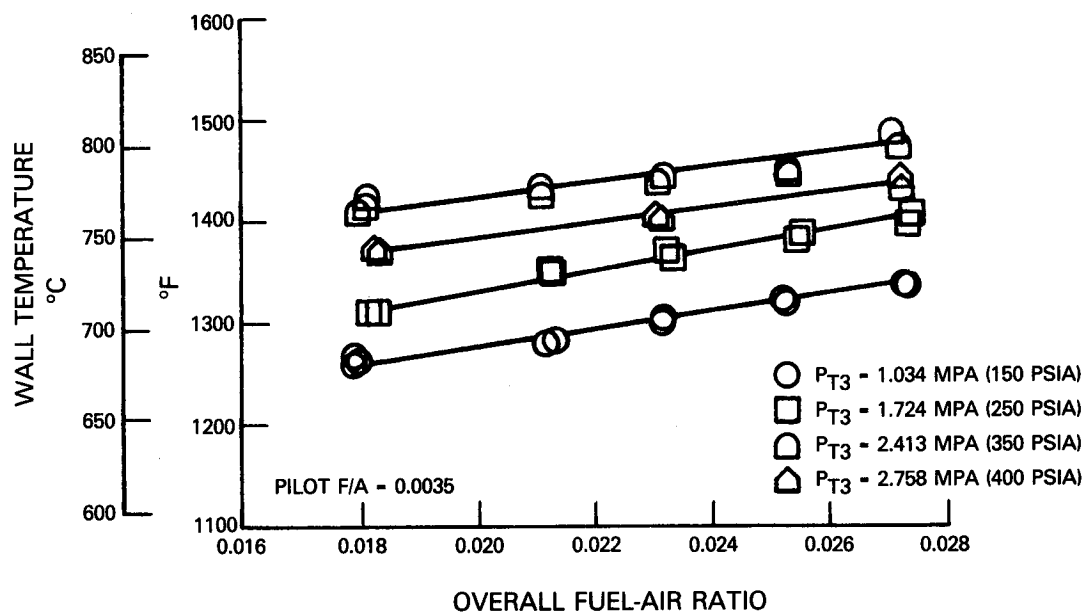
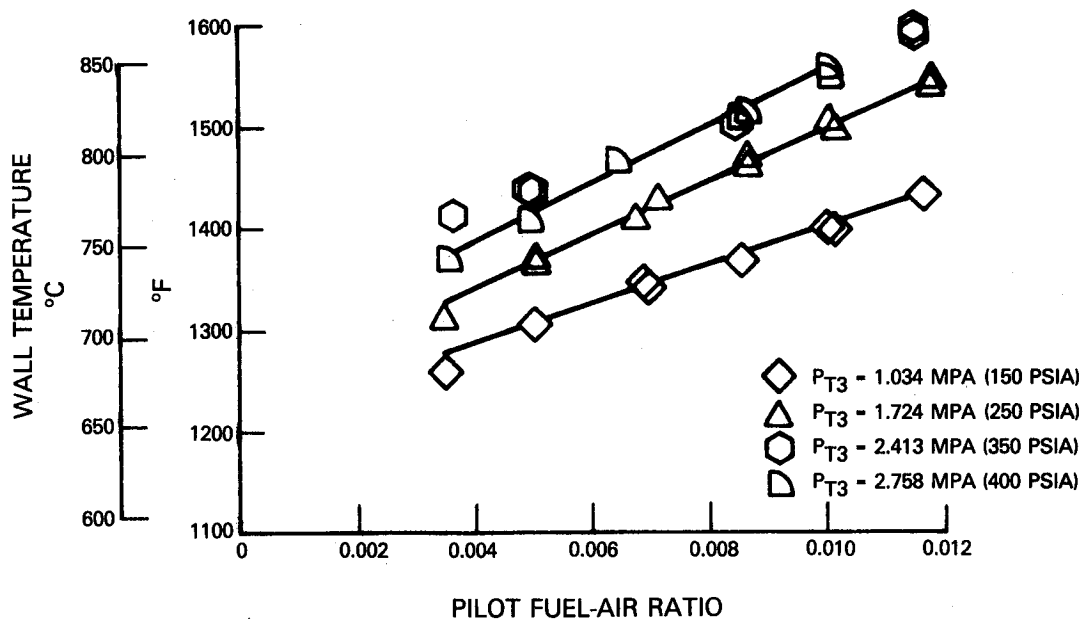


Figure 5-14 Variations in Main Zone Panel Temperature (Thermocouple No. 29)

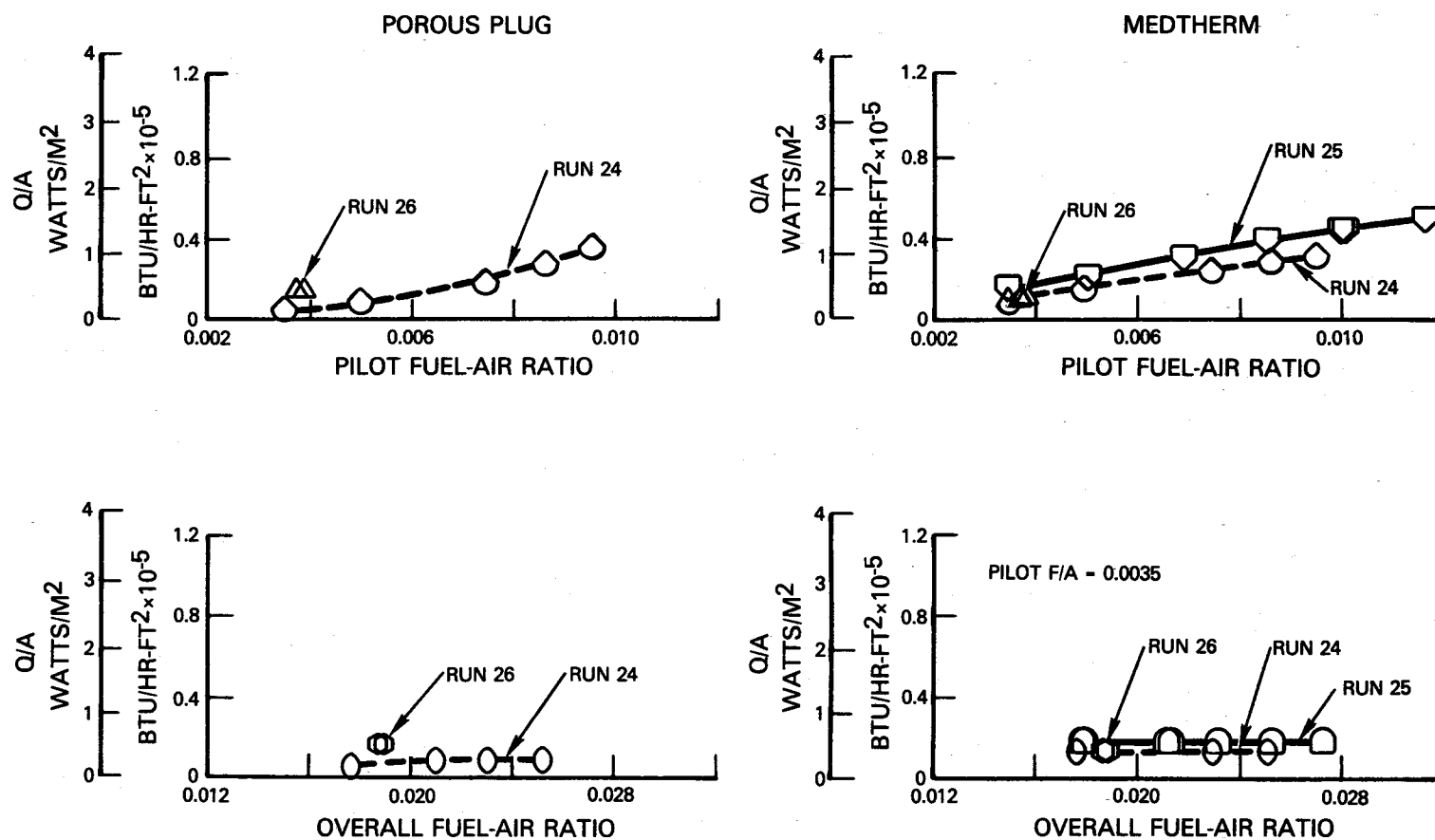


Figure 5-15 Pilot Zone Radiometer Measurements at $P_{T3} = 1.034$ MPa (150 psia); Radiometers 1 and 2

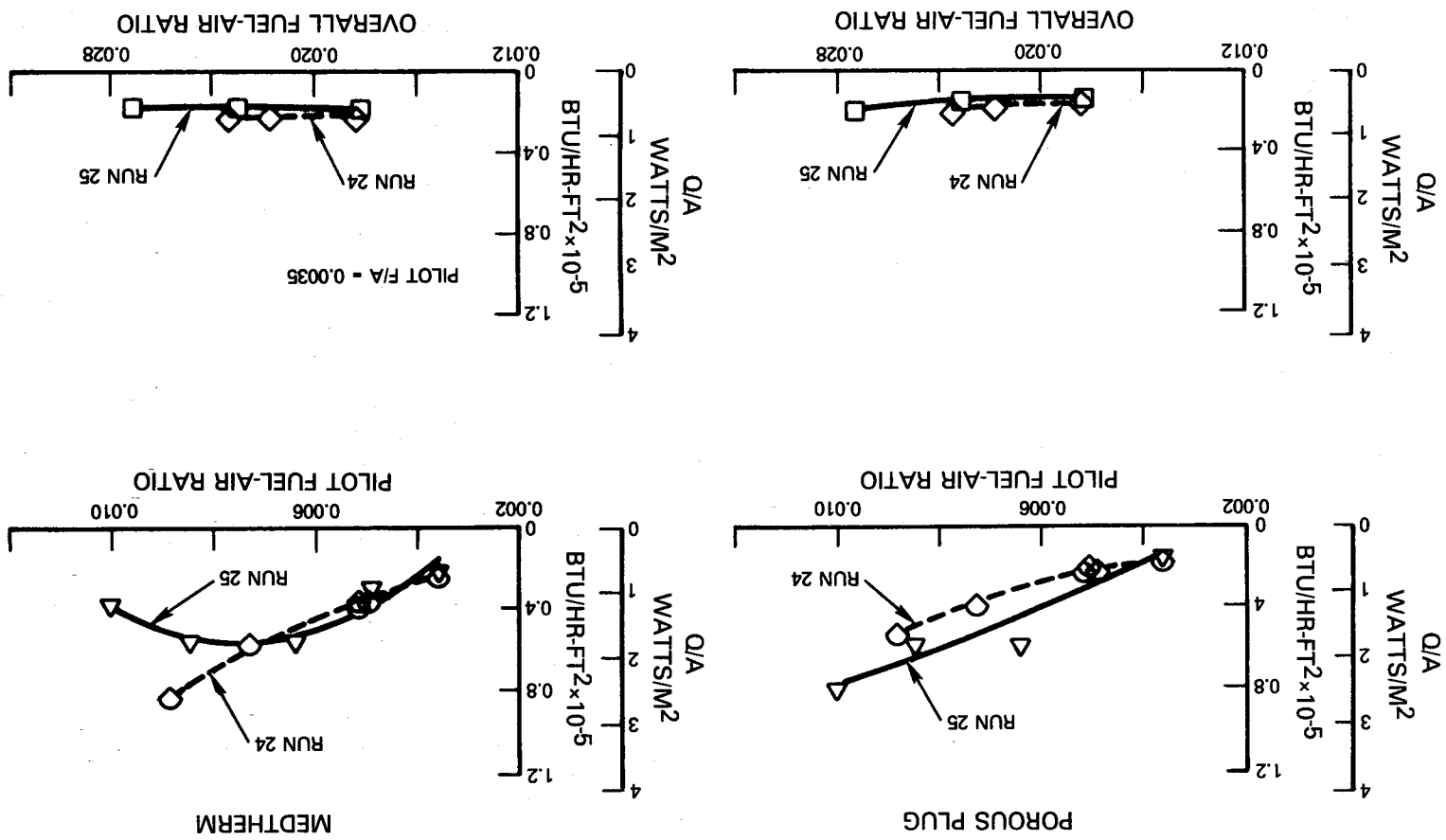


Figure 5-16 Pilot Zone Radiation Measurements at $P_{r3} = 2.758$ MPa (400 psia); Radiometers 1 and 2

Radiation flux data at 2.8 MPa (400 psia) inlet pressure for the first row of radiometers in the main zone are presented in Figure 5-17. Regardless of whether the pilot or main zone fuel flow is increased, the total radiation flux to the main zone liner is $0.4\text{--}0.7 \times 10^{-5}$ Btu/hr-sq ft-F. This is an extremely low value, but can be explained by the very fuel lean operation of main combustion zone. As will be discussed in a later section this is also consistent with the wall temperatures that were measured.

Figure 5-18 shows data from the downstream Medtherm radiometer at 2.8 MPa (400 psia) inlet pressure. Here a more pronounced difference in radiation flux levels are seen between Runs 24 and 25. This may have been a function of the degree of cleanliness of the sapphire window.

5.2.5 Wall Temperature Variation with Pressure

Variation of liner wall temperatures with combustor pressure were found to be weak. Especially in the main zone the maximum increase observed was approximately 55°C (100°F) from a pressure level of 1.0 MPa (150 psia) to 2.8 MPa (400 psia). The cross-plot of one of the fifth panel trailing edge thermocouples is shown in Figure 5-19. It should be noted that this not a cross plot of Figure 5-15 but data from an adjacent sensor. The decrease in slope or even a change in the sign of the slope of temperature with increasing pressure is again evident at all pilot/main fuel flow splits.

A similar cross plot for one of the few pilot zone thermocouples is presented in Figure 5-20. In this combustion region the dependence of wall temperature on pressure is seen to be stronger.

5.2.6 Radiation Flux Variation with Pressure

Pilot zone radiation fluxes as a function of combustor pressure are presented in Figure 5-21. Porous plug radiometer malfunctioned during the early phases of the test program (run 25), and only the high pressure data were available. When pressure data overlap is available there is good agreement between the two types of radiometers. This is somewhat contrary to the observation in Run 24 where the Medtherm radiometer indicated higher radiation fluxes than the porous plug. There is little or no dependence on pressure at low pilot fuel flow rates. As combustion gases get hotter the slope increases rapidly. Unfortunately the Medtherm radiometer failed at the 2.8 MPa (400 psia) point and therefore the reduction in radiation between the two highest pressure levels could not be confirmed.

Main zone characteristics as measured by the two radiometers are shown in Figure 5-22. The porous plug radiometer failed during the second half of the testing and again no corroboration could be had for the behavior at high pressures. The same trend was observed in trailing edge thermocouple readings on the fifth panel and also in Run 24. Although the slopes of the two radiometers are very similar, the difference in the level of radiation is substantial. This may be attributable to the differences in view factor between the two instruments. Medtherm has a narrower field of view (50° degrees) compared to the porous plug (180° degrees), implying that the Medtherm radiometer is being affected by local phenomena.

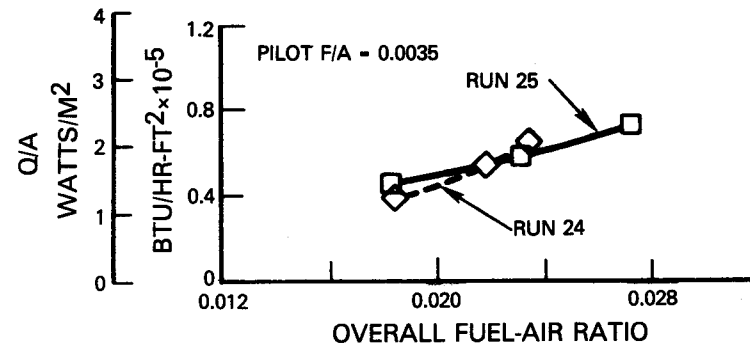
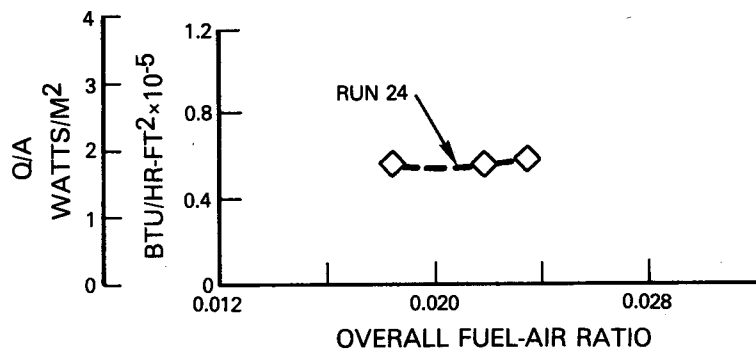
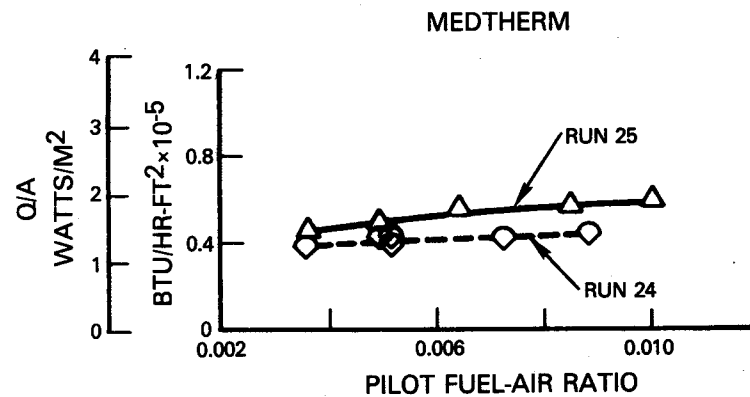
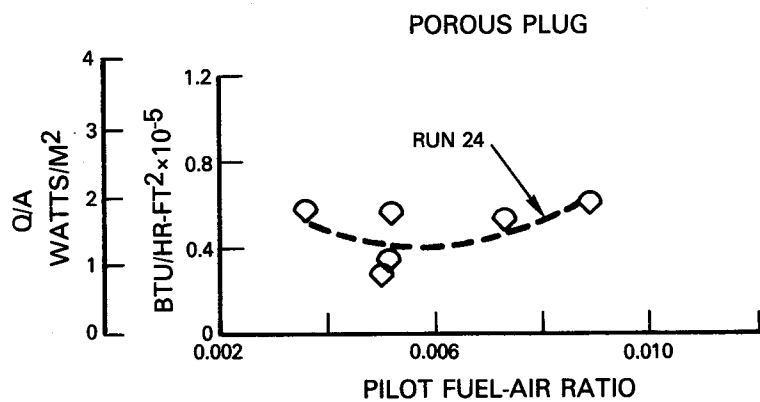


Figure 5-17 Main Zone Radiometer Measurements at $P_{T3} = 2.758$ MPa (400 psia); Radiometers 3 & 4

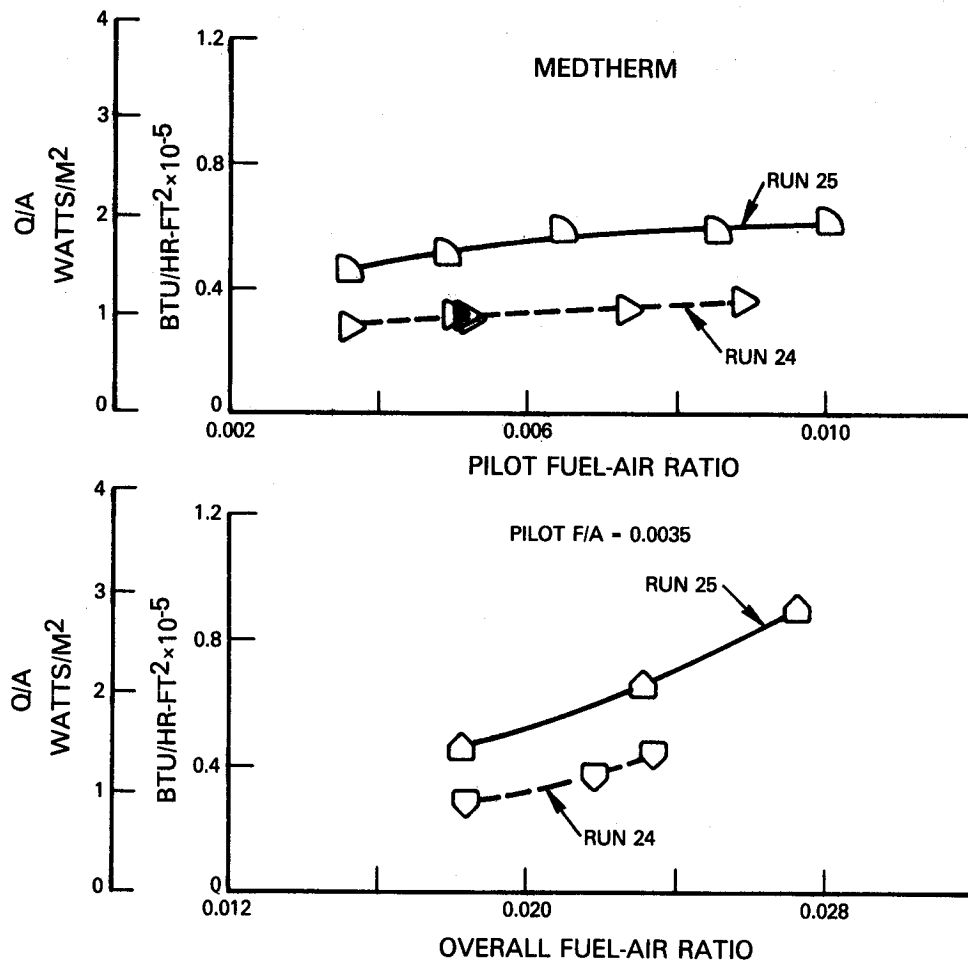


Figure 5-18 Main Zone Radiometer Measurements at $P_{T3} = 2.758$ MPa (400 psia); Radiometer 5

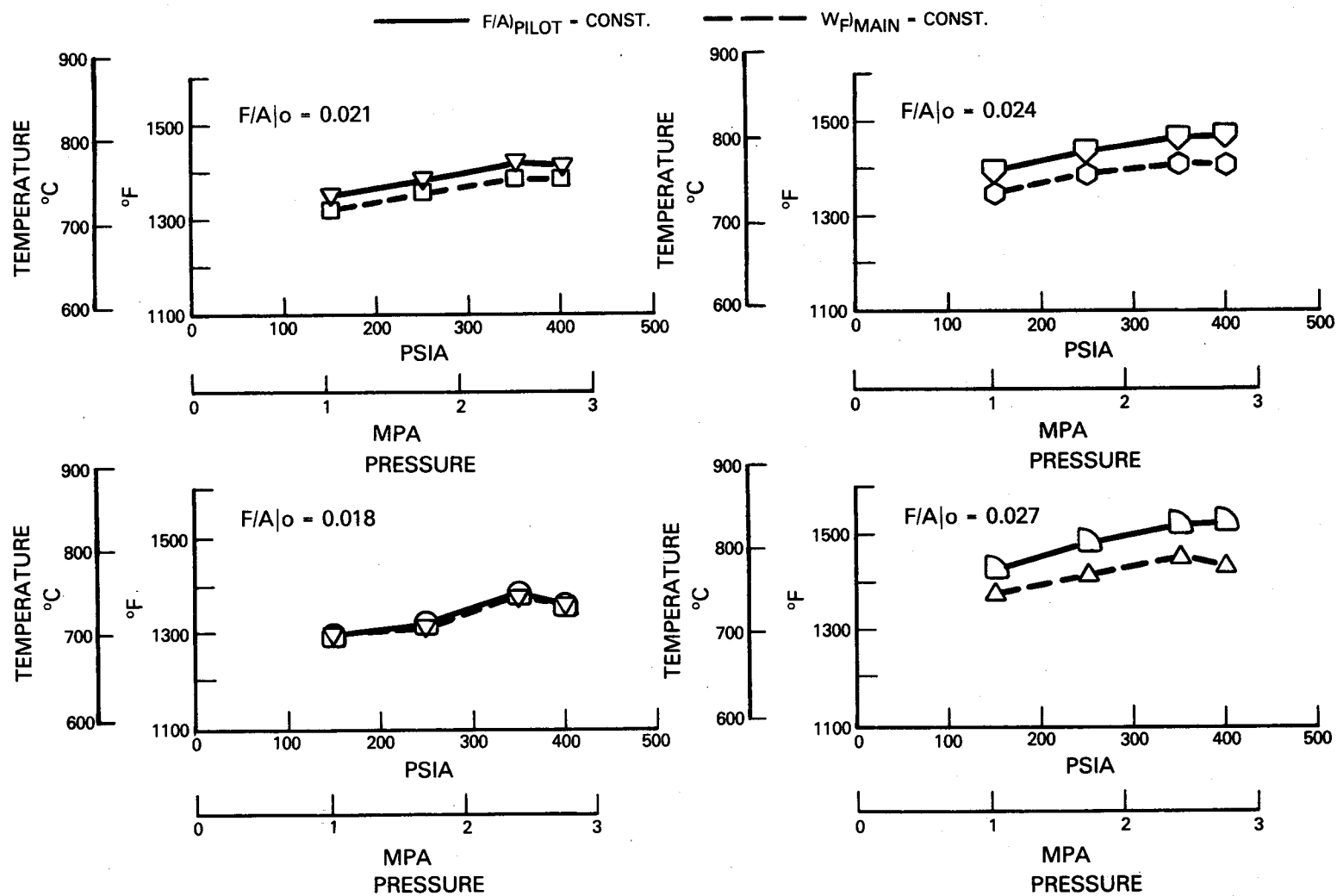


Figure 5-19 Variation of Main Zone Panel Wall Temperatures with Pressure
 (T/C #30)

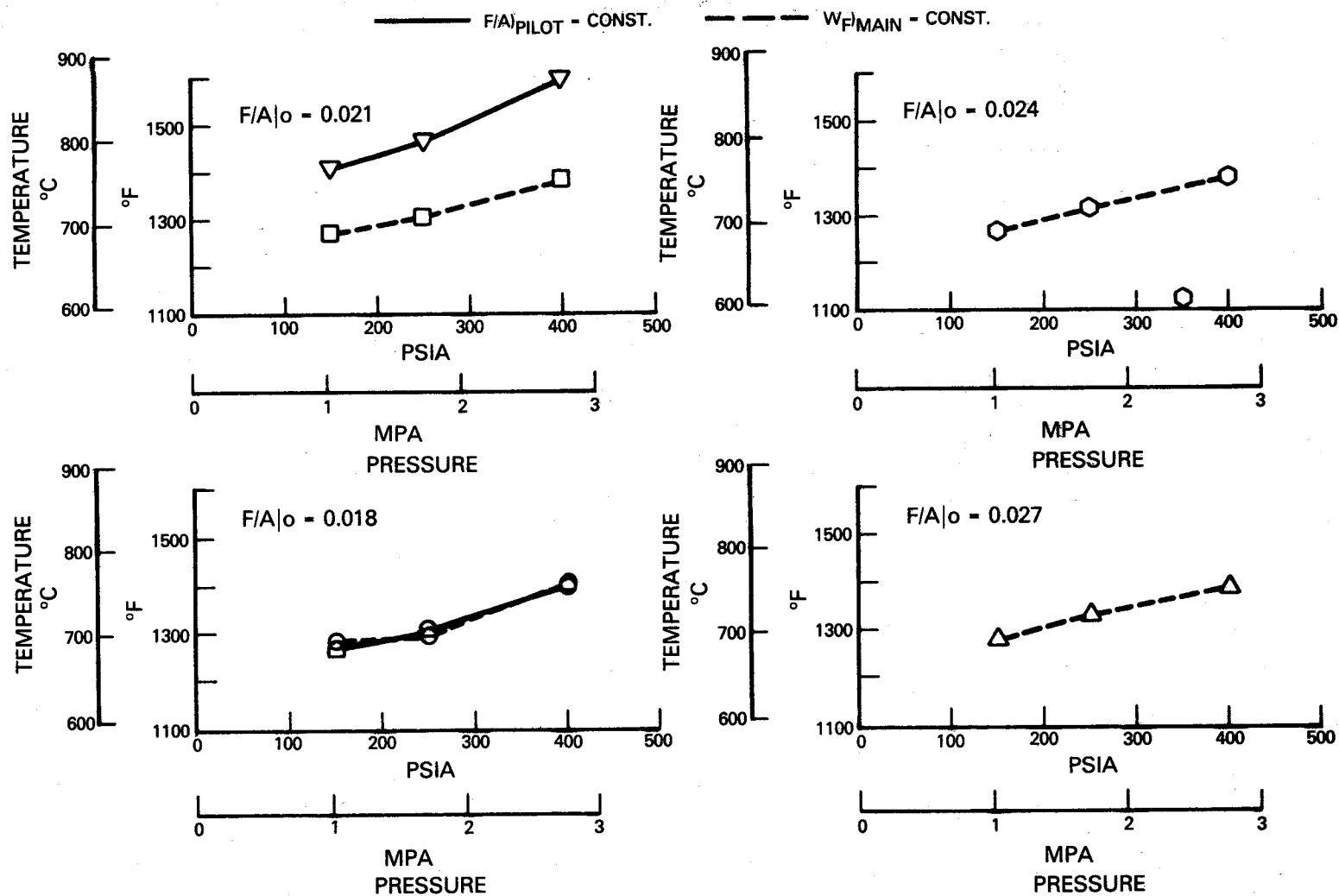


Figure 5-20 Variation of Pilot Zone Panel Wall Temperatures with Pressure (T/C #3)

OPEN SYMBOLS - MEDTHERM; SOLID SYMBOLS - POROUS PLUG

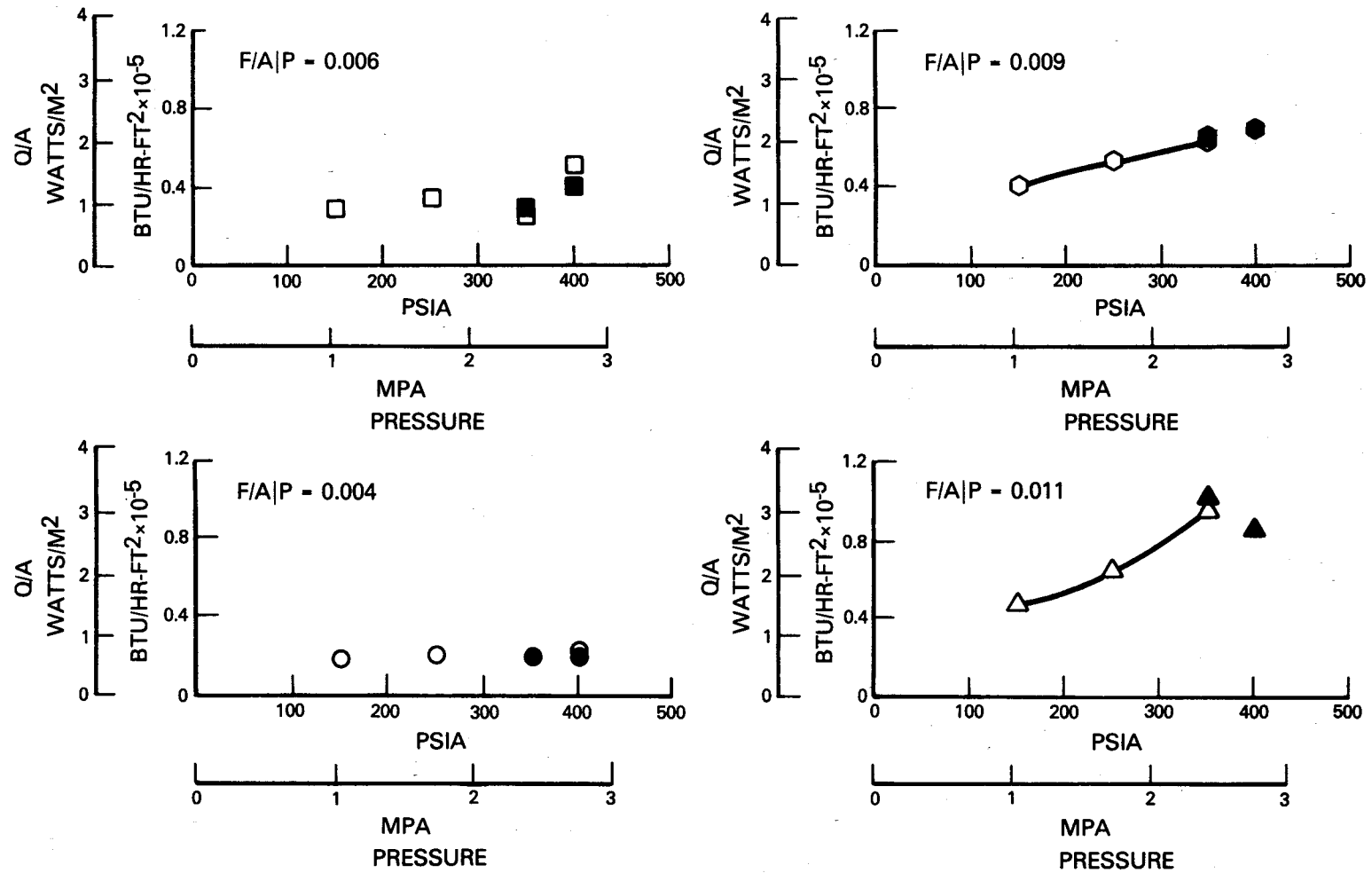


Figure 5-21 Variation of Pilot Zone Radiation Flux with Pressure

OPEN SYMBOLS - MEDTHERM; SOLID SYMBOLS - POROUS PLUG

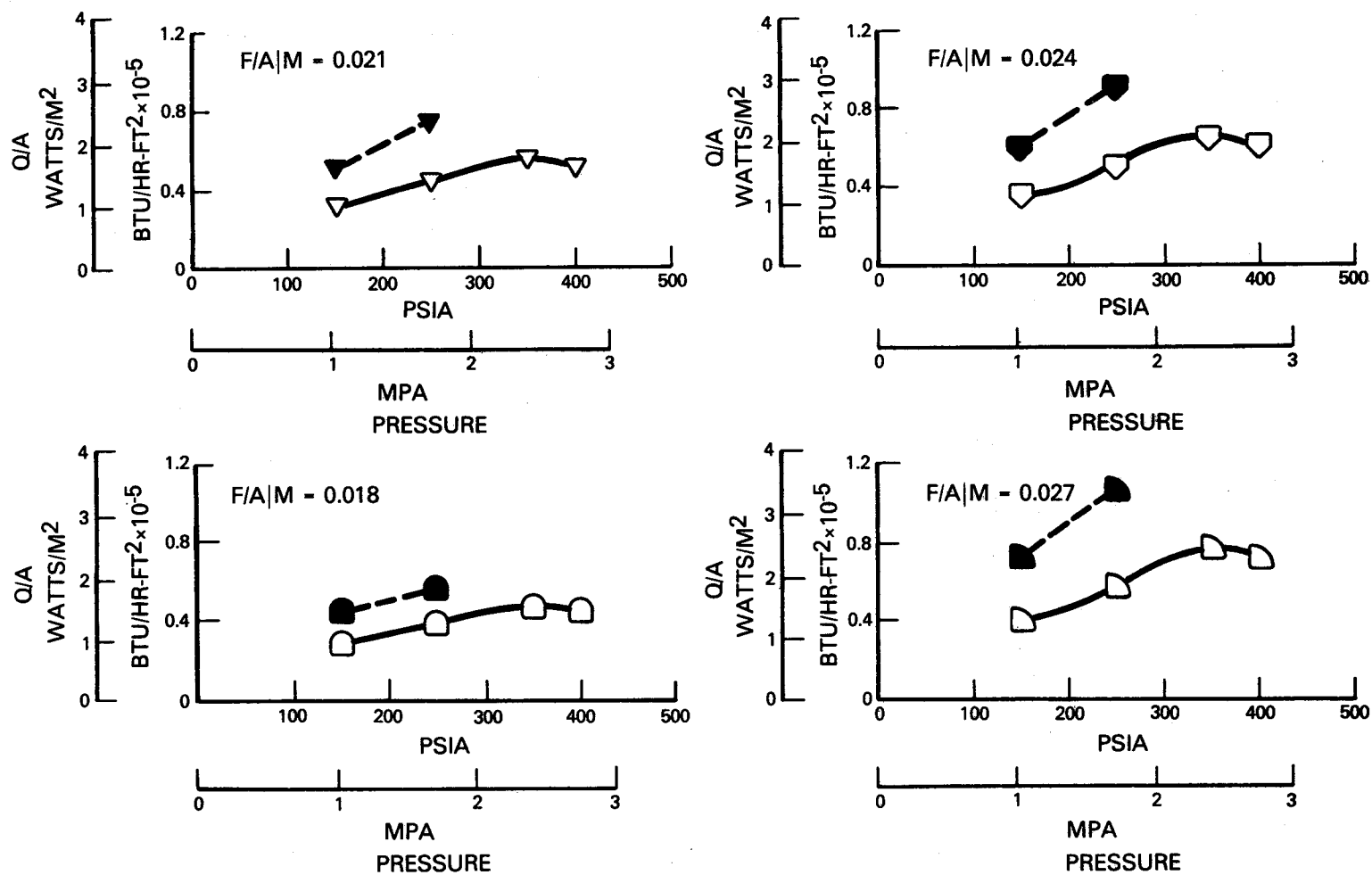


Figure 5-22 Variation of Main Zone Radiation Flux with Pressure

5.2.7 Analysis

5.2.7.1 Estimation of Flame Temperature Distribution

The ability to predict radiation loads on the liner and to subsequently predict the wall temperatures hinges on the estimation of the flame temperature distribution. An effective fuel-air mixing model was constructed in the liner design phase by simply back calculating the required gas temperatures to match observed wall temperatures on the CPFW liner (see Section 3.2.2.1). In order to get an independent evaluation of hot gas temperature distribution, the Energy Efficiency Engine combustor was modeled with the Pratt & Whitney computational fluid dynamics (CFD) code - TEACH (Reference 13). The combustor was simplified to a two-dimensional form with the proper cross-sectional area distribution. Figure 5-23(a) shows the resulting grid. Liquid fuel injection was modeled both in the pilot and main zones using measured fuel spray characteristics Figure 5-23(b). The resulting two dimensional gas temperature distribution is shown in terms of isotherms in Figure 5-23(c). The resulting temperature distribution was integrated radially at various axial stations. In this way a comparison could be made between the simplified one-dimensional model and the TEACH predictions. The results of the comparison are shown for a fuel-lean and a fuel-rich pilot zone in Figure 5-24(a) and 5-24(b). The one dimensional mixing model compares quite reasonably to its two dimensional counterpart. The simplified mixing model was retained to conduct the analysis.

The radiation model employed is one used extensively in gas turbine combustion analysis (Reference 14).

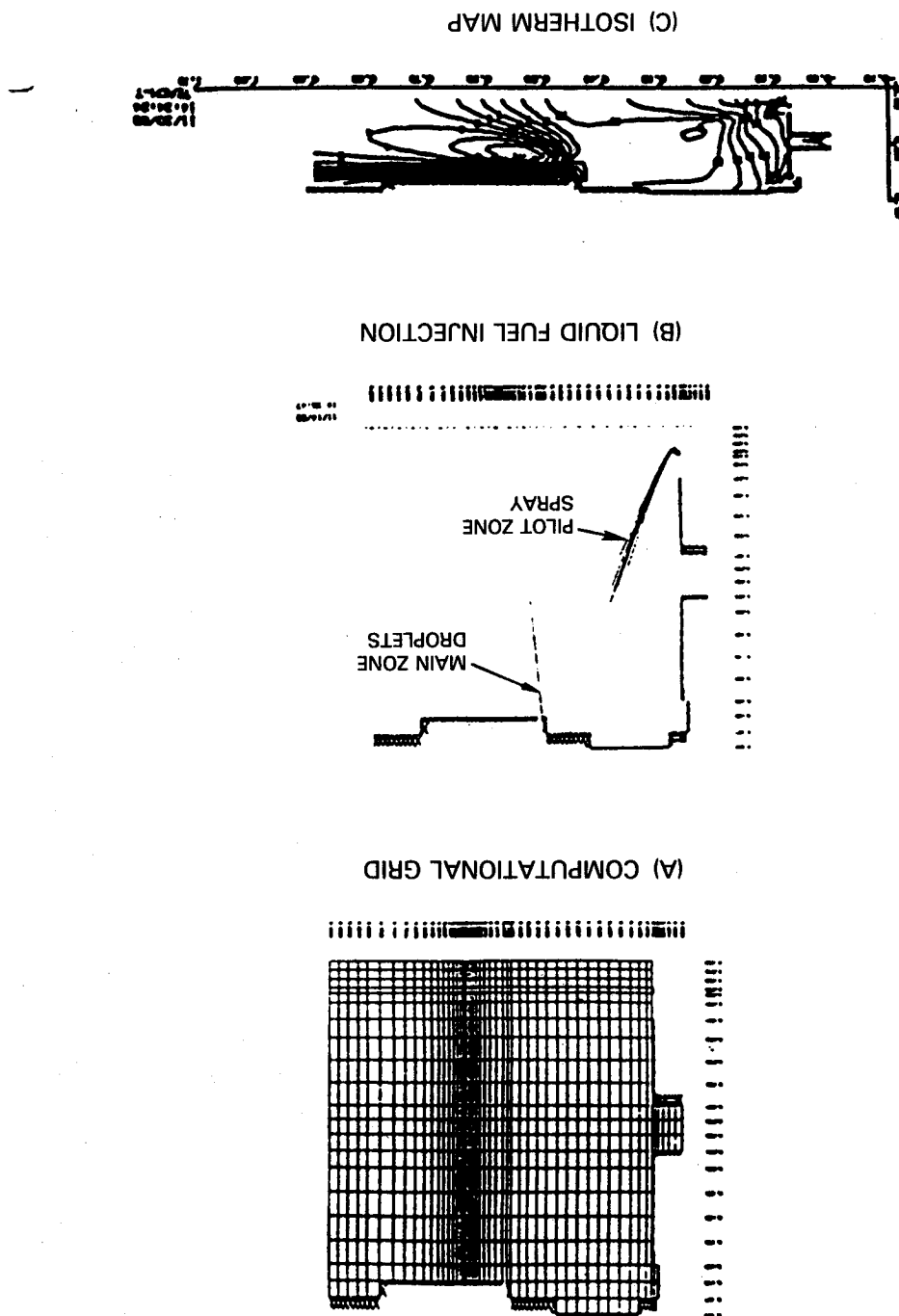
$$(Q/A)_{\text{RAD}} = K_1 \sigma \left\{ \epsilon_f T_f^4 - \alpha_f T_w^4 \right\}$$

$$\epsilon_f, \alpha_f = 1 - \exp \left\{ -K_2 L P^a \ell^b (f/a)^c T_f^d, T_w^d \right\}$$

where: L = luminosity factor
P = combustor pressure
 ℓ = beam length;
f/a = local fuel/air
 T_f, T_w = flame, wall temperature.

Inspection of data indicates a choice of 1.0 for luminosity. Both pilot and main combustion zones operate at or below stoichiometric fuel-air mixtures. Luminosity generally becomes dominant in fuel-rich combustion zones. Another indication is the lack of measured particulate emissions (maximum smoke number of 4).

Figure 5-23 Computational Fluid Dynamics Model of Combustor



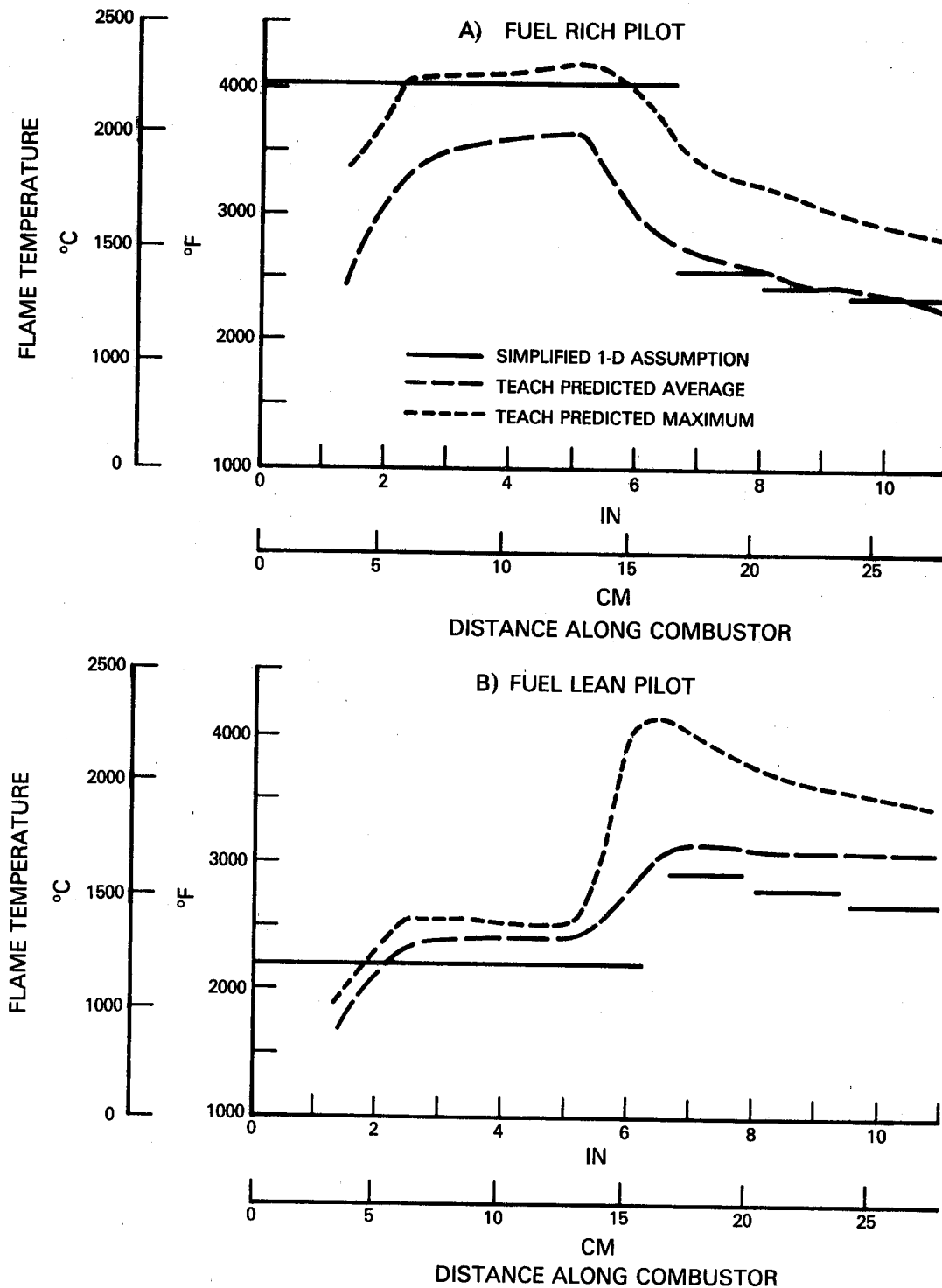


Figure 5-24 One-Dimensional Flame Temperature Distribution vs. TEACH Prediction

The calculated gas temperature distribution and the radiation model were used in conjunction with film cooling and pedestal cooling models to conduct a thermal balance on the liner.

5.2.7.2 Comparison of Calculated and Measured Quantities

Predicted radiation fluxes are compared to those measured in Run 25 and all five of the radiometers are presented in Figure 5-25. In general the agreement is good considering the simplifying assumptions. The only comparison that shows a major deviation is the porous plug data from the main zone. There is a tendency to under predict radiation with the assumed luminosity factor of 1.0, and improvement can be made with a slightly higher value.

Not all thermocouples data are amenable to comparison with predictions. The thermal model is two dimensional in the axial and radial sense, and thus does not recognize such three dimensional effects as dilution hole interruptions, mount posts, cooling passage blockages, etc. The panel that is most uniform in terms of cooling geometry features and one that is heavily instrumented is the fifth inner liner panel. Accordingly, comparisons are made on the trailing edge thermocouples in Figure 5-26. The comparison indicates no general bias. The level of disagreement is as expected with the uncertainties of the boundary conditions. On the average, wall temperatures were estimated with this methodology to within $\pm 33^{\circ}\text{C}$ (60°F).

5.2.7.3 Effect of Geometric Changes on Wall Temperature

Three changes were made to the liner configuration between Runs 24 and 25. These changes summarized below were intended to reduce already observed high temperatures in the pilot zone or to evaluate sensitivity of the cooling configuration to geometric changes.

1. The flow blockage caused by improper casting of the mount post pads was corrected by electro-discharge machining in the first panel.
2. Cooling level in panel number 3 was increased by 30 percent. This was accomplished by increasing the cooling hole openings in the shell.
3. Panel number 5 was replaced by an alternate design (see Figure 3-12). The new configuration featured the amount of pin blockage as the previous configuration but with smaller diameter pins.

The effects of the first and third modifications were established in Run 25. Failure of the thermocouples on the third panel and the inconclusive reading of the thermal sensitive paint precluded any judgment on the magnitude of the liner cooling increase effect.

The impact of thinning out the blockage around the mount post pads is evident in Figure 5-27. The thermocouple (No. 3) is installed on the hot surface in very close proximity to the modification. Wall temperature reduction of approximately 30°C (50°F) was achieved.

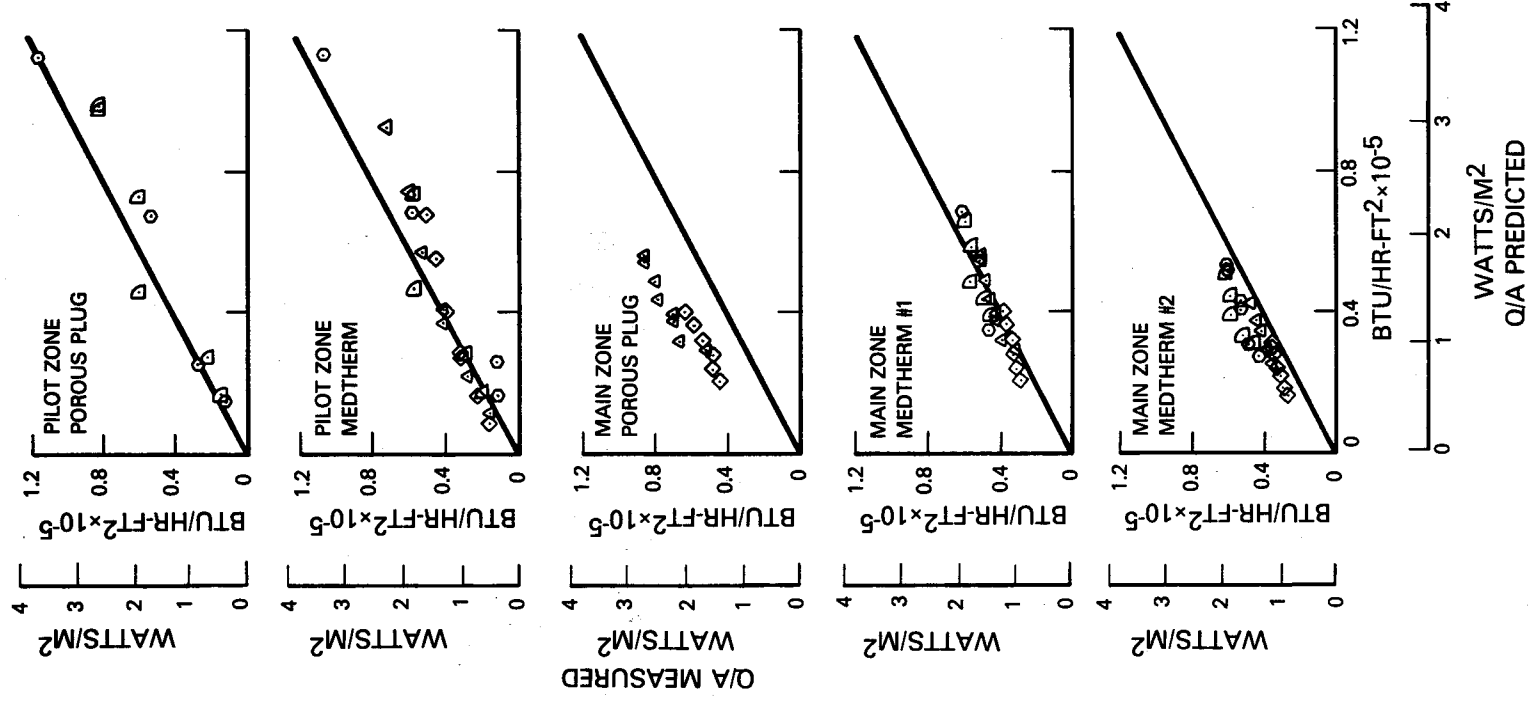


Figure 5-25 Predicted vs. Measured Heat Flux

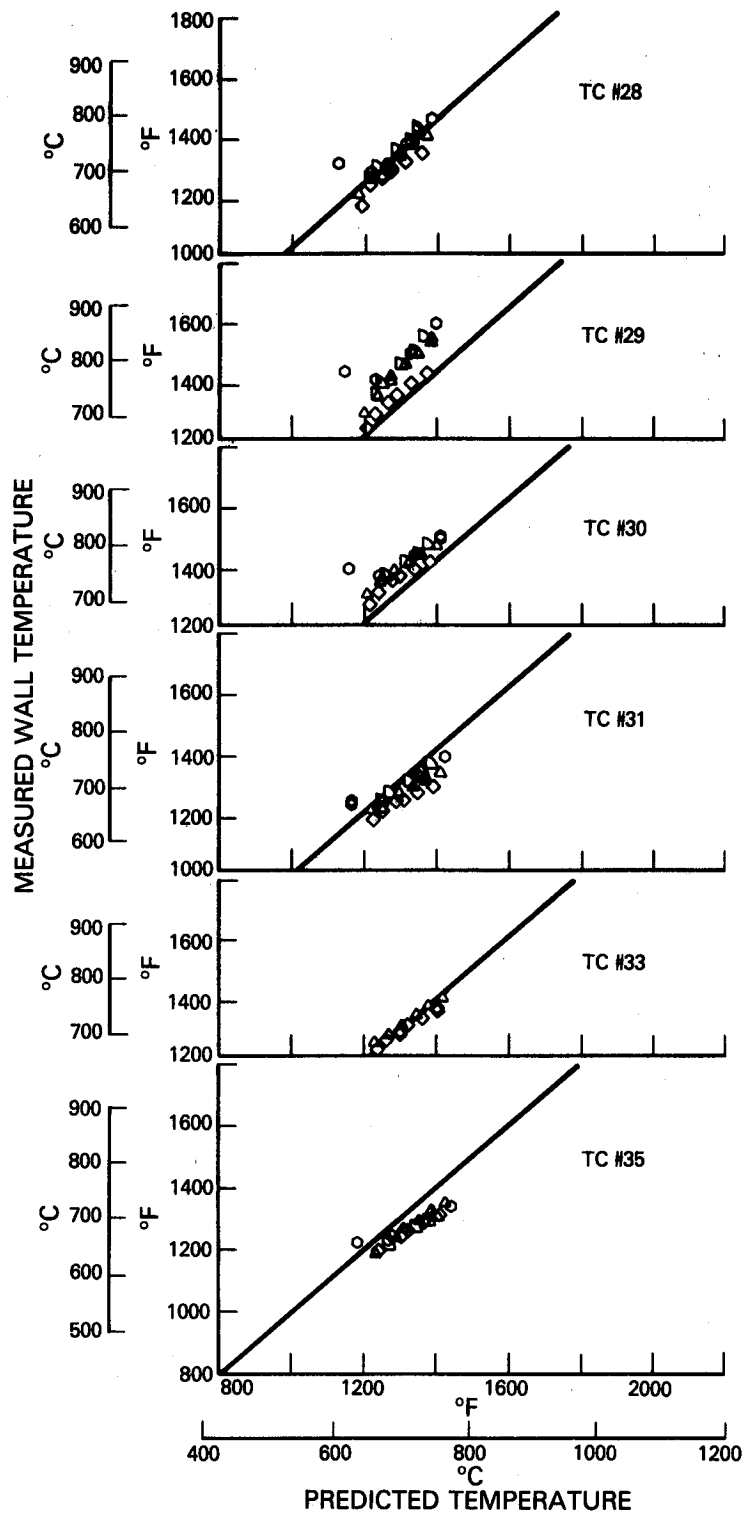


Figure 5-26 Comparison of Predicted and Wall Temperatures on Panel #5

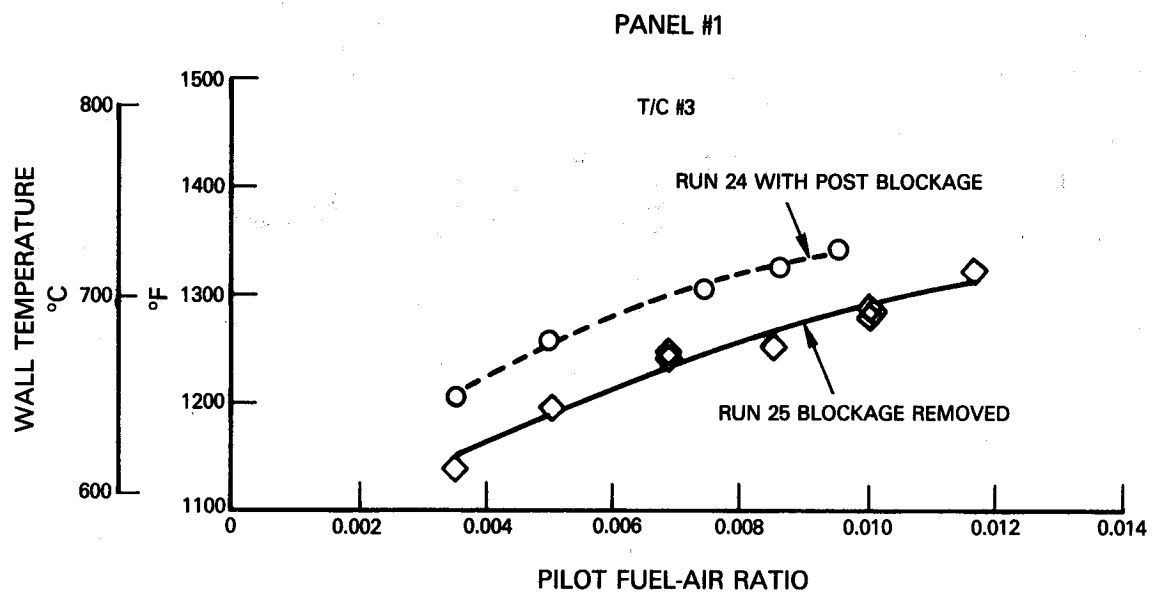


Figure 5-27 Effect of Removing Casting Blockage on Panel #1 Wall Temperature

One of the prime reasons for the large number of thermocouples in the fifth panel in both Runs 24 and 25 was to assess the thermal efficiency of a panel with a substantially different pin array. Both arrays were designed to yield the same amount of blockage so cooling flow between the two runs would be constant. The results are presented in Figure 5-28 as Run 24 trailing edge temperature minus Run 25 values. Four thermocouples were available at a broad range of conditions to make the assessment. On the average the configuration with the higher density of pin-fins is 20C (40F) cooler than the larger diameter pin-fin configuration. Analytical predictions indicated approximately 14°C (25°F) advantage.

5.3 CERAMIC COMPOSITE LINER EVALUATION RESULTS

The principal objective of the evaluation of the SIC-LAS ceramic composite liner panels in the combustor sector rig was to assess the durability of these components. The results of the studies conducted under the NASA/P&W Advanced Composite Combustor Structural Concepts Program (Reference 1), as described in Section 3.2.3.1 had indicated that the most likely failure mode for these panels would be deterioration from exposure to elevated temperatures, as opposed to the cyclic thermal fatigue processes that generally limit the life of metallic liners. Consequently, the experimental evaluation of Run 26 was structured to maximize the time of exposure of the combustor liner to elevated temperatures and included ten hours of continuous operation at a simulated sea level takeoff operating condition.

When the composite liner panels were removed from the shell the thermal paint on the cold side of the panels was found to be in very good condition and provided good indications of the temperature distribution on these surfaces. Figure 5-29a shows the entire set of 18 panels laid out from top to bottom in the positions they occupied on the liner shell. The fidelity of temperature indication is demonstrated in the ease with which the point of impingement of each cooling air jet may be observed. This is particularly evident on the panels of Row 5 (with the 5 dilution holes in each panel) and Row 6 shown in Figure 29b. In some locations the Type C-3 thermal paint on the panels on the right side and in the center of the rig adhered to the metal shell and peeled off the composite panels. These spots are most evident in Figure 5-29 near the attachment holes and in locations circumferentially adjacent to these holes. There also was evidence of some deposits on the downstream end of the panels of Row 7. This was found to be deposits from the water that had been sprayed into the facility exhaust chamber and had recirculated under the downstream lip of the panels in that last row.

The thermal paint also survived well on the hot side of the composite liner panels. As indicated previously the light colored regions on the panels on the left side of the liner in Figure 4-10 are Type GT-1 thermal paint that has experienced only moderate temperature levels, i.e., 815°C to 870°C (1500°F to 1600°F) or less. Note that the left side panel of Row 6 did not have any thermal paint on its hot side because it was the only panel in the rig fabricated with the LAS II matrix material.

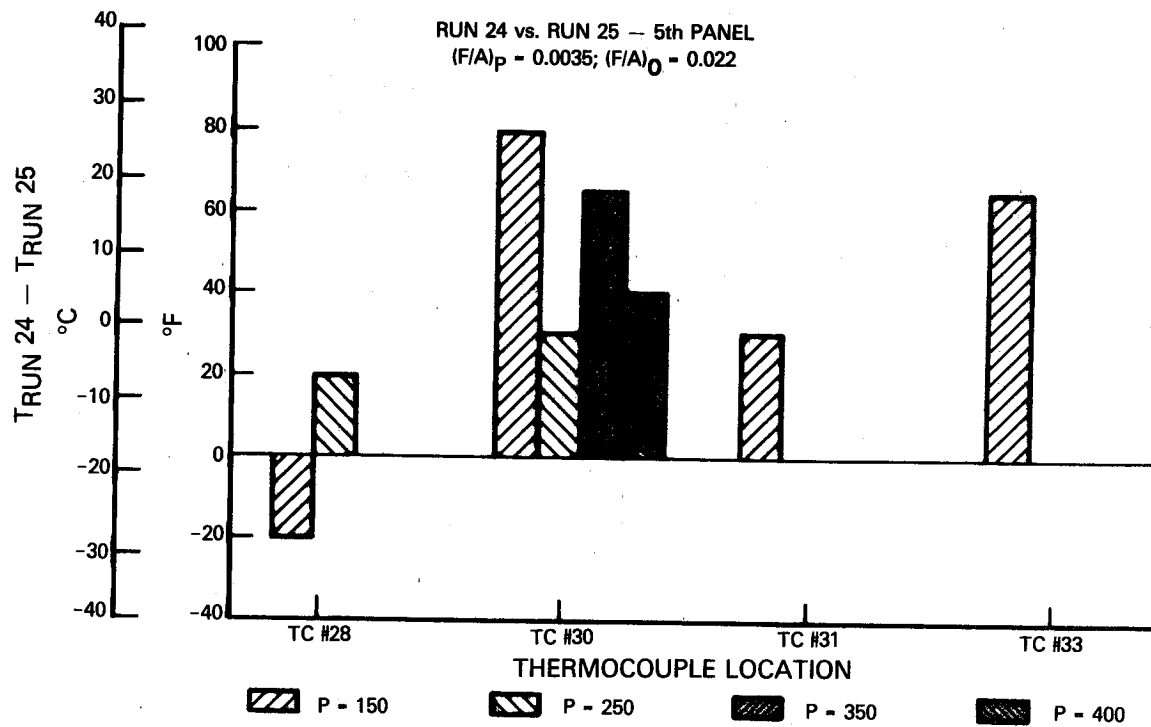
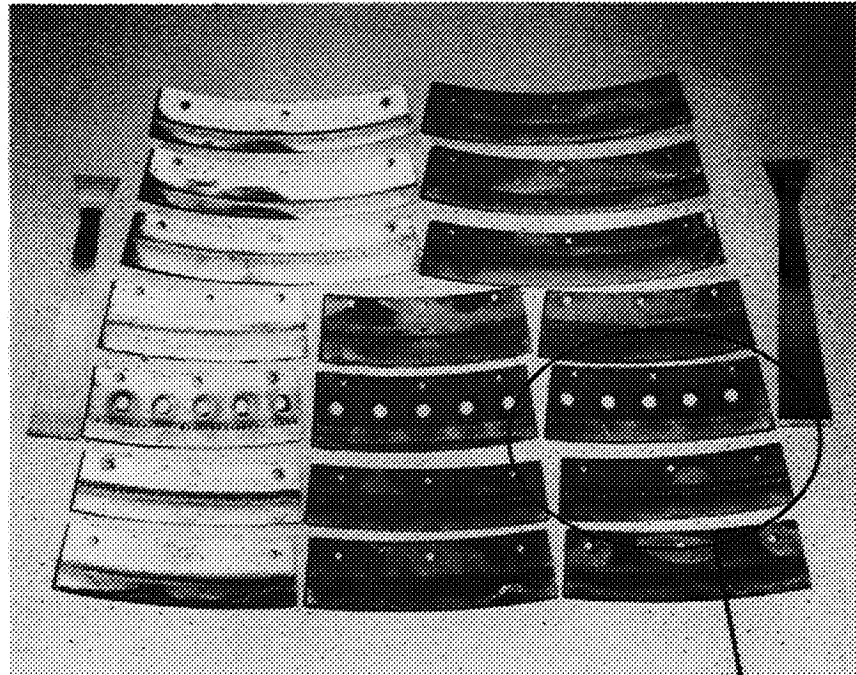


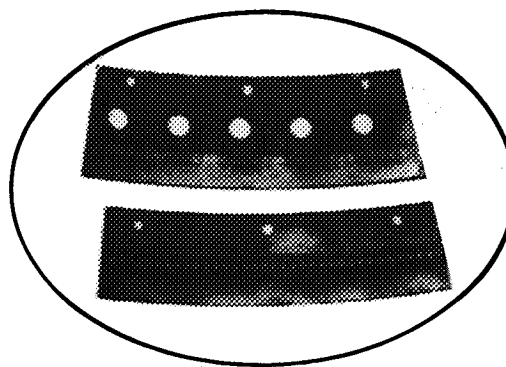
Figure 5-28 Comparison of Dense (Run 25) vs Sparse (Run 24) Pin-Fin Array

ORIGINAL PAGE IS
OF POOR QUALITY

ORIGINAL PAGE
BLACK AND WHITE PHOTOGRAPH



a) CERAMIC COMPOSITE PANELS



b) ROW 5 & 6 PANELS

Figure 5-29 Thermal Paint on Cold Side Surfaces of Ceramic Composite Liner Panels

In interpreting the thermal paint color changes the simulated takeoff condition at which the ten hour durability assessment was conducted was also the highest temperature operating condition encountered and was the temperature which set the paints. Figure 5-30 shows the temperature distribution on the hot side surface of the panels as deduced from the color changes of the paint. The paint on the panels in Rows 1 through 4 indicate the surface temperature of the upstream parts of the panels, most of which was under the lip of the upstream panel, was less than 648°C (1200°F) then it increased abruptly to about 926°C (1700°F) slightly downstream. This was followed in most locations by a more gradual increase in temperature until levels of 1036°C to 1091°C (1900°F to 2000°F) or higher were observed at the downstream end of the panel. This characteristic axial temperature distribution is very consistent with the distribution predicted in the thermal analysis conducted during the design of the liner in Section 3.2.3.4. Relative to the computed temperature distributions of Figure 3-26 the only departure from the qualitative similarity is in the experiment not revealing the predicted surface temperature depression where the cooling air is impinging on the cold surface. The temperature levels observed at the downstream lips of these panels are also consistent with those projected during the design analysis as comparison with Figure 3-27 indicates.

There is also some evidence of the effect of temperature streaks associated with the five pilot zone fuel injectors in the hot side temperature distribution on these panels. The distribution on the panel from Row 1 shows a definite two and one half cycle pattern while those from Rows 2 and 3 indicate higher temperature levels further upstream where the panels abut on the centerline of the rig which coincides with a fuel injector.

The Row 5 panels had dilution air jets penetrating through them and the presence of these jets led to higher hot surface temperatures across the entire width of the panel and not just behind or between the jets. Nonetheless, the surface temperature levels downstream of the dilution holes, at 926°C to 1036°C (1700°F to 1900°F) are moderate compared to predicted levels of Figure 3-27. It is of interest that the unpainted hot sides of the ceramic composite panels generally retained their original grey color during the test. The only exceptions appeared to be: 1) the presence of darker grey streaks, which are visible in Figure 4-10, between the dilution air holes on the Row 5 panels. These streaks persisted to a lesser extent onto the downstream Row 6 and 7 panels, and 2) an orange colored stain on the downstream surfaces of the Row 4 and 5 panels in the vicinity of the center to right panel juncture. Because of its singular appearance, the latter is thought to be caused by a carburetor tube on the outer liner producing a stronger than nominal jet penetration.

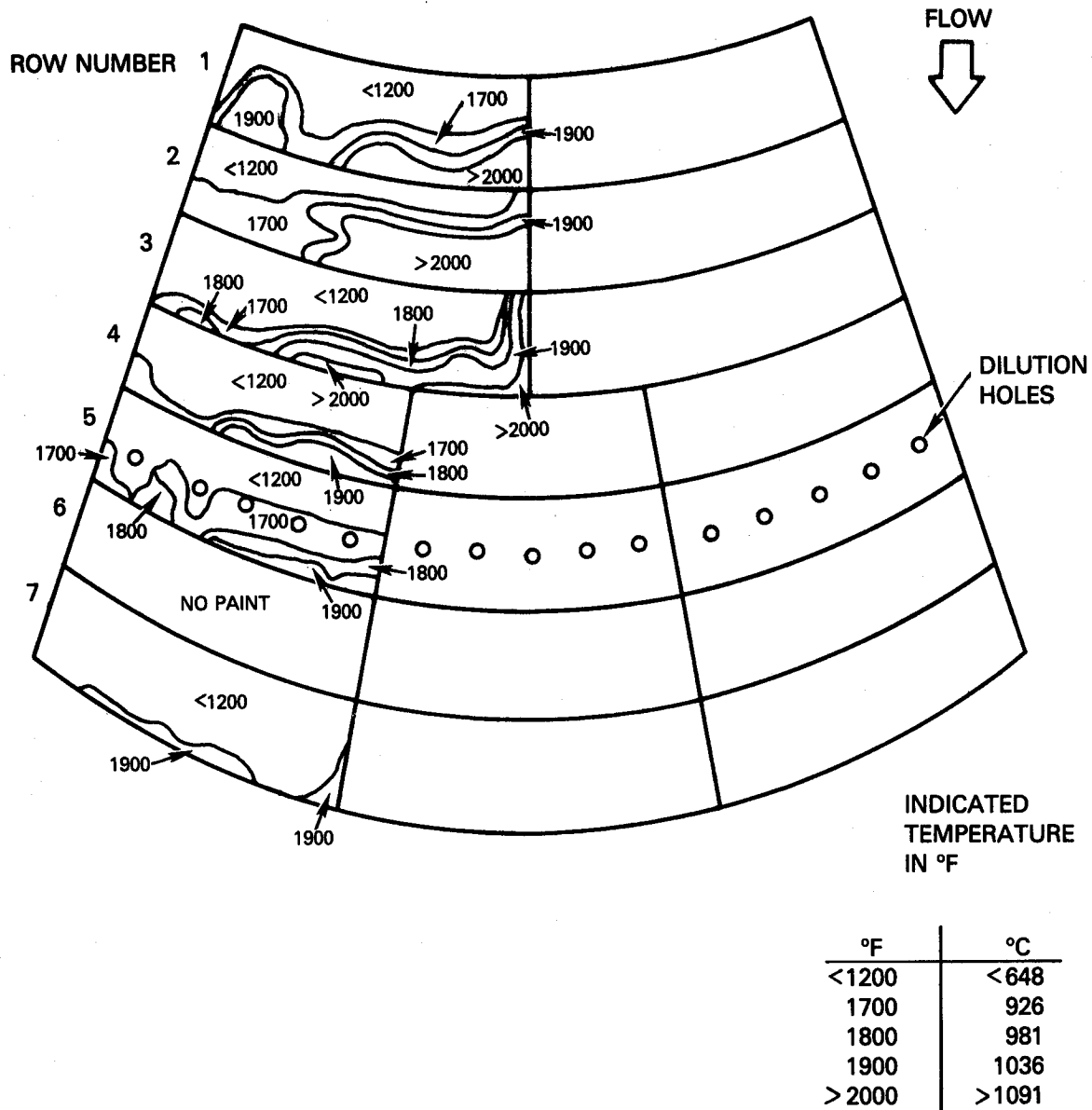


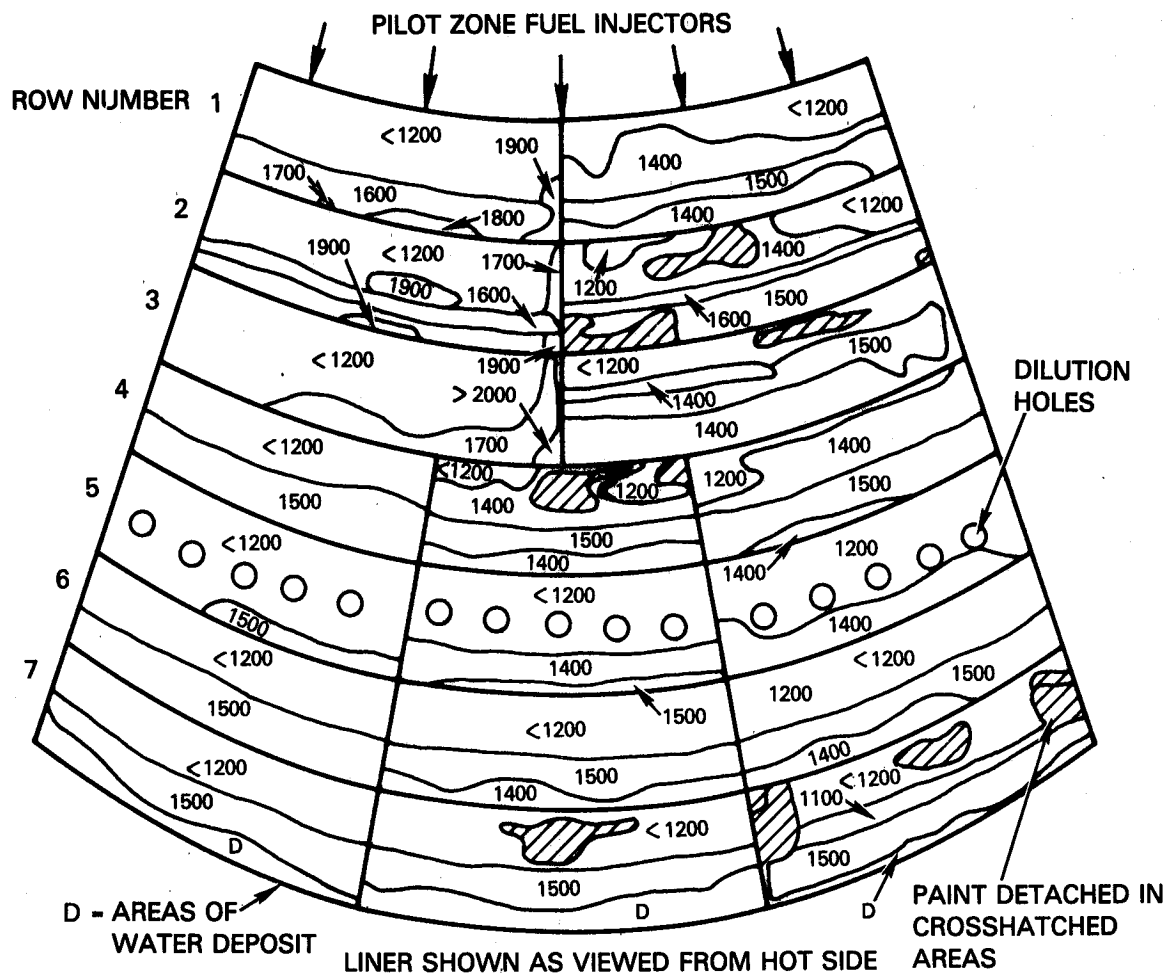
Figure 5-30 Ceramic Composite Liner Panel Hot Side Temperature Distribution

The only abnormality in the reading of the panel hot side temperatures with thermal paints was on the Row 7 panel on which the less than 648°C (1200°F) region persisted over most of the axial length of the panel. However, the downstream lip of the panel reached temperature levels of 1036°C (1900°F). A more gradual increase would have been anticipated based on both the design analysis of Section 3.2.3.4 and the readings from the hot side of the upstream panels. In addition, the thermal paint on the cold side surface of this panel also indicated that higher temperatures were being observed in the mid length region of that side of the panel.

Figure 5-31 shows the temperature distribution on the cold side surfaces of the composite liner panels as deduced from the thermal paint on these surfaces. For clarity the bands produced by impingement of the cooling air on the panels have been omitted on this figure. Comparison of the experimental results with the design intent is most evident on examination of the temperature distributions on the panels in Rows 4 through 7. These indicate that the surface temperatures are less than 648°C (1200°F) over the upstream half of the panel length where they are sheltered under the lip of the upstream panel. While the cooling air impingement area was generally visible as a very narrow band of low temperatures the nominal temperature levels over the downstream half of the panel are in the range of 759°C to 814°C (1400°F to 1500°F). In conjunction with the observed surface temperatures on the hot side of the panels, these results confirm the existence of through thickness temperature differentials of as much as 280°C (500°F) at the downstream end of the panels that were predicted in the design analysis.

The thermal paint on the cold side of the panels of Rows 1, 2, and 3, which enclosed the pilot combustion zone of the burner, show greater non-uniformity in the temperature distributions and regions of considerably hotter surface temperatures. This is particularly evident near the junction between the panels at the centerline of the rig where temperatures are in the 926°C to 1036°C (1700°F to 1900°F) range and at the downstream end of Row 3 even exceed 91°C (2000°F). This panel juncture is also on the centerline of a pilot zone fuel injector and it is suspected that these locally high temperatures were caused by hot gases getting under the composite panels through the gap between the panels.

In addition to this centerline region, localized areas of temperatures in the 926°C to 1036°C (1700°F to 1900°F) are also evident on the first three panels on the left side of the liner. The thermal paint on the hot side surface of these panels had indicated a transverse periodicity that correlated with the locations of the pilot zone fuel injectors. Comparison of Figures 5-30 and 5-31 indicates that the hotter regions on the cold side surface of these panels appears to coincide with the high temperature streaks on the hot side.



5.3.1 Nondestructive Inspection

Following the reading of the thermal paint the SIC-LAS ceramic composite panels involved were cleaned to remove the paint to facilitate inspection. This was accomplished with 00 steel wool followed by immersion in a boiling trichloroethylene solution. All of the panels were X-rayed to supplement the visual inspection for cracks and regions of delaminations.

As indicated previously, with the exception of a few local regions, the exposure in the sector combustor rig did not produce any change in the appearance of the surface of the panels and they retained their characteristic grey color and surface texture. The panel fabricated with the LAS II matrix material initially had a slightly coarser surface texture than those made from LAS III and this texture did not change with exposure in the combustor rig. Figure 5-32 shows a summary of the condition of the liner panels before and after the combustor rig test. Prior to testing two cracks had been detected in the Row 2 panels. One was at the upstream edge of the left panel and the other was at the downstream end of the right panel. The later crack was of particular interest because it was located in one of the hottest regions of the liner and extended through all eight plies of the panel. However, the exposure in the combustor sector rig did not aggravate this crack significantly because it didn't propagate any further into the panel. Figure 5-33 shows a magnified view of the region around this crack.

As shown on Figure 5-32 the exposure in the sector combustor rig created four new cracks in the panels. Two of these, in the trailing edge of the right side panel of Row 1 and in the abutting edge of the left side panel of Row 2 were in the high temperature region produced by the pilot stage fuel injector on the rig centerline. The Row 2 crack in particular is in an area where the interpretation of the thermal paint had indicated hot gases may have gotten under the panel at the juncture. The other two new cracks occurred near the trailing edge of the Row 5 panels. There is no immediate reason for their occurring in this area but it is possible they could be associated with stresses induced by the machining of the dilution air holes in these panels. None of the new cracks were as severe as that present prior to test in Row 2 in that they did not penetrate the full thickness of the panel. All of these cracks started on the hot side surface and extended through 4, 4, 6, and 1 of the eight plies in the Row 1, Row 2, Row 5 center and Row 5 right panels respectively. Curiously the cracks in the Row 5 panels are in the region of orange staining that was previously considered as being caused by impingement of flow from a carburetor tube.

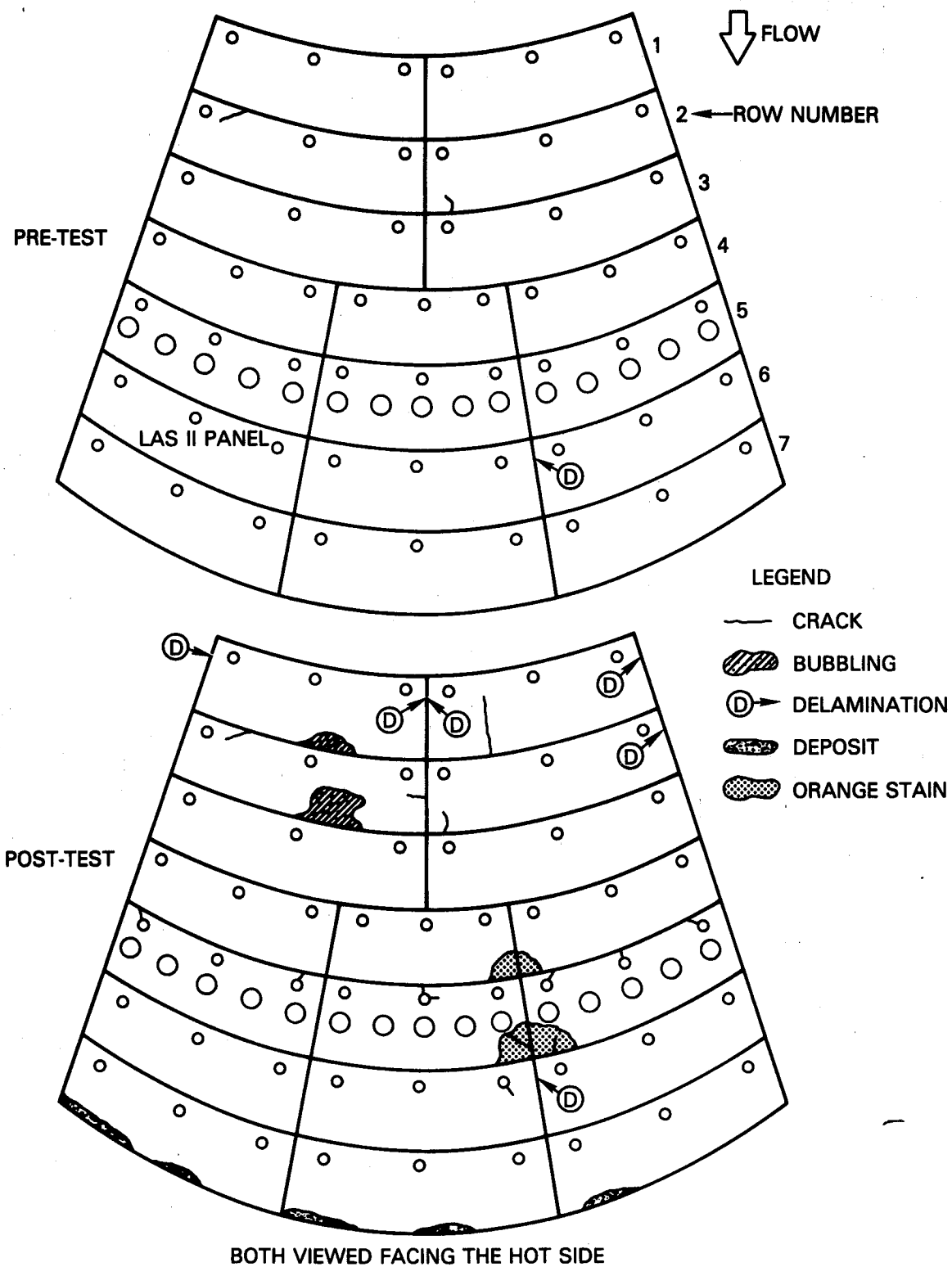
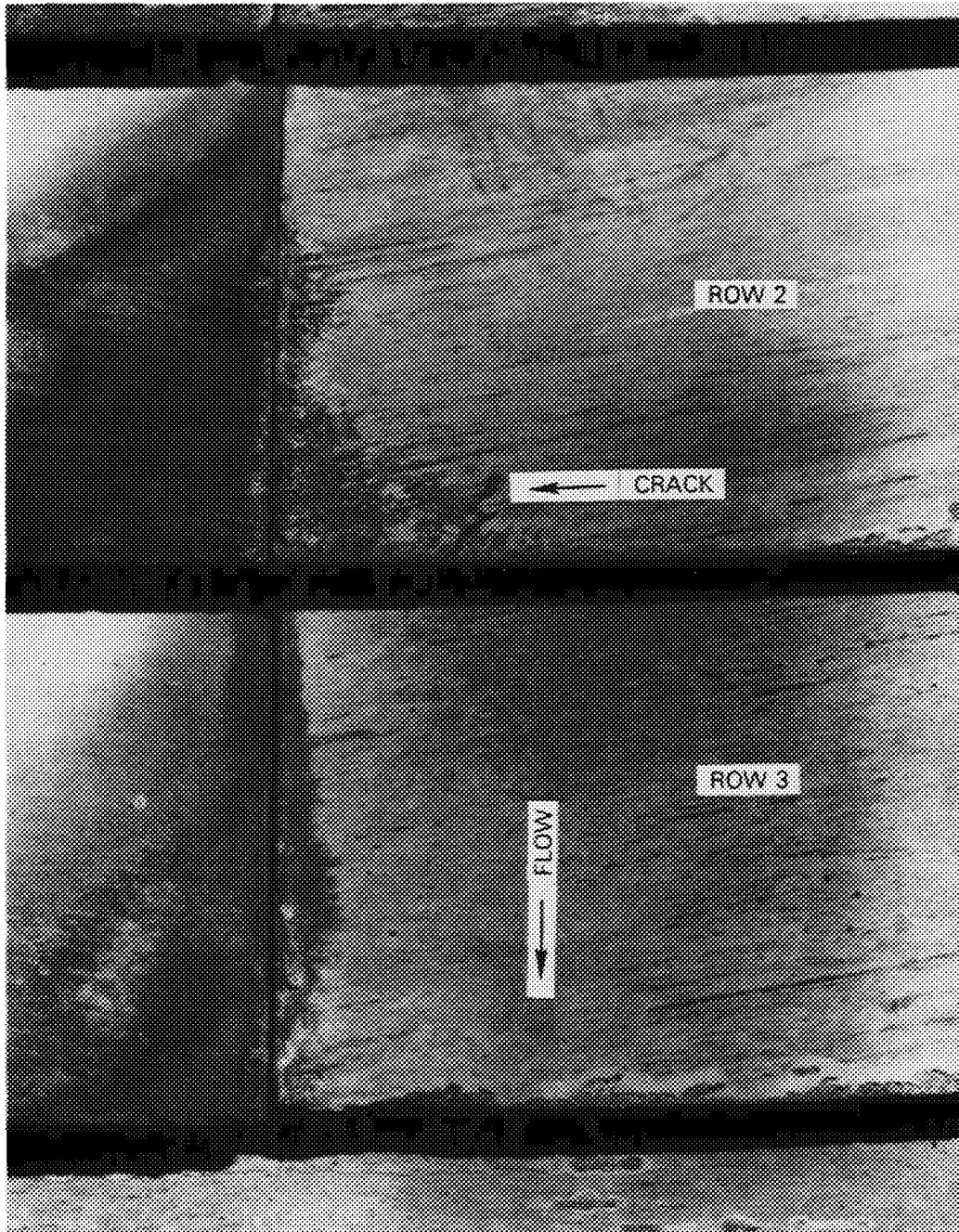


Figure 5-32 Condition of Composite Ceramic Liner Panels Before and After Combustor Rig Testing

ORIGINAL PAGE IS
OF POOR QUALITY



ORIGINAL PAGE
BLACK AND WHITE PHOTOGRAPH

Figure 5-33 Post-Test View of Row 2 and 3 Panels Showing the Through Thickness Crack in the Corner of the Row 2 Panel

Small cracks were also detected at ten of the fifty-four attachment holes in the liner panels. However, six of these ten holes were concentrated in the panels of Row 5. There are two possible explanations for the higher incidence of cracking in this row:

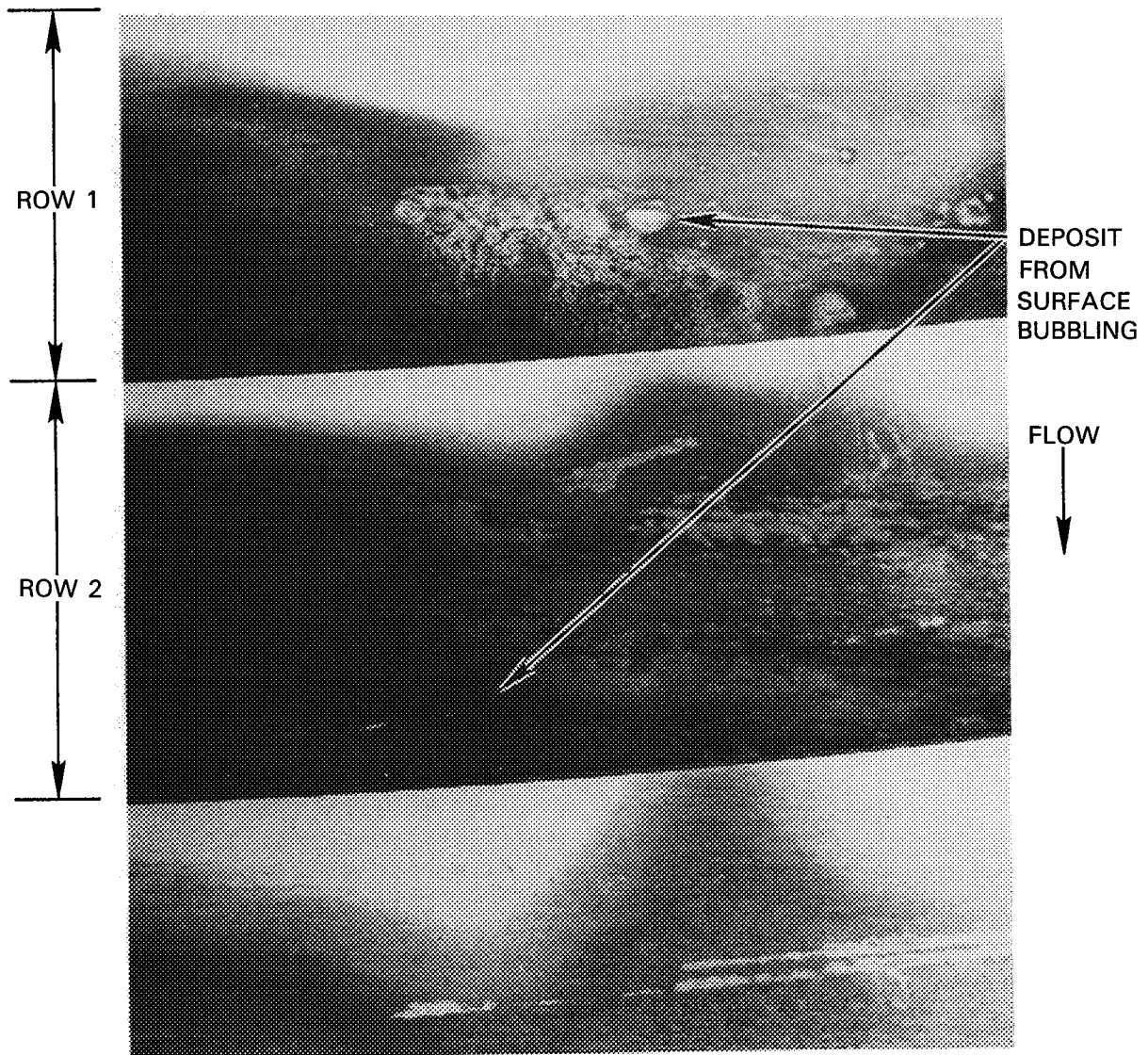
- 1) The attachment holes were located closer to the upstream edge of the panels in this row and in Row 4 than they were in other rows. While there were no cracks around the attachment holes in Row 4, the panels in that row were also constrained by a ring.
- 2) It is suspected that the attachment bolts on Row 5 may have been tightened more than in other rows because impressions from the bolt heads were more evident on the surface of these panels than on any of the others.

The edges of the panels were inspected carefully for separation of the plies or delamination. Prior to the test one small area of delamination was detected on the end of the right panel of Row 6. This was caused either by incomplete consolidation during fabrication or by tearing during the grinding of the end of the panel to achieve the proper fit to the adjacent panel during the trial assembly of the liner. After test, delamination was observed at five more locations. As shown on Figure 5-32 these included the four ends of the Row 1 panels and an end of a Row 2 panel. While the cause is not certain, it is suspected that this delamination may also be associated with the end grinding operation during the fitting of the panels to the shell. The fitting was started at the front end of the combustor and the machinist had the least experience with grinding the ceramic composite material when trimming these edges.

Another form of visible distress on the panels consisted of the formation of a bubbly light colored deposit on the hot surface of the left side panels of Rows 1 and 2. These formations are shown in Figure 5-34 and occurred in regions where the thermal paint had been completely oxidized indicating a surface temperature in excess of 1091°C (2000°F). This same deposit formation had been encountered during the long duration thermal exposure tests conducted during the materials characterization task discussed in Appendix B and was caused by outgassing from the surface of the SIC-LAS material. During those tests, which were conducted at atmospheric pressure in a nonreacting environment, the threshold of this process with materials having the LAS III matrix occurred at about 1200°C (2200°F).

The only other usual condition observed during the inspection of the composite liner panels was the previously mentioned deposits on the downstream lip of the last row of panels in the liner, i.e., Row 7. The deposits were more pronounced on the cold side of the panels and were caused by mineral deposition from water that was sprayed into the exhaust chamber of the test facility to quench the combustor gases.

ORIGINAL PAGE IS
OF POOR QUALITY



ORIGINAL PAGE
BLACK AND WHITE PHOTOGRAPH

Figure 5-34 Surface Bubbling on the Hot Side of Row 1 and 2 Panels

5.3.2 Destructive Testing

Following the completion of all inspections several of the liner panels were selected for additional examination by cutting parts of them into strips that could be tested for residual strength. Figure 5-35 shows the series of test specimens that were cut from each of four composite liner panels. One of the panels was the left side panel of Row 4 in the combustor rig while another was a spare Row 4 panel of identical geometry that had not been used in the combustor rig. This panel served as a reference for the strength of material that had not been exposed to high temperatures in the combustor rig. The other two panels were from Row 6 of the rig combustor liner and differed in that one was made with the LAS II rather than the LAS III matrix material used in the remainder of the panels.

The test specimens were cut to nominal dimensions of 6.35 mm (0.25 inches) by 38.1 mm (1.50 inches) long and were tested to failure in a three point flexure mode. The spacing between supports was 31.8 mm (1.25 inches) and the specimen was positioned convex side up with the load applied at midspan. The stresses shown on Figure 5-34 are those computed in the tensile surface of the specimen on the basis of a simple flat beam at the failure load.

Comparison of the residual strength of the specimens from the spare and the combustor rig tested Row 4 panels indicates that the exposure of the material to elevated temperature caused a reduction of more than 50 percent in the strength of the ceramic composite material. Likewise, specimens from the Row 6 center panel, fabricated from the same LAS III matrix shows comparably low residual strengths relative to those from the unexposed Row 4 panel. The loss in residual strength does not appear to correlate with the temperature level experienced by the specimen. Specimens were cut from the Row 6 center panel at positions far upstream between the attachment bolt holes where the panel had experienced temperatures less than 648°C (1200°F) and the reduction in strength is still substantial. In addition, comparison of the residual strength data from the left and central panel of Row 6, fabricated from the LAS II and LAS III matrix material respectively, indicates that the residual strength of the specimens having the LAS II matrix are comparable to or even slightly lower than those with the LAS III matrix. Since the data of Reference 1 and Appendix B indicated that composites made with the LAS II and the LAS III matrix had comparable room temperature ultimate strengths in the as-fabricated state, it is evident that the thermal exposure in the combustor rig had a similar adverse effect on the residual strength of the material made with LAS II matrix.

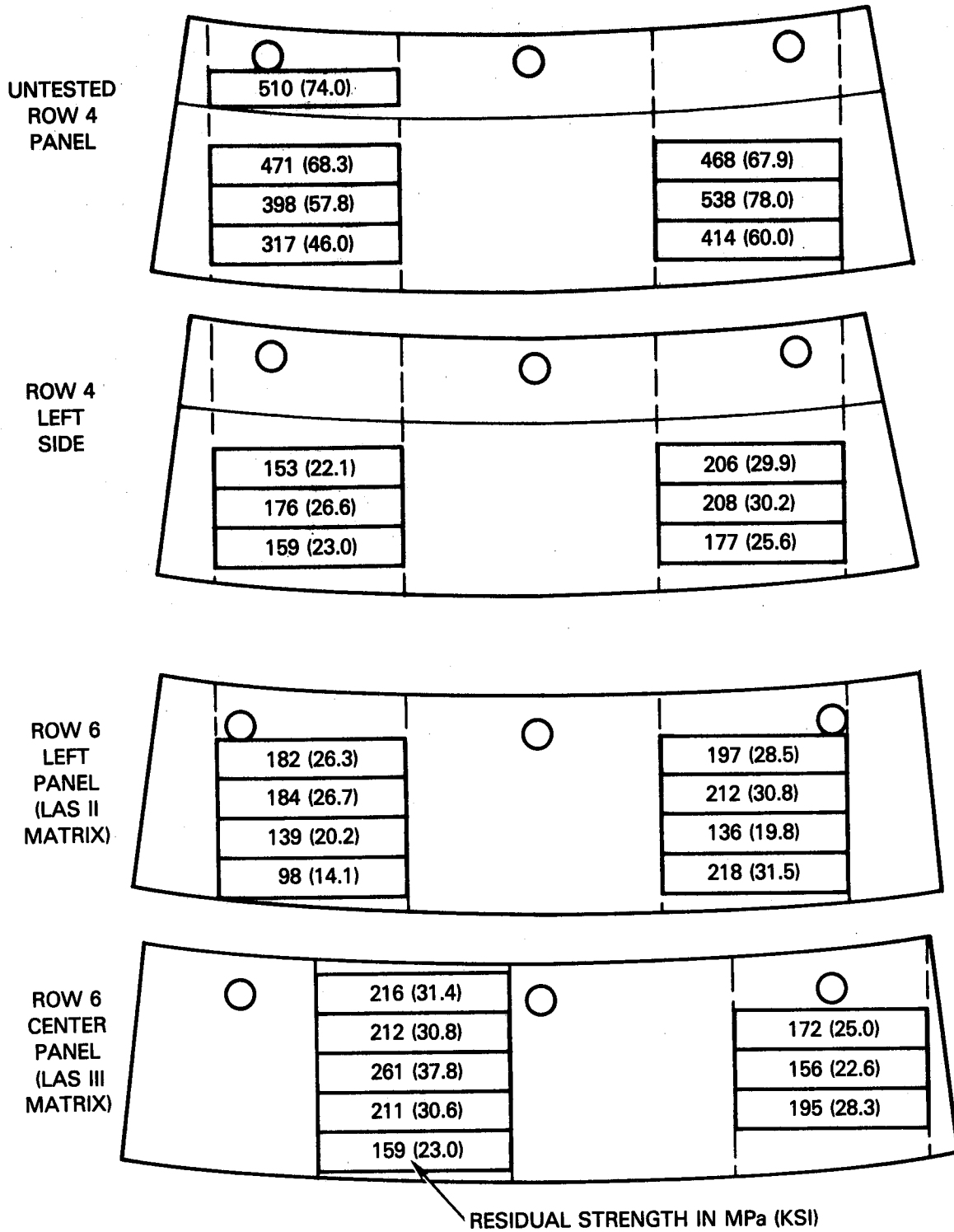


Figure 5-35 Residual Strength of Specimens from Ceramic Composite Liner Panels

The reduction in residual strength of the material with exposure to elevated temperature may be attributed to changes in the nature of the bond between the silicon carbide fibers and the lithium aluminosilicate matrix. With a potentially brittle matrix such as LAS the optimum reinforcement is achieved when the fiber-matrix bond is only moderate and the fiber has some opportunity for local elongation relative to the matrix. The strain absorbed by the relative motion of the fiber provides the toughness that is characteristic of fiber reinforced ceramic materials. However, reactions can occur at the fiber matrix interface that lead to strong bonding and the loss of capability for relative motion. This results in embrittlement of the composite with local failure being more brittle as is characteristic of the ceramic matrix material itself. The presence of embrittlement can be detected in the morphology of the fracture surface of the residual strength test specimens. Figure 5-36 shows fracture surfaces of test specimens from both the spare Row 4 panel and that run in the combustor rig. Both specimens show regions across the depth of the specimens where there was extensive fiber retention and pullout which is representative of failure of a normal composite. However, near the hot and cold surface of the specimen from the rig tested panel the fracture surface is abrupt with the fibers having broken at the plane of the fracture. These regions are representative of embrittlement.

Examination of all of the residual strength test specimens from panels that were in the combustor rig indicated the embrittlement extended 0.2 to 0.3 mm (0.008 to 0.012 inches) into the material from both the hot and cold sides. With about half the net thickness of the specimen, including the more highly loaded surface regions embrittled it is not surprising that the test specimen revealed such a large decline in residual strength when subjected to flexural loading.

Prior laboratory scale experiments, including those reported in Appendix B have demonstrated this form of embrittlement at moderate temperature levels of 649°C (1200°F), but the surprising aspect of the current results is the depth to which the embrittlement penetrated in a relatively short period of thermal exposure. The reason for the higher than anticipated fiber-matrix bond interaction is uncertain but it could have been caused by the elevated pressure (1.73 MPa or 250 psia) at which the combustor rig test was run whereas the prior laboratory scale testing was all conducted at atmospheric pressure.

Another fiber-matrix bond deterioration mechanism that was evident in some of the residual strength specimens also produced embrittlement but by a different process. Examination of the fibers from failed residual strength test specimens that were cut from near the edges of liner panels indicated a bluish surface color rather than the characteristic black. This is caused by oxidation of carbon along the fiber surface that ultimately destroys the fiber-matrix bond and eliminates reinforcement. This phenomena has been studied extensively at United Technologies Research Center (Reference 9) and has been found to be caused by oxygen from the environment permeating gaps in

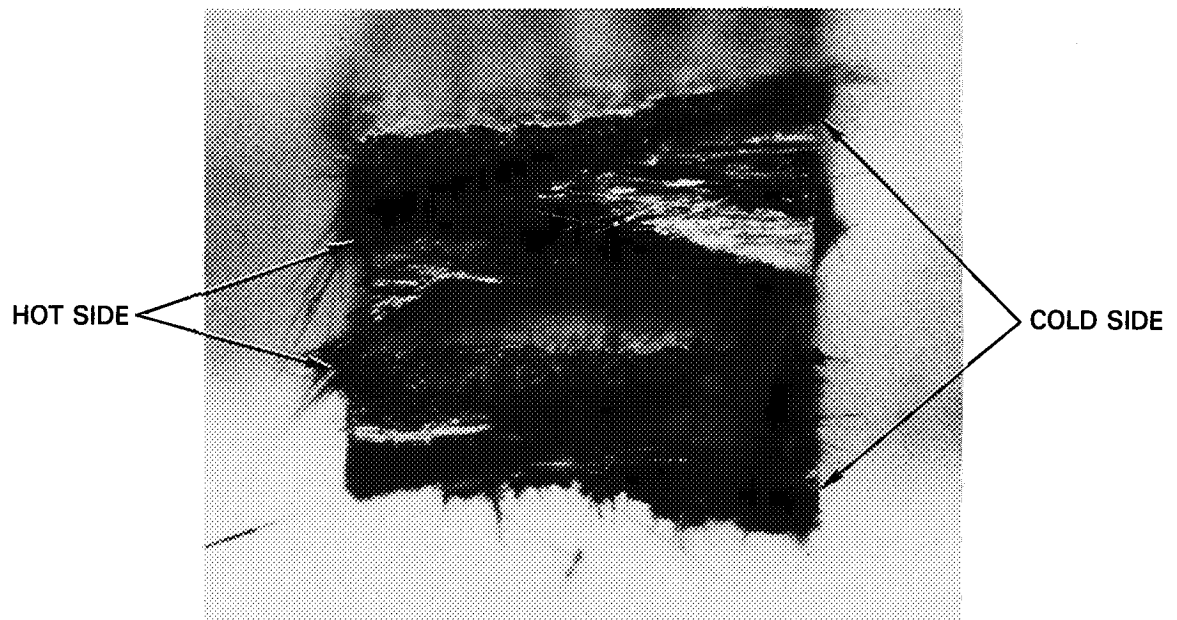
the fiber-matrix juncture from the edges of the panel and oxidizing the carbon at the interface. The destruction of the fiber-matrix bond progresses inward with time as the gap left by the oxidized carbon provides a conduit for further permeation of the oxygen along the fiber. The extent of this mode of deterioration is difficult to determine but it appears in the current combustor rig test. However, it was restricted to regions near the edges of the panel and did not contribute substantially to the deterioration in strength of the liner panels.

Despite the deterioration in their ultimate strength, because of surface embrittlement, the SIC-LAS ceramic composite combustor liner panels did retain the overall resilience typical of a composite material. Relative to the predicted tensile stresses in the liner panels of Figure 5-32, the residual strength of the panel materials remained respectively high after thermal exposure in the combustor rig and they probably had adequate margin for much more sustained operation at these temperature levels.

ORIGINAL PAGE IS
OF POOR QUALITY

ORIGINAL PAGE
BLACK AND WHITE PHOTOGRAPH

UNHEATED CONTROL SPECIMEN



SPECIMEN FROM PANEL USED IN COMBUSTOR RIG

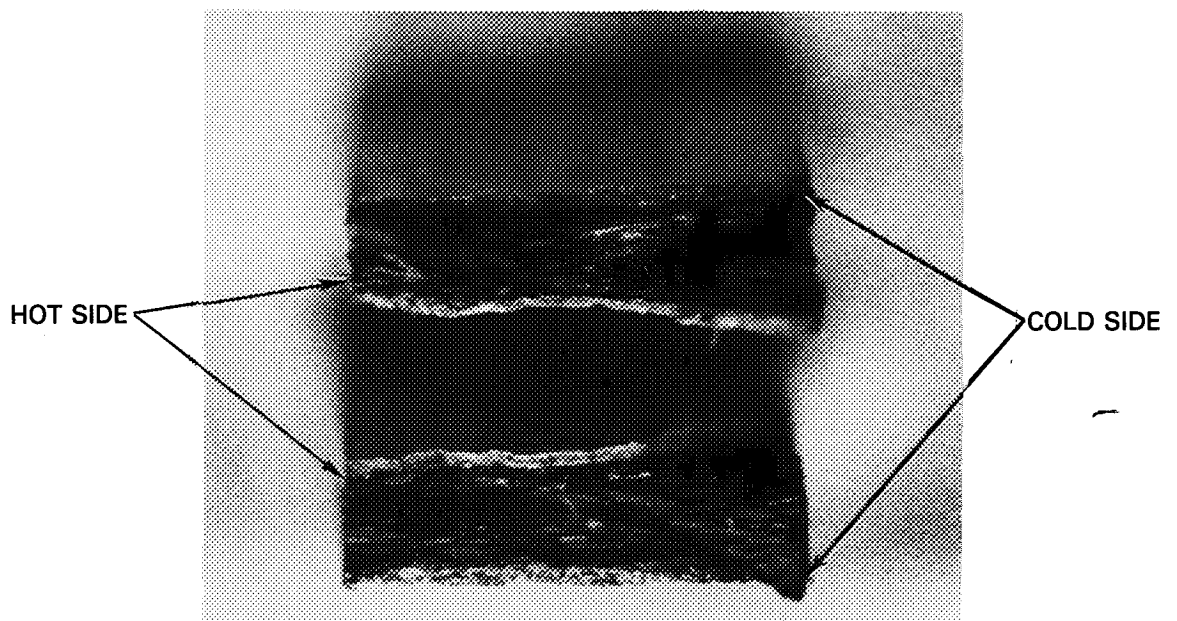


Figure 5-36 Fracture Morphology of Residual Strength Specimens from Ceramic Composite Liner Panels

SECTION 6.0 CONCLUDING REMARKS

The Energy Efficient Engine Combustor Sector Rig has provided a very valuable platform for the evolution of the segmented liner concept. Building on the successful characteristics of the first generation CPFW liner, design features for a second generation of reduced weight, lower cost, and improved performance segmented liner were identified. These design features, which were a natural extension to the successful CPFW liner, were substantiated through representative high pressure and temperature testing in a combusting environment.

The results of the ceramic composite liner test in the combustor sector rig demonstrated that, on the basis of thermal paint color changes which indicate local temperature, the temperature distributions and through thickness temperature gradients in the silicon carbide reinforced lithium aluminosilicate ceramic composite liner panels were qualitatively consistent with thermal analyses conducted during their design. The combustor rig tests demonstrated that no large scale damage or distress was incurred by the panels during more than 18 hours at high temperature exposure including 10 hours at simulated takeoff operation of the Energy Efficient Engine. The two pre-existing cracks in the liner panels did not propagate further and the few new cracks formed during the thermal exposure only penetrated through a few of the eight plies of fibers in the panels. Local delamination of the plies was observed at the edge of a few panels and is attributed to improper grinding procedures used in fitting these panels to the shell. This problem was alleviated with experience leading to a proper grinding technique. Flexural testing of specimens cut from some of the liner panels indicated that the material had lost about 50 percent of its strength as a result of the thermal exposure in the sector combustor rig. This was found attributable to embrittlement of the material near the panel surfaces. While this process was anticipated in local regions where the temperature exceeded 981°C (1800°F) it was found to occur on surfaces of the panels that had experienced much more moderate temperatures. While this result implies that the silicon carbide, lithium aluminosilicate system must be further refined to achieve acceptable long term combustor life the overall success of Run 26 of the sector combustor rig demonstrated the strong potential of ceramic composite materials for combustor liner applications.

As engine pressure ratios increase with demand for higher efficiency cycles, the radiant portion of the total heat flux to the combustor liner increases substantially. The ability to test the sector rig at elevated pressure and temperature levels, provided a vehicle to supplement the meager radiation heat flux database available. As a complement to radiation measurements, more accurate and effective ways to measure liner wall temperatures were explored in a realistic combustion environment.

Closure with the Annular Component Program was effected by the demonstration of main zone fuel injection modifications that substantially reduced inefficiency at part power conditions where fuel staging between the two zones takes place. The demonstrated reduction in Co and THC emissions were adequate to meet program emissions goals.

Overall, the "Pin Fin and Ceramic Composite Liner Combustor Sector Rig Test Program" has provided a firm basis for the design of advanced combustor liners. The technology evolved through these efforts is applicable to the next generation of gas turbine engine combustors. Furthermore, it has provided a significant step toward the design of light weight, highly durable, and cost effective combustor liners that meets the operating demands for commercial or military aircraft operating in the late 1980's to early 1990's.

APPENDIX A DATA ANALYSIS PROCEDURES

A.1 PERFORMANCE DATA

Measured and calculated combustor performance parameters are listed in Table A-I and defined below.

TABLE A-I
SUMMARY OF REPORTED COMBUSTOR PERFORMANCE PARAMETERS

<u>Parameter</u>	<u>Symbol</u>	<u>Units</u>	<u>Measured</u>	<u>Calculated</u>
Total Airflow	W_{a3}	kg/s	X	
Total Combustor Airflow	W_{ab}	kg/s		X
Pilot Fuel Flow	$W_{f \text{ pri}}$	kg/s	X	
Main Fuel Flow	$W_{f \text{ sec}}$	kg/s	X	
Total Fuel Flow	$W_{f \text{ tot}}$	kg/s	X	
Inlet Total Temperature	T_{t3}	K	X	
Inlet Total Pressure	P_{t3}	Pa	X	
Pattern Factor	PF	--		X
Inlet Air Humidity	H	gH ₂ O/kg air	X	
Fuel/Air Ratio f/a	--			X

Total Combustor Airflow

The total combustor airflow is calculated by subtracting the measured inner and outer turbine cooling air bleed flows and the estimated combustor liner sidewall cooling airflow from the total airflow.

Pattern Factor

The pattern factor at the combustor exit is defined by the expression:

$$\text{Pattern Factor} = \frac{T_{t4 \text{ max}} - T_{t4 \text{ avg}}}{T_{t4 \text{ avg}} - T_{t3}}$$

where: $T_{t4 \text{ max}}$ = Highest local temperature observed at the combustor exit plane

$T_{t4 \text{ avg}}$ = Average combustor exit temperature

T_{t3} = Combustor inlet temperature

Fuel/Air Ratio

The fuel/air ratio is the ratio of fuel flow to total combustor airflow. Fuel/air ratio is calculated from measured values of total fuel flow and airflow. The independent fuel/air ratios for the pilot and main zones are determined by dividing the total fuel/air ratio in proportion to the measured fuel flow rates of each combustion zone. Hence, the sum of the pilot and main zone fuel/air ratios equals the total fuel/air ratio.

A.2 EMISSION DATA

Fuel/Air Ratio Calculations

Fuel/air ratios are reported on the basis of measured fuel and airflows (performance basis). In analyzing the data, emission indices are calculated using the local carbon-balance fuel/air ratios, and correlations are then made using overall average fuel/air ratios calculated on the performance basis.

Combustion Efficiency

Combustion efficiency is calculated on a deficit basis using the measured concentrations of carbon monoxide and total unburned hydrocarbons from the gas sample data. The calculation is based on the assumption that the total concentration of unburned hydrocarbons could be assigned the heating value of methane (CH_4). The equation is:

$$\eta_c = 100 - 100 \left(\frac{4343x + 21500y}{18.4 (10)^6} \right)$$

where: x = Measured carbon monoxide concentration is g/kg fuel

y = Measured total unburned hydrocarbon concentration in g/kg fuel

Extrapolation of Rig Data to Engine Conditions

Since the sector combustor rig is unable to simulate the combustor inlet pressure at conditions above approach, the emissions data for oxides of nitrogen, carbon monoxide, and total unburned hydrocarbons obtained at the rig test conditions required correction to the engine conditions. The correlations used are described in the following paragraphs.

Correlation for Oxides of Nitrogen

Oxides of nitrogen are reported as equivalent NO₂.

The correlation used to scale oxides of nitrogen values to engine pressure levels and to correct the values for small differences between the actual rig conditions and the desired engine conditions is as follows:

$$\text{NO}_x \text{ corr.} = \text{NO}_x \text{ meas.} \left[\left(\frac{P_{t3 \text{ corr.}}}{P_{t3 \text{ meas.}}} \right)^{0.5} \left(\frac{V_{\text{ref. meas.}}}{V_{\text{ref. corr.}}} \right) T_{t4 \text{ meas.}} \right. \\ \left. e^{18.8 (H_{\text{meas.}} - H_{\text{corr.}})} e^{\left(\frac{T_{t3 \text{ corr.}} - T_{t3 \text{ meas.}}}{288} \right)} \right]$$

where NO_x = Emission index of oxides of nitrogen

P_{t3} = Inlet total pressure (atm)

T_{t3} = Inlet total temperature (°K)

V_{ref} = Reference velocity (m/s)

H = Inlet specific humidity (gH₂O/kg air)

and subscripts:

corr. = Relates to value at corrected condition

meas. = Relates to value at measured condition

Correlations for Carbon Monoxide and Total Unburned Hydrocarbons

Total unburned hydrocarbons are reported as equivalent CH₄.

Emission indices for carbon monoxide and total unburned hydrocarbons are scaled to engine pressure levels by scaling inversely to inlet pressure.

Calculation of EPAP Values

Values for the Environmental Protection Agency Parameter (EPAP) are calculated on the basis of the emission indices extrapolated to engine conditions. The parameter is defined as follows:

$$EPAP = \frac{\sum_{i=1}^4 EI_i W_{fi} TIM_i}{\sum_{i=1}^4 F_{Ni} TIM_i}$$

where: EI = Emissions index
W_f = Fuel flow rate
TIM = Time in mode
i = Mode index (idle, approach, climb, takeoff)
F_N = Net thrust

The mode indices and times in each mode are defined in Table A-II.

Since the fuel flow, time in mode, and net thrust for the Energy Efficient Engine are all known for each operating condition, the calculations for this program are simplified by defining coefficients combining these terms for each operating condition. These coefficients are defined as:

$$EPAP \text{ Coefficient}_c = \frac{W_{fc} TIM_c}{\sum_{i=1}^4 F_{Ni} TIM_i}$$

where c denotes the operating condition for the particular coefficient. The resulting values for the coefficients are presented in Table A-II. With these coefficients, EPAP values could be calculated by multiplying the emission indices for each operating condition by the appropriate coefficient and summing.

TABLE A-II
DEFINITION OF EPAP CONDITIONS
AND EPAP COEFFICIENTS FOR ENERGY EFFICIENT ENGINE

<u>Index Number</u>	<u>Operating Condition</u>	<u>Time in Mode (Minutes)</u>	<u>EPAP Coefficient (lb/hr/lb)</u>
1	Idle	26.0	0.1156 (Unbled)
2	Approach	4.0	0.060
3	Climb	2.2	0.1025
4	Take-Off	0.7	0.0397

APPENDIX B CERAMIC COMPOSITE MATERIAL CHARACTERIZATION

B.1 INTRODUCTION

Because of the rapid advances being made in the field of ceramic composite materials, several new material and construction approaches had been developed since the NASA/P&W Advanced Composite Combustor Structural Concepts Program (Reference B-1) was completed. The material characterization activity was included in the current program to provide for assessment of these new approaches as possible candidates for construction of the segment rig combustor liner panels. The three approaches investigated were described in Section 3.2.3, and the details of the fiber lay-up were shown in Figures 3-24 and 3-25 of that section. The first candidate material had a lithium aluminosilicate matrix designated LAS II with eight layers of silicon carbide fibers laid-up with a (0/+45/90/-45) orientation. The second material was of the same fiber construction as the first, but the matrix material was of a slightly different composition and was designated LAS III. The third material had LAS III matrix material, but the fiber construction was a 12 harness satin weave. Each fiber in the 12 harness satin weave was retained by every 12th fiber, instead of every other fiber as in a conventional weave.

Evaluation of the three candidate materials consisted of definition of mechanical properties and small-scale rig testing to assess thermal integrity. The mechanical tests were flexural bend tests to determine ultimate strength, stress-strain characteristics, and creep and fatigue properties. Two rigs were used for the thermal integrity evaluation. One rig tested the low cycle thermal fatigue resistance of the material, and the other tested the ability of the material to withstand steady state high temperature exposure in conditions approximating those found in a combustor environment. Because the experimental phase of the effort under the NASA/P&W Advanced Composite Combustor Structural Concepts Program had already addressed the mechanical properties of a SiC-LAS II composite having a fiber lay-up only slightly different from that of the first candidate material in the current program, the assessment of that material under the current effort was restricted to those aspects not investigated sufficiently in the prior program.

All of the specimens used in the experimental investigation were fabricated at the United Technologies Research Center (UTRC), and the majority of the tests were also conducted at that facility. The individual specimens were cut to the required size from panels that had been pressed to nominal dimensions of 7.6 cm (3.0 in) or 10.2 cm (4.0 in) square. The panels had nominal thicknesses of 1.15 mm (0.045 in) or 2.3 to 3.1 mm (0.09 to 0.12 in), depending on their intended use. The thin panels were constructed with eight layers of fibers as shown in Figure 3-25 and were used exclusively in the thermal evaluation tests. The thicker panels were made with 16 layers of fibers, and those with the laid-up construction had a sequence of layer directions of 0/+45/90/-45/0/+45/90/-45 on either side of the plane of symmetry. Each panel was identified by a four-digit serial number, and an individual specimen cut from that panel was assigned the panel serial number followed by a dash and a fifth digit (e.g., 2926-4).

B.2 STATIC LOAD CHARACTERISTICS

The static load bearing capability of specimens of the woven and the laid-up SiC-LAS III material were determined by tests in a beam flexure test facility, shown in Figure B-1. With all ceramic test fixtures, this system is capable of operating in air up to temperatures of approximately 1204°C (2200°F). The loading rams and specimen holders are made of siliconized silicon-carbide while the actual loading pins are alumina. The specimens were 7.6 cm (3.0 in) long and had a rectangular cross section of 2.3 to 3.1 by 10.0 mm (0.09 to 0.12 by 0.40 in) with the plane of the fibers parallel to the 10.0 mm dimension. The tests were conducted in a four-point flexural mode as shown in Figure B-2 with the major and minor spans being 6.35 and 1.91 cm (2.50 and 0.75 in), respectively, and the load being applied normal to the plane of the fibers. All of the tests were conducted in an air environment.

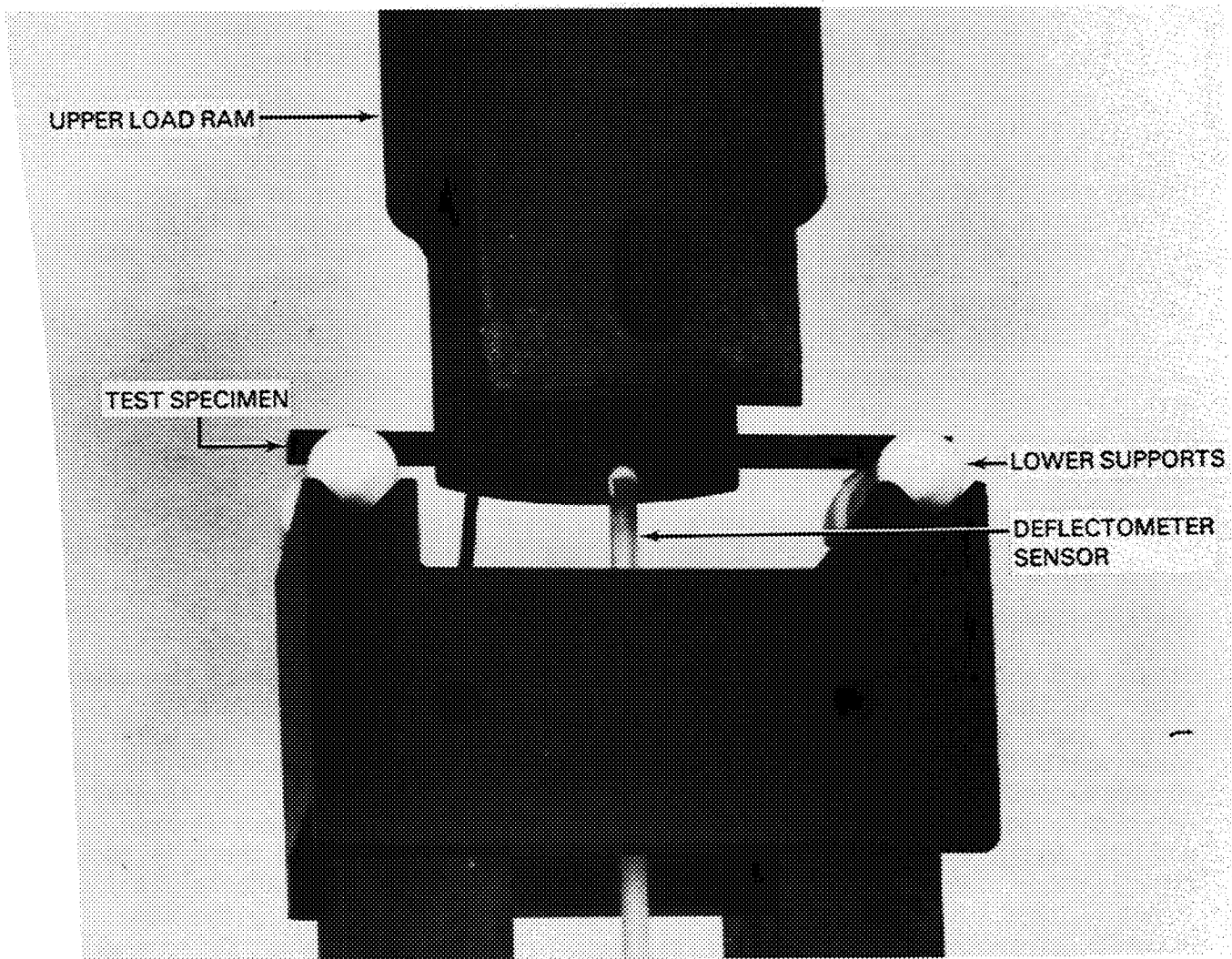


Figure B-1 High Temperature Flexural Test Facility

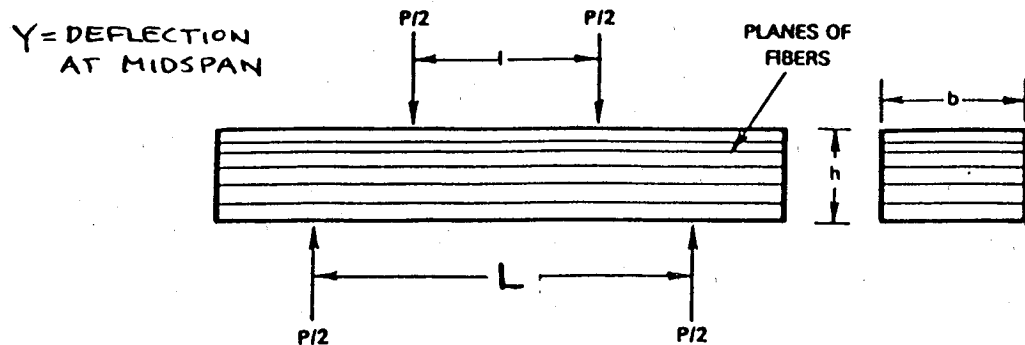


Figure B-2 Four Point Flexural Test Geometry

The initial tests were conducted at room temperature, and the strain on the top and bottom surfaces of the specimens was measured with strain gages. During the elevated temperature tests, the midspan deflection of the specimen was measured with a remotely situated linear variable differential transformer (LVDT) that was in contact with the specimen through a ceramic extension rod, and the strain on the tensile surface of the specimen was deduced from Equation (B-1):

$$\text{Strain} = \frac{6hY}{(L - l)(L + 2l)} \quad (\text{B-1})$$

while the stress on the top and bottom surfaces of the test specimen at the midspan location was calculated from Equation (B-2):

$$\text{Stress} = \pm \frac{3}{2} \frac{(L - l) P}{bh^2} \quad (\text{B-2})$$

where the nomenclature is defined on Figure B-2.

Figure B-3 shows the stress-strain characteristics of one of each of the woven fiber and the layered fiber specimens evaluated at room temperature with strain gages on the tension and compression surfaces. As anticipated, both sides exhibit an almost identical strain history. Following an initial linear region extending to about 150 MPa (20 to 22 ksi) applied stress, the layered fiber material exhibits a slight decline in slope, or equivalently elastic modulus, until the ultimate strength is reached, at which point there is an occurrence of considerable strain. The 12 harness satin woven material is shown to have a slightly higher elastic modulus and approximately the same ultimate strength as the layered fiber material but a more abrupt failure with none of the ductile type characteristics exhibited by the layered material. Figure B-4 shows the fracture surfaces of layered and woven fiber specimens that were loaded to failure at room temperature. The extremely fibrous nature is evident in both surfaces and is not indicative of a brittle type of failure.

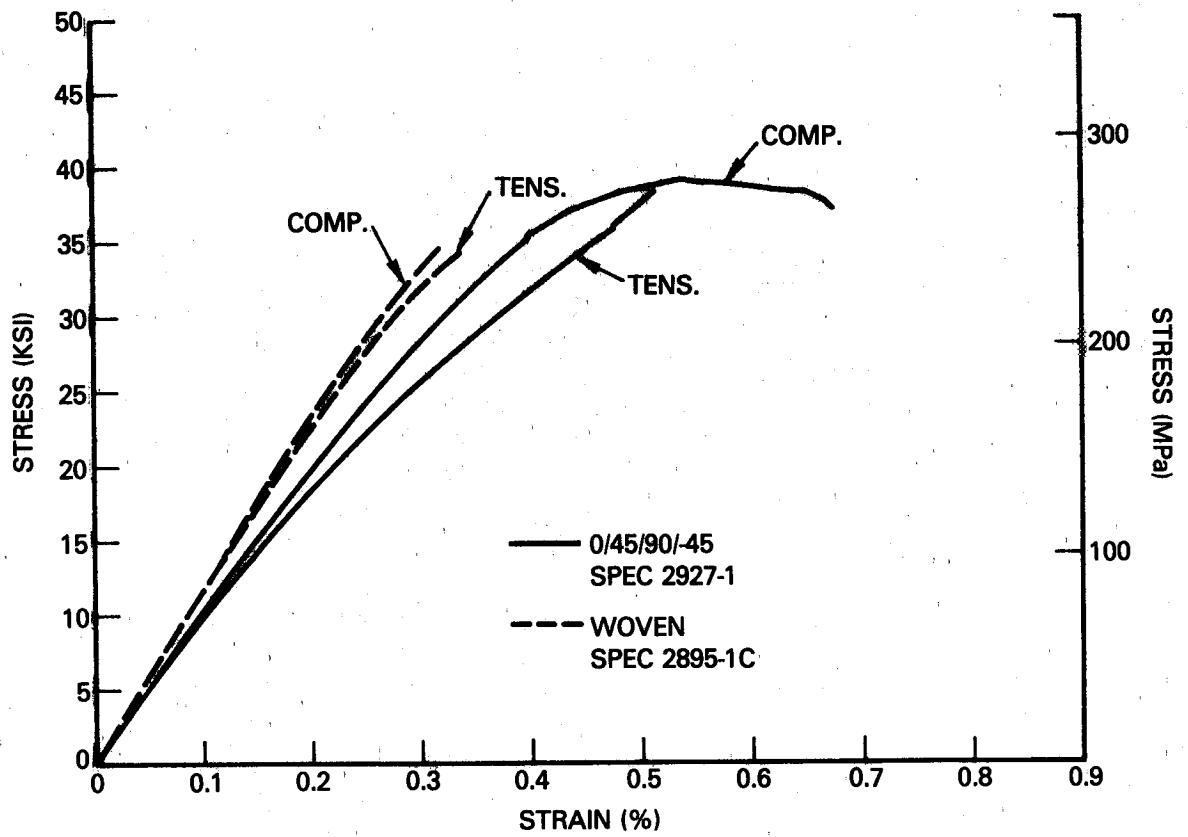


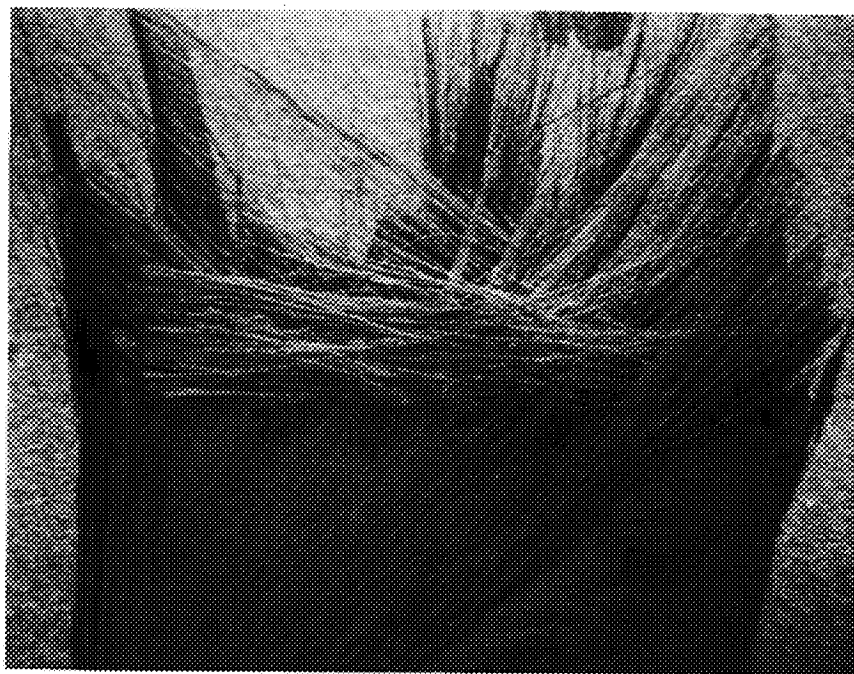
Figure B-3 Stress-Strain Behavior for SiC-LAS III Specimens at Room Temperature

ORIGINAL PAGE IS
OF POOR QUALITY



ORIGINAL PAGE
BLACK AND WHITE PHOTOGRAPH

12HS SiC-LAS III; Spec. 2894-1C



0/45/90/-45 SiC/LAS III; Spec 2927-1

Figure B-4 Fracture Surfaces of SiC-LAS III Specimens Failed in Flexure at Room Temperature

Table B-1 presents a summary of the static strength characteristics of all of the specimens evaluated at room temperature. The general trends of Figure B-3 are evident in the tabulated data in that the specimens with the 12 harness satin woven fiber construction had lower ultimate strength but higher elastic moduli than the multidirectional layered fiber specimens, but the latter had characteristically twice the strain level before specimen failure occurred. There also appears to be little difference in either the elastic moduli or the ultimate strength of the 12 harness satin woven specimens when they are cut with the surface fiber layers parallel to or transverse to the length of the specimen. Finally, comparison of the room temperature properties of the 0/+45/90/-45 lay-up SiC-LAS III specimens with those of the SiC-LAS II specimens having a slightly different (0/+45/-45/90) lay-up sequence in Reference B-1 indicates that the elastic moduli and ultimate strength are of similar magnitude.

Figure B-5 shows applied load versus midspan deflection curves for specimens with both fiber lay-ups over a range of elevated temperatures. In all cases, the specimen failed gradually with significant additional deflection, that is, strain, being absorbed before failure finally occurred. This characteristic is evidence of significant reinforcement of the otherwise brittle glass-like matrix at these temperature levels. Noting the difference in the deflection scales in Figure B-5, it is evident that the ability of the multidirectional layered fiber composite to absorb more strain before failure is also characteristic of its high temperature properties.

Figures B-6 and B-7 show the ultimate strengths of the SiC-LAS III specimens evaluated at both room and elevated temperature levels. The data indicate that the 12 harness satin woven fiber specimens of Figure B-6 retain their ultimate strength well to the 1038°C (1900°F) temperature level and even have a slightly higher mean strength at that temperature than at room temperature. While not evident at room temperature, there does appear to be some advantage to having the surface fibers parallel to the specimen axis, that is, orientation = 0° on Figure B-6, at the elevated temperatures.

The corresponding data from the multidirectional layered fiber composite of Figure B-7 indicate that, while this material had greater ultimate strength than the woven fiber material at room temperature, it experienced a decline in strength at high temperature. The net result is that the ultimate strengths of the composites with the two different fiber constructions are comparable at 200 to 250 MPa (30 to 35 ksi) at temperatures of the order of 1000°C (1832°F). Comparison with the corresponding data on the multidirectional layered fiber composite with an LAS II matrix in Figure B-8 indicates that, while both had about the same ultimate strength at room temperature and at 926°C (1700°F), the strength of the composite with the LAS III matrix declined rapidly with increasing temperature; whereas the composites with the LAS II matrix exhibit a trend of increasing ultimate strength at temperature levels up to 1100°C (2000°F).

TABLE B-1
 STATIC STRENGTH CHARACTERISTICS OF SIC-LAS III
 COMPOSITES AT ROOM TEMPERATURE

Composite Type	Specimen Number	Surface Fiber Orientation	Ultimate Strength, MPa (ksi)	Elastic Moduli Tensile Side GPa (Msi) Compr. Side GPa (Msi)	Average Failure Strain, %	Failure Mode *
12HS SIC-LAS III	2894-1C	0°	210 (30.5)	84.0 (12.2)	84.8 (12.3)	0.28 C, Fibrous
	2895-1C	0°	238 (34.5)	83.4 (12.1)	80.0 (11.6)	0.32 C, Fibrous
	2894-1T	90°	209 (30.4)	70.3 (10.2)	73.0 (10.6)	0.32 C/S, Fibrous
	2895-1T	90°	207 (30.0)	84.8 (12.3)	82.0 (11.9)	0.27 C/S/T, Fibrous
	2926-1	0°	365 (53)	62.7 (9.1)	62.7 (9.1)	0.74 C/T, Fibrous
	2927-1	0°	276 (40)	81.3 (11.8)	79.3 (11.5)	0.51 C, Fibrous
SIC-LAS III	2928-1	0°	220 (32)	59.3 (8.6)	57.2 (8.3)	0.54 C, Fibrous
	0/+45/90/-45					

* C = Compression Surface
 S = Shear
 T = Tensile Surface

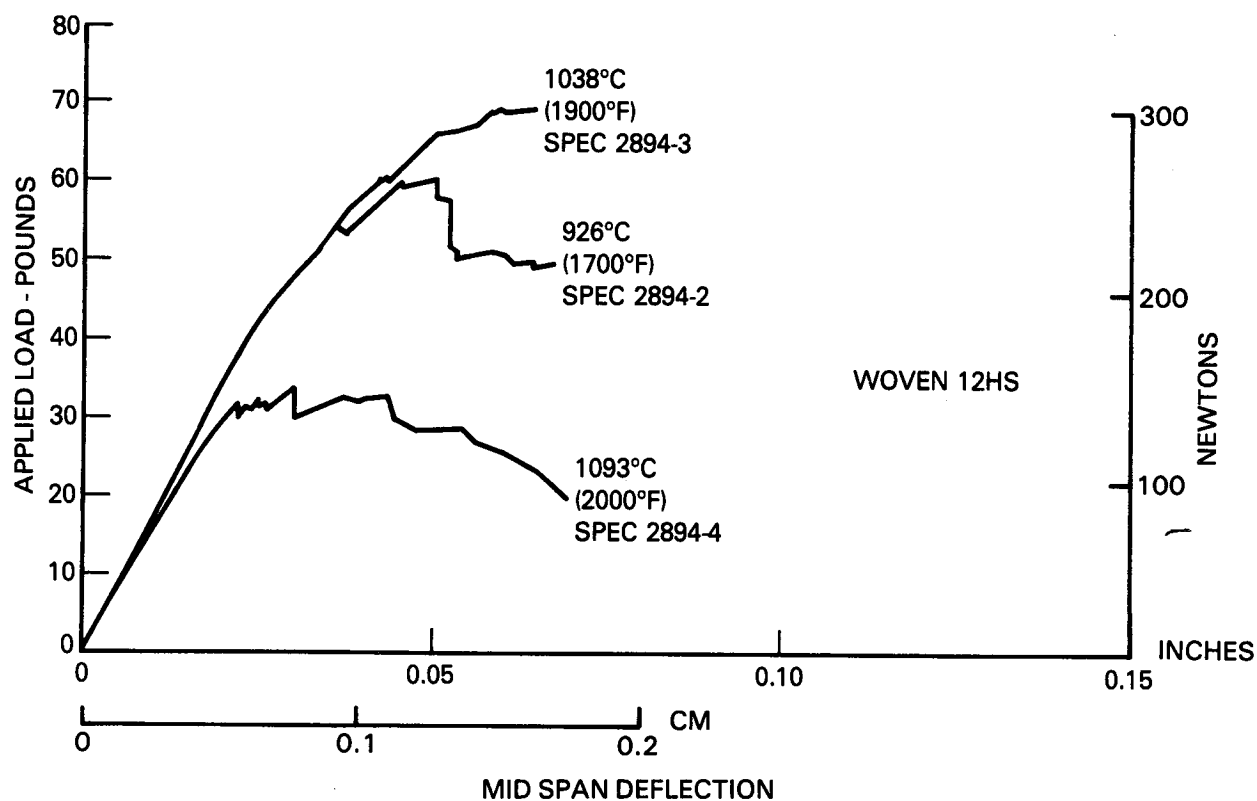
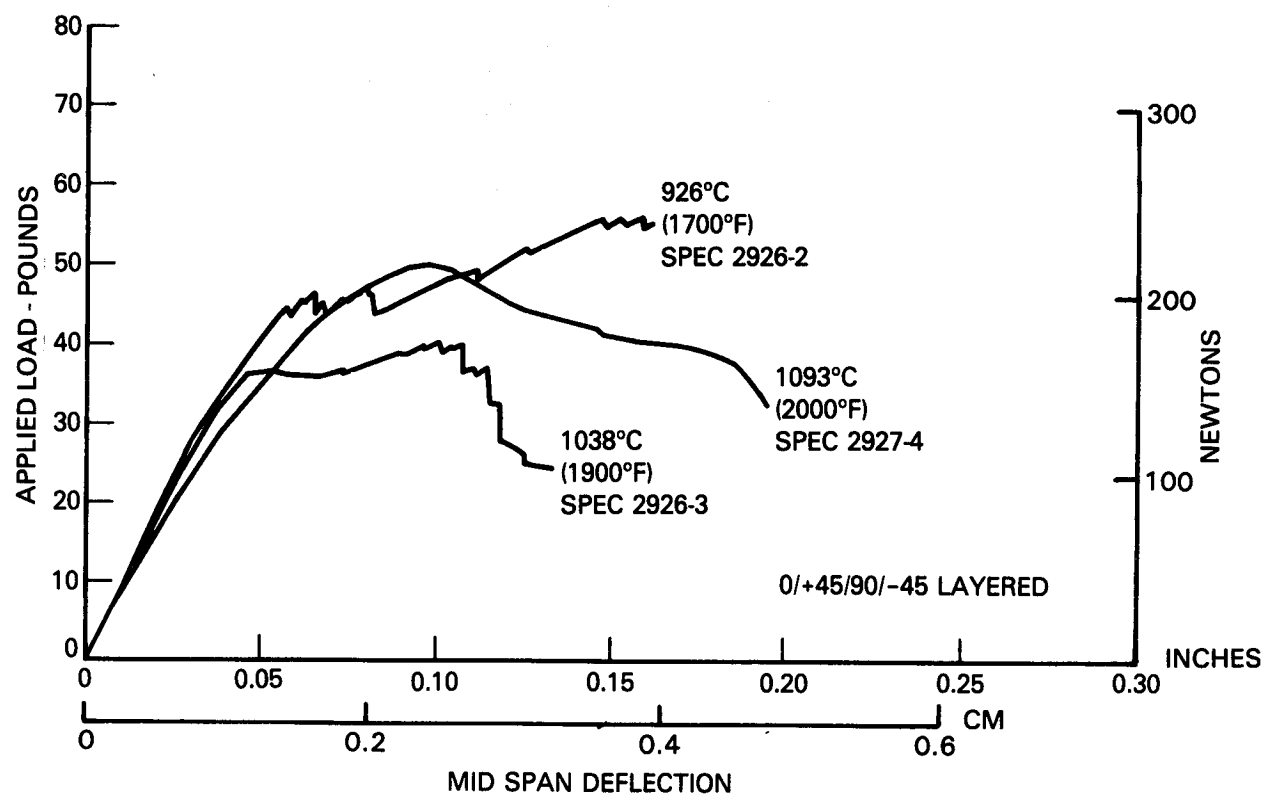


Figure B-5 Load-Deflection Characteristics of SiC-LAS III Composites at Elevated Temperatures

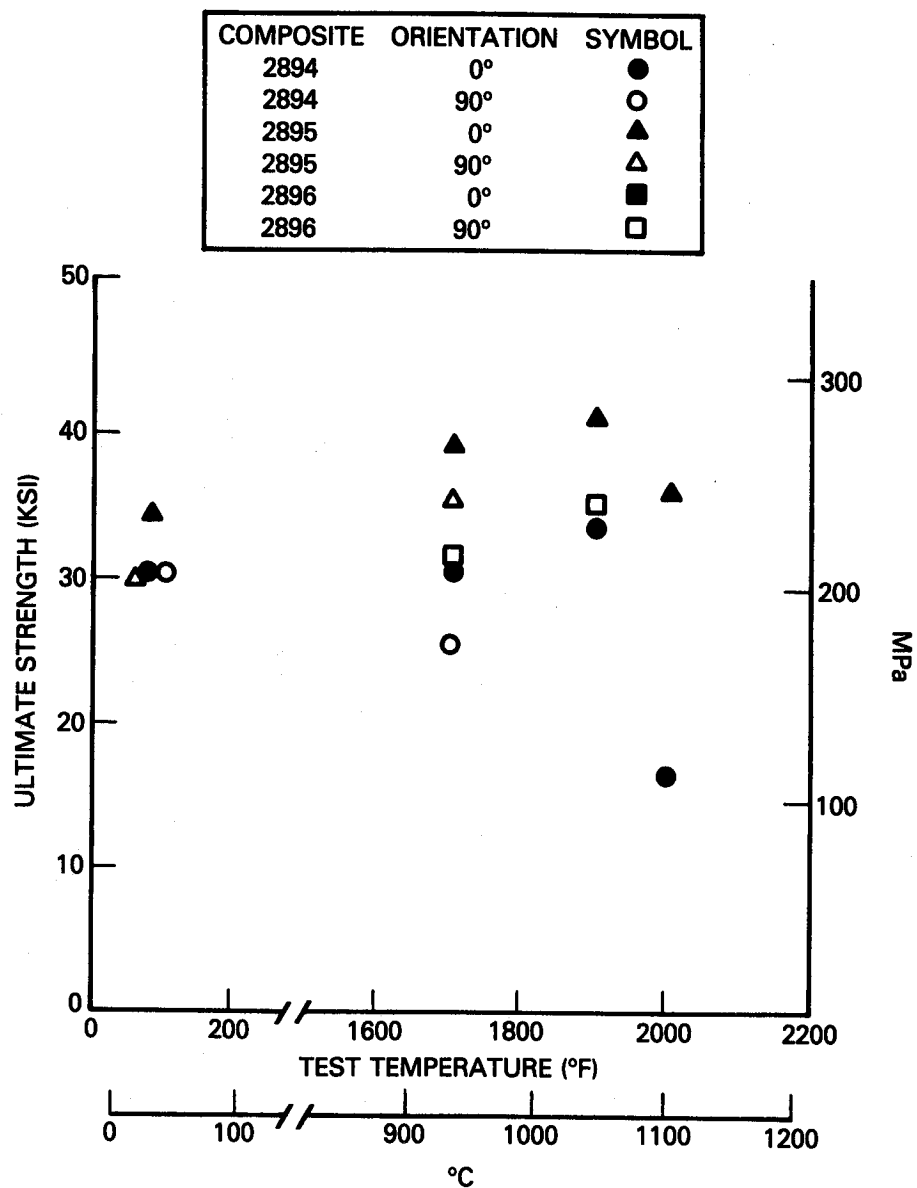


Figure B-6 Ultimate Strength of 12HS SiC-LAS III Composite in Air

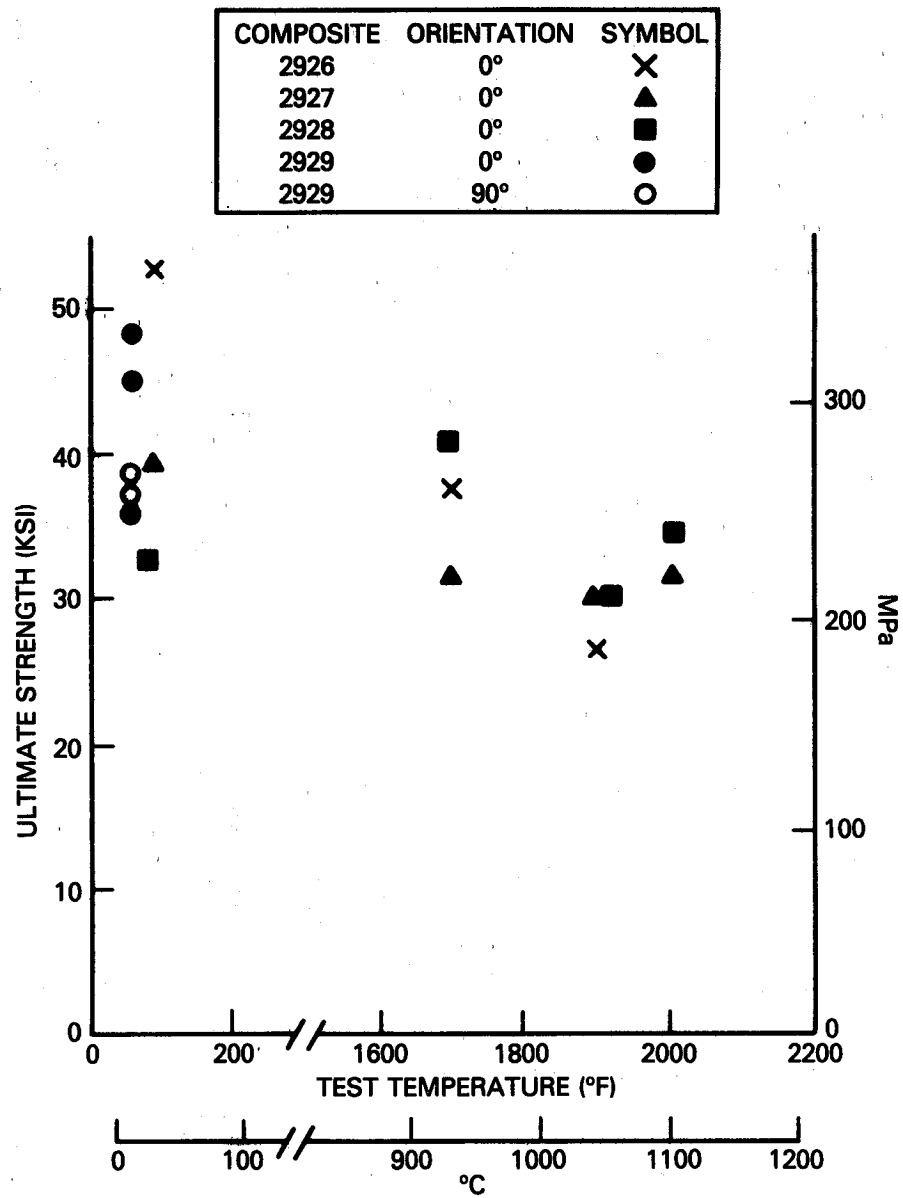


Figure B-7 Ultimate Strength of (0/+45/90/-45) SiC-LAS III Composite in Air

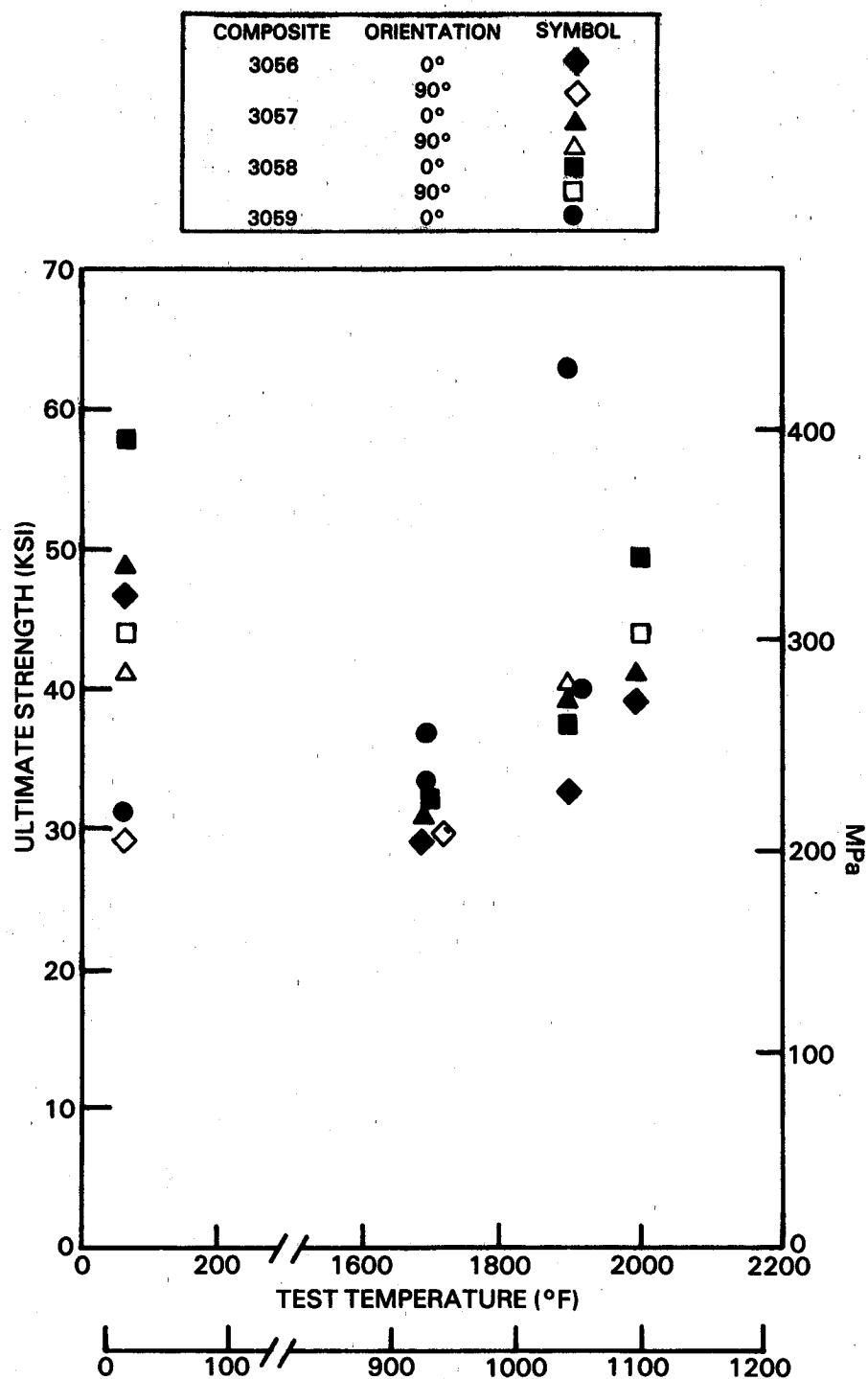


Figure B-8 Ultimate Strength of (0/+45/90/-45) SiC-LAS II Composite in Air

B.3 MECHANICAL FATIGUE TESTING

Cyclic mechanical fatigue tests were conducted in the same four-point flexure apparatus that was used for the static loading tests, described previously. The dimensions of the test specimens and the loading fixture were also maintained identical to those of the static tests. The tests were conducted in an air environment at temperatures of 926°C (1700°F) and 1038°C (1900°F), and specimens of all three material-fiber structure candidates were evaluated. During the fatigue tests, the load on the specimens was varied cyclically with a maximum-to-minimum load ratio of ten at a frequency of about 0.5 Hertz (Hz) for test durations up to 100,000 cycles. In each case, traces of the specimen load/midspan-deflection curve were recorded at initial loading and at intervals of 5, 1000, 10,000, and 100,000 cycles. These traces, and specimen dimensions, were used to calculate effective composite elastic moduli. Thus, the relative specimen stiffness could be tracked as a function of fatigue. If the specimen survived the 100,000-cycle duration of the test, it was statically loaded to failure to determine its residual strength. Table B-II presents a summary of the results of this sequence of tests and a graphical presentation of the results is shown in Figure B-9.

The results indicate that if the loading was restricted to 100 to 140 MPa (15 to 20 ksi) stress levels, which is about half the ultimate strength at static loaded conditions, many of the specimens survived the 100,000 cycle test duration. The probability of survival at this loading level appears to be a statistical parameter as opposed to a function of matrix composition or fiber lay-up. However, some sensitivities to material/construction parameters are evident. In the case of the multidirectional layered fiber composites with the LAS II matrix, the specimen exhibited a rapid drop in cyclic fatigue load-carrying capability followed by retention of strength for long durations thereafter. The same construction with the LAS III matrix exhibited a more gradual decline in fatigue strength with time. Neither of these materials exhibited much sensitivity to temperature levels, whereas the specimens made from the 12 harness satin woven fibers showed considerable differences. For this construction, the specimens tested at 1038°C (1900°F) demonstrated consistently higher fatigue strength than those evaluated at 926°C (1700°F).

The data of Table B-II also show a general trend of increasing stiffness, that is, elastic modulus, with increasing number of load cycles, regardless of the material structure or composition.

Measurements were made of the residual strength of the specimens that did not fail during the cyclic fatigue tests, and the results are also listed on Table B-II. Comparison with the corresponding data for nonfatigued specimens at the same temperature indicates that, while there was considerable spread in the range of ultimate strengths, specimens which were fatigue tested did not appear to experience any significant decline in ultimate strength. However, differences in the morphology of the fracture surface were evident following the determination of the residual strength of the run-out specimens. Figures B-10 and B-11 show the fracture surfaces of a woven fiber and a 0/+45/90/-45 layer fiber specimen after each was evaluated for residual strength following

100,000 fatigue cycles at 1038°C (1900°F). Comparison with similar fracture surfaces on specimens failed under static load at room temperature in Figure B-4 indicates that the surface is not as fibrous, that is, more of the fibers appear to have broken rather than pulled out of the adjacent matrix as they did in the low temperature test. Recalling that a 100,000 cycle fatigue test has a duration of about 50 hours, it is possible that the failure of the fibers themselves may have been caused by thermal exposure rather than by the mechanical fatigue process itself.

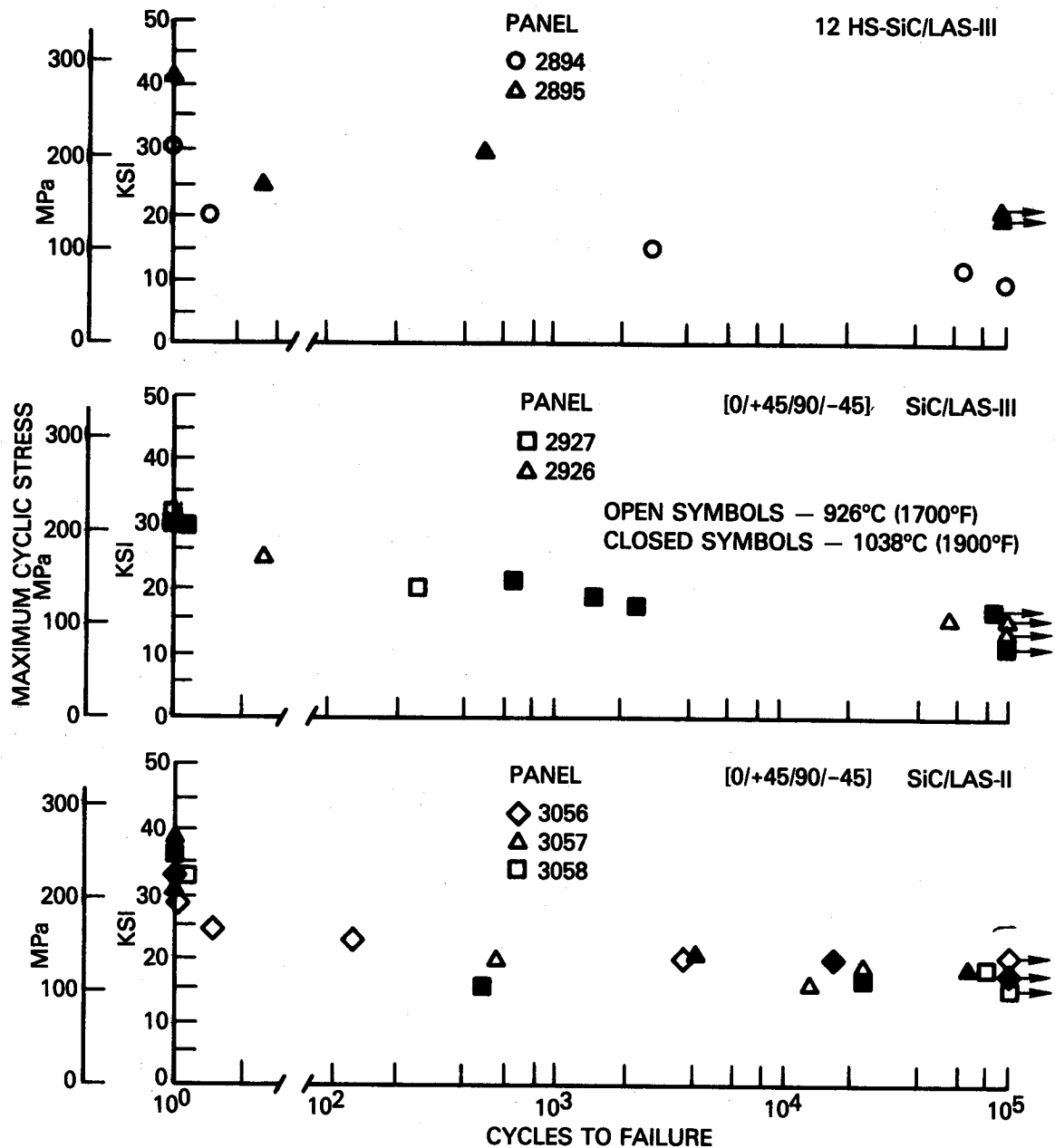


Figure B-9 Cyclic Fatigue Strength of SiC-LAS Composites in Air

TABLE B-II
RESULTS OF SiC-LAS SPECIMEN FATIGUE TESTS

Composite Type	Specimen Number	Test Temperature, °C (°F)		Stress at Maximum Loading, MPa (ksi)		Specimen Stiffness at Indicated Cycles										Cycles to Failure	Residual Strength, MPa (ksi)	
						1	5	1,000	10,000	100,000								
Woven 12HS SiC-LAS III	2894-5	926	(1700)	137.896	(20)	65.29 (9.47)	-	-	-	-	-	-	-	-	2	-	-	
	2894-6	926	(1700)	104.802	(15.2)	70.32 (10.2)	73.08 (10.6)	79.29 (11.5)	-	-	-	-	-	2,680	-	-		
	2894-7	926	(1700)	68.948	(10)	66.53 (9.65)	73.77 (10.5)	77.91 (11.3)	82.05 (11.9)	92.39 (13.5)	-	-	-	Run-Out	-	-		
	2894-8	926	(1700)	86.185	(12.5)	71.016 (10.3)	73.77 (10.7)	81.36 (11.8)	88.25 (12.8)	-	-	-	-	55,124	-	-		
	2895-5	1038	(1900)	137.896	(20)	75.15 (10.9)	74.46 (10.8)	83.43 (12.1)	85.50 (12.4)	75.15 (10.9)	-	-	-	99,300	262.0	(38)		
	2895-6	1038	(1900)	172.32	(25)	70.326 (10.2)	-	-	-	-	-	-	-	4	-	-		
	2895-7	1038	(1900)	206.844	(30)	65.64 (9.52)	65.57 (9.51)	-	-	-	-	-	-	512	-	-		
	2895-8	1038	(1900)	137.896	(20)	83.43 (12.1)	75.15 (10.9)	81.36 (11.8)	84.81 (12.3)	82.74 (12)	-	-	-	Run-Out	272.3	(39.5)		
(0/+45/90/-45) SiC-LAS III	2926-4	926	(1700)	172.37	(25)	66.12 (9.59)	-	-	-	-	-	-	-	4	-	-		
	2926-5	926	(1700)	119.969	(17.4)	66.95 (9.71)	68.121 (9.88)	70.33 (10.2)	73.08 (10.6)	-	-	-	-	55,686	-	-		
	2926-6	926	(1700)	96.527	(14)	61.64 (8.94)	61.23 (8.88)	66.74 (9.68)	68.47 (9.93)	70.33 (10.2)	-	-	-	Run-Out	253.73	(36.8)		
	2926-7	926	(1700)	117.211	(17)	63.63 (9.23)	62.60 (9.08)	68.19 (9.89)	68.19 (9.89)	66.40 (9.63)	-	-	-	Run-Out	239.25	(34.7)		
	2927-5	926	(1700)	137.86	(20)	56.8 (8.24)	54.33 (7.88)	-	-	-	-	-	-	258	-	-		
	2927-6	1038	(1900)	82.73	(12)	48.8 (7.08)	50.26 (7.29)	59.98 (8.7)	60.88 (8.83)	63.36 (9.19)	-	-	-	Run-Out	215.12	(31.2)		
	2927-7	1038	(1900)	117.211	(17)	49.71 (7.21)	49.23 (7.14)	54.81 (7.95)	57.5 (8.34)	55.43 (8.04)	-	-	-	Run-Out	208.22	(30.2)		
	2928-5	1038	(1900)	153.06	(22)	50.3 (7.3)	50.81 (7.37)	-	-	-	-	-	-	671	-	-		
	2928-6	1038	(1900)	134.448	(19.5)	56.12 (8.14)	52.68 (7.64)	59.50 (8.63)	-	-	-	-	-	1,689	-	-		
	2928-7	1038	(1900)	127.55	(18.5)	49.64 (7.2)	45.71 (6.63)	51.44 (7.46)	-	-	-	-	-	2,309	-	-		
(0/+45/90/-45) SiC-LAS II	3056-5	926	(1700)	124.106	(18)	58.67 (8.51)	57.36 (8.32)	66.05 (9.58)	67.43 (9.78)	62.67 (9.09)	-	-	-	Run-Out	212.36	(30.8)		
	3056-6	926	(1700)	165.4	(24)	56.74 (8.23)	-	-	-	-	-	-	-	2	-	-		
	3056-7	926	(1700)	151.68	(22)	59.502 (8.63)	56.19 (8.15)	-	-	-	-	-	-	125	-	-		
	3057-5	926	(1700)	137.896	(20)	67.43 (9.78)	64.12 (9.3)	-	-	-	-	-	-	538	-	-		
	3057-6	926	(1700)	124.106	(18)	67.63 (9.81)	63.71 (9.24)	72.4 (10.5)	73.77 (10.7)	-	-	-	-	23,534	-	-		
	3057-7	926	(1700)	117.211	(17)	63.71 (9.24)	62.95 (9.13)	72.4 (10.5)	73.77 (10.7)	-	-	-	-	13,259	-	-		
	3058-5	926	(1700)	117.211	(17)	63.43 (9.2)	68.19 (9.89)	78.6 (11.4)	82.74 (12)	74.46 (10.8)	-	-	-	Run-Out	177.89	(25.8)		
	3058-6	926	(1700)	131.0	(19)	69.64 (10.1)	66.88 (9.7)	75.15 (10.9)	-	-	-	-	-	3,716	-	-		
	3058-7	926	(1700)	124.106	(18)	74.46 (10.8)	68.53 (9.94)	84.12 (12.2)	82.74 (12)	-	-	-	-	79,859	-	-		
	3056-8	1038	(1900)	137.896	(20)	49.85 (7.23)	43.92 (6.37)	59.43 (8.62)	60.61 (8.79)	-	-	-	-	17,229	-	-		
	3056-9	1038	(1900)	124.106	(18)	45.51 (6.6)	43.51 (6.31)	58.12 (8.43)	60.74 (8.81)	57.50 (8.34)	-	-	-	Run-Out	236.49	(34.3)		
	3057-8	1038	(1900)	131.0	(19)	45.23 (6.56)	46.2 (6.7)	46.33 (6.72)	63.15 (9.16)	-	-	-	-	65,750	-	-		
	3057-9	1038	(1900)	137.896	(20)	45.23 (6.56)	46.61 (6.76)	57.43 (8.33)	-	-	-	-	-	4,099	-	-		
	3058-8	1038	(1900)	124.106	(18)	49.99 (7.25)	52.33 (7.59)	62.19 (9.02)	60.88 (8.83)	-	-	-	-	23,359	-	-		
	3058-9	1038	(1900)	117.211	(17)	47.44 (6.88)	44.61 (6.47)	-	-	-	-	-	-	458	-	-		

ORIGINAL PAGE
BLACK AND WHITE PHOTOGRAPH

ORIGINAL PAGE IS
OF POOR QUALITY

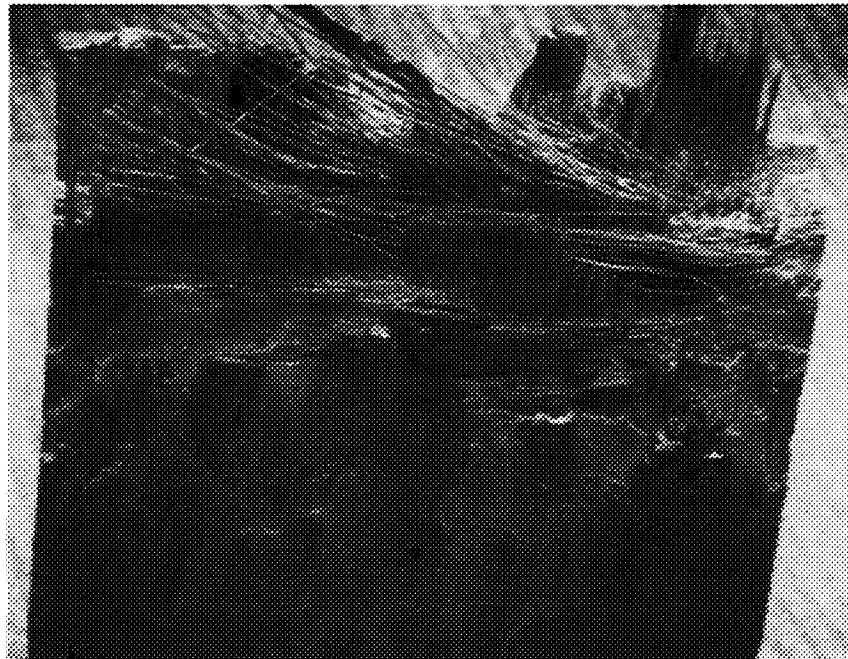


Figure B-10 Fracture Surface of 12 HS Woven Fiber Specimen After Static Failure Following 100,000 Fatigue Cycles at 1038°C (1900°F)



Figure B-11 Fracture Surface of 0/+45/90/-45 SiC-LAS III Specimen After Static Failure Following 100,000 Fatigue Cycles at 1038°C (1900°F)

B.4 CREEP CHARACTERISTICS

The creep characteristics of the ceramic composites were determined in tests conducted at the Southern Research Institute (SRI) using test specimens fabricated at the United Technologies Research Center. The tests were conducted in air at temperatures of 926°C (1700°F) and 1038°C (1900°F) in a four-point flexural apparatus that was geometrically identical to that described in Section B.2, that is, the spans between loads were 6.35 and 1.91 cm (2.5 and 0.75 inches). The test specimens had the same nominal dimensions as those of Section B.2, that is, 7.6 cm (3.0 in) long with 2.3 by 10 mm (0.09 by 0.4 in) rectangular cross section with the plane of the fiber parallel to the 10 mm (0.4 in) dimension and the load applied perpendicular to this plane.

The nominal test duration was 160 hours, and the data recorded consisted of measurements of the midspan deflection at 4 to 8 hour intervals while the specimen was subjected to a constant load in the range of 30 to 50 percent of the ultimate strength of the material as established in the tests of Section B.2. The deflection was converted to strain at the tensile surface of the specimen by Equation (B-1). Materials evaluated consisted of composites with both the 0/+45/90/-45 layered and the 12 harness satin woven fiber construction with the LAS III matrix.

Figures B-12 and B-13 show typical results for specimens with the multidirectional layered and the woven fiber lay-ups, respectively. The total strain consists of an initial increment equivalent to the static deflection resulting from the application of the load. This increment is followed by a significantly nonlinear primary creep regime extending to about 40 hours. Thereafter, a secondary creep regime exists in which the additional strain increases linearly with time at a slow rate. The steady state creep rate was defined graphically by measuring the slope of the strain-time curve in this regime. Table B-III presents a summary of the creep characteristics of the ten specimens evaluated. Attempting to load the specimens to 130 to 140 MPa (19 to 20 ksi) led to failure of the specimen in the first few minutes of testing in three out of four cases. In the fourth case, the specimen failed during the primary creep regime, 38 hours into the test. All of the specimens loaded to the lower 86 and 117 MPa (12.5 and 17 ksi) stress levels survived the duration of the test. From the data obtained on the six valid specimens of Table B-III, it appears that the creep rate of the multidirectional layered fiber specimens was very low and nearly independent of temperature at the nominal stress level of 86 MPa (12.5 ksi), whereas the creep rate was higher and more temperature sensitive at the 117 MPa (17 ksi) stress level. The performance of the woven-fiber specimens relative to those with multidirectional fiber orientations is inconclusive with one specimen loaded to 117 MPa (17 ksi) at 1038°C (1900°F) indicating a comparable creep rate, while another specimen tested at 86 MPa (12.5 ksi) and 927°C (1700°F) had about double the creep rate of the corresponding 0/+45/90/-45 fiber specimen.

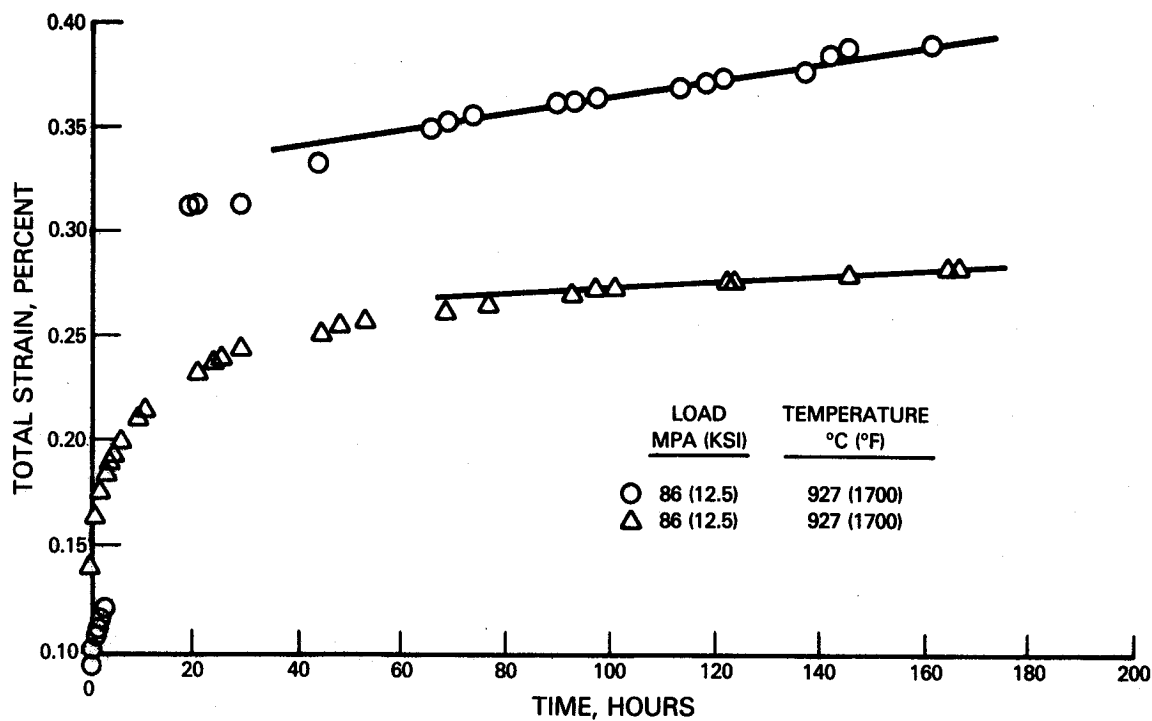


Figure B-12 Creep Characteristics of 12 HS Woven SiC-LAS III Composite Material

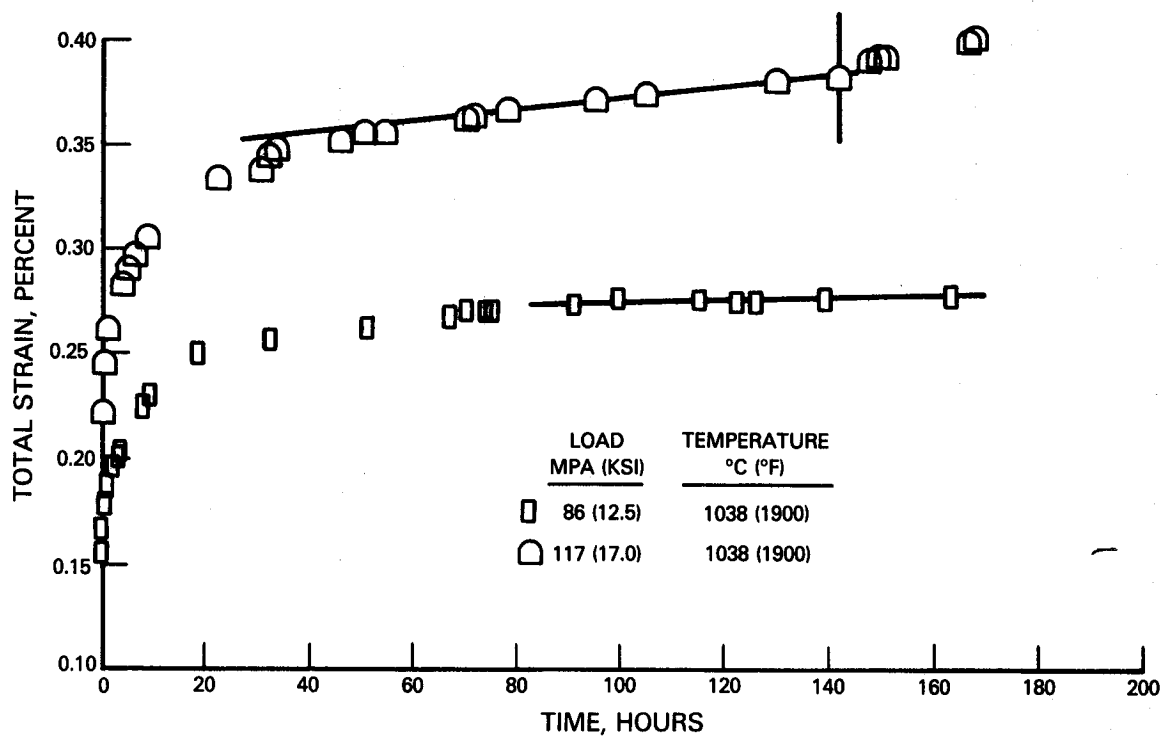


Figure B-13 Creep Characteristics of (0/+45/90/-45) SiC-LAS III Composite Material

TABLE B-III
RESULTS OF FLEXURAL CREEP TESTING OF
SiC-LAS MATERIAL IN AIR

Specimen Number	Temperature, °C (°F)		Applied Stress, MPa (ksi)		Time, hours	Steady State Creep Rate, hr ⁻¹ x 10 ⁶
12HS WOVEN SiC-LAS III:						
2896-1	927	(1700)	86.2	(12.5)	0 - 161	[4.0] ¹
2896-2	927	(1700)	138.0	(20.0)	0 - 38	[25.0] ²
2896-3	927	(1700)	138.0	(20.0)	0 - 0.2	---
2896-4	1038	(1900)	86.2	(12.5)	0 - 165	[8.9] ³
2896-5	927	(1700)	86.2	(12.5)	0 - 167	1.6
2896-6	1038	(1900)	117.1	(17.0)	0 - 167	2.5
(0/+45/90/-45) SiC-LAS III:						
2929-1	927	(1700)	86.2	(12.5)	0 - 167	0.68
2929-2	927	(1700)	117.2	(17.0)	0 - 165	1.4
2929-3	927	(1700)	131.0	(19.0)	0 - 0.7	---
2929-7	1038	(1900)	86.2	(12.5)	0 - 163	0.73
2929-8	1038	(1900)	131.0	(19.0)	0 - 0.18	---
2929-9	1038	(1900)	117.0	(17.0)	0 - 167	2.8

NOTES:

1. Deflection measurement apparatus slipped. Specimen 2896-5 tested at same conditions and is considered more accurate.
2. Creep rate after a maximum of 31 hours. Creep still in primary regime.
3. Deflection measurements in error after 72.5 hours. Slope defined at that time.

Reference B-1 reports on the results of similar tests conducted on specimens of SiC-LAS II with a 0/+45/-45/90 fiber lay-up sequence and indicates steady state creep rates in the range of 3.7 to 5.0×10^{-6} per hour at the same temperature levels. The SiC-LAS III specimens tested in the current program generally have only half this creep rate or less. In addition, the SiC-LAS III specimens were tested in air where they were susceptible to an oxidation process that is known to cause embrittlement of the composite, whereas the SiC-LAS II specimens were tested in an inert argon environment where they were immune from this form of attack. Consequently, the creep strength of SiC-LAS III composites is superior to that of the earlier SiC-LAS II material.

B.5 THERMAL FATIGUE TESTS

Thermal fatigue tests were conducted on specimens of the SiC-LAS III composite material on a test rig located in the Materials Engineering Laboratory at Pratt & Whitney. This apparatus, shown schematically in Figure B-14, has the capability to substantially reproduce localized creep-buckling failures (bulges) similar to those observed in engine operated burner liners. Testing involved repetitive creation of a small diameter high temperature spot in the center of a rotating 7.62 cm (3.0 in) diameter test specimen using a focused oxy-acetylene torch. The cyclic heating was affected by shuttling the torch laterally into and out of position in front of the specimen. The frequency of the shuttling depends on the properties of the test material and the desired temperature excursions but is typically one to eight cycles per minute.

The temperatures of the hot and cold surfaces of the specimens were measured by Irkon pyrometers - one sighting the front face of the specimen disk and another sighted through the bore of the specimens holder at the back side of the rotating disk. The periphery of the disk is heated with a diffuse gas-air flame and is controlled to a temperature of the order of 540°C (1000°F). The rotation of the specimen ensures an axisymmetric temperature distribution. The speed of rotation is typically 400 rpm.

During company-sponsored tests with metallic materials, cycling the center of the disk from the 540°C (1000°F) temperature maintained at the periphery to a maximum temperature in the range of 870 to 1090°C (1600 to 2000°F) was found to produce a progressive permanent deflection, and, in some cases, eventual cracking of the disk surface. The total accumulated distress was a function of the number of thermal cycles experienced, the disk edge-to-center maximum temperature difference, and the physical and mechanical properties of the disk material.

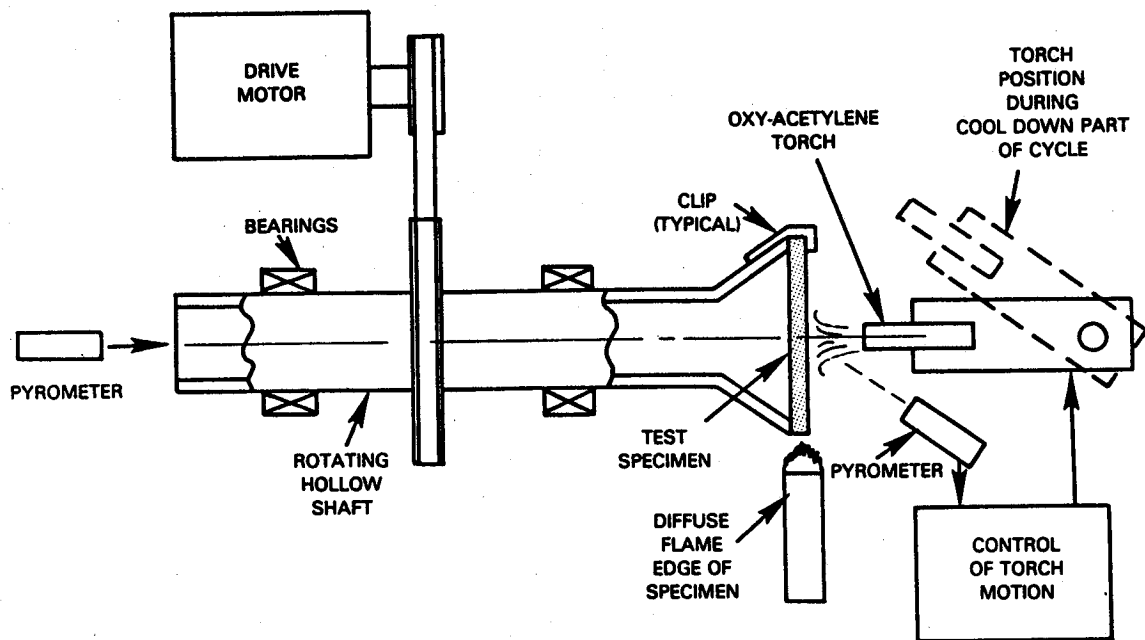


Figure B-14 Schematic View of Thermal Fatigue Test Apparatus

Under the NASA/P&W Advanced Composite Combustor Structural Concepts Program (Reference B-1), tests were conducted in this apparatus on specimens of SiC-LAS II ceramic composite having a multidirectional fiber lay-up with an orientation of 0/+45/-45/90. The first specimen evaluated under that contract was subjected to cyclic operation between 537 and 1095°C (1000 and 2000°F) during which the through thickness temperature differential at the center of the disk was 222°C (400°F) at the time of peak front-surface temperature. [For reference purposes, the prior company-sponsored research indicated that at peak hot-side surface temperatures on the order of 1040°C (2000°F) Hastelloy specimens developed sizable central deflections after only five or ten cycles and that cracks developed on the hot-side surface after about 500 cycles. Due to its higher thermal conductivity, the temperature differential through the Hastelloy X specimen was also an order of magnitude less than that in the SiC-LAS II specimen.] Conversely, no such distress was encountered in the evaluation of the first SiC-LAS specimen, and the test was terminated after 1000 thermal cycles. Profilometer measurements indicated no deflection or change in thickness of the specimen, and the only evidence of its exposure was a local discoloration of the surface of the specimen. The color change appeared as a light gray against the darker gray normal color of the material. The discoloration was limited to an area of about 12.7 mm (0.5 in) diameter where the hot jet impinged. This area was surrounded by a ring that appeared to consist of minute beads of glassy material. Likewise, a second specimen tested at even more severe conditions with peak hot-side surface temperatures of 1150°C (2100°F) for 2400 thermal cycles indicated no structural distress even after sectioning and micrographic examination. In order to inflict damage

on a third SiC-LAS II specimen in the thermal fatigue test apparatus, it was necessary to increase the test duration to 3800 cycles at this temperature level. The increased duration produced minute surface cracks in addition to the discoloration and glass beading seen on prior specimens, and sectioning revealed slight internal microcracking.

The remarkable performance of the SiC-LAS II specimens relative to metallic materials in the thermal fatigue rig is attributable to the lower thermal stress associated with its low coefficient of thermal expansion and was a major factor in the continuing interest in these ceramic composite materials for combustor liners.

Under the current program, the thermal fatigue testing was continued to obtain comparative information on the cyclic durability of the candidate ceramic composites made with the SiC-LAS III material. Four specimens were evaluated, two having a 12 harness satin woven fiber lay-up and two having a 0/+45/-45/90 fiber lay-up, the latter being identical to the lay-up of the SiC-LAS II specimens evaluated in this same test apparatus. Two different test sequences were established, and one specimen of each lay-up was subjected to each test sequence. Sequence A, as defined in Table B-IV, was formulated to define the threshold of damage to the SiC-LAS III material, and consisted of a progressive increase in severity of thermal exposure.

TABLE B-IV
THERMAL FATIGUE TEST SEQUENCE A

Thermal Cycles	Maximum Surface Temperature			
	Hot-Side		Cold-Side	
	°C	(°F)	°C	(°F)
1000	1370	(2500)	1092	(2000)
500	1398	(2550)	1120	(2050)
500	1426	(2600)	1134	(2075)
500	1481	(2700)	1203	(2200)
2500 Total				

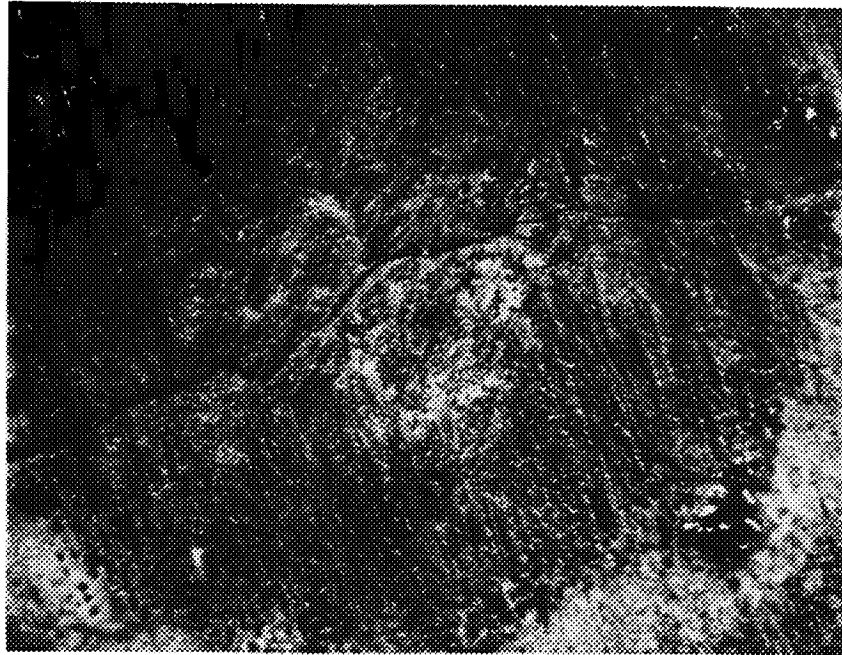
This test sequence was formulated on the basis of the above cited experience with SiC-LAS II specimens in the thermal fatigue test apparatus and the expectation that the SiC-LAS III matrix formulation had even higher temperature capabilities. This expectation was confirmed when exposure of both of the specimens to the 1370°C (2500°F) maximum hot-side temperature portions of Test Sequence A indicated that the only distress was the slight discoloration of the hot-side surface and the formulation of a ring of glassy beads around this region. The appearance was similar to that observed in the above cited prior test of SiC-LAS II specimens (Reference B-1), and the only difference between the multidirectional layered fiber specimen and that with woven fibers was a slightly greater quantity of glassy bead material on the hot-side surface of the latter. It appears that the beads were formed from the LAS matrix, and the presence of larger regions of matrix material in the woven fiber construction may have led to greater transport of this material to the surface of the specimen.

The second step of Test Sequence A, which involved an additional 500 cycles at a maximum hot-side surface temperature of 1398°C (2550°F), led to the onset of physical damage to both specimens. Cracks were visible on the hot-side surface of each specimen, and more glassy material had effluxed from the surface of the woven fiber specimen. Returning the specimens to test for an additional 500 cycles at maximum hot side surface temperature of 1426°C (2600°F) led to increasing the crack penetration on the hot side and a visible crack on the cold side. The final 500 cycles at a hot-side surface temperature of 1481°C (2700°F) led to substantially more distress in that this exposure drove the cracks through the specimen and caused flowing of the hot-side matrix material, exposing the underlying fibers to oxidation.

Figures B-15 and B-16 show the specimen with the (0/+45/-45/90) fiber orientation after completion of its cyclic thermal exposure. In an area at the center of the disk, on the hot side, fibers are exposed and a crack is visible. The area of exposed fibers is bounded by a ring of black glassy beads. Outside of the ring of beads there is an area of darkened material with a grainy surface finish. The tips of the central crack extend into this region. Beyond this area is a ring of material which shows little effect of the thermal exposure. At a radius of approximately 2 cm (0.8 in) there is an area with a glazed appearance. Beyond this area the material shows no evidence of exposure to a high temperature. On the cold side of the specimen there is a darkened area in the center of the disk which is about 3 cm (1.2 in) in diameter. The crack in the specimen extends through the thickness of the specimen and is discernable on the cold side.

While the Sequence A tests demonstrated that the SiC-LAS III composite material had significantly greater thermal fatigue resistance than SiC-LAS II, it did not define a damage threshold adequately to establish design limits. An additional test was conducted on the two remaining specimens to assess distress tolerance at more moderate temperature levels but over longer test durations. A maximum hot-side surface temperature of 1315°C (2400°F) and a test duration of 5000 cycles was selected for this test sequence. At the conclusion of these tests, the distress to the specimens was comparable to that observed after the 1426°C (2600°F) step of the Sequence A test. Since those specimens had been subject to only 2000 thermal cycles, an obvious trade between maximum exposure temperature and cyclic fatigue life must exist for the SiC-LAS III composite systems.

ORIGINAL PAGE IS
OF POOR QUALITY



ORIGINAL PAGE
BLACK AND WHITE PHOTOGRAPH

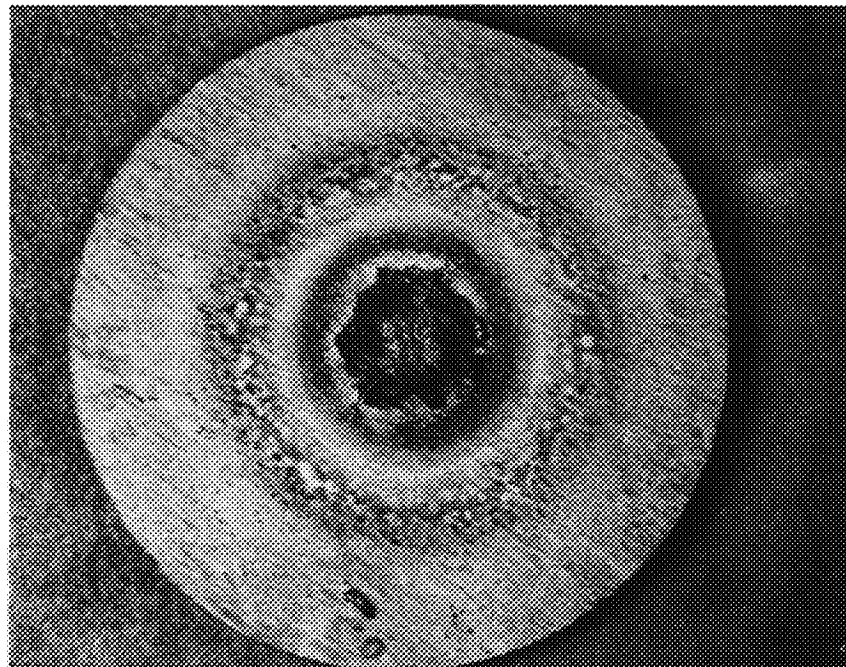
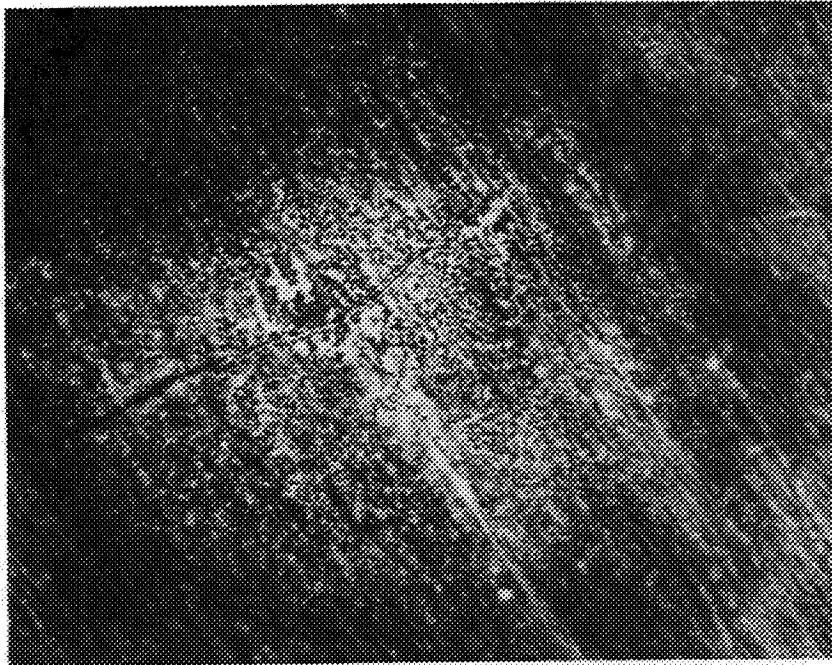


Figure B-15 Hot Side of 0/+45/-45/90 SiC-LAS III Specimen After Sequence A Thermal Fatigue Test

ORIGINAL PAGE IS
OF POOR QUALITY



ORIGINAL PAGE
BLACK AND WHITE PHOTOGRAPH

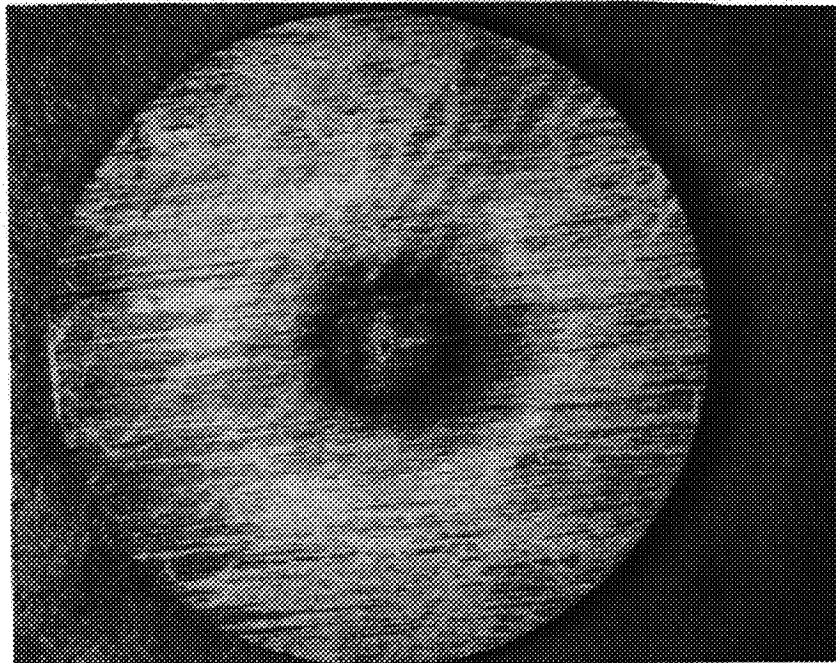


Figure B-16 Cold Side of 0/+45/-45/90 SiC-LAS•III Specimen After Sequence A Thermal Fatigue Test

B.6 LONG DURATION THERMAL DURABILITY

At the completion of the studies under the NASA/P&W Advanced Composite Combustor Structural Concepts Program, it was concluded that the life-limiting process for a ceramic composite combustor liner would be some form of thermal degradation of the material rather than the low cycle fatigue cracking that limits conventional metallic combustor liners. Lacking data on this process, the need for long duration tests in which specimens of the materials could be exposed to the thermal environment encountered in a combustor became evident, and these tests were incorporated into the current program.

Figure B-17 shows a schematic view of the apparatus used for these tests. The heater utilized seven quartz filament lamps mounted in a water cooled reflector. This source is capable of heating a flat target area approximately 100 x 250 mm (4 x 10 in) with heat fluxes comparable to those encountered by high pressure-ratio combustor liners. The test surface, fabricated in a plate of the above dimensions, was mounted on a water cooled support with an internal plenum for cooling air feed to the test specimens. A fixture was fabricated that held five 46 x 94 mm (1.8 x 3.7 in) composite specimens in an overlapping sequence as shown in Figure B-17. Cooling air admitted beneath each panel film cooled the hot-side surface of the next downstream panel to simulate the thermal boundary conditions of the film cooled combustor liner concept defined under the NASA/P&W Advanced Composite Combustor Structural Concepts Program.

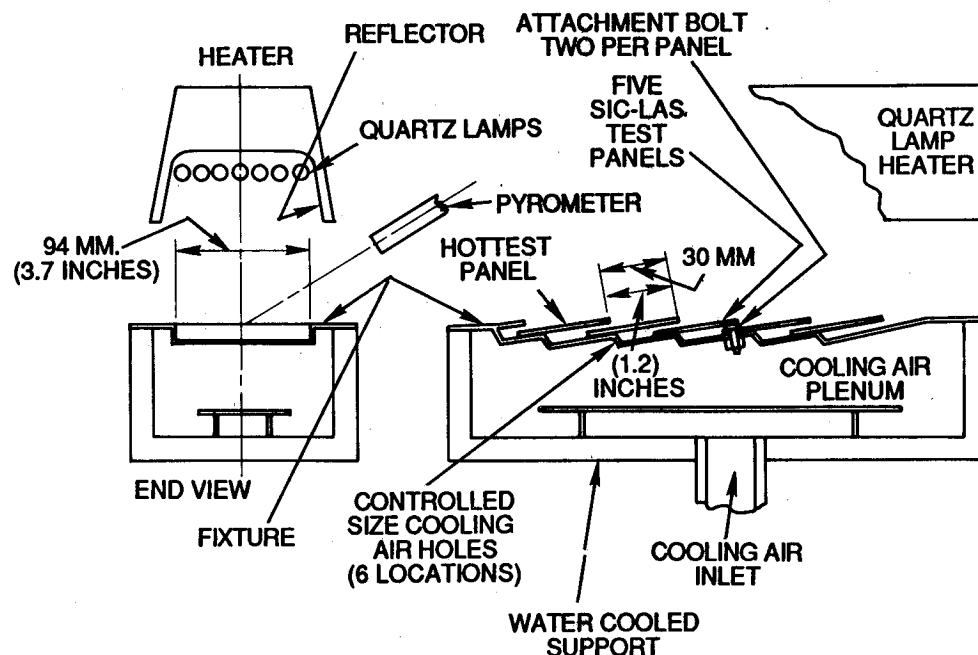


Figure B-17 Test Apparatus for Long Duration Thermal Exposure Tests

The test apparatus shown in Figure B-17 permitted exposure of the specimens to not only the peak temperatures anticipated in the engine application but also, at least qualitatively, to similar axial and through-thickness temperature gradients. Additionally, the panels were retained in the fixture by bolts that simulated the attachment of the panels to the liner shell in the actual liner construction. In order to assess the effect of temperature level on the durability of the specimens, the size of the cooling air apertures was also varied from panel to panel to produce different cooling air flow rates and hence different specimen temperature levels. The instrumentation on the test rig included a measurement of static pressure in the cooling air supply plenum in the specimen support. Shielded air temperature thermocouple probes were also located in the air plenum, and a flowmeter was installed in the cooling air supply line. An axially traversing pyrometer was installed on the side of the rig, as shown in Figure B-17, to view the surface of the test specimens along their centerline.

Two series of tests were performed on the quartz lamp rig; one test was of SiC-LAS II material and the other of SiC-LAS III. Both materials had a multidirectional fiber lay-up and were subjected to elevated temperatures for a period of 100 hours. The test specimens were subjected to only a small number of thermal cycles corresponding to daily shutdowns and occasional shutdowns for repairs. Table B-V lists the temperatures of the downstream end of the hot surface of each panel at its centerline during these tests as determined by the traversing pyrometer. The range of panel temperatures was selected primarily on the basis of the experience derived in the thermal cyclic tests described in Section B.5 to encompass what appeared to be the maximum useful operating temperature of each material. The panels fabricated with the LAS III matrix material were operated at peak temperature levels of 80 to 135°C (140 to 240°F) higher than those panels made from LAS II.

TABLE B-V
MAXIMUM PANEL SURFACE TEMPERATURE
DURING LONG-TERM THERMAL DURABILITY TESTS

Panel Number	Panel Surface Maximum Temperature, °C (°F)	
	SiC-LAS II (0/+45/-45/90)	SiC-LAS III (0/+45/90/-45)
1	993 (1820)	1071 (1960)
2	1082 (1980)	1193 (2180)
3	1149 (2100)	1238 (2260)
4	1177 (2150)	1321 (2410)
5	1204 (2200)	1332 (2430)

Periodic inspection of the panels during the 100-hour tests indicated no catastrophic failure mechanisms and very little visible deterioration of the hot surfaces of the panels as the test progressed. The only unusual phenomenon observed was the formation of a glassy deposit in the hottest regions of some panels. During rig operation, the deposit had the appearance of a highly viscous liquid containing bubbles. On shutdown of the apparatus, the material solidified to a light gray deposit. The amount of deposit increased over the first ten hours of thermal exposure but remained constant thereafter. The presence of the bubbles suggested an outgassing phenomenon that may be related to the formation of glassy beadlike deposits on the hot surfaces of the thermal cyclic fatigue test specimens of Section B.5. Figure B-18 shows the SiC-LAS II panels, still mounted in the test fixture, after the completion of the 100-hour thermal exposure test. The glassy deposits are very evident on Panel 5 but are progressively less extensive on the cooler panels until there is only a trace on the lip of Panel 2. Based on the temperature levels of Table B-V, it appears that the threshold for the deposit generation phenomenon in SiC-LAS II is about 1080°C (1980°F). Figure B-19 shows the SiC-LAS III panels in the test fixture after completion of the 100 hour exposure test. Similar deposits were observed on these panels but, based on the same type of observations, their onset did not occur until surface temperatures on the order of 1200°C (2200°F) were encountered.

On removal of the panels from the fixture for more detailed examination after completion of the 100-hour tests, a distinct transverse line of discoloration was observed on the cold-side surface of most of the hotter panels. Measurements indicated that this band was located over the abrupt bend in the metal where the panel no longer made contact with the metal. The fixture was fabricated from a nickel-base alloy, and it is known that chemical interactions occur between those alloys and the lithium aluminosilicate at elevated temperatures. It is quite likely that the distinct band at this location may have been due to the local overbending of the fixture at the shoulder which created a raised ridge that made line contact with the cold-side surface of the ceramic composite panel where it was attached in the fixture, thereby localizing the region of chemical interaction.

The composite panels from the thermal exposure tests were also examined by X-radiography. Figures B-20 and B-21 show the results for the SiC-LAS II and SiC-LAS III panels, respectively. For reference, Figure B-20 also includes the analysis of an unexposed panel. Minute cracks are visible in several of the SiC-LAS II panels on Figure B-20. On Panel 2, an axial crack approximately 13 mm (0.5 in) in length grew from the lip toward the leading edge at a point about one-third of the panel width in from the side edge. The Panel 3 X-radiograph shows a crack of approximately the same length and in approximately the same location as Panel 2. A roughened area at the lip is also visible.

ORIGINAL PAGE
BLACK AND WHITE PHOTOGRAPH

ORIGINAL PAGE IS
OF POOR QUALITY

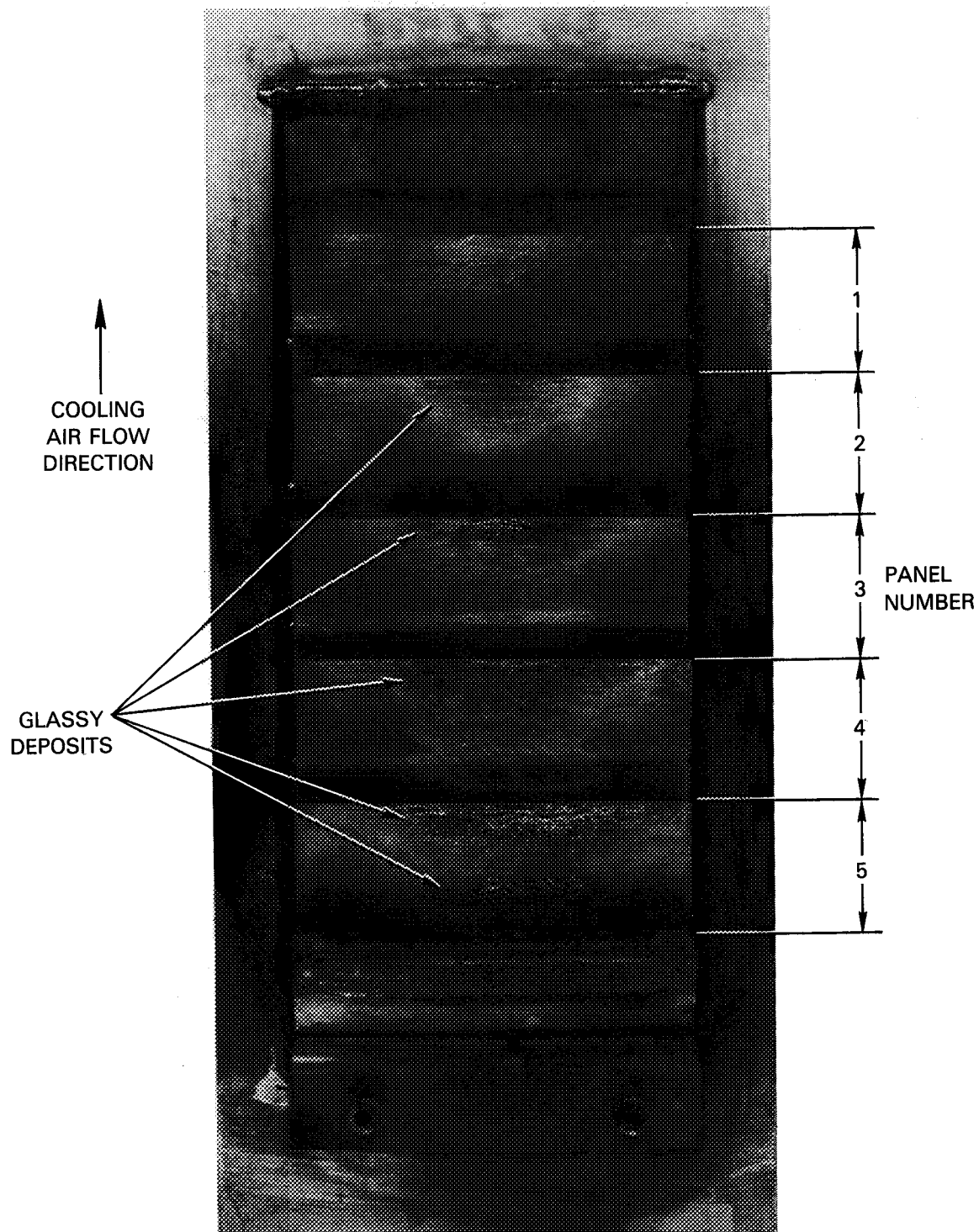


Figure B-18 SiC-LAS II Panels in Test Fixture After 100-Hour Thermal Durability Test

ORIGINAL PAGE
BLACK AND WHITE PHOTOGRAPH

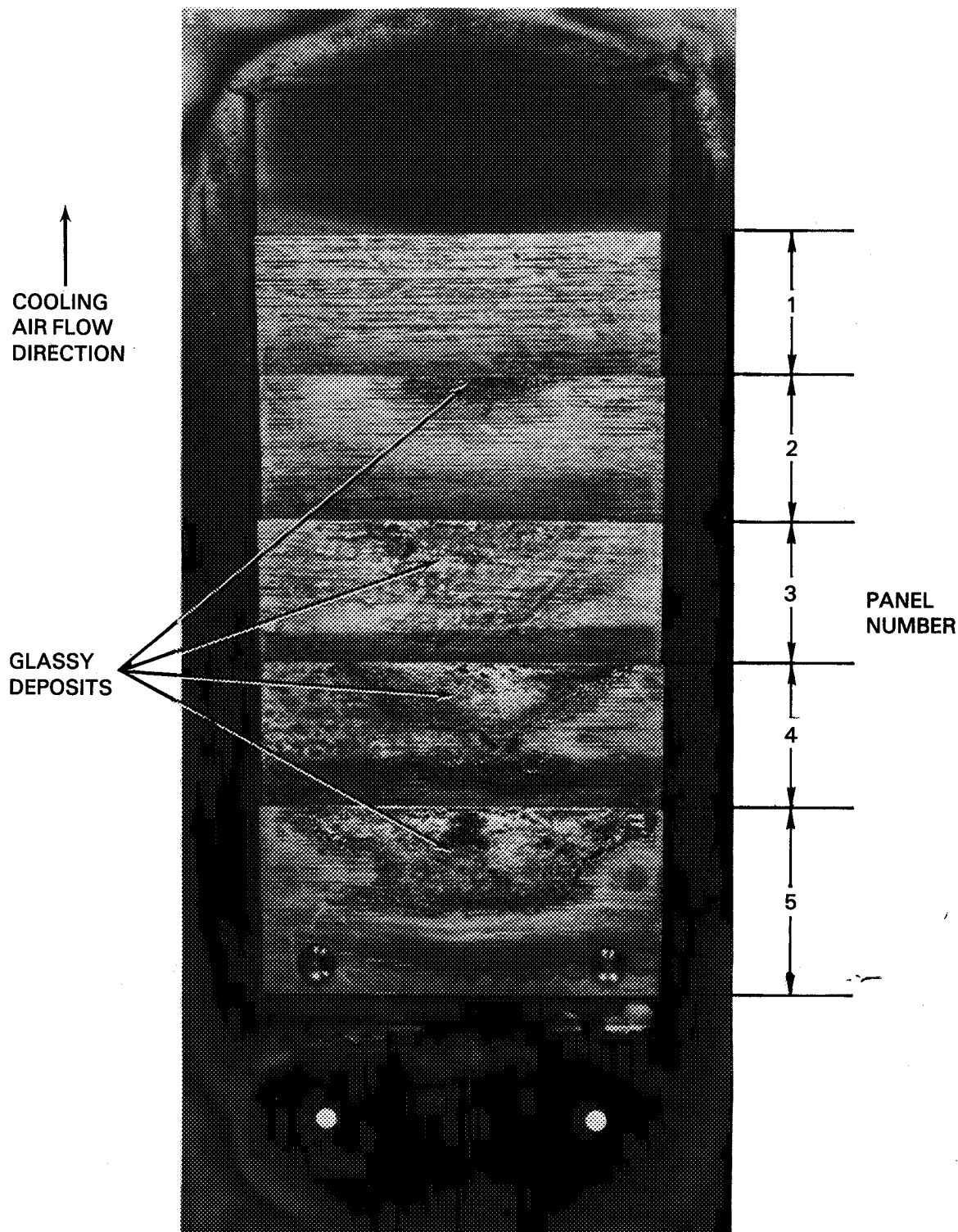
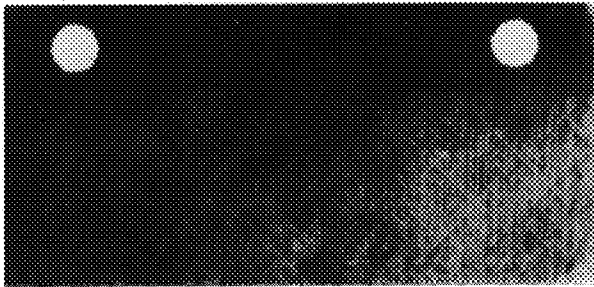
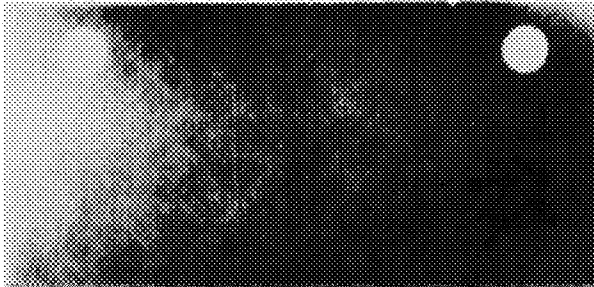


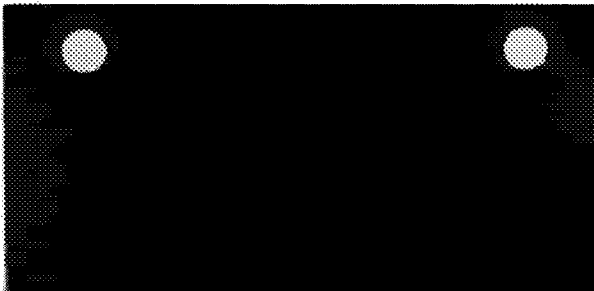
Figure B-19 SiC-LAS III Panels in Test Fixture After 100-Hour Thermal Durability Test



UNEXPOSED PANEL 2633B-2

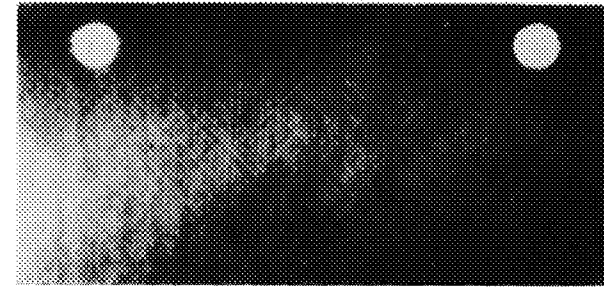


PANEL 1 — 993°C (1820°F)

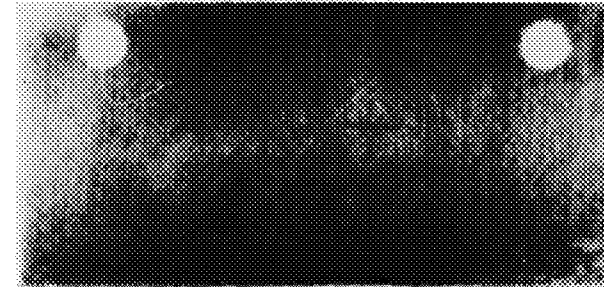


PANEL 2 — 1082°C (1980°F)

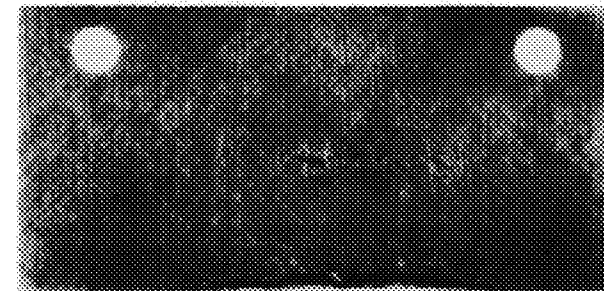
ORIGINAL PAGE
BLACK AND WHITE PHOTOGRAPH



PANEL 3 — 1149°C (2100°F)



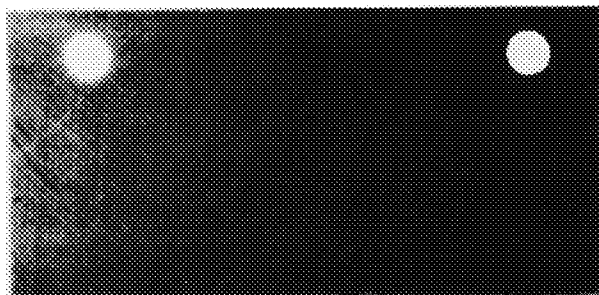
PANEL 4 — 1177°C (2150°F)



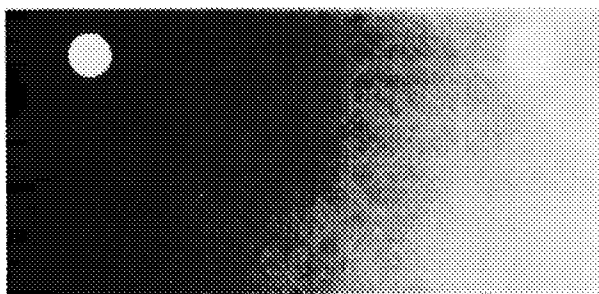
PANEL 5 — 1204°C (2200°F)

ORIGINAL PAGE IS
OF POOR QUALITY

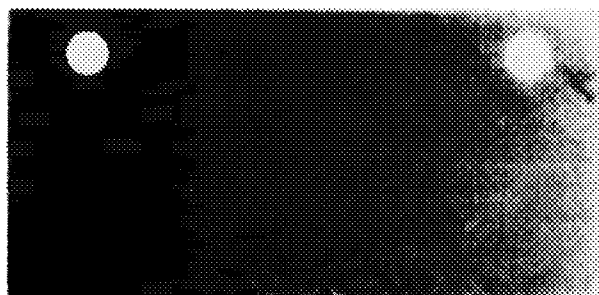
Figure B-20 Radiographic Analysis of Sic-LAS II Panels After Long Term Durability Tests



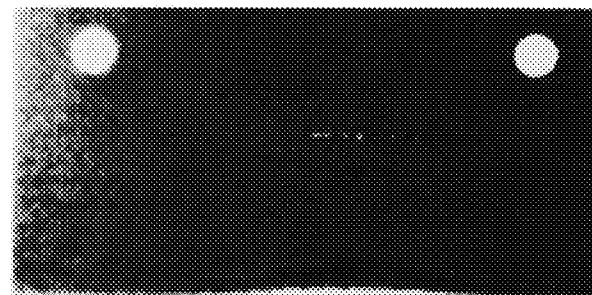
PANEL 1 — 1071°C (1960°F)



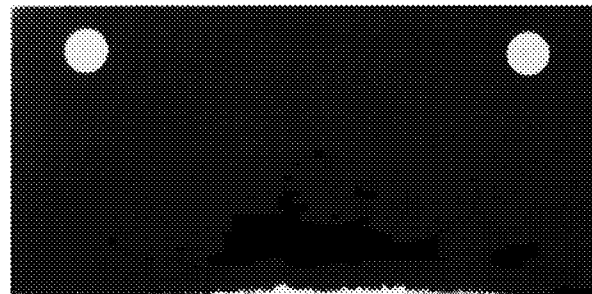
PANEL 2 — 1193°C (2180°F)



PANEL 3 — 1238°C (2260°F)



PANEL 4 — 1321°C (2410°F)



PANEL 5 — 1332°C (2430°F)

Figure B-21 Radiographic Analysis of SiC-LAS III Panels After Long Term Durability Test

ORIGINAL PAGE
BLACK AND WHITE PHOTOGRAPH

ORIGINAL PAGE IS
OF POOR QUALITY

Panel 4 has three axial cracks growing from the lip in the same position, relative to the panel centerline, as Panels 2 and 3. Additionally, there is a region near the center of Panel 4 containing several small cracks and there is a curved crack growing from one of the attachment holes. The area where bubbling of material is visible in Figure B-18 is also apparent on the X-radiograph of Panel 4. Panel 5 has no lip cracks but does contain numerous cracks in the central region, similar to Panel 4. Again, the bubbled areas are seen on the X-radiograph of Panel 5.

The X-radiographic analysis of the SiC-LAS III panels in Figure B-21 differs in that no cracks were detected in any of the specimens. However, distress is evident at the downstream (hot) end of Panels 4 and 5 where it appears some of the panel lip has been removed by chemical reaction or erosion. Distress is also evident on these two panels in the vicinity of the transverse line where local contact was evidently made between the cold side of the panel and the nickel alloy test fixture.

Following these nondestructive inspections, the test panels were cut for more extensive internal examination. Photomicrographs were made of selected sections. These indicated that; in sections where visual examination of the external surfaces and X-radiography had previously detected no flaws; the material integrity was excellent, free from microcracks and essentially indistinguishable from similar unexposed specimens. The previously discussed glassy deposit that had formed on the surface of some of the hotter panels was of particular interest, and Figure B-22 shows a photomicrograph through a region of extensive deposit formation of the surface of SiC-LAS III Panel 3. The layers of fiber aligned in various directions in the panel are evident in the photographs and the "deposit" layer occupies the entire top part of the photographs being nearly as thick as the entire panel (panel thickness = 1.15 mm = 0.045 in). It is evident from this figure that the definition "deposit" is a misnomer and the layer is actually a low density expansion of the material at the hot side surface of the panel. Remnants of some of the transversely aligned fibers from the surface layer of the panel are evident in the "deposit" material and it appears to contain a multitude of small cavities or voids that were probably filled with the outgassed material and gave it its cellular or foamy appearance. Based on the thickness of the remaining part of the transverse fiber layer on the hot side of the panel relative to that on the cold side at the bottom of the photographs, it would appear that the "deposit" consists of the material that was originally in about the top one-third of the thickness of the transverse fiber layer.

It is also evident from Figure B-22 that even though the hot side surface of this panel was severely overtemperated (maximum hot surface temperature measured by the pyrometer was 1238°C per Table B-V), the internal regions of the panel were not significantly deteriorated. A few microcracks are evident in the 45° fiber direction layers adjacent to the hot surface and some void areas can be seen surrounding fibers in that region. The voids are suspected of being caused by the oxidation at the surface of the silicon carbide fibers that can ultimately lead to brittle failure modes. The high structural integrity of the central and cold side regions of the panel is attributed to the lower material temperatures. Despite the high temperatures on the hot side surface, it is estimated that a through thickness temperature differential of about 220°C (400°F) existed across the downstream lip of this panel.

ORIGINAL PAGE IS
OF POOR QUALITY

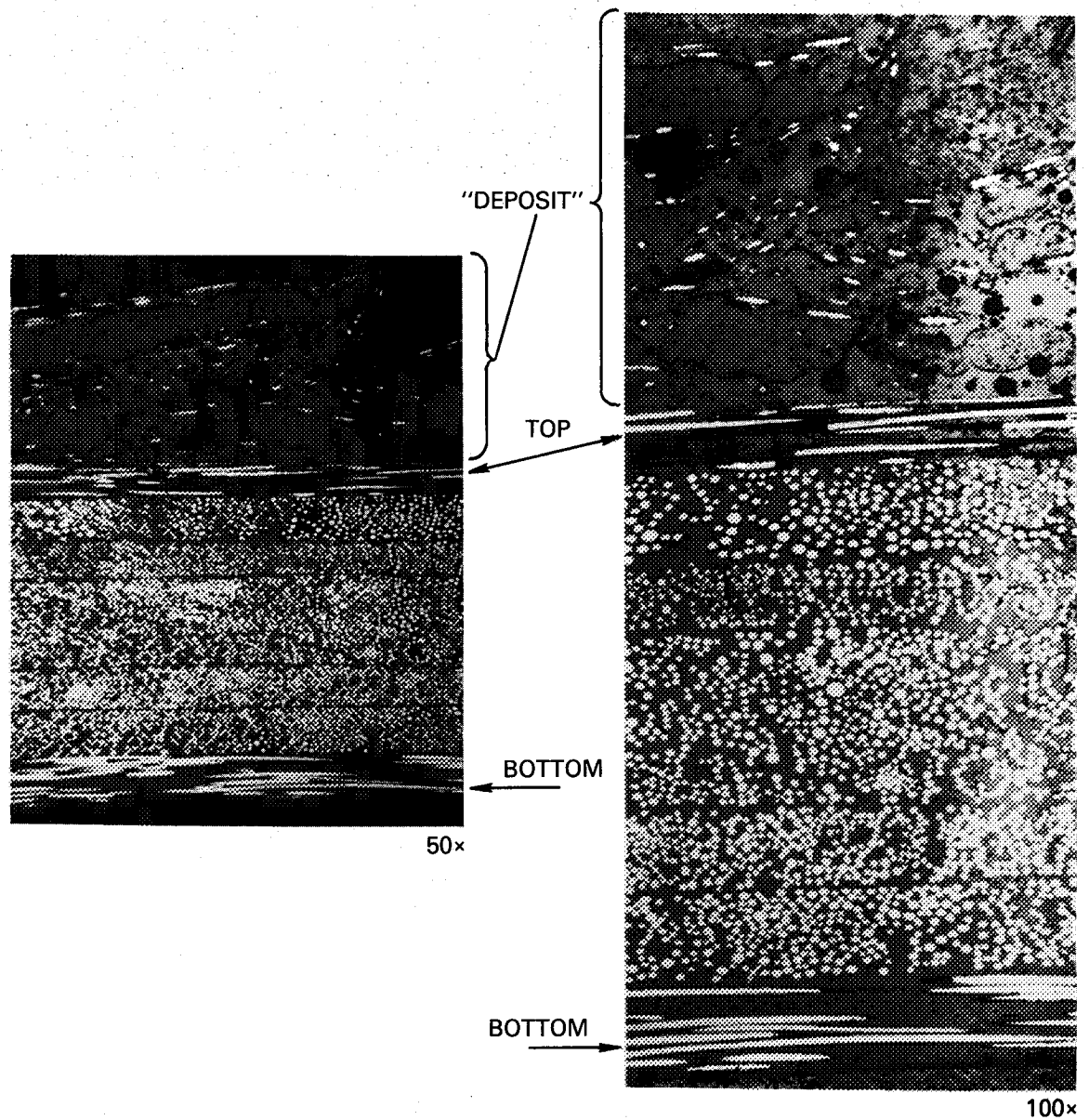


Figure B-22 Photomicrograph of a Transverse Section through SiC-LAS III
Panel 3 Showing "Deposit" Layer

The post exposure examination of the panels was concluded with an assessment of the residual strength of specimens cut from selected panels. Two parallel cuts were made through the panels in an axial direction immediately inside the attachment holes to remove the central 95 mm (2.4 in) wide portion of the panel. This portion was then cut into transverse strips to produce six specimens having a nominal width of 6.35 mm (0.25 in). The specimens were then loaded to failure in a three point flexure apparatus at room temperature and the residual strength and fracture morphology documented.

The data from the SiC-LAS II specimens were inconclusive because some of the specimens had been cracked during the thermal exposure. In addition, some difficulty was encountered in separating SiC-LAS II panels from the dies during fabrication and the surfaces of these panels had been ground. This removed some of the surface layer of fibers which were oriented in the axial direction of the specimen and created a nonsymmetric specimen geometry making interpretation of the residual strength data difficult. However, the SiC-LAS III panels produced valid test specimens and the data are listed in Table B-VI. In general, specimens cut from the hot downstream end of the panels (such as Numbers 5 and 6) retain their strength well despite exposure to high temperature levels. The variation in fracture morphology is of interest because it shows that specimens from the hot end break with the fibrous fracture surface that would be anticipated in a fiber reinforced composite; while those from the cold end of the panel (i.e., near the attachment bolts and under the lip of the upstream panel) in the endurance test apparatus failed in a brittle mode. In the latter failure mode, the fiber and matrix fail simultaneously with the fiber offering little reinforcement of the matrix. This appears to have been caused by oxidation of the surface of the SiC fibers which weakens them and compromises their reinforcement of the matrix. The fact that it is more prevalent in the colder region of the panels suggests that at elevated temperatures, the matrix becomes slightly plastic and flows to seal around the exposed ends of the fibers preventing access.

The final test conducted on the thermal exposure apparatus involved an assessment of thermal paints that were under consideration for use in the sector combustor rig to determine liner panel temperatures. The first panel, which encountered a maximum hot side surface temperature of 1149°C (2100°F) had been painted with a number of narrow axial strips of thermal paint, all of which changed color at single temperatures, on the hot and cold surfaces. The second panel which encountered maximum hot surface temperatures of 1234°C (2250°F) was painted on both sides with two different brands of thermal paints having a range of color change depending on maximum temperature encountered. Operation of the thermal exposure rig for 10 hours to simulate the exposure that would be encountered in the sector combustor rig indicated that the continuous change paints were generally superior to the discrete temperature paints on the first panel. Most of the latter paints spalled or burned off, whereas the continuous change paints adhered well to the cold side surface of the panel and revealed good temperature patterns.

Table B-VI
RESIDUAL STRENGTH AND FRACTURE MORPHOLOGY OF
SPECIMENS CUT FROM SiC-LAS III PANEL USED IN
100-HOUR THERMAL ENDURANCE TEST

<u>Panel Number</u> <u>Max. Temperature</u>	<u>Spec. No.</u>	<u>Tensile⁽¹⁾</u> <u>Surface</u>	<u>Residual</u> <u>Strength</u> MPa Ksi	<u>Fracture Mode⁽²⁾</u>
1 1071°C (1960°F)	1 (Cold End)	(T)	200 (29)	T - Partially brittle
	2	(B)	434 (63)	S - Fibrous
	3	(T)	516 (75)	T - Fibrous
	4	(B)	470 (68)	T - Fibrous
	5	(T)	358 (52)	T - Fibrous
	6 (Hot End)	(B)	496 (72)	S - Fibrous
3 1238°C (2260°F)	1 (Cold End)	(T)	207 (30)	T - Almost totally brittle
	2	(B)	200 (29)	T - Slightly brittle surface
	3	(T)	98 (14)	T - Slightly brittle surface
	4	(B)	138 (20)	T - Fibrous
	5	(T)	159 (23)	T - Fibrous
	6 (Hot End)	(B)	117 (17)	T - Slightly brittle surface
4 1321°C (2410°F)	1 (Cold End)	(T)	255 (37)	T - Slightly brittle side
	2	(B)	380 (55)	T - Fibrous
	3	(T)	255 (37)	T - Fibrous
	4	(B)	490 (71)	T - Fibrous
	5	(T)	255 (37)	T - Fibrous
	6 (Hot End)	(B)	304 (44)	C - Fibrous

Notes:

(1) (T) = Top or hot side, (B) = bottom or cold side

(2) T = Tensile failure, C = Compressive failure, S = Shear failure

One additional panel was installed in the thermal exposure rig during this ten hour test sequence to investigate the effect of surface fiber orientation on panel durability. The panel had the normal 0/+45/90/-45 fiber layup sequence with the LAS III matrix but was cut so that the direction of the surface fiber layers was axial, i.e., parallel to the cooling air flow direction rather than transverse as in all of the other panels evaluated in this apparatus. After the ten hour test at a maximum surface temperature of 1242°C (2270°F), the hot side downstream lip of the panel was found to be severely eroded. As shown in Figure B-23, nearly all of the matrix material was eroded from around the axial fibers in this area. Apparently the cooling air eroded the matrix material after it reached a plastic state, whereas the transverse surface fibers of the other panels effectively impede this process.

Reference

- B-1. Sattar, M. A. and R. P. Lohmann, "Advanced Composite Combustor Structural Concepts Program - Final Report," NASA CR-174733, December 1984.

ORIGINAL PAGE 13
OF POOR QUALITY

ORIGINAL PAGE
BLACK AND WHITE PHOTOGRAPH



AXIAL AFTER 10 HOURS AT
1242°C (2270°F)



TRANSVERSE AFTER
100 HRS AT 1238°C (2260°F)

Figure B-23 SiC-LAS III Panels with Axial and Transverse Surface Fiber
Direct Direction

APPENDIX C
RADIOMETER TEST DATA

ORIGINAL PAGE 55
OF POOR QUALITY

ORIGINAL PAGE
BLACK AND WHITE PHOTOGRAPH

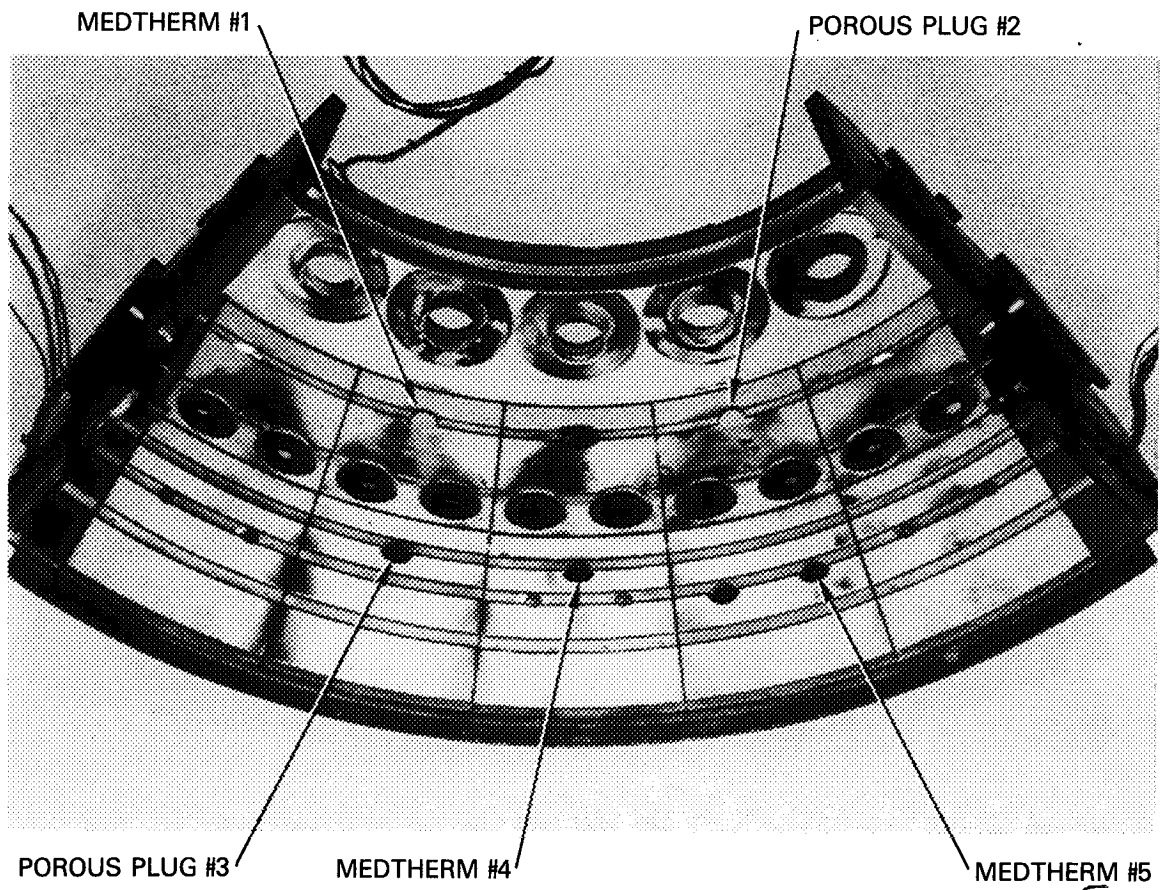


Figure C-1 Radiometer Nomenclature

DATA SUMMARY SHEET

*** RUN 24 ***

RADIOMETER DATA

** METRIC UNITS **

POINT #	1111	1112	1113	1114	1121	1122	1123	1124
WA3 (KG/S)	6.00	5.98	6.00	5.98	5.95	6.07	6.09	5.98
WAB (KG/S)	5.08	5.07	5.09	5.07	5.05	5.15	5.16	5.07
TT3 (K)	752.	750.	751.	751.	751.	751.	750.	751.
PT3 (MPA)	1.018	1.013	1.021	1.015	1.014	1.032	1.034	1.011
(F/A) 4.0	0.0179	0.0210	0.0231	0.0252	0.0195	0.0215	0.0229	0.0248
(F/A) PILOT	0.00353	0.00356	0.00354	0.00357	0.00501	0.00694	0.00858	0.01020

RADIOMETER 1	1.248E+04	1.475E+04	1.816E+04	2.497E+04	5.901E+04	1.158E+05	1.339E+05	1.180E+05
RADIOMETER 2	2.837E+04	3.064E+04	3.064E+04	3.178E+04	5.447E+04	8.625E+04	1.044E+05	1.021E+05
RADIOMETER 3	5.788E+04	7.717E+04	1.112E+05	2.213E+05	1.112E+05	1.124E+05	1.271E+05	1.271E+05
RADIOMETER 4	6.923E+04	8.852E+04	1.021E+05	1.158E+05	7.944E+04	9.874E+04	1.021E+05	1.078E+05
RADIOMETER 5	N/A	N/A	N/A	N/A	N/A	N/A	N/A	N/A

POINT #	2111	2112	2113	2114	2121	2122	2123	2124
WA3 (KG/S)	5.76	5.75	5.76	5.73	5.68	5.68	5.67	5.68
WAB (KG/S)	4.88	4.87	4.88	4.86	4.81	4.82	4.81	4.81
TT3 (K)	834.	835.	834.	833.	839.	842.	843.	842.
PT3 (MPA)	1.032	1.029	1.021	1.047	1.036	1.021	1.030	1.021
(F/A) 4.0	0.0177	0.0210	0.0230	0.0252	0.0196	0.0219	0.0232	0.0240
(F/A) PILOT	0.00351	0.00353	0.00356	0.00355	0.00499	0.00746	0.00863	0.00954

RADIOMETER 1	1.589E+04	2.383E+04	2.383E+04	2.497E+04	2.837E+04	5.788E+04	8.512E+04	1.089E+05
RADIOMETER 2	3.745E+04	3.859E+04	3.859E+04	4.086E+04	5.221E+04	8.058E+04	9.306E+04	1.033E+05
RADIOMETER 3	6.809E+04	7.490E+04	9.760E+04	1.112E+05	7.490E+04	7.944E+04	8.739E+04	9.647E+04
RADIOMETER 4	8.171E+04	9.874E+04	1.089E+05	1.316E+05	9.306E+04	1.033E+05	1.112E+05	1.135E+05
RADIOMETER 5	N/A	N/A	N/A	N/A	N/A	N/A	N/A	N/A

POINT #	2211	2212	2213	2214	2215
WA3 (KG/S)	9.41	9.42	9.42	9.42	9.42
WAB (KG/S)	7.98	7.98	7.99	7.99	7.98
TT3 (K)	837.	836.	837.	838.	837.
PT3 (MPA)	1.654	1.711	1.722	1.712	1.713
(F/A) 4.0	0.0184	0.0214	0.0237	0.0257	0.0279
(F/A) PILOT	0.00354	0.00356	0.00355	0.00357	0.00358

RADIOMETER 1	5.901E+04	5.901E+04	6.355E+04	4.653E+04	6.923E+04
RADIOMETER 2	5.561E+04	5.788E+04	5.901E+04	6.242E+04	6.355E+04
RADIOMETER 3	1.146E+05	1.362E+05	1.578E+05	1.634E+05	1.736E+05
RADIOMETER 4	1.033E+05	1.316E+05	1.555E+05	1.804E+05	2.088E+05
RADIOMETER 5	8.398E+04	1.328E+05	1.226E+05	1.419E+05	1.634E+05

ALL RADIOMETER DATA IN WATTS/METER**2

DATA SUMMARY SHEET

*** RUN 24 ***

RADIOMETER DATA

** METRIC UNITS **

POINT #	2311	2312	2313	2314	2321	2322	2323
WAB (KG/S)	13.12	13.11	13.13	13.11	13.17	13.17	13.20
WAB (KG/S)	11.12	11.11	11.13	11.11	11.16	11.16	11.19
TT3 (K)	843.	843.	843.	844.	839.	841.	842.
PT3 (MPA)	2.384	2.407	2.405	2.395	2.398	2.408	2.390
(F/A) 4.0	0.0184	0.0217	0.0239	0.0257	0.0204	0.0227	0.0247
(F/A) PILOT	0.00355	0.00357	0.00361	0.00365	0.00518	0.00772	0.00959

RADIOMETER 1	5.107E+04	8.171E+04	6.696E+04	6.809E+04	1.203E+05	1.873E+05	2.406E+05
RADIOMETER 2	6.696E+04	6.809E+04	7.263E+04	7.377E+04	9.079E+04	1.566E+05	2.213E+05
RADIOMETER 3	1.192E+05	1.668E+05	2.383E+05	2.610E+05	1.260E+05	1.214E+05	1.487E+05
RADIOMETER 4	1.362E+05	1.918E+05	2.349E+05	2.735E+05	1.339E+05	1.464E+05	1.487E+05
RADIOMETER 5	9.193E+04	1.237E+05	1.498E+05	1.793E+05	8.739E+04	9.760E+04	1.067E+05

POINT #	2411	2412	2413	2421	2421	2421	2422	2423
WAB (KG/S)	15.37	15.28	15.10	14.99	15.06	15.02	15.08	15.12
WAB (KG/S)	13.03	12.95	12.80	12.81	12.76	12.74	12.79	12.82
TT3 (K)	841.	841.	842.	844.	844.	841.	841.	842.
PT3 (MPA)	2.781	2.775	2.803	2.727	2.717	2.759	2.765	2.769
(F/A) 4.0	0.0184	0.0218	0.0234	0.0202	0.0201	0.0203	0.0223	0.0239
(F/A) PILOT	0.00359	0.00354	0.00369	0.00513	0.00500	0.00519	0.00730	0.00885

RADIOMETER 1	5.788E+04	5.788E+04	6.242E+04	7.490E+04	6.469E+04	7.490E+04	1.260E+05	1.668E+05
RADIOMETER 2	7.263E+04	7.490E+04	7.717E+04	1.146E+05	1.089E+05	1.214E+05	1.816E+05	2.599E+05
RADIOMETER 3	1.782E+05	1.770E+05	1.884E+05	1.067E+05	8.739E+04	1.770E+05	1.668E+05	1.895E+05
RADIOMETER 4	1.214E+05	1.691E+05	2.031E+05	1.351E+05	1.351E+05	1.226E+05	1.316E+05	1.419E+05
RADIOMETER 5	8.966E+04	1.169E+05	1.385E+05	9.987E+04	1.021E+05	9.647E+04	1.055E+05	1.158E+05

ALL RADIOMETER DATA IN WATTS/METER**2

DATA SUMMARY SHEET
*** RUN 24 ***
RADIOMETER DATA

** BRITISH UNITS **

POINT #	1111	1112	1113	1114	1121	1122	1123	1124
WA3 (LBM/S)	13.22	13.19	13.22	13.19	13.13	13.39	13.43	13.19
WAB (LBM/S)	11.20	11.18	11.21	11.18	11.13	11.36	11.38	11.19
TT3 (F)	893.	890.	893.	893.	893.	892.	890.	892.
PT3 (PSI)	147.580	146.950	148.080	147.240	147.140	149.610	149.920	146.660
(F/A) 4.0	0.0179	0.0210	0.0231	0.0252	0.0195	0.0215	0.0229	0.0248
(F/A) PILOT	0.00353	0.00356	0.00354	0.00357	0.00501	0.00694	0.00858	0.01020

RADIOMETER 1	3.960E+03	4.680E+03	5.760E+03	7.920E+03	1.872E+04	3.672E+04	4.248E+04	3.744E+04
RADIOMETER 2	9.000E+03	9.720E+03	9.720E+03	1.008E+04	1.728E+04	2.736E+04	3.312E+04	3.240E+04
RADIOMETER 3	1.836E+04	2.448E+04	3.528E+04	7.020E+04	3.528E+04	3.564E+04	4.032E+04	4.032E+04
RADIOMETER 4	2.196E+04	2.808E+04	3.240E+04	3.672E+04	2.520E+04	3.132E+04	3.240E+04	3.420E+04
RADIOMETER 5	N/A	N/A	N/A	N/A	N/A	N/A	N/A	N/A

POINT #	2111	2112	2113	2114	2121	2122	2123	2124
WA3 (LBM/S)	12.69	12.67	12.70	12.63	12.51	12.53	12.51	12.51
WAB (LBM/S)	10.75	10.74	10.76	10.71	10.60	10.63	10.60	10.61
TT3 (F)	1042.	1043.	1042.	1040.	1051.	1056.	1059.	1055.
PT3 (PSI)	149.680	149.180	148.020	151.810	150.220	148.030	149.460	148.060
(F/A) 4.0	0.0177	0.0210	0.0230	0.0252	0.0196	0.0219	0.0232	0.0240
(F/A) PILOT	0.00351	0.00353	0.00356	0.00355	0.00499	0.00746	0.00863	0.00954

RADIOMETER 1	5.040E+03	7.560E+03	7.560E+03	7.920E+03	9.000E+03	1.836E+04	2.700E+04	3.456E+04
RADIOMETER 2	1.188E+04	1.224E+04	1.224E+04	1.296E+04	1.656E+04	2.556E+04	2.952E+04	3.276E+04
RADIOMETER 3	2.160E+04	2.376E+04	3.096E+04	3.528E+04	2.376E+04	2.520E+04	2.772E+04	3.060E+04
RADIOMETER 4	2.592E+04	3.132E+04	3.456E+04	4.176E+04	2.952E+04	3.276E+04	3.528E+04	3.600E+04
RADIOMETER 5	N/A	N/A	N/A	N/A	N/A	N/A	N/A	N/A

POINT #	2211	2212	2213	2214	2215
WA3 (LBM/S)	20.75	20.77	20.77	20.76	20.76
WAB (LBM/S)	17.58	17.60	17.61	17.61	17.60
TT3 (F)	1047.	1045.	1048.	1048.	1048.
PT3 (PSI)	239.820	248.210	249.750	248.310	248.440
(F/A) 4.0	0.0184	0.0214	0.0237	0.0257	0.0279
(F/A) PILOT	0.00354	0.00356	0.00355	0.00357	0.00358

RADIOMETER 1	1.872E+04	1.872E+04	2.016E+04	1.476E+04	2.196E+04
RADIOMETER 2	1.764E+04	1.836E+04	1.872E+04	1.980E+04	2.016E+04
RADIOMETER 3	3.636E+04	4.320E+04	5.004E+04	5.184E+04	5.508E+04
RADIOMETER 4	3.276E+04	4.176E+04	4.932E+04	5.724E+04	6.624E+04
RADIOMETER 5	2.664E+04	4.212E+04	3.888E+04	4.500E+04	5.184E+04

ALL RADIOMETER DATA IN BTU/HR/FT**2

DATA SUMMARY SHEET

*** RUN 24 ***

RADIOMETER DATA

** BRITISH UNITS **

POINT #	2311	2312	2313	2314	2321	2322	2323
WA3 (LBM/S)	28.92	28.90	28.95	28.90	29.03	29.03	29.11
WAB (LBM/S)	24.52	24.50	24.54	24.50	24.61	24.61	24.68
TT3 (F)	1058.	1058.	1058.	1060.	1051.	1054.	1056.
PT3 (PSI)	345.820	349.090	348.810	347.370	347.810	349.190	346.650
(F/A) 4.0	0.0184	0.0217	0.0239	0.0257	0.0204	0.0227	0.0247
(F/A) PILOT	0.00355	0.00357	0.00361	0.00365	0.00518	0.00772	0.00959

RADIOMETER 1	1.620E+04	2.592E+04	2.124E+04	2.160E+04	3.816E+04	5.940E+04	7.632E+04
RADIOMETER 2	2.124E+04	2.160E+04	2.304E+04	2.340E+04	2.880E+04	4.968E+04	7.020E+04
RADIOMETER 3	3.780E+04	5.292E+04	7.560E+04	8.280E+04	3.996E+04	3.852E+04	4.716E+04
RADIOMETER 4	4.320E+04	6.084E+04	7.452E+04	8.676E+04	4.248E+04	4.644E+04	4.716E+04
RADIOMETER 5	2.916E+04	3.924E+04	4.752E+04	5.688E+04	2.772E+04	3.096E+04	3.384E+04

POINT #	2411	2412	2413	2421	2421	2421	2422	2423
WA3 (LBM/S)	33.89	33.69	33.30	33.06	33.20	33.12	33.24	33.34
WAB (LBM/S)	28.73	28.56	28.23	28.23	28.74	28.09	28.19	28.26
TT3 (F)	1053.	1055.	1056.	1060.	1060.	1054.	1054.	1055.
PT3 (PSI)	403.380	402.510	406.520	395.570	394.030	400.100	401.100	401.670
(F/A) 4.0	0.0184	0.0218	0.0234	0.0202	0.0201	0.0203	0.0223	0.0239
(F/A) PILOT	0.00359	0.00354	0.00369	0.00513	0.00500	0.00519	0.00730	0.00885

RADIOMETER 1	1.836E+04	1.836E+04	1.980E+04	2.376E+04	2.052E+04	2.376E+04	3.996E+04	5.292E+04
RADIOMETER 2	2.304E+04	2.376E+04	2.448E+04	3.636E+04	3.486E+04	3.852E+04	5.760E+04	8.244E+04
RADIOMETER 3	5.652E+04	5.616E+04	5.976E+04	3.684E+04	2.772E+04	5.616E+04	5.292E+04	6.012E+04
RADIOMETER 4	3.852E+04	5.364E+04	6.444E+04	4.284E+04	4.284E+04	3.888E+04	4.176E+04	4.500E+04
RADIOMETER 5	2.844E+04	3.708E+04	4.392E+04	3.168E+04	3.240E+04	3.060E+04	3.348E+04	3.672E+04

ALL RADIOMETER DATA IN BTU/HR/FT**2

DATA SUMMARY SHEET

*** RUN 25 ***

RADIOMETER DATA

** METRIC UNITS **

POINT #	2111	2112	2113	2114	2115	2121	2122	2123	2124	2125
WA3 (KG/S)	5.63	5.63	5.63	5.63	5.63	5.63	5.63	5.63	5.63	5.63
WAB (KG/S)	4.77	4.77	4.77	4.77	4.77	4.77	4.77	4.77	4.77	4.77
TT3 (K)	841.	839.	839.	839.	840.	840.	844.	836.	837.	839.
PT3 (MPA)	1.022	1.023	1.019	1.029	1.019	1.033	1.015	1.030	1.054	1.043
(F/A) 4.0	0.0179	0.0212	0.0232	0.0253	0.0273	0.0195	0.0215	0.0230	0.0246	0.0261
(F/A) PILOT	0.00351	0.00357	0.00352	0.00355	0.00351	0.00505	0.00688	0.00855	0.01001	0.01166

RADIOMETER 1	N/A	N/A	N/A	N/A	N/A	N/A	N/A	N/A	N/A	N/A
RADIOMETER 2	5.232E+04	5.118E+04	5.130E+04	5.243E+04	5.300E+04	7.173E+04	1.007E+05	1.250E+05	1.395E+05	1.545E+05
RADIOMETER 3	8.898E+04	9.942E+04	1.097E+05	1.188E+05	1.272E+05	9.749E+04	1.027E+05	1.070E+05	1.151E+05	1.209E+05
RADIOMETER 4	1.407E+05	1.651E+05	1.807E+05	2.114E+05	2.302E+05	1.542E+05	1.530E+05	1.716E+05	1.858E+05	2.012E+05
RADIOMETER 5	8.727E+04	9.942E+04	1.108E+05	1.201E+05	1.303E+05	9.363E+04	9.749E+04	1.045E+05	1.103E+05	1.161E+05

POINT #	2211	2212	2213	2214	2215	2221	2222	2223	2224	2225
WA3 (KG/S)	9.35	9.35	9.35	9.35	9.35	9.35	9.35	9.35	9.35	9.35
WAB (KG/S)	7.93	7.93	7.93	7.93	7.93	7.93	7.93	7.93	7.93	7.93
TT3 (K)	832.	838.	836.	836.	840.	837.	839.	839.	840.	838.
PT3 (MPA)	1.736	1.724	1.697	1.729	1.722	1.700	1.686	1.728	1.728	1.725
(F/A) 4.0	0.0183	0.0213	0.0233	0.0255	0.0274	0.0196	0.0218	0.0233	0.0248	0.0266
(F/A) PILOT	0.00349	0.00350	0.00348	0.00350	0.00351	0.00504	0.00713	0.00868	0.01006	0.01179

RADIOMETER 1	N/A	N/A	N/A	N/A	N/A	N/A	N/A	N/A	N/A	N/A
RADIOMETER 2	5.606E+04	5.833E+04	5.913E+04	6.026E+04	6.253E+04	8.864E+04	1.284E+05	1.629E+05	1.845E+05	2.218E+05
RADIOMETER 3	1.228E+05	1.406E+05	1.523E+05	1.685E+05	1.819E+05	1.231E+05	1.333E+05	1.437E+05	1.537E+05	1.601E+05
RADIOMETER 4	1.858E+05	2.365E+05	2.715E+05	3.181E+05	3.399E+05	2.109E+05	2.211E+05	2.479E+05	2.523E+05	2.721E+05
RADIOMETER 5	1.035E+05	1.223E+05	1.433E+05	1.559E+05	1.707E+05	1.128E+05	1.225E+05	1.307E+05	1.395E+05	1.507E+05

POINT #	2311	2312	2313	2314	2315	2321	2323	2325
WA3 (KG/S)	13.18	13.18	13.18	13.18	13.18	13.18	13.18	13.18
WAB (KG/S)	11.18	11.18	11.18	11.18	11.18	11.18	11.18	11.18
TT3 (K)	845.	836.	833.	840.	840.	841.	842.	842.
PT3 (MPA)	2.406	2.400	2.411	2.389	2.412	2.445	2.415	2.437
(F/A) 4.0	0.0180	0.0211	0.0232	0.0253	0.0272	0.0194	0.0231	0.0261
(F/A) PILOT	0.00345	0.00344	0.00340	0.00340	0.00342	0.00492	0.00846	0.01151

RADIOMETER 1	3.609E+04	3.756E+04	3.802E+04	3.700E+04	4.018E+04	3.722E+04	1.783E+05	3.292E+05
RADIOMETER 2	3.995E+04	4.483E+04	5.164E+04	5.618E+04	6.707E+04	8.682E+04	1.664E+05	3.623E+05
RADIOMETER 3	N/A	N/A	N/A	N/A	N/A	N/A	N/A	N/A
RADIOMETER 4	1.478E+05	1.780E+05	2.003E+05	2.129E+05	2.454E+05	1.414E+05	1.659E+05	1.943E+05
RADIOMETER 5	1.358E+05	1.669E+05	1.936E+05	1.966E+05	2.540E+05	1.545E+05	1.686E+05	1.924E+05

ALL RADIOMETER DATA IN WATTS/METER**2

DATA SUMMARY SHEET

*** RUN 25 ***

RADIOMETER DATA

** METRIC UNITS **

POINT #	2411	2413	2415	2421	2422	2423	2424
WA3 (KG/S)	15.11	15.11	15.11	15.11	15.11	15.11	15.11
WAB (KG/S)	12.81	12.81	12.81	12.81	12.81	12.81	12.81
TT3 (K)	843.	842.	843.	842.	842.	842.	843.
PT3 (MPA)	2.732	2.759	2.733	2.748	2.822	2.753	2.742
(F/A) 4.0	0.0183	0.0231	0.0273	0.0194	0.0207	0.0230	0.0246
(F/A) PILOT	0.00357	0.00342	0.00350	0.00491	0.00643	0.00849	0.00999

RADIOMETER 1	6.367E+04	5.913E+04	6.049E+04	9.056E+04	1.762E+05	1.762E+05	1.160E+05
RADIOMETER 2	4.585E+04	4.789E+04	6.389E+04	6.832E+04	1.863E+05	1.863E+05	2.543E+05
RADIOMETER 3	N/A	N/A	N/A	N/A	N/A	N/A	N/A
RADIOMETER 4	1.439E+05	1.812E+05	2.279E+05	1.560E+05	1.775E+05	1.775E+05	1.879E+05
RADIOMETER 5	1.446E+05	2.073E+05	2.830E+05	1.630E+05	1.843E+05	1.843E+05	1.943E+05

ALL RADIOMETER DATA IN WATTS/METER**2

DATA SUMMARY SHEET

*** RUN 25 ***

RADIOMETER DATA

** BRITISH UNITS **

POINT #	2111	2112	2113	2114	2115	2121	2122	2123	2124	2125
WA3 (LBM/S)	12.41	12.41	12.41	12.41	12.41	12.41	12.41	12.41	12.41	12.41
WAB (LBM/S)	10.52	10.52	10.52	10.52	10.52	10.52	10.52	10.52	10.52	10.52
TT3 (F)	1053.	1051.	1051.	1051.	1052.	1053.	1060.	1046.	1048.	1051.
PT3 (PSI)	148.24	148.39	147.73	149.22	147.82	149.89	147.17	149.37	152.86	151.33
(F/A) 4.0	0.0179	0.0212	0.0232	0.0253	0.0273	0.0195	0.0215	0.0230	0.0246	0.0261
(F/A) PILOT	0.00351	0.00357	0.00352	0.00355	0.00351	0.00505	0.00688	0.00855	0.01001	0.01166

RADIOMETER 1	N/A	N/A	N/A	N/A	N/A	N/A	N/A	N/A	N/A	N/A
RADIOMETER 2	1.660E+04	1.624E+04	1.627E+04	1.663E+04	1.681E+04	2.275E+04	3.193E+04	3.964E+04	4.424E+04	4.900E+04
RADIOMETER 3	2.822E+04	3.154E+04	3.481E+04	3.769E+04	4.036E+04	3.092E+04	3.258E+04	3.395E+04	3.650E+04	3.834E+04
RADIOMETER 4	4.464E+04	5.238E+04	5.731E+04	6.707E+04	7.301E+04	4.892E+04	4.853E+04	5.443E+04	5.893E+04	6.383E+04
RADIOMETER 5	2.768E+04	3.154E+04	3.514E+04	3.809E+04	4.133E+04	2.970E+04	3.092E+04	3.316E+04	3.499E+04	3.683E+04

POINT #	2211	2212	2213	2214	2215	2221	2222	2223	2224	2225
WA3 (LBM/S)	20.62	20.62	20.62	20.62	20.62	20.62	20.62	20.62	20.62	20.62
WAB (LBM/S)	17.48	17.48	17.48	17.48	17.48	17.48	17.48	17.48	17.48	17.48
TT3 (F)	1038.	1049.	1045.	1045.	1052.	1047.	1051.	1051.	1052.	1049.
PT3 (PSI)	251.80	250.04	246.15	250.75	249.82	246.52	244.52	250.66	250.69	250.17
(F/A) 4.0	0.0183	0.0213	0.0233	0.0255	0.0274	0.0196	0.0218	0.0233	0.0248	0.0266
(F/A) PILOT	0.00349	0.00350	0.00348	0.00350	0.00351	0.00504	0.00713	0.00868	0.01006	0.01179

RADIOMETER 1	N/A	N/A	N/A	N/A	N/A	N/A	N/A	N/A	N/A	N/A
RADIOMETER 2	1.778E+04	1.850E+04	1.876E+04	1.912E+04	1.984E+04	2.812E+04	4.072E+04	5.166E+04	5.854E+04	7.034E+04
RADIOMETER 3	3.895E+04	4.460E+04	4.831E+04	5.346E+04	5.771E+04	3.906E+04	4.230E+04	4.558E+04	4.874E+04	5.080E+04
RADIOMETER 4	5.893E+04	7.502E+04	8.611E+04	1.009E+05	1.078E+05	6.689E+04	7.013E+04	7.862E+04	8.003E+04	8.633E+04
RADIOMETER 5	3.263E+04	3.881E+04	4.547E+04	4.946E+04	5.414E+04	3.578E+04	3.884E+04	4.147E+04	4.424E+04	4.781E+04

POINT #	2311	2312	2313	2314	2315	2321	2323	2325
WA3 (LBM/S)	29.06	29.06	29.06	29.06	29.06	29.06	29.06	29.06
WAB (LBM/S)	24.64	24.64	24.64	24.64	24.64	24.64	24.64	24.64
TT3 (F)	1062.	1046.	1040.	1052.	1053.	1054.	1056.	1056.
PT3 (PSI)	348.98	348.14	349.74	346.45	349.81	354.56	350.20	353.40
(F/A) 4.0	0.0180	0.0211	0.0232	0.0253	0.0272	0.0194	0.0231	0.0261
(F/A) PILOT	0.00345	0.00344	0.00340	0.00340	0.00342	0.00492	0.00846	0.01151

RADIOMETER 1	1.145E+04	1.192E+04	1.206E+04	1.174E+04	1.274E+04	1.181E+04	5.656E+04	1.044E+05
RADIOMETER 2	1.267E+04	1.422E+04	1.638E+04	1.782E+04	2.128E+04	2.754E+04	5.278E+04	1.149E+05
RADIOMETER 3	N/A	N/A	N/A	N/A	N/A	N/A	N/A	N/A
RADIOMETER 4	4.687E+04	5.645E+04	6.354E+04	6.754E+04	7.783E+04	4.486E+04	5.263E+04	6.163E+04
RADIOMETER 5	4.309E+04	5.296E+04	6.142E+04	6.235E+04	8.057E+04	4.900E+04	5.350E+04	6.102E+04

ALL RADIOMETER DATA IN BTU/HR/FT**2

DATA SUMMARY SHEET

*** RUN 25 ***

RADIOMETER DATA

** BRITISH UNITS **

POINT #	2411	2413	2415	2421	2422	2423	2424
WA3 (LBM/S)	33.31	33.31	33.31	33.31	33.31	33.31	33.31
WAB (LBM/S)	28.24	28.24	28.24	28.24	28.24	28.24	28.24
TT3 (F)	1058.	1057.	1058.	1057.	1056.	1055.	1057.
PT3 (PSI)	396.31	400.14	396.42	398.57	409.30	399.27	397.65
(F/A) 4.0	0.0183	0.0231	0.0273	0.0194	0.0207	0.0230	0.0246
(F/A) PILOT	0.00357	0.00342	0.00350	0.00491	0.00643	0.00849	0.00999

RADIOMETER 1	2.020E+04	1.876E+04	1.919E+04	2.873E+04	5.591E+04	5.591E+04	3.679E+04
RADIOMETER 2	1.454E+04	1.519E+04	2.027E+04	2.167E+04	5.911E+04	5.911E+04	8.068E+04
RADIOMETER 3	N/A	N/A	N/A	N/A	N/A	N/A	N/A
RADIOMETER 4	4.565E+04	5.749E+04	7.229E+04	4.950E+04	5.630E+04	5.630E+04	5.962E+04
RADIOMETER 5	4.586E+04	6.577E+04	8.978E+04	5.170E+04	5.846E+04	5.846E+04	6.163E+04

ALL RADIOMETER DATA IN BTU/HR/FT**2

DATA SUMMARY SHEET

*** RUN 26 ***

RADIOMETER DATA

** BRITISH UNITS **

POINT #	5	6	7	8	9
WA3 (LBM/S)	12.24	16.44	20.94	21.25	20.44
WAB (LBM/S)	10.37	13.94	17.75	18.00	17.32
TT3 (F)	1076.	1071.	1058.	1060.	1064.
PT3 (PSI)	150.00	199.00	244.00	246.00	246.00
(F/A) 4.0	0.0189	0.0176	0.0180	0.0205	0.0239
(F/A) PILOT	0.00383	0.00352	0.00358	0.00352	0.00352

RADIOMETER 1	1.242E+04	1.224E+04	1.260E+04	1.368E+04	1.116E+04
RADIOMETER 2	1.476E+04	1.800E+04	1.872E+04	1.980E+04	2.160E+04
RADIOMETER 3	N/A	N/A	N/A	N/A	N/A
RADIOMETER 4	4.284E+04	4.860E+04	5.148E+04	6.336E+04	7.380E+04
RADIOMETER 5	3.690E+04	4.068E+04	4.284E+04	5.220E+04	5.976E+04

ALL RADIOMETER DATA IN BTU/HR/FT**2

DATA SUMMARY SHEET

*** RUN 26 ***

RADIOMETER DATA

** METRIC UNITS **

POINT #	5	6	7	8	9
WA3 (KG/S)	5.55	7.46	9.50	9.64	9.27
WAB (KG/S)	4.70	6.32	8.05	8.17	7.86
TT3 (K)	853.	850.	843.	844.	846.
PT3 (MPA)	1.034	1.372	1.682	1.696	1.696
(F/A) 4.0	0.0189	0.0176	0.0180	0.0205	0.0239
(F/A) PILOT	0.00383	0.00352	0.00358	0.00352	0.00352
<hr/>					
RADIOMETER 1	3.915E+04	3.859E+04	3.972E+04	4.313E+04	3.518E+04
RADIOMETER 2	4.653E+04	5.674E+04	5.901E+04	6.242E+04	6.809E+04
RADIOMETER 3	N/A	N/A	N/A	N/A	N/A
RADIOMETER 4	1.351E+05	1.532E+05	1.623E+05	1.997E+05	2.326E+05
RADIOMETER 5	1.163E+05	1.282E+05	1.351E+05	1.646E+05	1.884E+05

ALL RADIOMETER DATA IN WATTS/METER**2

LINER THERMOCOUPLE DATA

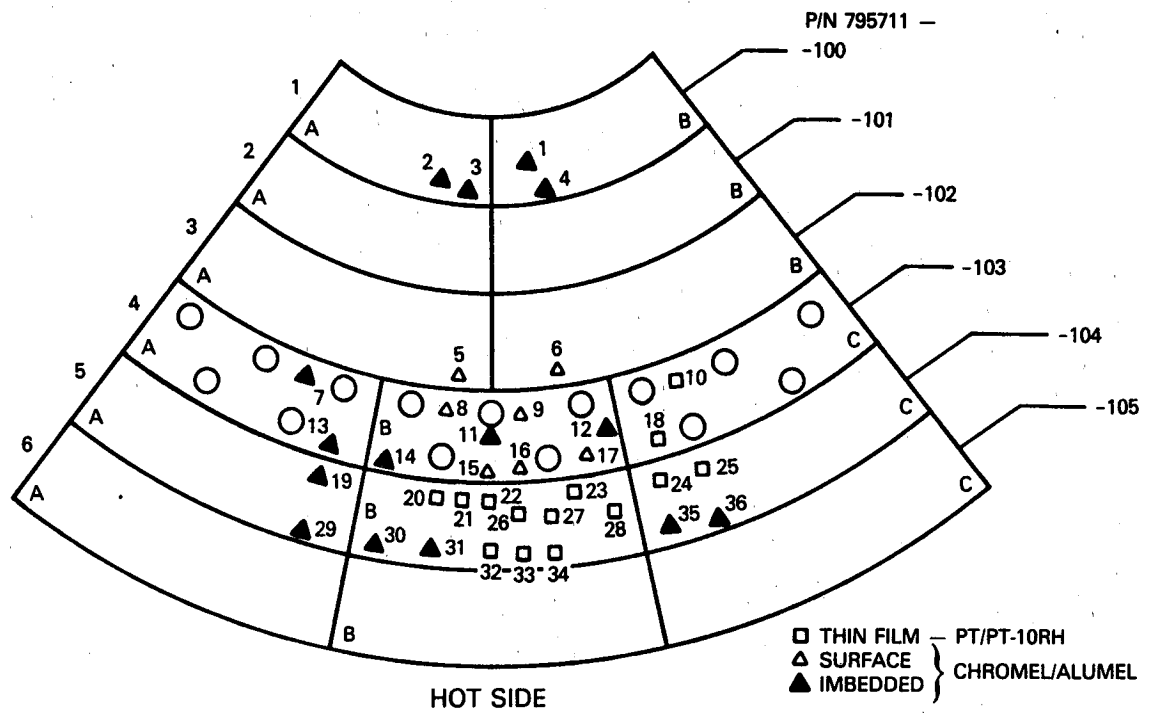


Figure C-2 Thermocouple Installation Layout for Run 24

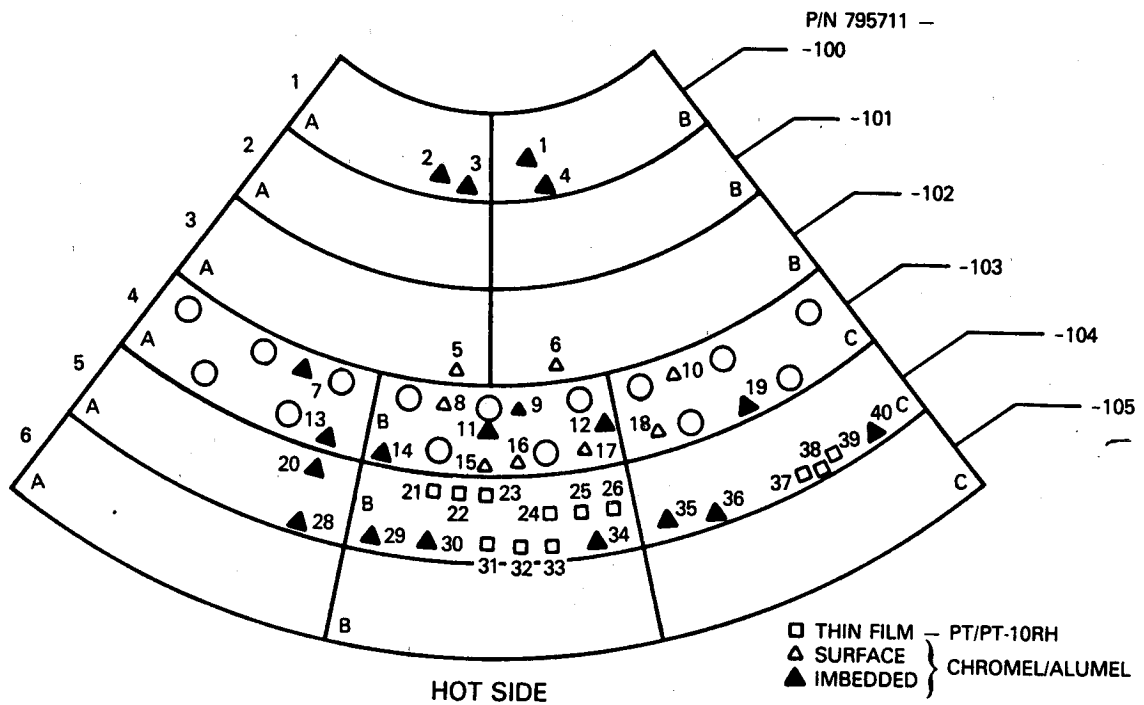


Figure C-3 Thermocouple Installation Layout for Run 25

DATA SUMMARY SHEET

*** RUN 24 ***

INNER LINER THERMOCOUPLE DATA ** METRIC UNITS **

POINT #	1111	1112	1113	1114	1121	1122	1123	1124
WA3 (KG/S)	6.00	5.98	6.00	5.98	5.95	6.07	6.09	5.98
WAB (KG/S)	5.08	5.07	5.09	5.07	5.05	5.15	5.16	5.07
TT3 (K)	752.	750.	751.	751.	751.	751.	750.	751.
PT3 (MPA)	1.018	1.013	1.021	1.015	1.014	1.032	1.034	1.011
(F/A) 4.0	0.0179	0.0210	0.0231	0.0252	0.0195	0.0215	0.0229	0.0248
(F/A) PILOT	0.00353	0.00356	0.00354	0.00357	0.00501	0.00694	0.00858	0.01020

T/C # 1	771.	771.	775.	776.	787.	794.	804.	841.
T/C # 2	867.	870.	871.	869.	898.	899.	899.	874.
T/C # 3	839.	843.	844.	841.	857.	914.	944.	914.
T/C # 4	790.	791.	796.	805.	809.	792.	804.	899.
T/C # 5	816.	821.	828.	828.	817.	820.	828.	835.
T/C # 6	848.	857.	867.	872.	888.	905.	915.	912.
T/C # 8	796.	800.	806.	807.	800.	801.	802.	803.
T/C # 9	762.	764.	770.	771.	765.	768.	769.	773.
T/C #10	941.	972.	1008.	1038.	1040.	1134.	1165.	1203.
T/C #11	815.	822.	829.	833.	834.	856.	875.	886.
T/C #12	800.	808.	817.	820.	810.	819.	820.	819.
T/C #13	901.	913.	919.	923.	927.	984.	1023.	1066.
T/C #14	879.	891.	900.	910.	884.	900.	902.	909.
T/C #15	825.	833.	841.	847.	846.	870.	891.	905.
T/C #16	848.	859.	872.	893.	859.	836.	840.	863.
T/C #17	907.	929.	940.	950.	929.	958.	962.	972.
T/C #18	846.	861.	878.	895.	881.	911.	937.	970.
T/C #19	778.	781.	785.	787.	782.	787.	792.	799.
T/C #21	808.	814.	819.	824.	811.	814.	815.	816.
T/C #22	823.	833.	842.	848.	832.	841.	844.	847.
T/C #23	948.	955.	968.	968.	956.	988.	992.	985.
T/C #24	776.	786.	796.	802.	786.	791.	795.	803.
T/C #28	801.	806.	814.	819.	810.	829.	832.	827.
T/C #29	842.	852.	857.	862.	861.	874.	890.	913.
T/C #30	866.	880.	891.	901.	873.	891.	895.	904.
T/C #31	931.	953.	967.	977.	946.	956.	959.	958.
T/C #32	843.	853.	862.	872.	857.	876.	894.	916.
T/C #34	904.	929.	941.	961.	921.	921.	932.	970.

THERMOCOUPLE TEMPERATURE UNITS °K

DATA SUMMARY SHEET

*** RUN 24 ***

INNER LINER THERMOCOUPLE DATA ** METRIC UNITS **

POINT #	2111	2112	2113	2114	2121	2122	2123	2124
WA3 (KG/S)	5.76	5.75	5.76	5.73	5.68	5.68	5.67	5.68
WAB (KG/S)	4.88	4.87	4.88	4.86	4.81	4.82	4.81	4.81
TT3 (K)	834.	835.	834.	833.	839.	842.	843.	842.
PT3 (MPA)	1.032	1.029	1.021	1.047	1.036	1.021	1.030	1.021
(F/A) 4.0	0.0177	0.0210	0.0230	0.0252	0.0196	0.0219	0.0232	0.0240
(F/A) PILOT	0.00351	0.00353	0.00356	0.00355	0.00499	0.00746	0.00863	0.00954

T/C # 1	856.	859.	860.	861.	873.	901.	913.	921.
T/C # 2	937.	946.	950.	950.	984.	1009.	1008.	1002.
T/C # 3	925.	928.	929.	927.	955.	980.	992.	1001.
T/C # 4	880.	897.	908.	905.	907.	937.	953.	980.
T/C # 5	904.	902.	907.	912.	909.	917.	925.	928.
T/C # 6	928.	943.	950.	965.	960.	993.	1005.	1009.
T/C # 8	N/A	N/A	N/A	N/A	N/A	N/A	N/A	N/A
T/C # 9	846.	850.	853.	857.	855.	863.	866.	867.
T/C #10	1051.	1040.	1058.	1057.	1147.	1266.	1292.	1306.
T/C #11	902.	909.	912.	920.	928.	963.	976.	982.
T/C #12	883.	896.	902.	914.	897.	906.	910.	910.
T/C #13	982.	989.	994.	1000.	1017.	1086.	1115.	1141.
T/C #14	953.	966.	974.	987.	975.	999.	1010.	1015.
T/C #15	913.	919.	925.	934.	938.	973.	988.	993.
T/C #16	909.	939.	952.	969.	923.	929.	935.	932.
T/C #17	974.	1018.	1028.	1051.	1000.	1022.	1032.	1039.
T/C #18	972.	975.	976.	1000.	999.	1042.	1059.	1080.
T/C #19	862.	866.	868.	871.	873.	887.	893.	895.
T/C #21	892.	899.	903.	910.	903.	909.	913.	914.
T/C #22	898.	909.	915.	923.	908.	917.	920.	924.
T/C #23	1015.	1025.	1028.	1030.	992.	991.	993.	990.
T/C #24	871.	879.	883.	893.	882.	893.	898.	899.
T/C #28	891.	895.	898.	904.	898.	907.	912.	912.
T/C #29	931.	936.	938.	942.	950.	979.	992.	1001.
T/C #30	936.	950.	961.	974.	951.	971.	981.	985.
T/C #31	1007.	1029.	1041.	1051.	1027.	1042.	1048.	1049.
T/C #32	931.	941.	944.	955.	939.	954.	961.	963.
T/C #34	965.	995.	1008.	1026.	977.	996.	1005.	1010.

THERMOCOUPLE TEMPERATURE UNITS °K

DATA SUMMARY SHEET
 *** RUN 24 ***
 INNER LINER THERMOCOUPLE DATA ** METRIC UNITS **

POINT #	2211	2212	2213	2214	2215
WA3 (KG/S)	9.41	9.42	9.42	9.42	9.42
WAB (KG/S)	7.98	7.98	7.99	7.99	7.98
TT3 (K)	837.	836.	837.	838.	837.
PT3 (MPA)	1.654	1.711	1.722	1.712	1.713
(F/A) 4.0	0.0184	0.0214	0.0237	0.0257	0.0279
(F/A) PILOT	0.00354	0.00356	0.00355	0.00357	0.00358

T/C # 1	877.	879.	882.	886.	891.
T/C # 2	965.	966.	967.	969.	970.
T/C # 3	938.	939.	938.	941.	940.
T/C # 4	966.	968.	975.	982.	992.
T/C # 5	903.	908.	913.	918.	925.
T/C # 6	965.	981.	995.	1005.	1012.
T/C # 8	N/A	N/A	N/A	N/A	N/A
T/C # 9	850.	854.	858.	863.	867.
T/C #10	1113.	1060.	1077.	1084.	1093.
T/C #11	912.	922.	928.	938.	948.
T/C #12	905.	916.	929.	936.	941.
T/C #13	1006.	1016.	1027.	1037.	1043.
T/C #14	965.	978.	988.	1003.	1015.
T/C #15	930.	938.	946.	959.	968.
T/C #16	933.	956.	955.	968.	984.
T/C #17	1033.	1070.	1097.	1111.	1115.
T/C #18	991.	979.	990.	1002.	1009.
T/C #19	870.	876.	882.	889.	896.
T/C #21	903.	909.	914.	924.	927.
T/C #22	900.	905.	912.	919.	921.
T/C #23	1067.	1093.	1110.	1128.	1140.
T/C #24	N/A	N/A	N/A	N/A	N/A
T/C #28	910.	915.	924.	931.	939.
T/C #29	941.	951.	962.	966.	977.
T/C #30	940.	953.	965.	979.	995.
T/C #31	1009.	1028.	1042.	1058.	1074.
T/C #32	N/A	N/A	N/A	N/A	N/A
T/C #34	N/A	N/A	N/A	N/A	N/A

THERMOCOUPLE TEMPERATURE UNITS °K

DATA SUMMARY SHEET

*** RUN 24 ***

INNER LINER THERMOCOUPLE DATA ** METRIC UNITS **

POINT #	2311	2312	2313	2314	2321	2322	2323
W43 (KG/S)	13.12	13.11	13.13	13.11	13.17	13.17	13.20
W4B (KG/S)	11.12	11.11	11.13	11.11	11.16	11.16	11.19
TT3 (K)	843.	843.	843.	844.	839.	841.	842.
PT3 (MPA)	2.384	2.407	2.405	2.395	2.398	2.408	2.390
(F/A) 4.0	0.0184	0.0217	0.0239	0.0257	0.0204	0.0227	0.0247
(F/A) PILOT	0.00355	0.00357	0.00361	0.00365	0.00518	0.00772	0.00959

T/C # 1	883.	889.	894.	896.	908.	930.	946.
T/C # 2	987.	996.	993.	1000.	1032.	1082.	1091.
T/C # 3	954.	959.	956.	964.	991.	1020.	1016.
T/C # 4	980.	991.	997.	1000.	1023.	1090.	1142.
T/C # 5	928.	951.	941.	947.	952.	942.	939.
T/C # 6	983.	998.	1008.	1009.	991.	1016.	1038.
T/C # 8	N/A	N/A	N/A	N/A	N/A	N/A	N/A
T/C # 9	857.	862.	871.	874.	855.	861.	864.
T/C #10	1178.	1111.	1177.	N/A	N/A	N/A	N/A
T/C #11	930.	946.	959.	973.	936.	954.	963.
T/C #12	921.	928.	940.	941.	909.	915.	921.
T/C #13	1029.	1052.	1066.	1081.	1058.	1128.	1170.
T/C #14	990.	1013.	1026.	1039.	1019.	1049.	1066.
T/C #15	959.	952.	982.	997.	962.	972.	978.
T/C #16	942.	959.	982.	981.	924.	946.	943.
T/C #17	1054.	1079.	1098.	1094.	1006.	1039.	1063.
T/C #18	1022.	1013.	1010.	1020.	1018.	1054.	1067.
T/C #19	877.	887.	895.	904.	882.	892.	900.
T/C #21	920.	924.	929.	934.	929.	935.	944.
T/C #22	919.	928.	933.	939.	N/A	N/A	N/A
T/C #23	1086.	1123.	1115.	1156.	1040.	1034.	1024.
T/C #24	N/A	N/A	N/A	N/A	N/A	N/A	N/A
T/C #28	920.	927.	934.	939.	907.	915.	917.
T/C #29	954.	966.	977.	987.	983.	1012.	1027.
T/C #30	956.	982.	994.	1005.	968.	991.	1005.
T/C #31	1027.	1055.	1069.	1082.	1034.	1051.	1059.
T/C #32	N/A	N/A	N/A	N/A	N/A	N/A	N/A
T/C #34	N/A	N/A	N/A	N/A	N/A	N/A	N/A

THERMOCOUPLE TEMPERATURE UNITS °K

DATA SUMMARY SHEET

*** RUN 24 ***

INNER LINER THERMOCOUPLE DATA ** METRIC UNITS **

POINT #	2411	2412	2413	2421	2421	2421	2422	2423
WA3 (KG/S)	15.37	15.28	15.10	14.99	15.06	15.02	15.08	15.12
WAB (KG/S)	13.03	12.95	12.80	12.81	12.76	12.74	12.79	12.82
TT3 (K)	841.	841.	842.	844.	844.	841.	841.	842.
PT3 (MPA)	2.781	2.775	2.803	2.727	2.717	2.759	2.765	2.769
(F/A) 4.0	0.0184	0.0218	0.0234	0.0202	0.0201	0.0203	0.0223	0.0239
(F/A) PILOT	0.00359	0.00354	0.00369	0.00513	0.00500	0.00519	0.00730	0.00885

T/C # 1	877.	875.	880.	928.	928.	894.	935.	945.
T/C # 2	950.	943.	946.	1014.	1004.	1000.	1041.	1059.
T/C # 3	908.	905.	908.	982.	978.	942.	1013.	1023.
T/C # 4	960.	963.	972.	1033.	1029.	997.	1086.	1127.
T/C # 5	929.	939.	948.	948.	954.	918.	930.	940.
T/C # 6	971.	977.	988.	1004.	1002.	1004.	1026.	1047.
T/C # 8	N/A	N/A	N/A	N/A	N/A	N/A	N/A	N/A
T/C # 9	852.	858.	862.	860.	859.	854.	859.	863.
T/C #10	N/A	N/A	N/A	N/A	N/A	N/A	N/A	N/A
T/C #11	910.	924.	928.	933.	931.	912.	932.	948.
T/C #12	905.	910.	918.	919.	919.	915.	921.	926.
T/C #13	1028.	1048.	1057.	1085.	1081.	1077.	1139.	1180.
T/C #14	978.	998.	1008.	1026.	1024.	1007.	1048.	1072.
T/C #15	952.	961.	966.	965.	961.	946.	961.	974.
T/C #16	963.	956.	975.	933.	937.	956.	935.	931.
T/C #17	995.	1004.	1017.	1029.	1027.	1014.	1038.	1057.
T/C #18	1013.	N/A	N/A	1040.	1032.	N/A	N/A	N/A
T/C #19	875.	885.	891.	888.	887.	886.	895.	903.
T/C #21	919.	929.	937.	936.	935.	931.	942.	947.
T/C #22	N/A	N/A	N/A	N/A	N/A	N/A	N/A	N/A
T/C #23	N/A	N/A	N/A	N/A	N/A	N/A	N/A	N/A
T/C #24	N/A	N/A	N/A	N/A	N/A	N/A	N/A	N/A
T/C #28	N/A	N/A	N/A	N/A	N/A	N/A	N/A	N/A
T/C #29	961.	974.	979.	996.	995.	993.	1018.	1037.
T/C #30	945.	962.	975.	973.	970.	960.	986.	1002.
T/C #31	1014.	1043.	1055.	1031.	1029.	1018.	1028.	1042.
T/C #32	N/A	N/A	N/A	N/A	N/A	N/A	N/A	N/A
T/C #34	N/A	N/A	N/A	N/A	N/A	N/A	N/A	N/A

THERMOCOUPLE TEMPERATURE UNITS °K

DATA SUMMARY SHEET
*** RUN 24 ***
INNER LINER THERMOCOUPLE DATA ** BRITISH UNITS **

POINT #	1111	1112	1113	1114	1121	1122	1123	1124
WA3 (LBM/S)	13.22	13.19	13.22	13.19	13.13	13.39	13.43	13.19
WAB (LBM/S)	11.20	11.18	11.21	11.18	11.13	11.36	11.38	11.19
TT3 (F)	893.	890.	893.	893.	893.	892.	890.	892.
PT3 (PSI)	147.580	146.950	148.080	147.240	147.140	149.610	149.920	146.660
(F/A) 4.0	0.0179	0.0210	0.0231	0.0252	0.0195	0.0215	0.0229	0.0248
(F/A) PILOT	0.00353	0.00356	0.00354	0.00357	0.00501	0.00694	0.00858	0.01020

T/C # 1	928.	929.	935.	937.	957.	969.	988.	1054.
T/C # 2	1101.	1107.	1109.	1105.	1156.	1159.	1158.	1113.
T/C # 3	1050.	1057.	1059.	1054.	1083.	1186.	1240.	1185.
T/C # 4	962.	964.	972.	990.	996.	966.	987.	1158.
T/C # 5	1008.	1018.	1031.	1030.	1011.	1016.	1030.	1044.
T/C # 6	1067.	1083.	1101.	1111.	1139.	1170.	1188.	1182.
T/C # 8	973.	981.	991.	993.	981.	982.	985.	994.
T/C # 9	912.	916.	926.	928.	917.	922.	925.	931.
T/C #10	1235.	1289.	1354.	1408.	1413.	1582.	1637.	1706.
T/C #11	1008.	1020.	1032.	1040.	1042.	1082.	1115.	1135.
T/C #12	980.	996.	1010.	1017.	998.	1014.	1016.	1015.
T/C #13	1161.	1184.	1195.	1202.	1209.	1311.	1383.	1460.
T/C #14	1122.	1143.	1161.	1178.	1131.	1161.	1164.	1177.
T/C #15	1025.	1040.	1054.	1065.	1062.	1107.	1144.	1169.
T/C #16	1067.	1087.	1111.	1148.	1087.	1045.	1052.	1094.
T/C #17	1173.	1212.	1233.	1251.	1212.	1265.	1271.	1291.
T/C #18	1063.	1091.	1121.	1152.	1127.	1180.	1226.	1286.
T/C #19	941.	946.	954.	957.	948.	958.	966.	978.
T/C #21	995.	1005.	1014.	1023.	1001.	1005.	1007.	1010.
T/C #22	1022.	1041.	1056.	1066.	1038.	1054.	1060.	1065.
T/C #23	1247.	1260.	1283.	1283.	1262.	1318.	1326.	1314.
T/C #24	938.	954.	973.	984.	954.	964.	972.	986.
T/C #28	982.	990.	1006.	1014.	998.	1032.	1038.	1028.
T/C #29	1056.	1074.	1083.	1092.	1090.	1113.	1142.	1183.
T/C #30	1099.	1124.	1145.	1163.	1111.	1145.	1152.	1167.
T/C #31	1215.	1255.	1280.	1298.	1242.	1261.	1266.	1265.
T/C #32	1059.	1077.	1093.	1111.	1083.	1118.	1149.	1188.
T/C #34	1168.	1213.	1234.	1270.	1198.	1199.	1218.	1286.

THERMOCOUPLE TEMPERATURE UNITS °F

DATA SUMMARY SHEET

*** RUN 24 ***

INNER LINER THERMOCOUPLE DATA

** BRITISH UNITS **

POINT #	2111	2112	2113	2114	2121	2122	2123	2124
WA3 (LBM/S)	12.69	12.67	12.70	12.63	12.51	12.53	12.51	12.51
WAB (LBM/S)	10.75	10.74	10.76	10.71	10.60	10.63	10.60	10.61
TT3 (F)	1042.	1043.	1042.	1040.	1051.	1056.	1059.	1055.
PT3 (PSI)	149.680	149.180	148.020	151.810	150.220	148.030	149.460	148.060
(F/A) 4.0	0.0177	0.0210	0.0230	0.0252	0.0196	0.0219	0.0232	0.0240
(F/A) PILOT	0.00351	0.00353	0.00356	0.00355	0.00499	0.00746	0.00863	0.00954

T/C # 1	1082.	1087.	1089.	1090.	1112.	1162.	1183.	1198.
T/C # 2	1227.	1242.	1251.	1250.	1312.	1357.	1355.	1344.
T/C # 3	1206.	1210.	1212.	1208.	1259.	1305.	1326.	1343.
T/C # 4	1124.	1156.	1175.	1170.	1173.	1227.	1257.	1305.
T/C # 5	1168.	1164.	1173.	1182.	1176.	1192.	1206.	1211.
T/C # 6	1210.	1238.	1251.	1278.	1269.	1328.	1349.	1356.
T/C # 8	N/A	N/A	N/A	N/A	N/A	N/A	N/A	N/A
T/C # 9	1062.	1070.	1076.	1083.	1080.	1094.	1099.	1100.
T/C #10	1433.	1412.	1444.	1442.	1605.	1820.	1865.	1891.
T/C #11	1164.	1176.	1182.	1197.	1212.	1274.	1297.	1309.
T/C #12	1129.	1153.	1164.	1185.	1155.	1172.	1179.	1179.
T/C #13	1309.	1320.	1330.	1340.	1371.	1495.	1547.	1594.
T/C #14	1256.	1280.	1294.	1317.	1295.	1339.	1358.	1367.
T/C #15	1183.	1195.	1206.	1221.	1229.	1292.	1319.	1327.
T/C #16	1177.	1231.	1254.	1285.	1202.	1213.	1223.	1218.
T/C #17	1294.	1374.	1391.	1432.	1341.	1380.	1398.	1410.
T/C #18	1290.	1295.	1298.	1341.	1339.	1415.	1446.	1485.
T/C #19	1092.	1099.	1102.	1109.	1112.	1136.	1147.	1152.
T/C #21	1147.	1158.	1165.	1179.	1166.	1177.	1183.	1186.
T/C #22	1158.	1177.	1188.	1201.	1175.	1192.	1196.	1203.
T/C #23	1367.	1386.	1391.	1394.	1326.	1324.	1327.	1322.
T/C #24	1108.	1122.	1129.	1148.	1127.	1148.	1157.	1159.
T/C #28	1145.	1152.	1156.	1168.	1157.	1174.	1182.	1182.
T/C #29	1216.	1226.	1230.	1236.	1250.	1303.	1327.	1342.
T/C #30	1224.	1251.	1270.	1293.	1253.	1289.	1306.	1313.
T/C #31	1353.	1393.	1414.	1431.	1389.	1416.	1427.	1429.
T/C #32	1216.	1234.	1240.	1260.	1231.	1257.	1270.	1273.
T/C #34	1277.	1332.	1355.	1387.	1299.	1333.	1349.	1358.

THERMOCOUPLE TEMPERATURE UNITS °F

DATA SUMMARY SHEET
*** RUN 24 ***

INNER LINER THERMOCOUPLE DATA

** BRITISH UNITS **

POINT #	2211	2212	2213	2214	2215
WA3 (LBM/S)	20.75	20.77	20.77	20.76	20.76
WAB (LBM/S)	17.58	17.60	17.61	17.61	17.60
TT3 (F)	1047.	1045.	1048.	1048.	1048.
PT3 (PSI)	239.820	248.210	249.750	248.310	248.440
(F/A) 4.0	0.0184	0.0214	0.0237	0.0257	0.0279
(F/A) PILOT	0.00354	0.00356	0.00355	0.00357	0.00358

T/C # 1	1118.	1122.	1128.	1136.	1144.
T/C # 2	1277.	1279.	1281.	1285.	1286.
T/C # 3	1228.	1230.	1228.	1234.	1233.
T/C # 4	1279.	1283.	1295.	1308.	1326.
T/C # 5	1166.	1176.	1183.	1193.	1205.
T/C # 6	1277.	1307.	1332.	1349.	1361.
T/C # 8	N/A	N/A	N/A	N/A	N/A
T/C # 9	1070.	1078.	1085.	1094.	1100.
T/C #10	1543.	1448.	1479.	1492.	1508.
T/C #11	1182.	1200.	1211.	1229.	1247.
T/C #12	1170.	1190.	1212.	1225.	1234.
T/C #13	1351.	1369.	1388.	1408.	1418.
T/C #14	1278.	1301.	1318.	1345.	1368.
T/C #15	1215.	1228.	1243.	1267.	1282.
T/C #16	1221.	1261.	1260.	1282.	1312.
T/C #17	1400.	1467.	1515.	1539.	1548.
T/C #18	1325.	1302.	1322.	1344.	1357.
T/C #19	1106.	1118.	1129.	1141.	1153.
T/C #21	1166.	1176.	1186.	1203.	1209.
T/C #22	1160.	1170.	1183.	1194.	1198.
T/C #23	1461.	1507.	1538.	1572.	1593.
T/C #24	N/A	N/A	N/A	N/A	N/A
T/C #28	1179.	1188.	1204.	1216.	1231.
T/C #29	1235.	1253.	1272.	1279.	1299.
T/C #30	1232.	1256.	1278.	1303.	1331.
T/C #31	1357.	1390.	1416.	1445.	1474.
T/C #32	N/A	N/A	N/A	N/A	N/A
T/C #34	N/A	N/A	N/A	N/A	N/A

THERMOCOUPLE TEMPERATURE UNITS °F

DATA SUMMARY SHEET
*** RUN 24 ***

POINT #	2311	2312	2313	2314	2321	2322	2323
WAB (LBM/S)	28.92	28.90	28.95	28.90	29.03	29.03	29.11
WAB (LBM/S)	24.52	24.50	24.54	24.50	24.61	24.61	24.68
TT3 (F)	1058.	1058.	1058.	1060.	1051.	1054.	1056.
PT3 (PSI)	345.820	349.090	348.810	347.370	347.810	349.190	346.650
(F/A) 4.0	0.0184	0.0217	0.0239	0.0257	0.0204	0.0227	0.0247
(F/A) PILOT	0.00355	0.00357	0.00361	0.00365	0.00518	0.00772	0.00959
<hr/>							
T/C # 1	1130.	1141.	1150.	1154.	1176.	1215.	1243.
T/C # 2	1318.	1334.	1328.	1340.	1398.	1488.	1504.
T/C # 3	1258.	1266.	1262.	1276.	1324.	1376.	1369.
T/C # 4	1304.	1324.	1334.	1340.	1382.	1502.	1596.
T/C # 5	1211.	1251.	1234.	1244.	1253.	1236.	1231.
T/C # 6	1311.	1337.	1355.	1356.	1324.	1368.	1410.
T/C # 8	N/A	N/A	N/A	N/A	N/A	N/A	N/A
T/C # 9	1083.	1093.	1107.	1113.	1080.	1090.	1095.
T/C #10	1662.	1541.	1658.	N/A	N/A	N/A	N/A
T/C #11	1214.	1243.	1266.	1292.	1226.	1258.	1273.
T/C #12	1198.	1210.	1232.	1234.	1176.	1188.	1199.
T/C #13	1393.	1434.	1458.	1487.	1445.	1572.	1646.
T/C #14	1322.	1364.	1387.	1411.	1375.	1429.	1458.
T/C #15	1267.	1254.	1308.	1334.	1272.	1290.	1300.
T/C #16	1235.	1266.	1309.	1307.	1204.	1243.	1239.
T/C #17	1437.	1482.	1517.	1510.	1352.	1411.	1454.
T/C #18	1381.	1365.	1358.	1376.	1373.	1437.	1462.
T/C #19	1119.	1137.	1152.	1168.	1128.	1147.	1160.
T/C #21	1196.	1203.	1213.	1222.	1213.	1224.	1240.
T/C #22	1194.	1210.	1220.	1230.	N/A	N/A	N/A
T/C #23	1495.	1562.	1548.	1621.	1412.	1401.	1384.
T/C #24	N/A	N/A	N/A	N/A	N/A	N/A	N/A
T/C #28	1196.	1210.	1222.	1231.	1172.	1188.	1191.
T/C #29	1257.	1278.	1298.	1318.	1309.	1362.	1389.
T/C #30	1261.	1309.	1330.	1349.	1284.	1325.	1350.
T/C #31	1388.	1439.	1464.	1487.	1402.	1432.	1447.
T/C #32	N/A	N/A	N/A	N/A	N/A	N/A	N/A
T/C #34	N/A	N/A	N/A	N/A	N/A	N/A	N/A

THERMOCOUPLE TEMPERATURE UNITS °F

DATA SUMMARY SHEET
*** RUN 24 ***

INNER LINER THERMOCOUPLE DATA

** BRITISH UNITS **

POINT #	2411	2412	2413	2421	2421	2421	2422	2423
WA3 (LBM/S)	33.89	33.69	33.30	33.06	33.20	33.12	33.24	33.34
WAB (LBM/S)	28.73	28.56	28.23	28.23	28.14	28.09	28.19	28.26
TT3 (F)	1053.	1055.	1056.	1060.	1060.	1054.	1054.	1055.
PT3 (PSI)	403.380	402.510	406.520	395.570	394.030	400.100	401.100	401.670
(F/A) 4.0	0.0184	0.0218	0.0234	0.0202	0.0201	0.0203	0.0223	0.0239
(F/A) PILOT	0.00359	0.00354	0.00369	0.00513	0.00500	0.00519	0.00730	0.00885

T/C # 1	1119.	1116.	1124.	1211.	1211.	1149.	1224.	1242.
T/C # 2	1250.	1239.	1243.	1366.	1348.	1340.	1415.	1447.
T/C # 3	1175.	1170.	1174.	1309.	1301.	1237.	1363.	1382.
T/C # 4	1268.	1273.	1289.	1399.	1392.	1334.	1495.	1569.
T/C # 5	1212.	1231.	1246.	1247.	1257.	1194.	1215.	1233.
T/C # 6	1289.	1299.	1318.	1347.	1344.	1348.	1388.	1426.
T/C # 8	N/A	N/A	N/A	N/A	N/A	N/A	N/A	N/A
T/C # 9	1074.	1085.	1092.	1089.	1087.	1078.	1087.	1094.
T/C #10	N/A	N/A	N/A	N/A	N/A	N/A	N/A	N/A
T/C #11	1179.	1204.	1210.	1219.	1216.	1182.	1218.	1248.
T/C #12	1169.	1179.	1192.	1194.	1194.	1188.	1198.	1207.
T/C #13	1391.	1428.	1443.	1494.	1486.	1479.	1591.	1664.
T/C #14	1302.	1336.	1355.	1387.	1384.	1353.	1427.	1470.
T/C #15	1254.	1271.	1279.	1277.	1271.	1243.	1271.	1294.
T/C #16	1274.	1261.	1296.	1220.	1227.	1260.	1223.	1217.
T/C #17	1331.	1348.	1372.	1393.	1389.	1366.	1409.	1442.
T/C #18	1363.	N/A	N/A	1413.	1397.	N/A	N/A	N/A
T/C #19	1116.	1133.	1145.	1139.	1138.	1135.	1151.	1165.
T/C #21	1195.	1212.	1226.	1225.	1224.	1217.	1236.	1245.
T/C #22	N/A	N/A	N/A	N/A	N/A	N/A	N/A	N/A
T/C #23	N/A	N/A	N/A	N/A	N/A	N/A	N/A	N/A
T/C #24	N/A	N/A	N/A	N/A	N/A	N/A	N/A	N/A
T/C #28	N/A	N/A	N/A	N/A	N/A	N/A	N/A	N/A
T/C #29	1270.	1294.	1303.	1333.	1332.	1328.	1373.	1407.
T/C #30	1242.	1272.	1296.	1292.	1287.	1269.	1315.	1343.
T/C #31	1365.	1417.	1439.	1396.	1393.	1373.	1391.	1415.
T/C #32	N/A	N/A	N/A	N/A	N/A	N/A	N/A	N/A
T/C #34	N/A	N/A	N/A	N/A	N/A	N/A	N/A	N/A

THERMOCOUPLE TEMPERATURE UNITS °F

DATA SUMMARY SHEET
 *** RUN 25 ***
 INNER LINER THERMOCOUPLE DATA ** METRIC UNITS **

POINT #	2111	2112	2113	2114	2115	2121	2122	2123	2124	2125
WA3 (KG/S)	5.63	5.63	5.63	5.63	5.63	5.63	5.63	5.63	5.63	5.63
WA8 (KG/S)	4.77	4.77	4.77	4.77	4.77	4.77	4.77	4.77	4.77	4.77
TT3 (K)	841.	839.	839.	839.	840.	840.	844.	836.	837.	839.
PT3 (MPA)	1.022	1.023	1.019	1.029	1.019	1.033	1.015	1.030	1.054	1.043
(F/A) 4.0	0.0179	0.0212	0.0232	0.0253	0.0273	0.0195	0.0215	0.0230	0.0246	0.0261
(F/A) PILOT	0.00351	0.00357	0.00352	0.00355	0.00351	0.00505	0.00688	0.00855	0.01001	0.01166
<hr/>										
T/C # 3	890.	892.	892.	893.	895.	919.	946.	952.	969.	987.
T/C # 4	969.	961.	963.	960.	966.	983.	1058.	1067.	1077.	1109.
T/C #12	885.	890.	896.	904.	908.	887.	896.	890.	896.	900.
T/C #20	872.	877.	881.	884.	889.	878.	889.	887.	893.	900.
T/C #23	909.	918.	927.	933.	940.	921.	937.	935.	946.	956.
T/C #25	958.	975.	995.	1012.	1029.	979.	995.	1003.	1020.	1038.
T/C #26	906.	917.	922.	928.	932.	909.	915.	906.	909.	914.
T/C #27	940.	946.	953.	955.	963.	945.	952.	954.	966.	977.
T/C #28	911.	809.	817.	922.	957.	947.	969.	976.	990.	1004.
T/C #29	954.	965.	978.	988.	998.	981.	1003.	1015.	1034.	1052.
T/C #30	973.	990.	1000.	1012.	1022.	992.	1014.	1021.	1030.	1047.
T/C #31	920.	927.	934.	941.	950.	933.	952.	954.	967.	978.
T/C #33	950.	961.	981.	996.	1006.	967.	985.	993.	1007.	1025.
T/C #34	1010.	1052.	1070.	1088.	1099.	1016.	1020.	1014.	1018.	1024.
T/C #35	922.	931.	936.	940.	946.	935.	952.	958.	974.	989.
T/C #36	959.	967.	980.	987.	994.	969.	980.	984.	995.	1015.
T/C #38	886.	886.	893.	895.	898.	882.	885.	883.	893.	902.
T/C #40	886.	888.	890.	892.	894.	909.	925.	932.	945.	957.

THERMOCOUPLE TEMPERATURE UNITS °K

DATA SUMMARY SHEET
 *** RUN 25 ***
 INNER LINER THERMOCOUPLE DATA ** METRIC UNITS **

POINT #	2211	2212	2213	2214	2215	2221	2222	2223	2224	2225
WA3 (KG/S)	9.35	9.35	9.35	9.35	9.35	9.35	9.35	9.35	9.35	9.35
WAB (KG/S)	7.93	7.93	7.93	7.93	7.93	7.93	7.93	7.93	7.93	7.93
TT3 (K)	832.	838.	836.	836.	840.	837.	839.	839.	840.	838.
PT3 (MPA)	1.736	1.724	1.697	1.729	1.722	1.700	1.686	1.728	1.728	1.725
(F/A) 4.0	0.0183	0.0213	0.0233	0.0255	0.0274	0.0196	0.0218	0.0233	0.0248	0.0266
(F/A) PILOT	0.00349	0.00350	0.00348	0.00350	0.00351	0.00504	0.00713	0.00868	0.01006	0.01179
<hr/>										
T/C # 3	888.	897.	896.	900.	903.	921.	955.	971.	991.	1004.
T/C # 4	977.	984.	984.	986.	996.	1033.	1087.	1124.	1158.	1182.
T/C #12	881.	893.	893.	899.	906.	890.	893.	895.	898.	900.
T/C #20	N/A	N/A	N/A	N/A	N/A	N/A	N/A	N/A	N/A	N/A
T/C #23	925.	936.	944.	950.	954.	938.	954.	960.	967.	976.
T/C #25	966.	978.	984.	997.	1011.	978.	996.	1013.	1027.	1043.
T/C #26	905.	922.	926.	932.	938.	911.	913.	917.	917.	918.
T/C #27	959.	971.	973.	980.	986.	961.	975.	991.	997.	1007.
T/C #28	932.	945.	948.	956.	962.	957.	983.	1004.	1020.	1034.
T/C #29	983.	1005.	1012.	1024.	1033.	1013.	1047.	1069.	1091.	1114.
T/C #30	988.	1012.	1024.	1036.	1044.	1009.	1031.	1046.	1061.	1074.
T/C #31	934.	951.	958.	965.	969.	949.	967.	978.	989.	1002.
T/C #33	962.	981.	986.	998.	1009.	975.	992.	1012.	1027.	1043.
T/C #34	1009.	1044.	1060.	1080.	1100.	1023.	1031.	1035.	1040.	1044.
T/C #35	920.	938.	940.	950.	961.	941.	963.	978.	995.	1009.
T/C #36	N/A	N/A	N/A	N/A	N/A	N/A	N/A	N/A	N/A	N/A
T/C #38	880.	892.	895.	901.	910.	879.	882.	887.	890.	897.
T/C #40	872.	882.	879.	883.	884.	901.	913.	923.	933.	943.

THERMOCOUPLE TEMPERATURE UNITS °K

DATA SUMMARY SHEET

*** RUN 25 ***

INNER LINER THERMOCOUPLE DATA ** METRIC UNITS **

POINT #	2311	2312	2313	2314	2315	2321	2323	2325
WA3 (KG/S)	13.18	13.18	13.18	13.18	13.18	13.18	13.18	13.18
WAB (KG/S)	11.18	11.18	11.18	11.18	11.18	11.18	11.18	11.18
TT3 (K)	845.	836.	833.	840.	840.	841.	842.	842.
PT3 (MPA)	2.406	2.400	2.411	2.389	2.412	2.445	2.415	2.437
(F/A) 4.0	0.0180	0.0211	0.0232	0.0253	0.0272	0.0194	0.0231	0.0261
(F/A) PILOT	0.00345	0.00344	0.00340	0.00340	0.00342	0.00492	0.00846	0.01151

T/C # 3	N/A	N/A	N/A	N/A	N/A	N/A	N/A	N/A
T/C # 4	887.	880.	877.	878.	881.	913.	1183.	1300.
T/C #12	888.	880.	879.	880.	886.	879.	897.	906.
T/C #20	N/A	N/A	N/A	N/A	N/A	N/A	N/A	N/A
T/C #23	949.	950.	954.	960.	964.	949.	970.	994.
T/C #25	965.	968.	967.	970.	976.	951.	997.	1021.
T/C #26	919.	920.	917.	920.	930.	909.	923.	929.
T/C #27	992.	997.	1006.	1012.	1039.	996.	1025.	1046.
T/C #28	969.	969.	970.	977.	992.	987.	1023.	1065.
T/C #29	1039.	1052.	1057.	1058.	1073.	1055.	1089.	1141.
T/C #30	1018.	1025.	1034.	1047.	1061.	1034.	1060.	1089.
T/C #31	942.	941.	943.	959.	962.	952.	996.	1030.
T/C #33	N/A	N/A	N/A	N/A	N/A	N/A	N/A	N/A
T/C #34	1013.	1024.	1038.	1028.	1053.	1001.	1041.	1058.
T/C #35	939.	949.	958.	954.	972.	937.	973.	1003.
T/C #36	N/A	N/A	N/A	N/A	N/A	N/A	N/A	N/A
T/C #38	N/A	N/A	N/A	N/A	N/A	N/A	N/A	N/A
T/C #40	893.	884.	886.	886.	892.	913.	937.	959.

THERMOCOUPLE TEMPERATURE UNITS °K

DATA SUMMARY SHEET

*** RUN 25 ***

INNER LINER THERMOCOUPLE DATA ** METRIC UNITS **

POINT #	2411	2413	2415	2421	2422	2423	2424
WA3 (KG/S)	15.11	15.11	15.11	15.11	15.11	15.11	15.11
WAB (KG/S)	12.81	12.81	12.81	12.81	12.81	12.81	12.81
TT3 (K)	843.	842.	843.	842.	842.	842.	843.
PT3 (MPA)	2.732	2.759	2.733	2.748	2.822	2.753	2.742
(F/A) 4.0	0.0183	0.0231	0.0273	0.0194	0.0207	0.0230	0.0246
(F/A) PILOT	0.00357	0.00342	0.00350	0.00491	0.00643	0.00849	0.00999

T/C # 3	N/A	N/A	N/A	N/A	N/A	N/A	N/A
T/C # 4	1033.	1023.	1028.	1091.	1150.	1204.	1254.
T/C #12	889.	892.	898.	894.	898.	897.	901.
T/C #20	N/A	N/A	N/A	N/A	N/A	N/A	N/A
T/C #23	941.	948.	962.	948.	962.	970.	980.
T/C #25	968.	974.	993.	977.	988.	999.	1012.
T/C #26	915.	922.	931.	919.	921.	924.	923.
T/C #27	1003.	1003.	1034.	997.	1024.	1036.	1041.
T/C #28	964.	980.	991.	979.	1010.	1026.	1049.
T/C #29	1016.	1036.	1056.	1036.	1069.	1089.	1119.
T/C #30	1013.	1035.	1054.	1022.	1045.	1061.	1078.
T/C #31	951.	966.	979.	965.	986.	1004.	1021.
T/C #33	N/A	N/A	N/A	N/A	N/A	N/A	N/A
T/C #34	1010.	1040.	1075.	1027.	1038.	1044.	1055.
T/C #35	933.	954.	960.	947.	966.	976.	988.
T/C #36	N/A	N/A	N/A	N/A	N/A	N/A	N/A
T/C #38	N/A	N/A	N/A	N/A	N/A	N/A	N/A
T/C #40	892.	890.	894.	917.	928.	944.	952.

THERMOCOUPLE TEMPERATURE UNITS °K

DATA SUMMARY SHEET ~
 *** RUN 25 ***
 INNER LINER THERMOCOUPLE DATA ** BRITISH UNITS **

POINT #	2111	2112	2113	2114	2115	2121	2122	2123	2124	2125
WA3 (LBM/S)	12.41	12.41	12.41	12.41	12.41	12.41	12.41	12.41	12.41	12.41
WAB (LBM/S)	10.52	10.52	10.52	10.52	10.52	10.52	10.52	10.52	10.52	10.52
TT3 (F)	1053.	1051.	1051.	1051.	1052.	1053.	1060.	1046.	1048.	1051.
PT3 (PSI)	148.24	148.39	147.73	149.22	147.82	149.89	147.17	149.37	152.86	151.33
(F/A) 4.0	0.0179	0.0212	0.0232	0.0253	0.0273	0.0195	0.0215	0.0230	0.0246	0.0261
(F/A) PILOT	0.00351	0.00357	0.00352	0.00355	0.00351	0.00505	0.00688	0.00855	0.01001	0.01166

T/C # 3	1142.	1147.	1147.	1147.	1151.	1194.	1243.	1254.	1284.	1317.
T/C # 4	1284.	1271.	1273.	1268.	1279.	1311.	1445.	1461.	1478.	1537.
T/C #12	1133.	1143.	1154.	1167.	1176.	1138.	1153.	1143.	1152.	1161.
T/C #20	1111.	1118.	1127.	1132.	1140.	1121.	1140.	1136.	1149.	1160.
T/C #23	1177.	1193.	1210.	1219.	1232.	1199.	1227.	1224.	1243.	1262.
T/C #25	1265.	1296.	1332.	1362.	1392.	1302.	1331.	1345.	1377.	1408.
T/C #26	1172.	1192.	1200.	1210.	1218.	1176.	1188.	1172.	1177.	1185.
T/C #27	1232.	1244.	1256.	1260.	1275.	1242.	1253.	1258.	1279.	1299.
T/C #28	1180.	997.	1012.	1200.	1263.	1246.	1285.	1297.	1322.	1347.
T/C #29	1257.	1277.	1300.	1318.	1337.	1306.	1346.	1368.	1402.	1434.
T/C #30	1291.	1322.	1340.	1362.	1380.	1327.	1366.	1378.	1395.	1424.
T/C #31	1197.	1208.	1222.	1234.	1251.	1220.	1255.	1258.	1282.	1301.
T/C #33	1251.	1270.	1306.	1334.	1350.	1282.	1314.	1328.	1352.	1385.
T/C #34	1358.	1433.	1467.	1499.	1519.	1369.	1376.	1365.	1373.	1384.
T/C #35	1201.	1215.	1225.	1232.	1244.	1224.	1254.	1265.	1293.	1320.
T/C #36	1267.	1281.	1304.	1316.	1330.	1285.	1304.	1312.	1332.	1368.
T/C #38	1135.	1135.	1147.	1151.	1157.	1127.	1133.	1131.	1148.	1165.
T/C #40	1135.	1138.	1143.	1146.	1150.	1176.	1206.	1218.	1242.	1264.

THERMOCOUPLE TEMPERATURE UNITS °F

DATA SUMMARY SHEET

*** RUN 25 ***

INNER LINER THERMOCOUPLE DATA

** BRITISH UNITS **

POINT #	2211	2212	2213	2214	2215	2221	2222	2223	2224	2225
WA3 (LBM/S)	20.62	20.62	20.62	20.62	20.62	20.62	20.62	20.62	20.62	20.62
WAB (LBM/S)	17.48	17.48	17.48	17.48	17.48	17.48	17.48	17.48	17.48	17.48
TT3 (F)	1038.	1049.	1045.	1045.	1052.	1047.	1051.	1051.	1052.	1049.
PT3 (PSI)	251.80	250.04	246.15	250.75	249.82	246.52	244.52	250.66	250.69	250.17
(F/A) 4.0	0.0183	0.0213	0.0233	0.0255	0.0274	0.0196	0.0218	0.0233	0.0248	0.0266
(F/A) PILOT	0.00349	0.00350	0.00348	0.00350	0.00351	0.00504	0.00713	0.00868	0.01006	0.01179
<hr/>										
T/C # 3	1139.	1155.	1154.	1160.	1166.	1197.	1259.	1289.	1325.	1347.
T/C # 4	1298.	1311.	1311.	1315.	1334.	1400.	1497.	1563.	1625.	1669.
T/C #12	1126.	1147.	1148.	1158.	1171.	1142.	1148.	1152.	1157.	1160.
T/C #20	N/A	N/A	N/A	N/A	N/A	N/A	N/A	N/A	N/A	N/A
T/C #23	1206.	1225.	1240.	1250.	1258.	1229.	1258.	1269.	1280.	1298.
T/C #25	1278.	1301.	1312.	1335.	1359.	1301.	1332.	1363.	1388.	1418.
T/C #26	1169.	1201.	1207.	1218.	1228.	1180.	1185.	1191.	1191.	1192.
T/C #27	1267.	1287.	1292.	1305.	1315.	1271.	1295.	1324.	1336.	1353.
T/C #28	1219.	1241.	1247.	1261.	1272.	1263.	1310.	1347.	1376.	1401.
T/C #29	1310.	1349.	1362.	1384.	1400.	1363.	1426.	1464.	1504.	1546.
T/C #30	1319.	1362.	1383.	1405.	1420.	1356.	1395.	1423.	1450.	1474.
T/C #31	1222.	1252.	1266.	1277.	1284.	1248.	1281.	1301.	1321.	1345.
T/C #33	1271.	1306.	1314.	1336.	1356.	1296.	1327.	1362.	1399.	1417.
T/C #34	1356.	1419.	1449.	1485.	1520.	1382.	1397.	1404.	1412.	1419.
T/C #35	1197.	1230.	1232.	1250.	1270.	1235.	1274.	1301.	1332.	1356.
T/C #36	N/A	N/A	N/A	N/A	N/A	N/A	N/A	N/A	N/A	N/A
T/C #38	1124.	1146.	1152.	1163.	1178.	1123.	1128.	1137.	1143.	1155.
T/C #40	1110.	1127.	1123.	1130.	1132.	1163.	1183.	1202.	1220.	1238.

THERMOCOUPLE TEMPERATURE UNITS °F

DATA SUMMARY SHEET
 *** RUN 25 ***
 INNER LINER THERMOCOUPLE DATA ** BRITISH UNITS **

POINT #	2311	2312	2313	2314	2315	2321	2323	2325
WA3 (LBM/S)	29.06	29.06	29.06	29.06	29.06	29.06	29.06	29.06
WAB (LBM/S)	24.64	24.64	24.64	24.64	24.64	24.64	24.64	24.64
TT3 (F)	1062.	1046.	1040.	1052.	1053.	1054.	1056.	1056.
PT3 (PSI)	348.98	348.14	349.74	346.45	349.81	354.56	350.20	353.40
(F/A) 4.0	0.0180	0.0211	0.0232	0.0253	0.0272	0.0194	0.0231	0.0261
(F/A) PILOT	0.00345	0.00344	0.00340	0.00340	0.00342	0.00492	0.00846	0.01151

T/C # 3	N/A	N/A	N/A	N/A	N/A	N/A	N/A	N/A
T/C # 4	1136.	1124.	1119.	1121.	1127.	1185.	1670.	1881.
T/C #12	1138.	1124.	1123.	1124.	1135.	1122.	1156.	1172.
T/C #20	N/A	N/A	N/A	N/A	N/A	N/A	N/A	N/A
T/C #23	1249.	1250.	1258.	1269.	1276.	1249.	1287.	1330.
T/C #25	1277.	1283.	1281.	1286.	1297.	1253.	1335.	1378.
T/C #26	1194.	1196.	1191.	1197.	1215.	1177.	1201.	1213.
T/C #27	1326.	1335.	1350.	1363.	1410.	1334.	1386.	1424.
T/C #28	1285.	1284.	1287.	1299.	1326.	1317.	1381.	1457.
T/C #29	1411.	1434.	1443.	1445.	1472.	1439.	1501.	1593.
T/C #30	1372.	1385.	1402.	1426.	1450.	1401.	1448.	1500.
T/C #31	1235.	1234.	1237.	1267.	1272.	1254.	1333.	1394.
T/C #33	N/A	N/A	N/A	N/A	N/A	N/A	N/A	N/A
T/C #34	1363.	1384.	1408.	1390.	1436.	1342.	1414.	1445.
T/C #35	1230.	1248.	1265.	1258.	1290.	1227.	1291.	1345.
T/C #36	N/A	N/A	N/A	N/A	N/A	N/A	N/A	N/A
T/C #38	N/A	N/A	N/A	N/A	N/A	N/A	N/A	N/A
T/C #40	1147.	1132.	1136.	1135.	1145.	1183.	1227.	1266.

THERMOCOUPLE TEMPERATURE UNITS °F

DATA SUMMARY SHEET
 *** RUN 25 ***
 INNER LINER THERMOCOUPLE DATA ** BRITISH UNITS **

POINT #	2411	2413	2415	2421	2422	2423	2424
WA3 (LBM/S)	33.31	33.31	33.31	33.31	33.31	33.31	33.31
WAB (LBM/S)	28.24	28.24	28.24	28.24	28.24	28.24	28.24
TT3 (F)	1058.	1057.	1058.	1057.	1056.	1055.	1057.
PT3 (PSI)	396.31	400.14	396.42	398.57	409.30	399.27	397.65
(F/A) 4.0	0.0183	0.0231	0.0273	0.0194	0.0207	0.0230	0.0246
(F/A) PILOT	0.00357	0.00342	0.00350	0.00491	0.00643	0.00849	0.00999

T/C # 3	N/A	N/A	N/A	N/A	N/A	N/A	N/A
T/C # 4	1399.	1381.	1391.	1505.	1611.	1708.	1798.
T/C #12	1141.	1147.	1157.	1149.	1157.	1155.	1162.
T/C #20	N/A	N/A	N/A	N/A	N/A	N/A	N/A
T/C #23	1234.	1246.	1272.	1248.	1271.	1286.	1305.
T/C #25	1282.	1293.	1328.	1299.	1318.	1339.	1363.
T/C #26	1188.	1200.	1216.	1194.	1198.	1204.	1202.
T/C #27	1346.	1346.	1401.	1335.	1384.	1405.	1413.
T/C #28	1275.	1304.	1325.	1303.	1358.	1387.	1429.
T/C #29	1369.	1405.	1441.	1405.	1464.	1501.	1555.
T/C #30	1363.	1403.	1437.	1380.	1421.	1451.	1430.
T/C #31	1252.	1280.	1303.	1278.	1316.	1347.	1379.
T/C #33	N/A	N/A	N/A	N/A	N/A	N/A	N/A
T/C #34	1359.	1413.	1475.	1389.	1409.	1420.	1439.
T/C #35	1219.	1258.	1268.	1245.	1279.	1298.	1319.
T/C #36	N/A	N/A	N/A	N/A	N/A	N/A	N/A
T/C #38	N/A	N/A	N/A	N/A	N/A	N/A	N/A
T/C #40	1147.	1143.	1150.	1190.	1211.	1240.	1255.

THERMOCOUPLE TEMPERATURE UNITS °F

LIST OF ABBREVIATIONS AND SYMBOLS

AC_d	effective flow area
A_e	exit area
avg	average
CO	carbon monoxide
D_e	exit diameter
D_i	inlet diameter
EGV	exit guide vane
EI	emissions index
EPAP	Environmental Protection Agency Parameter
F/A	fuel/air ratio
FPS	Flight Propulsion System
ID	inner diameter
ICLS	Integrated Core/Low Spool
L	length
$L/\Delta R$	length to radius ratio
LBO	lean blowout
msec	millisecond
NO_x	oxides of nitrogen
OD	outer diameter
PDR	Preliminary Design Review
P_{T3}	diffuser inlet total pressure
ρ_j/ρ_∞	density ratio
$\Delta P/P$	pressure loss
R	radius
SAE	Society of Automotive Engineer
SLTO	sea level takeoff
SMD	Sauter mean diameter
T	temperature
ΔT	temperature rise
T_{T3}	diffuser inlet total temperature
T_{T4}	combustor exit total temperature
THC	total hydrocarbons
TOBI	tangential on-board injection
U	velocity
u_j/u	vane length swirler
W_A	air flow
W_{A3}	diffuser inlet flow
W_B	combustor flow
X/D	axial position
y/D	radial penetration
β	angle
Δ	difference
ϕ	equivalence ratio
γ	angle

REFERENCES

1. Sattar, M.A. and Lohmann, R.P. "Advanced Composite Combustor Structural Concepts Program - Final Report," NASA CR 174733, December 1984.
2. Layden, G.K. and K.M. Prewo, "Advanced Fabrication of SiC Fiber Reinforced Glass Ceramic Matrix Composites," Final Report, Office of Naval Research Contract N00014-81-C-0218, 1982.
3. Brennan, J.J., "Additional Studies of SiC Fiber Reinforced Glass-Ceramic Matrix Composites," Office of Naval Research Report R83-916018-2, February 1983.
4. Prewo, K.M., "Advanced Characterization of SiC Fiber Reinforced Glass Ceramic Matrix Composites," Office of Naval Research Report R83-915939-1, June 1983.
5. Prewo, K.M., J.J. Brennan and E.R. Thompson, "Study of Potential Engine Component Applications for Silicon Carbide-Glass Ceramic Materials," Office of Naval Research Report R81-915596-1, 1981.
6. Brennan, J.J., "Program to Study SiC Fiber Reinforced Glass Matrix Composites," Office of Naval Research Report R80-914401-4, November 1980.
7. Brennan, J.J. and K.M. Prewo, "Study of Lithium Aluminosilicate (LAS)/SiC Fiber Composites for Naval Gas Turbine Applications," Naval Air Systems Command Report R82-915778-4, October 1982.
8. McCormick, C.W., editor, "MSC/NASTRAN Users Manual," Macneal-Schwendler Corporation, Los Angeles, CA, May 1983.
9. Prewo, K.H., Brennan, J.J., Minford, E.J. and Layden, G.K., "Advanced Characterization of Silicon Carbide Fiber Reinforced Glass Ceramic Matrix Composites" Contract N00014-81-C-0571, Office of Naval Research, June 30, 1985.
10. Dubiel, D.J., W. Greene, C.V. Sundt, S. Tanrikut and M.H. Zeisser, "Energy Efficient Engine Sector Combustor Rig Test Program Technology Report," National Aeronautics and Space Administration CR-167913, September 1982.
11. Zeisser, M.H., W. Green and D.J. Dubiel, "Energy Efficient Engine Combustor Test Hardware Detailed Design Report," NASA CR-167945, March 1982.
12. Dubiel, D.J., "Energy Efficient Engine Combustor Component Performance Program," NASA CR-179533, September 1986.
13. Sturgess, G.J., "Aerothermal Modeling Phase I - Final Report," NASA CR-168202, May 1983.
14. Lefebvre, D.H., "Gas Turbine Combustion," McGraw Hill Series in Energy, Combustion and Environment, 1983.

DISTRIBUTION LIST

NASA Scientific and Technical
Information Facility
P.O. Box 8757
B.W.I. Airport, MD 21240

NASA Headquarters
600 Independence Avenue, S.W.
Washington, D.C. 20564
Attn: R/R. Rosen

NASA Headquarters
600 Independence Avenue, S.W.
Washington, D.C. 20564
Attn: RJ/C. Rosen

NASA Headquarters
600 Independence Avenue, S.W.
Washington, D.C. 20546
Attn: RP/E. Gabris

NASA Headquarters
600 Independence Avenue, S.W.
Washington, D.C. 20546
Attn: RP/J. Facey

NASA Lewis Research Center
21000 Brookpark Road
Cleveland, OH 44135
Attn: J.A. Ziemianski, MS 86-1

NASA Lewis Research Center
21000 Brookpark Road
Cleveland, OH 44135
Attn: C.C. Ciepluch, MS 77-10

NASA Lewis Research Center
21000 Brookpark Road
Cleveland, OH 44135
Attn: P.G. Batterton, MS 86-4

NASA Lewis Research Center
21000 Brookpark Road
Cleveland, OH 44135
Attn: G.K. Sievers, MS 86-7

NASA Lewis Research Center
21000 Brookpark Road
Cleveland, OH 44135
Attn: E.T. Meleason, MS 77-10

NASA Lewis Research Center
21000 Brookpark Road
Cleveland, OH 44135
Attn: Report Control, MS 60-1

NASA Lewis Research Center
21000 Brookpark Road
Cleveland, OH 44135
Attn: N.T. Saunders, MS 3-8

NASA Lewis Research Center
21000 Brookpark Road
Cleveland, OH 44135
Attn: M.J. Hartmann, MS 3-7

NASA Lewis Research Center
21000 Brookpark Road
Cleveland, OH 44135
Attn: J.C. Williams, MS 500-211

NASA Lewis Research Center
21000 Brookpark Road
Cleveland, OH 44135
Attn: L.J. Kiraly, MS 23-3

NASA Lewis Research Center
21000 Brookpark Road
Cleveland, OH 44135
Attn: D.C. Mikkelsen, MS 6-12

NASA Lewis Research Center
21000 Brookpark Road
Cleveland, OH 44135
Attn: R. Paginton, MS 500-305

NASA Lewis Research Center
21000 Brookpark Road
Cleveland, OH 44135
Attn: R.H. Johns, MS 49-8

NASA Lewis Research Center
21000 Brookpark Road
Cleveland, OH 44135
Attn: J.R. Mihalow, MS 86-4

NASA Lewis Research Center
21000 Brookpark Road
Cleveland, OH 44135
Attn: L. Reid, MS 5-3

DISTRIBUTION LIST (Continued)

NASA Lewis Research Center
21000 Brookpark Road
Cleveland, OH 44135
Attn: R.W. Niedzwiecki, MS 77-6

NASA Lewis Research Center
21000 Brookpark Road
Cleveland, OH 44135
Attn: AFSC Liaison Office, MS 501-3

NASA Lewis Research Center
21000 Brookpark Road
Cleveland, OH 44135
Attn: Army R&T Propulsion, MS 77-12

NASA Ames Research Center
Moffett Field, CA 94035
Attn: M.H. Waters, MS 202-7

NASA Dryden Flight Research Center
P.O. Box 273
Edwards, CA 93523
Attn: J.A. Albers

NASA Langley Research Center
Hampton, VA 23665-5225
Attn: Bob James, MS 258

Department of Defense
Washington, D.C. 20301
Attn: R. Standahar, 3D1089/Pentagon

Wright-Patterson Air Force Base
Dayton, OH 45433
Attn: APL Chief Scientist, AFWAL/PS

Wright-Patterson Air Force Base
Dayton, OH 45433
Attn: E.E. Abell, ASD/YZE

Wright-Patterson Air Force Base
Dayton, OH 45433
Attn: H.I. Bush, AFWAL/POT

Wright-Patterson Air Force Base
Dayton, OH 45433
Attn: R.P. Carmichael, ASD/XRHI

Wright-Patterson Air Force Base
Dayton, OH 45433
Attn: R. Ellis, ASD/YZN

Wright-Patterson Air Force Base
Dayton, OH 45433
Attn: W.H. Austin, Jr., ASD/ENF

Eustis Directorate
U. S. Army Air Mobility
R&D Laboratory
Fort Eustis, VA 23604
Attn: J. Lane, SAVDL-EU-Tapp

Navy Department
Naval Air Systems Command
Washington, D.C. 20361
Attn: W. Koven, AIR-03E

Navy Department
Naval Air Systems Command
Washington, D.C. 20361
Attn: J.L. Byers, AIR-53602

Navy Department
Naval Air Systems Command
Washington, D.C. 20361
Attn: E.A. Lichtman, AIR-330E

Navy Department
Naval Air Systems Command
Washington, D.C. 20361
Attn: G. Derderian, AIR-5362C

Naval Air Propulsion Test Center
Trenton, NJ 08628
Attn: J.J. Curry
A. Cifone

USAVRAD Command
P.O. Box 209
St. Louis, MO 63166
Attn: Robert M. Titus (ASTIO)

Department of Transportation
NASA/DOT Joint Office of
Noise Abatement
Washington, D.C. 20590
Attn: C. Foster

Federal Aviation Administration
Noise Abatement Division
Washington, D.C. 20590
Attn: E. Sellman, AEE-120

DISTRIBUTION LIST (Continued)

Federal Aviation Administration
12 New England Executive Park
Burlington, MA 18083
Attn: Jack A. Sain, ANE-200

Curtiss Wright Corporation
Woodridge, NJ 07075
Attn: S. Lombardo
S. Moskowitz

Detroit Diesel, Allison Div., GMC
P.O. Box 894
Indianapolis, IN 46206
Attn: D. Quick

AVCO/Lycoming
550 S. Main Street
Stratford, CT 06497
Attn: H. Moellmann

The Garrett Corporation
AiResearch Manufacturing Co.
Torrance, CA 90509
Attn: F.E. Faulkner

The Garrett Corporation
AiResearch Manufacturing Co.
402 South 36 Street
Phoenix, AZ 85034
Attn: M.L. Early

AiResearch Manufacturing Co.
111 South 34th Street
P.O. Box 5217
Phoenix, AZ 85010
Attn: C.E. Corrigan (93-120/503-4F)

General Electric Company/AEG
One Neumann Way
P.O. Box 15631
Cincinnati, OH 45215
Attn: R.W. Bucy
T.F. Donahue

General Electric Company/AEG
1000 Western Avenue
Lynn, MA 01910
Attn: R.E. Neitzel

Pratt & Whitney Group/UTC
Government Products Division
P.O. Box 109600
West Palm Beach, FL 23410-9600
Attn: B.A. Jones

Pratt & Whitney Group/UTC
Commercial Products Division
East Hartford, CT 06108
Attn: D. Gray MS 162-25

Lockheed-California Co.
Burbank, CA 91502
Attn: J.F. Stroud, Dept. 75-42
R. Tullis, Dept. 75-21

Williams Research Co.
2280 W. Maple Road
Walled Lake, MI 48088
Attn: R. Van Nimwegen
R. Horn
Library

Teledyne CAE, Turbine Engines
1330 Laskey Road
Toledo, OH 43612
Attn: E. Benstein

Douglas Aircraft Company
McDonnell Douglas Corp.
3855 Lakewood Blvd.
Long Beach, CA 90846
Attn: R.T. Kawai, Code 36-41
M. Klotzche

Boeing Commercial Airplane Co.
P.O. Box 3707
Seattle, WA 98124
Attn: P. E. Johnson, MS 9H-46

Boeing Commercial Airplane Co.
P.O. Box 3707
Seattle, WA 98124
Attn: D.C. Nordstrom, MS 73-4F

Brunswick Corporation
2000 Brunswick Lane
Deland, FL 32720
Attn: A. Erickson

Drexel University
College of Engineering
Philadelphia, PA 19104
Attn: A.M. Mellor

P0869464

**NASA
FORMAL
REPORT**

1